# The impact of turbulence modelling on large offshore wind turbine response

Astrid Nybø

Thesis for the degree of Philosophiae Doctor (PhD)
University of Bergen, Norway
2022

UNIVERSITY OF BERGEN

# The impact of turbulence modelling on large offshore wind turbine response

Astrid Nybø


Thesis for the degree of Philosophiae Doctor (PhD)
at the University of Bergen

Date of defense: 28.10.2022

Year: 2022

Title: The impact of turbulence modelling on large offshore wind turbine response

Name: Astrid Nybø

Print: Skipnes Kommunikasjon / University of Bergen

## Scientific environment

My PhD was carried out at the Geophysical Institute, University of Bergen. The work was funded by the University of Bergen.

I was lucky to have a wide scientific network. I have been a member of the Bergen Offshore Wind centre since its beginning in 2017. One of my co-authors work at Equinor, which has brought me possibilities to discuss issues with her professional network. I also got the opportunity to cooperate with the National Renewable Energy Laboratory (NREL), which led to a visit at their research facilities in Boulder, Colorado.

I have had the chance to attend excellent scientific courses, both through the University of Bergen and elsewhere. I was enrolled in the CHESS Research School, and attended courses both in Bergen and at the Alfred Wegener Institute in Bremerhaven. I also attended a course at the Technical University of Denmark (DTU).

Last, I would like to mention that I have done a significant amount of duty work as part of the PhD. This covered co-developing, administrating and lecturing the course ENE101 Introduction to Energy Resources and Consumption, and supervision of Master students.

CHESS
Research school on changing climates in the coupled earth system

UNIVERSITY OF BERGEN
*Bergen Offshore Wind Centre*

# Acknowledgements

First, I would like to express my gratitude to my supervisors, Finn Gunnar Nielsen, Joachim Reuder and Marte Godvik for excellent supervision of this PhD work. I am very grateful for your scientific guidance, useful suggestions and most importantly interesting discussions. You have all significantly improved the articles of this thesis. A special thanks goes to Finn Gunnar, for following my PhD work from beginning to end as my main supervisor.

I would furthermore like to thank my colleagues and fellow students at GFI, especially Maylinn Haaskjold Myrtvedt, Etienne Cheynet and Vegard Milde, for motivating and assisting me in this work.

A portion of this research was performed using computational resources sponsored by the U.S. Department of Energy's Office of Energy Efficiency and Renewable Energy and located at the National Renewable Energy Laboratory. Matthew Churchfield has run all the large eddy simulations and contributed with his knowledge on this topic. His support has significantly improved the quality of this PhD work and is highly appreciated.

I would like to thank Kjersti Birkeland Daae and Stephan Kral for making the template of this thesis available on Overleaf, and Tore Birkeland and Raymond Nepstad for creating the original version of the template.

Finally, I would like to thank my family and friends, especially mamma, pappa, and my brothers for believing in me. Thank you, Hans-Kristian, not only for personal support, but for being the very best office partner and helping me with all my scientific issues. Most importantly, a great thank you to my daughters, Frøya and Johanne, for distracting me and helping me keep my priorities straight.

Astrid Nybø
Bergen, July 2022

# Abstract

In order to reduce climate change, a large up-scaling of renewable energy capacity is necessary in the near future. Offshore wind is expected to play a key role in this green shift. The wind conditions offshore are in general superior to onshore, and large areas are available. Furthermore, costs of offshore wind turbines have decreased drastically and are expected to decrease even further. This is partly due to the trend of increasing rotor sizes, which increases the energy extraction per installed wind turbine.

In the design of wind turbines, it is crucial to simulate expected fatigue and power production. With increasing rotor sizes, the relative importance of the wind load increases, and its accurate characterization becomes essential. This, in turn, requires the proper understanding of the flow conditions over the whole rotor disk of large, modern wind turbines. With increasing turbine size in general, and for floating wind turbines with low eigen-frequencies in particular, larger time scales gain additional importance. The current wind turbine design standards recommend two simple turbulence models for estimating wind load in wind turbine design. These models are originally developed for small, onshore wind turbines, and do not account for variations in atmospheric stability.

This thesis highlights the challenges of existing turbulence models used in wind turbine design. Wind fields obtained by the standard turbulence models are compared to each other, to quality assured, high-frequency measurements, and to wind fields simulated by more complex turbulence models. The two more complex models are based on measurements and on large eddy simulations. The main focus of the turbulence modelling is directed towards the estimation of coherent structures over the rotor plane. The different turbulence models are evaluated for various atmospheric stability conditions, and the obtained wind fields are used in aero-hydro-servo-elastic simulations of a large bottom-fixed and floating wind turbine. The resulting differences in wind turbine response are evaluated.

As a first step, sonic anemometer measurements from an offshore meteorological mast are processed in this thesis, in order to obtain quality-assured, high-frequency measurements. The measurements are processed for wind energy applications, providing continuous and long enough time series for the proper consideration of the relevant low-frequency range. It is, however, a challenge to achieve stationarity in longer time series of the wind speed, as the true wind conditions are continuously changing.

The wind spectra obtained by the standard turbulence models are similar to each other. The standard turbulence models are unable to obtain low-frequency fluctuations in wind speed that are present in the measured spectra. It is known that an accurate modelling of low frequencies is important for floater response, but this thesis demonstrates the importance also for a bottom-fixed offshore wind turbine. An accurate representation of wind spectra is particularly important to the tower bottom fore-aft and blade root flapwise bending moments of the bottom-fixed wind turbine, and surge and pitch displacements of the floater. The standard turbulence models tend to underestimate these dynamic moments and motions due to their lack of large-scale fluctuations. Underestimation of loads in the design phase of wind turbines may in the worst case lead to reduced fatigue life and unexpected maintenance.

The two standard turbulence models differ in their coherence estimates. For state-of-

the-art rotor sizes, the coherence, representing the variation of wind speed over the rotor, is an important design parameter. As a consequence of modelling coherence differently, the wind turbine response varies significantly with the choice of turbulence model. With low coherence in the across wind direction, high dynamic yaw moments and motions are obtained. On the contrary, the dynamic thrust force is lower with lower coherence, and consequently also the moments and motions depending on it.

Knowledge of the true offshore coherence is limited as measurements are scarce, especially in the across wind direction. It is therefore challenging to evaluate the accuracy of existing coherence models. With improved coherence measurements, one could easier evaluate the accuracy of turbulence models, and even find a more realistic turbulence model than the ones that are used today.

The wind fields of the turbulence models based on measurements and large eddy simulation show significant differences with atmospheric stability conditions, which the standard turbulence models do not consider. These differences impact the dynamic response of the offshore wind turbines significantly. The more complex turbulence models have their own challenges, such as requirements of large amounts of high-frequency, quality assured measurements or high computational costs. Given the challenges of the turbulence models already discussed, one of the standard turbulence models was fitted to site specific measurements in this thesis. The resulting tower bottom and blade root response are more realistic, but the overall quantitative improvements are uncertain.

This thesis shows how different turbulence models cause significant differences in the dynamic response of large bottom-fixed and floating wind turbines. It concludes that it is time for the wind turbine standards and industry to consider more advanced turbulence models that account for atmospheric stability in wind turbine design.

# Samandrag

For å redusere klimaendringane, er ei stor oppskalering i kapasitet av fornybar energi naudsynt i næraste framtid. Havvind er forventa å spele ei viktig rolle i dette grøne skiftet. Vindforholda til havs er generelt betre enn på land, og store område er tilgjengelege. Dessutan har kostnadane på vindturbinar til havs gått drastisk ned, og dei er forventa å gå vidare ned. Dette er delvis grunna tendensen til aukande rotorstorleik som aukar energiutvinninga per installert vindturbin.

I design av vindturbinar er det avgjerande å simulere forventa utmatting og kraftproduksjon. Med aukande rotorstorleikar, aukar den relative viktigheita av vindlasten, og den nøyaktige karakteriseringa av vindlasten blir essensiell. Dette igjen, krev riktig forståing av strøymingsforholda over heile rotordisken til store, moderne vindturbinar. Med aukande turbinstorleik generelt, og for flytande vindturbinar med låge eigen-frekvensar spesielt, blir store tidsskala ekstra viktig. Dei aktuelle standardane for vindturbindesign anbefaler to enkle turbulensmodellar for å estimere vindlast i vindturbindesign. Desse modellane er i utgangspunktet meint for små vindturbinar på land, og tek ikkje omsyn til variasjonar i atmosfærisk stabilitet.

Denne avhandlinga framhevar utfordringane til eksisterande turbulensmodellar som er brukt i vindturbindesign. Vindfelt som er generert av turbulensmodellane frå standardane er samanlikna med kvarandre, med kvalitetssikra, høg-frekvente målingar, og med vindfelt simulert med meir komplekse turbulensmodellar. Dei to meir komplekse modellane er basert på målingar og "large eddy simulation" (stor virvelsimulering). Hovudfokuset av turbulensmodelleringa er retta mot estimering av koherente strukturar over rotorplanet. Turbulensmodellane er vurdert for ulike atmosfæriske stabilitetsforhold, og dei genererte vindfelta er brukt i "aero-hydro-servo-elastic" simuleringar av ein stor botnfast og flytande vindturbin. Dei resulterande forskjellane i vindturbinrespons er vurdert.

Som eit første steg, er målingar frå soniske anemometer på ein meteorologisk mast til havs prosesserte i denne avhandlinga, for å oppnå kvalitetssikra, høg-frekvente målingar. Målingane er prosesserte for vindenergiformål, med resulterande samanhengande og lange nok tidsseriar for å ta omsyn til det relevante låg-frekvente området. Det er ei utfordring å oppnå stasjonære, lange tidsseriar av vindfart, då dei sanne vindforholda endrast kontinuerleg.

Vindspektruma frå turbulensmodellane frå standardane liknar på kvarandre. Turbulensmodellane frå standardane er ikkje i stand til å oppnå storskala svingingar i vindfart som er til stades i dei målte spektruma. Det er kjend at ei nøyaktig modellering av låge frekvensar er viktig for flytarrespons, men denne avhandlinga demonstrerer viktigheita òg for ein botnfast vindturbin til havs. Ein nøyaktig representasjon av vindspektruma er spesielt viktig for tårnbotn for-akter og bladrot klaffevis bøyemoment for den botnfaste vindturbinen, og jag- og stamp-forskyvingar for flytaren. Turbulensmodellane frå standardane har ein tendens til å underestimere desse dynamiske momenta og rørslene på grunna av deira mangel på stor-skala svingingar. Underestimering av lastar i designfasen av vindturbinar kan i verste fall føre til redusert utmattingsliv og uventa vedlikehald.

Dei to standard turbulensmodellane er ulik i deira koherensestimat. For topp moderne rotorstorleikar er koherensen, som representerer variasjon i vindfart over rotoren, ein viktig designparameter. Som ein konsekvens av å modellere koherens ulikt, varierer

vindturbinresponsen vesentleg med val av koherensmodell. Med låg koherens i retninga på tvers av vinden, oppnår ein høge dynamiske gir-moment og -rørsler. Til motsetning, er den dynamiske skyvkrafta lågare med lågare koherens, og følgjeleg òg momenta og rørslene som er avhengige av ho.

Kunnskap om den sanne koherensen til havs er avgrensa, då tilgang på målingar er knapp, spesielt i retninga på tvers av vinden. Det er difor utfordrande å vurdere nøyaktigheita av eksisterande koherensmodellar. Med forbetra koherensmålingar, kan ein enklare vurdere nøyaktigheita av turbulensmodellar, og til og med finne ein meir realistisk turbulensmodell enn dei som blir brukt i dag.

Vindfelta til turbulensmodellane som er baserte på målingar og "large eddy simulation" viser betydelege forskjellar med atmosfæriske stabilitetsforhold, som turbulensmodellane frå standardane ikkje tek omsyn til. Desse forskjellane har betydeleg innverknad på den dynamiske responsen til vindturbinar til havs. Dei meir komplekse turbulensmodellane har eigne utfordringar, som behov for store mengder høg-frekvente, kvalitetssikra målingar eller høg kostnad for utrekningskraft. Gitt utfordringane til turbulensmodellane som allereie er diskutert, er ein av turbulensmodellane frå standardane tilpassa lokasjonsspesifikke målingar i denne avhandlinga. Den resulterande responsen i tårnbotn og bladrot er meir realistisk, men dei overordna kvantitative forbetringane er usikre.

Denne avhandlinga viser korleis ulike turbulensmodellar forårsakar betydelege forskjellar i dynamisk respons til store botnfaste og flytande vindturbinar. Ho konkluderer med at det er på tide at vindturbinstandardane og -industrien vurderer meir avanserte turbulensmodellar som tek omsyn til atmosfærisk stabilitet i vindturbindesign.

# List of publications

The present thesis consists of this synthesis and the following journal articles (1-5), which will be referred to by their numbers. I have done the majority of the data management, modelling, analysis and writing of these five works, with excellent guidance from the co-authors. The LES wind fields are generated by Matthew Churchfield at NREL.

1. **Processing of sonic anemometer measurements for offshore wind turbine applications.**
   A. Nybø, F. G. Nielsen and J. Reuder.
   In *Journal of Physics: Conference Series*, Trondheim, Norway 2019. doi:10.1088/1742-6596/1356/1/012006.

2. **Evaluation of different wind fields for the investigation of the dynamic response of offshore wind turbines.**
   A. Nybø, F. G. Nielsen, J. Reuder, M. J. Churchfield, and M. Godvik.
   *Wind Energy*, **23**(9):1810–1830, 2020. doi:10.1002/we.2518.

3. **Quasi-static response of a bottom-fixed wind turbine subject to various incident wind fields.**
   A. Nybø, F. G. Nielsen and M. Godvik.
   *Wind Energy*, **24**(12):1482–1500, 2021. doi:10.1002/we.2642.

4. **Analysis of turbulence models fitted to site, and their impact on the response of a bottom-fixed wind turbine.**
   A. Nybø, F. G. Nielsen and M. Godvik.
   In *Journal of Physics: Conference Series*, 2021. doi:10.1088/1742-6596/2018/1/012028.

5. **Sensitivity of the dynamic response of a multimegawatt floating wind turbine to the choice of turbulence model.**
   A. Nybø, F. G. Nielsen and M. Godvik.
   *Wind Energy*, **25**(6):1013-1029, 2022. doi:10.1002/we.2712.

In addition to the publications listed above, I have contributed as a co-author in the following journal articles (I-II), which are not to be considered as part of this thesis.

I. **Transitioning remote Arctic settlements to renewable energy systems - A modelling study of Longyearbyen, Svalbard.**
   H.-K. Ringkjøb, P. M. Haugan and A. Nybø.
   *Applied Energy*, **258**(114079):1–13, 2020. doi:10.1016/j.apenergy.2019.114079.

II. **The dynamic response of offshore wind turbines and their sensitivity to wind field models.**
   M. H. Myrtvedt, A. Nybø and F. G. Nielsen.
   In *Journal of Physics: Conference Series*, Trondheim, Norway, 2020. doi:10.1088/1742-6596/1669/1/012013.

# Contents

# 1 Introduction

The greenhouse gas emissions are higher than ever before, and evidence of climate change is seen all over the world. In their last report, the Intergovernmental Panel on Climate Change (IPCC) highlights the immediate need to act in order to minimize adverse effects of climate change [1]. The IPCC researchers point at renewable energy, especially solar and wind, as efficient and affordable solutions to reduce greenhouse gas emissions. Solar panels and wind turbines are mature and well-established technologies that are ready to be built in large scale today.

Offshore wind is expected to be a key technology in this context. The International Renewable Energy Agency (IRENA) expects close to 1000 GW of offshore wind installed globally in 2050 [2] and the International Energy Agency (IEA) projects offshore wind to become a $1 trillion industry by 2040 [3]. The IEA also predicts that by then offshore wind energy may become the number one source of power generation in Europe. Many countries have recently increased their offshore wind ambitions. The actual focus areas are Europe, Asia, and the US [4, 5, 6, 7]. In addition to the urgency of mitigating climate change, cost reductions and the current geopolitical situation have made offshore wind and other renewable energy solutions even more relevant [1, 8, 7].

One pathway to reduce the cost of offshore wind energy is to increase the size of the turbines. The latest generation of offshore wind turbines in the 15-MW class are approaching or even exceeding rotor diameters of 250 m [9]. With larger structures, it becomes increasingly important to model the wind load correctly in wind turbine design. Veers at al. [10] consider the improved understanding of atmospheric flow physics and aerodynamics of enlarged wind turbines as two of the grand challenges in the science of wind energy. The swept area of the current large wind turbine rotors covers great variations in the flow field.

In order to model the wind load correctly, one must first understand the actual offshore wind characteristics properly. As the infrastructural requirements of offshore measurements are considerable, observations are rather scarce. The infrastructural requirements are less significant in remote sensing, e.g. through LIDARs. However, LIDAR measurements face challenges of measuring turbulence properly [11, 12, 13, 14]. The sources of error cover cross-contamination of the horizontal velocity components due to large separation distances, time averaging effects, and line-of-sight averaging effects. Sonic anemometers capture turbulence successfully, and are commonly used for characterization of turbulence in the atmospheric boundary layer. One may still question the quality of sonic anemometer datasets, and their applicability to wind turbine considerations. E.g., sonic anemometer measurements are sensitive to rain and other disturbances. They are furthermore mounted at meteorological masts, which are limited in height. Meteorological measurements are commonly analysed in blocks of 10 minutes. The analysis of offshore wind turbine loads requires longer time series, as the low-frequency region ($f<0.1$ Hz) is of high importance on the total loads and motions. The low-frequency region is of particular importance for floaters that have eigenfrequencies in this frequency range.

The International Electrotechnical Commission [15] recommends two different turbulence models to represent the wind load in wind turbine design. These are referred

to as the Mann spectral tensor model [16], hereafter denoted "Mann", and the Kaimal spectrum [17] and exponential coherence model [15], hereafter denoted "Kaimal". Turbulence models generate a wind spectrum for every simulated point in space, and ensures coherence between these points. Coherence describes the correlation of wind speed over the rotor plane. The point spectra of the two standard turbulence models are similar, but they vary in their coherence formulations. The standard turbulence models have been originally derived for small onshore wind turbines, where the variation of wind speed over the rotor plane is less important. For state-of-the-art wind turbines with large rotors, however, coherence becomes an important design parameter. The variation of wind speed over the rotor plane vary significantly with the stability of the atmosphere, but this effect is not accounted for by the standard models [15].

Bachynski and Eliassen [18, 19], Doubrawa et al. [20], Godvik [21] and Putri et al. [22, 23] have shown that offshore wind turbine response is dependent on the turbulence model chosen. The mentioned studies all consider the Kaimal and Mann wind fields, but vary in type of wind turbine foundation considered, power capacity of the wind turbine(s) considered, and response loads and motions analysed. Bachynski and Eliassen and Putri et al. support their findings with comparisons of the Mann and Kaimal wind fields. These studies, and also the studies by Eliassen and Obhrai [24] and Eliassen and Andersen [25], show that the Mann and Kaimal models produce the same wind spectra, but vary in their coherence formulations. As mentioned, larger variations over the rotor plane are expected for larger wind turbine rotors. The turbulence models are also compared to offshore measurements by Eliassen and Obhrai [24] and Cheynet et al. [26, 27].

The majority of the mentioned studies consider relatively small wind turbines [18, 20, 21, 22, 23]. Moreover, the evaluation of the two mentioned turbulence models is commonly limited to comparisons to each other [18, 19, 21, 25], while comparisons to alternative models are not considered. This thesis builds on, and is inspired by the work of Godvik [21], Doubrawa et al. [20], Bachynski and Eliassen et al. [18, 19, 24, 25] and Cheynet et al. [26, 27].

The main objective of this thesis is to better understand the differences and challenges of existing ways of modelling turbulence for the design of large offshore wind turbines. The following research questions guide the scientific work addressed in the attached articles:

1. How should sonic anemometer measurements be processed to achieve a quality assured dataset for offshore wind turbine applications?

2. How do the Kaimal and Mann wind fields compare to each other, and to wind fields obtained by more realistic models based on measurements and large eddy simulations?

   (a) What are the main differences of these four wind fields, and how do they compare to measurements?

   (b) What are the main differences in the dynamic response of a large bottom-fixed wind turbine subject to these four wind fields?

   (c) What are the main differences in the dynamic response of a large floating wind turbine subject to these four wind fields?

   (d) How do the Kaimal and Mann models perform in various atmospheric stability conditions?

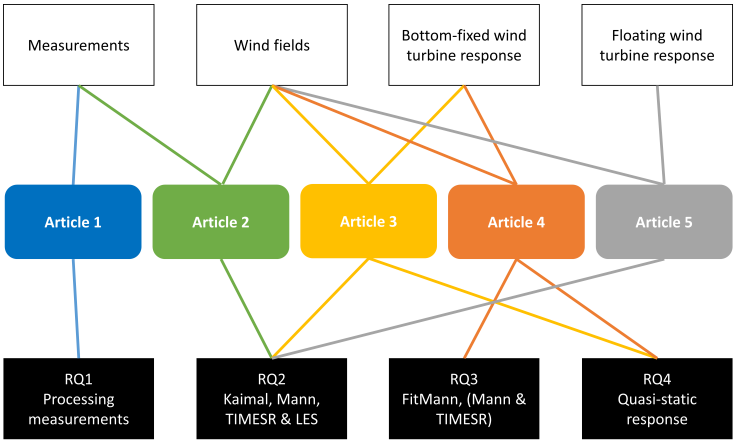


*Figure 1.1: Relation between articles (mid), research questions (RQ) (bottom) and main focus of the analysis (top)*

(e) What challenges do the "more realistic" models face, and are they really more realistic?

3. Is fitting of Mann parameters an easy solution to better represent the offshore wind field?

4. What is the importance of the quasi-static region on the total dynamic response of an offshore bottom-fixed wind turbine?

Figure 1.1 gives an overview of which articles answer the different research questions. It also shows whether the different articles focus on measurements, wind fields, bottom-fixed wind turbine response, floating wind turbine response or a combination of these.

Research question 1 is addressed in Article 1. This paper thoroughly describes a quality control routine specific for wind turbine applications, and a large quality assured dataset is presented. Existing literature is limited to processing procedures for boundary layer meteorology applications [28, 29, 30], or dedicate limited attention to the processing procedure of the data used [27, 26, 31, 24, 32, 33].

Research questions 2(a), (d) and (e) are addressed in Article 2. This paper describes, evaluates, and compares wind fields created by Mann, Kaimal, a turbulence model based on measurements (TIMESR), and large eddy simulations (LES). The comparison of Kaimal, Mann, TIMESR and LES to each other and to measurements is unique. The coherent structures are analysed, considering co-coherence, quad-coherence, and proper orthogonal decomposition (POD) modes. Comparisons are performed in three wind speed situations and three atmospheric stability situations. It is important to understand the wind fields properly in order to understand the differences in response they cause.

Research questions 2(b), (d), (e) and 4 are addressed in Article 3. As a succession of Article 2, the wind fields generated by four different turbulence models of various wind speeds and atmospheric stability conditions are used in a wind turbine design tool. Their impact on the dynamic response is assessed. The findings are supported by an assessment of the impact of individual wind characteristics on the turbine response. Again, the

comparison of all four models is unique. Furthermore, the analysis is performed on a larger wind turbine than many previous studies [18, 20, 21, 22, 23]. Last, Article 3 has a unique focus on the quasi-static region, and evaluates the statistical reliability of this region, and its importance on the overall loads.

Research questions 3 and 4 are addressed in Article 4. Article 4 evaluates whether fitting of the input parameters of the Mann model to actual site conditions serves as a good alternative to the standard Mann model, without adding time, cost, and complexity excessively. The wind fields obtained are referred to as "FitMann" wind fields. In contrast to previous studies considering fitting of Mann parameters [34, 35, 36, 37, 38, 39, 40, 41, 26, 27], Article 4 compares wind turbine response obtained by using "FitMann" to using other turbulence models (Mann and TIMESR). The wind turbine simulations are performed with the same bottom-fixed wind turbine as used in Article 3.

Research questions 2(c), (d) and (e) are addressed in Article 5. This paper answers most of the same research questions as Article 3, but for a floating wind turbine. As Article 3, it uniquely compares the responses of a wind turbine subject to the four considered turbulence models, and backs the results by a study of specific wind characteristics impact on dynamic response. In Article 5, an even larger wind turbine is considered. Only a few previous studies consider the specific wind turbine design of this article [42, 43, 44, 45, 46].

In the following, only the coherence of the streamwise wind component, the uu-coherence, is considered. The uu-coherence is assumed to be the most important for wind turbine response, as shown by e.g. Robertson et al. [47] for a 5-MW wind turbine. Any reference to coherence in the following corresponds to the uu-coherence. Coherence of time series separated by distances in the order of the rotor diameter is considered.

All wind turbine simulations are run without any waves or current, as the aerodynamic loading is in focus in this thesis. By removing waves, one can see the differences in responses of the various wind fields clearer. Moreover, wave loads play a less important role as the wind turbines get larger, as shown by e.g. Mahfouz et al. [42].

The effects of the floater controller on loads and fatigue are not discussed in this thesis. The controller settings of the wind turbine models are adapted without any modifications.

Discussions of the wind shear, or change in wind speed with height above surface are also out of scope of this thesis. The wind shear models mentioned by the wind turbine standard [15] are used.

In the following, any reference to response corresponds to the dynamic response.

# 2 Background

This chapter gives an overview of wind characteristics and wind turbine basics.

## 2.1 Atmospheric boundary layer

The atmospheric boundary layer, ABL, corresponds to the lowest part of the atmosphere directly impacted by surface effects. It is placed between the land/sea/ice surface of the earth and the free atmosphere. For state-of-the-art wind turbines, wind characteristics, e.g. mean wind speed, wind speed profile, turbulence, and coherence, up to 300 metres are relevant. A more or less consistent description of the interplay of those parameters exists essentially only in the surface layer, e.g. by the Monin-Obukhov similarity theory, MOST [48, 49]. The surface layer is characterized by efficient mixing, close to constant turbulent fluxes and large vertical gradients in wind speed, temperature, and humidity. The MOST assumes constant turbulent fluxes with height. The surface layer covers roughly only the lowest 10% of the ABL (Figure 2.1) [50], ranging from a few tens of metres to about a hundred metres, depending on the atmospheric stability. The MOST assumptions are consequently not valid over the entire rotor of state-of-the-art wind turbines. Another issue with the use of MOST for large offshore wind turbines, is that it has been derived from measurements at relatively short (30-40 m) masts over land.

The wind shear or wind profile, representing the increase of horizontal wind speed with height (Figure 2.1), may be estimated following the MOST. Two such wind shear models, the power law and the logarithmic law, are typically used by the industry today [15]. The power law, only valid in neutral atmospheric stratification, is defined by:

$$\overline{u}(z) = \overline{u}_{ref}\left(\frac{z}{z_{ref}}\right)^{\alpha}, \tag{2.1}$$

where $\overline{u}$ is the mean wind speed at the actual height, $\overline{u}_{ref}$ the wind speed at the reference height, $z$ the actual height above the surface, $z_{ref}$ the reference height, and $\alpha$ an empirical power law exponent. The logarithmic law for neutral atmospheric conditions is given by:

$$\overline{u}(z) = \overline{u}_{ref}\left(\frac{ln\left(\frac{z}{z_0}\right)}{ln\left(\frac{z_{ref}}{z_0}\right)}\right), \tag{2.2}$$

where $z_0$ is the surface roughness. The logarithmic law may also be used in non-neutral conditions by introducing a stability correction function, $\psi$:

$$\overline{u}(z) = \overline{u}_{ref}\left(\frac{ln\left(\frac{z}{z_0}\right) - \psi}{ln\left(\frac{z_{ref}}{z_0}\right) - \psi}\right). \tag{2.3}$$

$\psi$ is empirically defined as:

$$\psi = \begin{cases} -5\zeta, & \text{when stable,} \\ 2\ln\left(\frac{1+x}{2}\right) + ln\left(\frac{1+x^2}{2}\right) - 2tan^{-1}(x) + \frac{\pi}{2}, & \text{when unstable,} \end{cases} \tag{2.4}$$

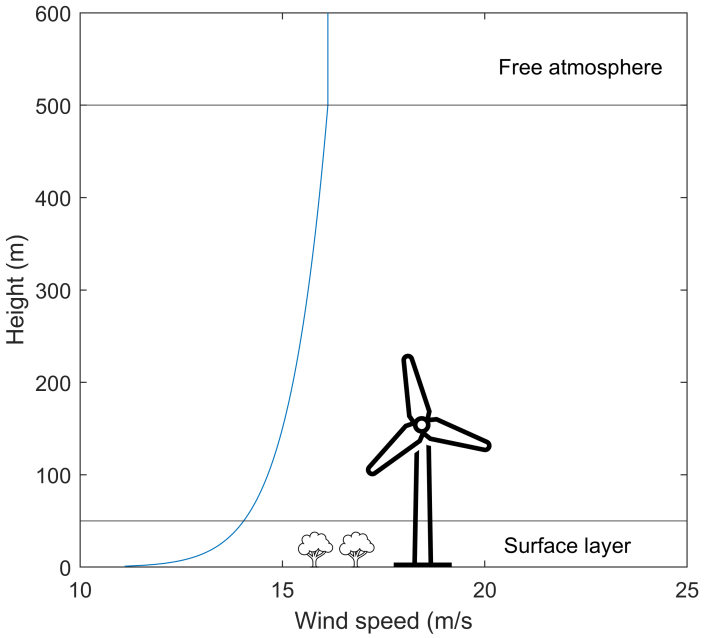


*Figure 2.1: Atmospheric boundary layer, surface layer and an idealized wind profile*

where $x = (1 - 15\zeta)^{1/4}$ [51, 52, 53]. The stability parameter, $\zeta$, is defined in Section 2.1.3, where atmospheric stability is discussed. As the MOST is only valid in the surface layer, the industry standard of wind shear characterization is typically not valid over the entire rotor disk of modern turbines. This is a challenge of increasing importance as the wind turbines are becoming larger and taller [54, 55]. This challenge is illustrated in Figure 2.1. In this illustration, the power law is assumed to be valid in the entire 500 m high ABL, while the surface layer only covers the lowest 50 m.

### 2.1.1 Turbulence

The horizontal wind speed, $u$, can be decomposed in a local mean and fluctuations around this mean, $u'$, following Equation 2.5:

$$u = \overline{u} + u'. \tag{2.5}$$

The deviations are referred to as turbulence [50].

For wind energy applications, turbulence is commonly characterized by the turbulence intensity, TI, defined as:

$$TI = \frac{\sigma_u}{\overline{u}}, \tag{2.6}$$

where $\sigma_u$ is the standard deviation of the wind speed. In wind energy-related meteorology, TI is commonly calculated from 1-Hz measurements, the typical temporal resolution of cup anemometers, averaged over 10 min. TI varies with wind speed and stability of

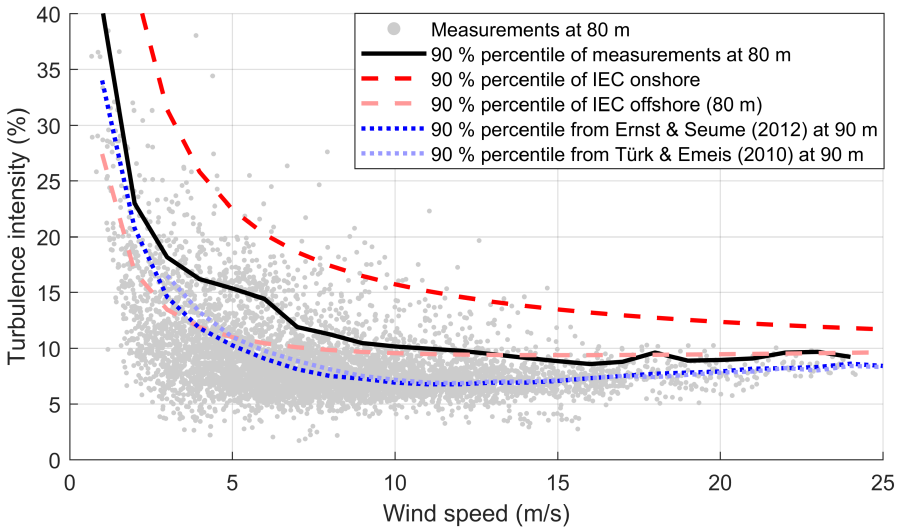


*Figure 2.2: Turbulence intensity (based on 20 Hz data over 30 minutes) as function of wind speed of the processed FINO1-data of Article 1, in addition to the 90th percentile of the same data set, the IEC standards and literature findings of FINO1 (Article 1)*

the atmosphere. The mean TI of a site typically decreases with increasing wind speed to about 10 m/s and stays close to constant at higher wind speeds (Figure 2.2).

The TI gives, however, no information on the temporal scale of turbulence. The temporal scale can rather be characterized by the wind spectrum. It is computed by a Fourier transform of the wind speed time series, assuming stationary conditions. As shown in Figure 2.3, the energy content decreases with frequency from the region where it is created, through the inertial subrange, to the region where turbulence is dissipated.

### 2.1.2 Coherence

In a turbulent wind field, as seen in nature, the wind speed varies with time and space. For small wind turbines, the wind speed is still rather coherent, or correlated, over the rotor plane. The largest wind turbine in operation today has a rotor diameter of more than 200 m [56]. With increasing diameters, the variation of wind speed over the rotor plane also increases. This variation may cause higher bending moments and corresponding fatigue of the rotor blades and tower, in addition to larger motions for floaters. The study of the variation of wind speed over the wind turbine rotor is therefore highly relevant today. This variation may be characterized by coherence.

Coherence is defined as the correlation between two time series separated in space, in the frequency domain. It provides information on the similarity of the energy content at different frequencies in the considered time series, but also whether the two time series are in phase. Equation 2.7 defines the root-coherence:

$$\gamma = \sqrt{\gamma_{co}^2 + \gamma_{quad}^2}, \tag{2.7}$$

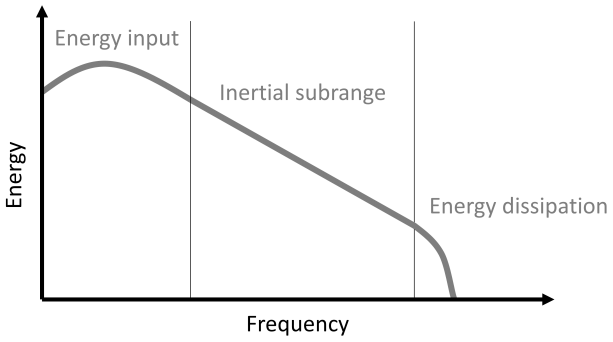


*Figure 2.3: Energy spectrum of turbulence (log-log)*

where $\gamma_{co}$ corresponds to the real part of coherence, the co-coherence, and $\gamma_{quad}$ the imaginary part, the quad-coherence. The quad-coherence is less significant than the co-coherence and is therefore commonly disregarded in the literature [57, 58, 24, 59, 22, 27, 25]. However, the quad-coherence contains information on the phase shift. Coherence is represented by co- and quad-coherence in Articles 2 and 3. In Article 3, the insignificance of the quad-coherence on the actual wind turbine response is proven for the moments considered, thus only the co-coherence is presented in Articles 4 and 5. The co-coherence is defined by:

$$\gamma_{co} = \mathrm{Re}\Big(\frac{S_{ij}}{\sqrt{S_{ii}S_{jj}}}\Big), \tag{2.8}$$

where $S_{ii}$ and $S_{jj}$ are one-sided auto-spectra of the wind velocities at two different positions, $i$ and $j$, and $S_{ij}$ is the cross spectrum between these two. As already mentioned, only the coherence of the streamwise wind component is considered in this thesis.

Proper orthogonal decomposition (POD) modes can be used to illustrate coherent structures or events in turbulent flows. The lowest modes explain the majority of the variation of the wind fields. These are of particular interest for wind turbine applications, as they are related to large coherent structures. The POD modes, $\Phi$, are defined by the matrices of eigenvectors, $\mathbf{G}$, eigenvalues, $\mathbf{\Lambda}$, and the turbulent part of the wind field, $\mathbf{U}$ [60]:

$$\mathbf{\Phi} = \mathbf{U}\mathbf{G}\mathbf{\Lambda}^{-1/2}. \tag{2.9}$$

### 2.1.3 Stability

Wind characteristics are strongly influenced by the stability of the atmosphere. The static stability of dry air is defined by the vertical potential temperature gradient, $\delta\theta/\delta z$, according to Equation 2.10:

$$\frac{\delta\theta}{\delta z}\begin{cases} = 0, & \text{when neutral,} \\ > 0, & \text{when stable,} \\ < 0, & \text{when unstable.} \end{cases} \tag{2.10}$$

The potential temperature is the temperature an air parcel would achieve if adiabatically restored to a reference surface pressure. The atmosphere is unstable when the land/sea/ice surface is warmer than the surrounding air, while it is stable when the surrounding air is warmer than the surface. In the North Sea, the atmosphere is typically unstable in winter when the sea surface temperature is warmer than the air above. In summer, the sea surface temperature is rather colder than the air above, and thus the atmosphere is considered stable. In neutral stratification, turbulence is generated by wind shear alone, while no heat flux, or turbulence generated by buoyancy, exists.

There are many ways to determine the stability of the atmosphere. It is common for wind energy applications to measure the temperature at different heights and determine the static stability according to Equation 2.10. Statically stable situations can, however, turn unstable by the effect of shear. It is common to characterize this dynamic stability through the Richardson number. Several variations exist (flux, gradient, bulk), where all of them characterize stability from the ratio of turbulence generated by buoyancy over turbulence generated by shear [50].

The Obukhov length [61], $L$, is a scaling parameter which is commonly used to determine the atmospheric, dynamic stability in the surface layer. The absolute value of the Obukhov length is referred to as a measure proportional to the height above the surface when buoyancy first dominates over mechanical shear production. The Obukhov length, as defined by Equation 2.11, is used to determine the atmospheric stability conditions in this thesis.

$$L = \frac{-\overline{\theta_v} u_*^3}{kg\left(\overline{w'\theta'}\right)_s}. \tag{2.11}$$

$\overline{\theta_v}$ is the virtual potential temperature (the virtual temperature is the temperature that dry air must have to equal the density of moist air at the same pressure). $u_*$ is the friction velocity defined by Equation 2.12, $k$ the von Karman constant, $g$ the gravitational constant, $\left(\overline{w'\theta'}\right)_s$ the surface vertical kinematic eddy heat flux and $u', v'$ and $w'$ the longitudinal, lateral, and vertical velocity fluctuations, respectively.

$$u_*^2 = \sqrt{\overline{u'w'}^2 + \overline{v'w'}^2}. \tag{2.12}$$

A small, positive Obukhov length defines a stable atmosphere, while a small, negative Obukhov length defines an unstable atmosphere. The neutral condition corresponds to the absolute value tending towards infinity. Van Wijk et al. [62] and Gryning et al. [54] propose limits for classifying atmospheric stability based on the Obukhov lengths. In this thesis, the stability classification is based on van Wijk et al., as shown in Table 2.1. The "very (un)stable" and "(un)stable" of Table 2.1 are both considered as "(un)stable" in parts of Article 2, Article 3 and Article 5. The stability parameter in Equation 2.4 is a non-dimensional alternative to the Obukhov length, given by Equation 2.13:

$$\zeta = \frac{z}{L}. \tag{2.13}$$

The various wind characteristics discussed above, shear, turbulence, coherence and stability, are all connected. A stable atmosphere is characterized by small eddies with short lifetimes, while an unstable atmosphere has large, long-lasting eddies. A stable atmosphere is typically associated with significant shear and low mixing. An unstable atmosphere is far more turbulent, and thus the shear is lower, while the TI and coherence

*Table 2.1: Stability classification after van Wijk et al. [62]. L=Obukhov length*

| | |
|---|---|
| Very stable | 0<L<200 m |
| Stable | 200<L<1000 m |
| Near-neutral | \|L\|>1000m |
| Unstable | -1000<L<-200 m |
| Very unstable | -200<L<0 m |

in the order of the rotor diameter are typically higher. Reflecting the higher turbulence, an unstable atmosphere is associated with higher power spectral densities in the wind spectrum compared to a stable atmosphere. The higher power spectral densities are most prominent at low frequencies.

## 2.2 Wind turbine design

Wind turbines, or windmills, have been operating for centuries. At the end of the 19th century, wind turbines were mainly used for grinding grain and pumping water. In 1888, the first wind turbine for electricity production was built [63]. Since then, the world has seen many different designs, from single-bladed designs to designs of more than a hundred blades. Today, many original designs are still relevant, e.g. vertical axis wind turbines [64] or multi-rotor designs [65].

The most common wind turbine design of today is referred to as the Danish concept [63]. The first wind turbine of the Danish concept was built in 1956. It gained popularity in the 1970s and has become the dominant design both onshore and offshore since then. The Danish concept is three-bladed, has a horizontal rotational axis and is oriented upwind. An upwind orientation means that the wind hits the rotor before it hits the rest of the nacelle.

Several offshore foundation designs are relevant for commercial use today. In addition to cost, water depth and soil type are relevant constraints in the design choice. Figure 2.4 shows some of the most common designs today. Bottom-fixed wind turbines are typically placed in areas where the water depth is less than 50 m, while floaters may be used in much deeper waters. In this thesis, one monopile (Articles 3 and 4) and one spar foundation (Article 5) are analysed. Monopiles are currently the dominating foundation design [66]. Less than 1% of offshore wind turbines are floaters. The most common floater designs are semisubmersible, spar, tension-leg platform (TLP) and barge. The spar foundation is ballast stabilized, having the centre of gravity far below the centre of buoyancy. The first wind park of floating wind turbines used spar foundations (Hywind Scotland in operation since 2017 [67]). Spar foundations will also be used in what will be the world's largest floating wind park, Hywind Tampen (operations expected in 2022 [68]).

All wind turbines are equipped with a controller that ensures maximal power production and minimal loads. Below the so-called rated wind speed, the pitch angle of the blades are kept at an optimal, constant value. Consequently, the rotational speed of the rotor increases with the wind speed, keeping the tip speed ratio as well at a close to optimal value. Below rated, efficient operation and maximum power production are thus achieved. Above the rated wind speed, a variable pitch angle of the blades is applied

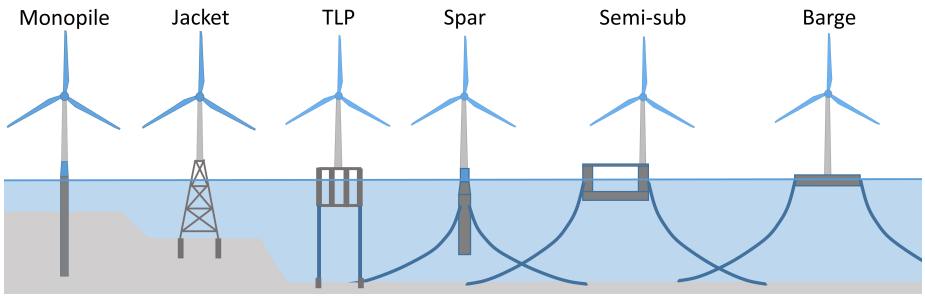


*Figure 2.4: Offshore wind turbine foundations. TLP=Tension-Leg Platform and Semi-sub=Semisubmersible*

so that the rotational speed and power output are limited to their rated values. Consequently, the loads at high wind speeds are reduced. The controller is also responsible for shutdown at very low or very high wind speeds. For floaters, the controller may also reduce motions and corresponding loads [69].

### 2.2.1 Aerodynamic loads

The blade element momentum (BEM) theory [70] is commonly used for calculating power generation from wind turbines. It is a combination of the blade element theory [71, 72] and the momentum theory [73, 74] (the latter is also referred to as the Froude-Rankine theory or the actuator disk model). Wind turbine design tools rely on the BEM theory for determining the wind load and power generation. It is used by both aero-hydro-servo-elastic tools (OpenFAST [75] and SIMA [76] used in this thesis), and more advanced tools such as large eddy simulations (LES).

The BEM theory combines 2D airfoil theory with momentum balance in the stream-tube. The blade is split into a number of blade elements. Each blade element has certain properties, depending on the airfoil used. The force generated by the airfoil due to the pressure of the incoming wind, is divided in a lift and a drag force (Figure 2.5). These forces are calculated for each blade element:

$$dL = \frac{1}{2}\rho c V_{rel}^2 C_L dr. \tag{2.14}$$

$$dD = \frac{1}{2}\rho c r V_{rel}^2 C_D dr. \tag{2.15}$$

$\rho$ is the air density, $c$ the chord, $r$ the length of the blade element and $V_{rel}$ the relative velocity seen by the blade element (Figure 2.5). The lift and drag coefficients, $C_L$ and $C_D$, are airfoil properties. These depend on the angle of attack (AOA), which is the angle between the relative velocity and the chord line (Figure 2.5).

In the BEM theory, the power of the wind turbine is calculated from the incoming wind and the properties of the airfoil. The theory defines an axial and a circumferential induction factor. An iterative process is used to find the values of these: For each blade element, an initial guess of the induction factors is performed, the AOA is calculated from the induction factors, the lift and drag coefficients are found from an airfoil table relating these to the AOA, and the induction factors are again calculated from the lift

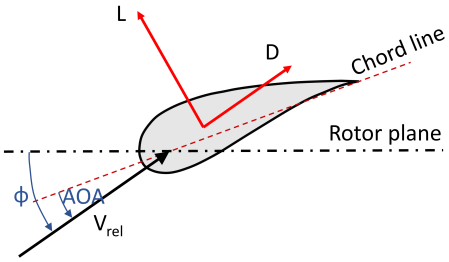


*Figure 2.5: Illustration of an airfoil with lift (L) and drag (D) forces, relative velocity ($V_{rel}$), and angle of attack (AOA)*

and drag coefficients. The torque, $M$, and power, $P$, may thereafter be calculated for each blade element, according to Equations 2.16 and 2.17.

$$dM = B\frac{1}{2}\rho V_{rel}^2(C_L \sin\phi - C_D \cos\phi)crdr. \tag{2.16}$$

$$dP = \Omega dM. \tag{2.17}$$

$B$ is the number of blades, and $\phi$ the angle between the relative velocity and the rotor plane (Figure 2.5). The total torque and power are calculated by integration over the wind turbine blade. It is therefore important to consider the variation of wind speed over the rotor blade in wind turbine design. For reference, the simple expression for wind turbine thrust in homogeneous incoming wind is given as:

$$T = \frac{1}{2}\rho\overline{u}^2 AC_T, \tag{2.18}$$

where $A$ is the area of the rotor, and $C_T$ the thrust coefficient.

The BEM theory assumes steady flow, momentum conservation in axial and tangential directions, no aerodynamic interaction between blade elements, 2D flow over each blade element, and no pre-rotation of the stream tube before entering the rotor. In order to compensate for some of these assumptions, several corrections to the BEM theory exist and are commonly applied. For example, 3D effects and transients are included through corrections.

### 2.2.2 Wind turbine loads and motions

In the design of wind turbines, bending moments of the tower and blades are calculated in order to determine the fatigue and lifetime of various components. For floaters, it is also relevant to study the motions and corresponding mooring tensions.

For the bottom-fixed wind turbine (Articles 3 and 4), the tower top yaw moment, $M_z$, the tower top bending moment fore-aft, $M_{T,y}$, the tower bottom bending moment fore-aft, $M_{B,y}$, and the blade root flapwise bending moment, $M_F$, are considered. These are illustrated in Figure 2.6. For the floater (Article 5), the surge, pitch, and yaw motions, in addition to the tension of the upper part of the most heavily loaded mooring

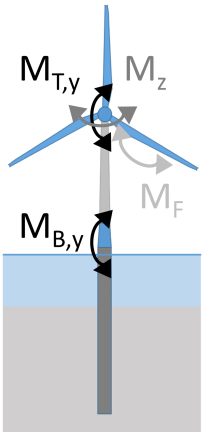


*Figure 2.6: Moments in consideration for the bottom-fixed wind turbine. $M_z$ is the tower top yaw moment, $M_{T,y}$ the tower top bending moment fore-aft, $M_{B,y}$ the tower bottom bending moment fore-aft, and $M_F$ the blade root flapwise bending moment*

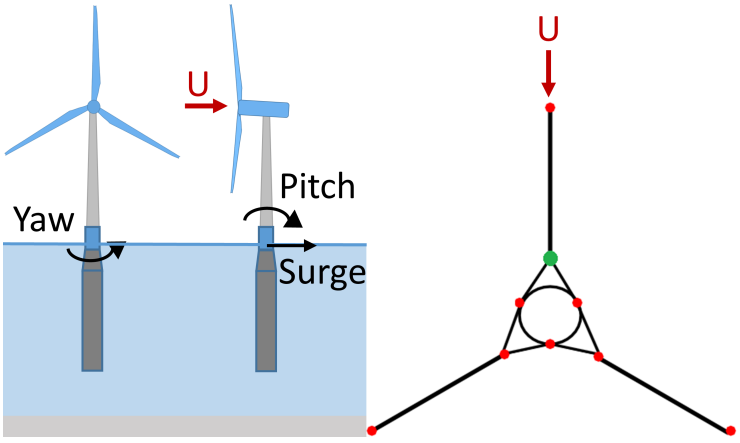


*Figure 2.7: Left: Rigid body motions in consideration for the floating wind turbine. Right: Mooring design and the considered connection point for mooring line tension (green dot). U corresponds to the incoming wind [77]*

line are considered. These are illustrated in Figure 2.7. The mentioned moments, motions and tension are chosen as they are expected to react differently on the considered wind characteristics. For example, the local moments of the bottom-fixed wind turbine tower top, and yaw motion of the floating wind turbine are expected to increase with decreased coherence over the rotor plane. On the other hand, the other considered moments, motions and tension are expected to be large when subject to large coherent structures covering the entire rotor plane. Furthermore, the chosen moments and tension are important for the total damage and lifetime of the structures. Surge and pitch are the largest platform motions of the considered floater design. Information on the wind turbine designs is found in Section 3.3.

The damage equivalent load/moment (DEL/DEM) is used to evaluate the damage experienced by the wind turbine in this thesis. The DEL/DEM, or $R_{eq}$, accounts for the amplitudes of the bending moment/tension time series, $R_i$, and the number of cycles, $n_i$, according to Equation 2.19 [78].

$$R_{eq} = \left( \frac{\Sigma_i (R_i^m n_i)}{n_{eq}} \right)^{1/m} . \tag{2.19}$$

$m$ is the Wöhler exponent of the material of the tower (steel, m=3), blades (composite, m=10) or mooring line (steel, m=3). $n_{eq}$ is the equivalent number of response cycles, in this case for an equivalent frequency of 1 Hz. The rainflow algorithm developed by Nieslony [79] is used to compute the DEL/DEM. In Articles 3 and 4, the DEL/DEM is calculated on low-pass filtered time series, as it is shown that frequencies below 0.1 Hz are particularly important for the total response in Article 3. The floater motions (Article 5) are evaluated in terms of the standard deviations of surge displacement, pitch displacement and yaw rotation. Additionally, the wind turbine response spectra are analysed in this thesis.

# 3 Models and data

This chapter gives an overview of the wind data, turbulence models, aero-hydro-servo-elastic tools and wind turbine models used in this thesis.

## 3.1 Offshore measurements

In order to measure turbulence, one is dependent on equipment that can measure wind speed at high frequency. The higher the frequency, the more of the turbulence dissipation range is resolved (Figure 2.3). Sonic anemometers measure wind speed in three directions and sonic temperature at about 20 Hz. They are therefore well suited for turbulence measurements. Offshore, several meteorological masts equipped with sonic anemometers exist for research purposes (e.g. FINO1, 2 and 3 [80]). Disadvantages of mast based measurements offshore cover cost of installing the mast, height limitation of the mast, and an unavoidable flow distortion by the mast structure. The masts installed today range typically 100 m above sea level, covering less than half of state-of-the-art wind turbine rotors. Remote sensing of turbulence through LIDARs is therefore a topic of ongoing research (e.g. [81, 82]). However, several studies have pointed at challenges of measuring turbulence with LIDARs [11, 12, 13, 14].

In this thesis, measurements from the FINO1 platform are used (Figure 3.1) [83]. The FINO1 platform is a research mast densely equipped with instrumentation that has been in operation in the North Sea for almost 20 years. It is equipped with standard meteorological sensors for wind, temperature, and humidity at 30-100 m above sea level [84]. Additional meteorological and hydrological instrumentation has been in operation at the site for shorter periods [85]. When FINO1 first was in operation, the measurements represented free wind conditions. Over the years, several wind parks have been placed in close vicinity to the meteorological mast. Currently, the measurements may therefore be used in combination with wind park data.

Data from 2015/2016 are used in this thesis. In 2015/2016, only one wind park in immediate proximity existed. In addition to the sonic wind speed and temperature measurements of high frequency at 40, 60 and 80 m, 10-min data of rain and wind direction are used in Article 1.

In Article 1, the wind speed and temperature measurements of FINO1 are quality assured for offshore wind turbine applications. After quality assurance, only 27% of the data in the period June 2015 to September 2016 are available. However, this amount of data is more than enough for the purpose of Articles 2-5. The situations of Table 3.1 are used in these articles. The nine situations cover three operating regions of a wind turbine (below, at and above the rated wind speed), and three stability conditions of the atmosphere.

## 3.2 Turbulence models and simulators

The IEC standards require the use of a structural dynamics model to predict design load effects [15, 86, 87]. For these simulations, they recommend two turbulence models for

*Figure 3.1: The FINO1 platform (Photo: Martin Flügge)*

*Table 3.1: Chosen 1-hour situations of measurements. The wind speed and TI (turbulence intensity) is given for the hub height of the bottom-fixed wind turbine (119 m), calculated from the measurements by the logarithmic law. L=Obukhov length, $\alpha$=Power law exponent*

| Date and time | Wind speed (m/s) | Stability | L (m) | TI (%) | $\alpha$ | Articles |
|---|---|---|---|---|---|---|
| 15.06.2015 06:00 | 7.5 | Unstable | -123 | 8.1 | 0.01 | 2 |
| 18.07.2015 20:00 | 7.4 | Neutral | -1107 | 5.5 | 0.04 | 2, 3, 5 |
| 05.06.2016 00.30 | 7.4 | Stable | 8 | 2.3 | 0.29 | 2 |
| 22.02.2016 19:00 | 12.6 | Unstable | -451 | 6.1 | 0.02 | 2, 3, 5 |
| 18.04.2016 04:30 | 12.4 | Neutral | 2753 | 6.2 | 0.06 | 2, 3, 4, 5 |
| 02.06.2016 16:30 | 12.5 | Stable | 158 | 2.8 | 0.20 | 2, 3, 5 |
| 06.09.2015 04:30 | 18.1 | Unstable | -407 | 6.2 | 0.00 | 2 |
| 30.01.2016 27:30 | 17.6 | Neutral | 2051 | 6.6 | 0.06 | 2, 3, 5 |
| 01.06.2016 18:30 | 17.8 | Stable | 57 | 2.7 | 0.29 | 2 |

estimating the wind load on the wind turbine:

- The Kaimal wind spectrum [17] and exponential coherence model [15], referred to as **Kaimal**.
- The Mann spectral tensor model [16], referred to as **Mann**.

The IEC standard [15] recommends the use of several 10-min simulations for estimating fatigue and extreme loads. However, longer intervals are relevant for offshore wind turbines, where the quasi-static response is of relatively high importance. The importance of the quasi-static frequency region is discussed in Article 3. The outputs of the Kaimal and Mann models are yz planes discretized in time and x direction, respectively (x corresponds to the mean wind direction, y to the across wind direction and z to the vertical direction). The time series of Kaimal are used directly as inputs in aero-hydro-servo-elastic tools. The three-dimensional wind boxes of Mann are moved through the wind turbine by assuming Taylor's hypothesis of "frozen" turbulence.

Four turbulence models are used in this thesis. In addition to Kaimal and Mann, the following two turbulence models are considered:

- A model with input time series and coherence parameters from measurements, referred to as **TIMESR**.
- Large eddy simulations, referred to as **LES**.

These two are in principle able to create wind fields in a more realistic manner than the Mann and Kaimal models. A summary of the models and how they are used in the attached articles are given in Figure 3.2 and detailed in Sections 3.2.1 to 3.2.4. The different turbulence models may be characterized by how they model the wind spectra of each point, and how these are correlated in space (coherence). As mentioned, the standard Mann and Kaimal models generate similar wind spectra despite being different in their spectral formulations. The wind spectra of TIMESR are interpolated from measurements, while the LES spectra are obtained through computational fluid dynamics. The coherence formulations vary between all the models, as elaborated below. Other turbulence models relevant for wind turbine design are not considered in this thesis, but discussed by e.g. Rinker [88], Cheynet et al. [27], Putri et al. [22, 23, 89] and Højstrup [90]. The turbulence simulator, TurbSim [51], also offers a range of wind spectra and a few different coherence models for generating wind fields.

### 3.2.1 Mann - The Mann spectral tensor model

The Mann model is described by Mann in his work from 1994 [16] and 1998 [34]. It is based on the isotropic wind energy spectrum of von Kármán [94], but assumes that this spectrum is distorted by a uniform mean velocity shear. The Mann model is intended for neutral atmospheric conditions and high wind speeds in the surface layer. However, it is commonly used in all atmospheric stability conditions and all wind speeds over the entire rotor plane [15, 86, 87]. The model assumes a stationary, homogeneous, and Gaussian velocity field where Taylor's hypothesis of "frozen" turbulence is valid.

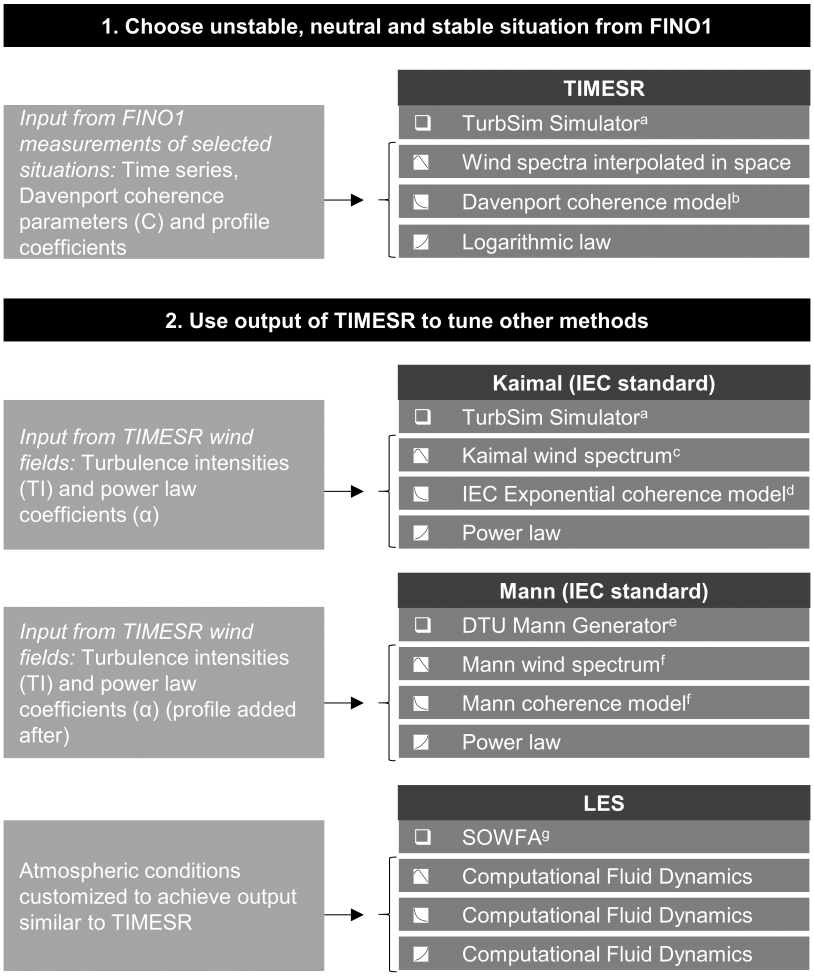


*Figure 3.2: Scheme of wind field models, describing inputs, simulation software, spectra and coherence models and profile laws (from Article 3). a =[51], b=[91], c=[17], d=[15], e=[92], f=[16] and g=[93]*

The root-coherence of Mann is given by the integral of the spectral tensor, $\phi$, and is commonly formulated as:

$$|\gamma| = \frac{|\iint \phi_{ij}(\mathbf{k}) exp(-ik_y\delta_y) exp(-ik_z\delta_z) dk_y dk_z|}{\sqrt{\iint \phi_{ii}(\mathbf{k}) dk_y dk_z \phi_{jj}(\mathbf{k}) dk_y dk_z}}, \tag{3.1}$$

where $i$ and $j = 1, 2, 3$ for the longitudinal, lateral, and vertical turbulent wind components, $\mathbf{k}$ is the wave vector, $k_y$ the wave number in the lateral direction, $k_z$ the wave number in the vertical direction, $\delta_y$ the separation distance in the lateral direction and $\delta_z$ the separation distance in the vertical direction. The coherence of Equation 3.1 is given as function of the wave number, but may be transformed to depend on frequency, $f$, through Taylor's frozen turbulence hypothesis:

$$f = \frac{k\overline{u}}{2\pi}. \tag{3.2}$$

The Mann wind fields of this thesis are generated by the DTU (Technical University of Denmark) Mann Generator [92]. It requires only three input parameters, except for the domain size and resolution: The Kolmogorov constant multiplied with the rate of the viscous dissipation of specific turbulent kinetic energy to the two thirds, $\alpha\epsilon^{2/3}$, the length scale describing the size of the largest energy-containing eddies, $l$, and the non-dimensional parameter related to the lifetime of the eddies, $\Gamma$. An increase in $\alpha\epsilon^{2/3}$ increases the energy levels of the entire wind spectrum, while an increase in $l$ or $\Gamma$ rather increases the energy levels at low frequencies. All wind fields referred to as Mann wind fields in Articles 2-5 are generated with input parameters adapted from the IEC standard [15]. With these input parameters, the obtained wind spectrum is similar to the spectrum of Kaimal. The wind fields in Articles 2-5 are sometimes referred to as unstable and stable. However, only the TI and wind shear are adapted to the given situation, as recommended by the standard.

The output of the Mann model is a wind box spanning a given x, y, z domain of turbulent wind speed in three directions. The wind shear must be added to the streamwise wind speed when used in aero-hydro-servo-elastic tools.

In Article 4, a model called "FitMann" is considered. In FitMann, the Mann input parameters are determined in order to fit the spectra generated by Mann to the measured wind spectra. In Article 4, the fitting is only performed in neutral atmospheric conditions. Fitting/adaption of the Mann model to other atmospheric stability conditions is outside the scope of this thesis, but has been performed by e.g. Sathe et al. [35], de Maré and Mann [36], Penã et al. [37] and Chougule et al. [39, 40, 41].

### 3.2.2 Kaimal - The Kaimal spectrum and exponential coherence model

The Kaimal model corresponds to the Kaimal spectrum [17] with the IEC exponential coherence model [15] implemented by the method described by Veers [57]. The Kaimal spectrum is based on the framework of similarity theory in the surface layer. However, except for the Kolmogorov law of the inertial subrange, the spectral formulation is rather defined empirically than physically. Some modifications of the original Kaimal spectrum are performed by the IEC standard [15].

The coherence model proposed by the IEC standard [15] is as following:

$$\gamma = \exp\left( -12\Big(\big(f\delta/\overline{u}_{hub}\big)^2 + \big(0.12\delta/L_c\big)^2\Big)^{0.5}\right), \tag{3.3}$$

where $\delta$ the magnitude of the separation distance on a plane normal to the mean wind direction, $\overline{u}_{hub}$ the wind speed at hub height and $L_c$ the coherence scale parameter, recommended as $8.1\Lambda_1$, where $\Lambda_1$ is the turbulence scale parameter in meters. In contrast to the Mann model, coherence is only considered for the velocity in the mean wind direction.

The Kaimal wind fields of this thesis are generated by TurbSim [51]. TurbSim is a flexible wind field simulator based on Veers' method [57], combining a wind spectrum and a coherence model. All selected input parameters of this thesis are according to the IEC standard. As for Mann, the Kaimal wind fields are sometimes referred to as unstable or stable, but only the TI and shear are adapted to the given situation. The output of TurbSim are time series of wind speed in three components for all given grid points in a yz plane (y corresponds to the across wind direction and z to the vertical direction). Wind shear is added to the turbulent wind fields by the TurbSim software.

### 3.2.3 TIMESR - The model based on measurements

The TIMESR wind fields are created in the same manner as Kaimal, where TurbSim [51] simulates time series from a chosen spectrum and ensures correlation of these through a chosen coherence model. Input time series are transformed to spectra, which are interpolated in space to all grid points of the wind field domain. In this thesis, three time series of high sampling rates are used as input (40, 60 and 80 m elevation from processed FINO1 data).

In this thesis, the coherence of the TIMESR model is estimated according to Davenport [91]:

$$\gamma_{i,j\,K} = \exp\left( -C_K \frac{f\delta}{\overline{u}_m}\right), \tag{3.4}$$

where $i$ and $j$ are two points separated in space, $C_K$ the decay coefficient, and $\overline{u}_m$ the mean wind speed of the two points. Coherence is estimated in all three wind speed components, $K = u, v, w$. The Davenport model is chosen as it is proven to model coherence well at FINO1 for the horizontal wind components [27].

In addition to the three time series already mentioned, decay coefficients obtained from vertical measurements are used as input in the TIMESR model. Shear coefficients are also input to TurbSim, and thus the output wind fields already contain mean wind speeds. The output spectra at 40, 60 and 80 m are equal to the input spectra. At one chosen height (80 m), also the input time series is reproduced by TurbSim. When the TIMESR wind fields are referred to as stable, neutral, or unstable, the input time series, decay coefficients and shear coefficients are found from a situation with the corresponding atmospheric stability. Consequently, the obtained wind spectra and coherence represent the desired atmospheric stability.

### 3.2.4 LES - Large eddy simulations

LES is a turbulence model used in computational fluid dynamics (CFD). It is a realistic and complex model based on physics. The great disadvantage of LES is the high

computational effort required. However, the development of computers and the need for realistic wind fields in wind turbine design have made LES an interesting option. LES may be used to simulate the ABL alone as in this thesis. One may also place wind turbines (through actuator models) in the domain in order to calculate the response instead of using aero-hydro-servo-elastic tools. LES is also a suitable tool for simulating wakes [95, 96, 97, 98, 99, 100], although the computational effort increases with the number of wind turbines. Last, LES may be used in combination with aero-hydro-servo-elastic tools as a compromise between computational effort and complexity [101].

LES solves a filtered form of the governing equations of fluid flow (Navier-Stokes) and directly resolves the larger, more important, energy-containing turbulent scale of the flow. A subgrid-scale model is used to model the effect of the unresolved scales on the resolved scales.

LES may be performed in a range of CFD tools. The simulations of this thesis are performed at the National Renewable Energy Laboratory (NREL) in their simulator for wind farm applications (SOWFA) [93].

The characteristics of the LES wind fields may be adjusted by controlling the surface heat flux, the hub height wind speed through a pressure gradient force, the potential temperature profile and the surface roughness. In order to achieve the unstable wind fields of this thesis, a positive surface heat flux is added. The initial potential temperature profile and surface roughness are also adjusted to typical values. With these input conditions, large coherent structures appear, as desired in unstable atmospheric conditions. On the other hand, a surface cooling rate is used when simulating the stable situations. In contrast to the previously discussed turbulence models, the TI (in combination with the desired stability and shear) is not easily controlled by the inputs. As shown in Article 2, it may therefore be challenging to "fit" LES wind fields to measurements or wind fields obtained by other turbulence models.

The LES are performed in a larger domain than the other mentioned turbulence models in order to resolve the ABL properly. In this thesis, nested simulations are performed. A refinement zone covers a hypothetical wind turbine rotor with a finer grid than used in the other turbulence models. High-frequency time series of wind speed in three directions are saved in grid points of a yz plane at the location of the hypothetical wind turbine. These time series are converted to the wind box format of Mann for further analysis in this thesis.

## 3.3 Aero-hydro-servo-elastic tools and wind turbine models

As mentioned, the IEC standards require the use of a structural dynamics model to predict design load effects [15, 86, 87]. In Articles 3 and 4, a bottom-fixed wind turbine model is used in SIMA, while in Article 5, a floating wind turbine model is used in OpenFAST. These wind turbine models and design tools are discussed in the following.

### 3.3.1 SIMA and OpenFAST

Aero-hydro-servo-elastic tools perform coupled analysis of wind turbine aerodynamics, hydrodynamics, control, structural dynamics, and mooring/substructure dynamics in the case of offshore wind turbines. The simulations of this thesis are performed without any waves or current. The focus is rather on the aerodynamics, and especially the inflow

*Table 3.2: Main characteristics of the two wind turbine models*

| | **Bottom-fixed** | **Floating** |
|---|---|---|
| Rated power (MW) | 10 | 15 |
| Diameter (m) | 178.5 | 240 |
| Hub height (m) | 119 | 135 |
| Cut-in, rated, and cut-out wind speed (m/s) | 4, 11.4, 25 | 3, 10.59, 25 |
| Structure depth below mud line/sea surface (m) | 43 | 155 |
| Diameter of substructure (m) | 9 | 18.6 |
| Water depth (m) | 30 | 200 |

wind fields. SIMA and OpenFAST both follow the BEM theory. However, some minor differences in the implementation and following response were found when Sørum et al. compared the two models [102].

SIMA [76], short for simulation and engineering analysis of marine operations and floating systems, is a tool developed and maintained at the Norwegian University of Science and Technology, NTNU, and SINTEF. It was originally intended for marine structures and marine operations, but has later been extended to include aerodynamics in order to model wind turbines. It is based on two underlying programs, RIFLEX and SIMO. RIFLEX is used for finite element modelling (FEM) of flexible structures. SIMO is used to model rigid bodies. The software contains 3D models of structures, and allows for visualization of the simulations.

OpenFAST [75], short for Fatigue, Aerodynamics, Structures, and Turbulence, is a tool developed at NREL. Originally, several separate modules were made for e.g. aerodynamics, structural dynamics etc. These were intended for onshore wind turbines, but hydrodynamic, substructure and mooring dynamic modules were developed later. OpenFAST is an open-source framework for all these modules. The structural dynamics are analysed using modal models or FEM.

### 3.3.2 Wind turbine models

The bottom-fixed wind turbine model used in this thesis is a version of the DTU reference turbine [103]. Reference turbines are well suited for research as they are well documented. The DTU reference turbine has a rated power of 10 MW. Even though it was developed almost ten years ago, it is still highly relevant. It is e.g. larger than the turbines that will be installed at Hywind Tampen [68]. The DTU reference turbine is originally an onshore wind turbine. The monopile wind turbine used in Articles 3 and 4 is based on the modifications by Bachynski and Ormberg [104] and Sørum et al. [105]. The main wind turbine characteristics are given in Table 3.2. The lowest natural frequencies of the structure (1st tower side-side and fore-aft modes) are at about 0.23 Hz, and the first excitation frequency (1P) is 0.16 Hz, higher than the frequency region in focus in Articles 3 and 4.

The floating wind turbine model used in Article 5 is a version of the IEA (International Energy Agency) Wind 15-MW offshore reference wind turbine [106]. This is a new large reference wind turbine, with two associated foundations; one monopile and one semi-submersible [107]. The models are developed through a collaboration between

NREL, DTU and the University of Maine. The spar wind turbine used in Article 5 results from the CoreWind project [42]. The CoreWind spar wind turbine model, referred to as WindCrete, consists of the IEA 15-MW rotor, a concrete tower, a concrete spar foundation and mooring lines with delta connections. The OpenFAST model is adapted from Mahfouz et al., available on Zenodo [108]. Figure 2.7 shows the mooring line setup of the WindCrete floater. The main characteristics of the model are given in Table 3.2. The natural frequencies are 0.013 Hz in surge and sway, 0.024 Hz in pitch and roll, 0.029 Hz in heave, and 0.091 Hz in yaw.

# 4 Summary and main findings of the articles

This thesis compares and evaluates existing ways of modelling turbulence in wind turbine design. First, offshore measurements are quality assured and assessed (Article 1). Second, a thorough analysis of measurements, and simulated wind fields are performed (Article 2). Thereafter, the response of a bottom-fixed and a floating wind turbine subject to wind fields of various turbulence simulators is evaluated (Articles 3, 4 and 5). In the following, a summary of the articles is presented.

## Article 1

Article 1 describes a thorough processing procedure for wind measurements from sonic anemometers, starting from available raw data and ending in a complete set of processed time series. The processing is performed with the intention of creating a quality assured dataset that may be used for wind turbine purposes.

Measurements from the meteorological mast, FINO1 (Section 3.1), are processed according to the following procedure:

- Assessing data gaps and removing corrupted raw data
- Spike detection and removal
- Disregarding data close to precipitation events
- Disregarding data influenced by other disturbances
- Disregarding data influenced by the mast and land
- Rotation to mean flow direction
- Organizing in 30-minute periods

Finally, an approach to evaluate the stationarity is proposed, but not applied to the dataset.

Only 27% of the original data from the summer of 2015 to the fall of 2016 are left after the conservative processing procedure is followed (no stationarity assessment). Still, the obtained dataset contains thousands of quality assured situations with a great variety of wind speed and turbulence intensity. This dataset is ready to use for a wide range of applications related to offshore wind turbines.

Research question 1 is answered by Article 1. In contrast to previous works [28, 29, 30, 27, 26, 31, 24, 32, 33], great attention is devoted to the processing procedure of the sonic anemometers for wind turbine applications. The focus is on large offshore wind turbines, and thus the obtained dataset contains long continuous time series.

## Article 2

Article 2 evaluates the turbulence models recommended by the IEC standard, and compares them to measurements and more complex models. The purpose is to highlight the differences in wind characteristics of wind fields generated by different turbulence models. Wind characteristics which are expected to have an impact on the response of a wind turbine are in focus. The turbulence models are assessed in situations of various wind speed and atmospheric stability conditions.

First, a few situations are chosen from the dataset of Article 1 (Table 3.1). Thereafter, wind fields are generated by the Mann, Kaimal, TIMESR and LES models according to Figure 3.2. An overview of the generated wind fields is presented, in terms of wind speed distribution, shear, TI (and Obukhov length for the TIMESR and LES wind fields). The differences in coherent structures, important for the response of large offshore wind turbines, are evaluated. The co-coherence and quad-coherence at distances in the order of the rotor diameter, in addition to the proper orthogonal decomposition (POD) modes, of the various models are compared.

The unstable wind fields have less wind shear and higher turbulence intensity than the stable ones. The presence of coherent structures in TIMESR and LES wind fields depends on the stability. Unstable wind fields have larger and more energetic coherent structures with respect to the stable ones.

In general, large similarities are found between the Mann and Kaimal wind fields. In comparison, the LES wind fields contain lower variations in wind speed, while the TIMESR wind fields contain larger variations in wind speed. Similarly, the turbulence intensity is typically highest in the TIMESR wind fields, and lower in the LES wind fields.

As expected, the co-coherence of the Kaimal and Mann wind fields tend to fit the co-coherence of the TIMESR and LES wind fields best in the situations of neutral stratification. However, the Mann model predicts less significant co-coherence than Kaimal, especially for horizontal separation distances, and is therefore closer to the LES and TIMESR wind fields in the stable situations. Quad-coherence is only present in the Mann and LES wind fields. The POD modes reflect the findings mentioned above. The shape of the POD modes and the magnitude of explained variation of the Kaimal wind fields are in general more similar to LES and TIMESR than Mann. It is highlighted in Article 2 that neither the TIMESR model nor the LES model are able to represent the true offshore wind field, and thus the authors cannot determine whether the Kaimal model or the Mann model is more realistic in a general manner. It is although clear that there are significant differences in wind fields generated by various turbulence models and in various atmospheric stability conditions. These differences are expected to influence the dynamic response of large offshore wind turbines.

Research questions 2(a), (d) and (e) are answered by Article 2. The differences in the standard turbulence models found in this article are consistent with previous findings [18, 25]. In contrast to previous works, Article 2 also shows how the standard turbulence models compare to turbulence models based on both measurements and LES.

## Article 3

In Article 3, the wind fields presented in Article 2 are used in wind turbine simulations. The response of a bottom-fixed wind turbine is evaluated. The low-frequency range, below 0.1 Hz, where the response is expected to be quasi-static, is in focus. The purpose of Article 3 is to highlight the differences in wind turbine response when subject to wind fields of various turbulence generators.

The wind spectra and coherence estimates (in the order of the rotor diameter) between the different wind fields are first presented. A so-called wind characteristics test is performed, in order to evaluate the effect of certain wind characteristics on response. The wind characteristics test refers to simulations where the exclusive effect of shear, turbulence and coherence on response is evaluated. The response moments considered are $M_z$, $M_{T,y}$, $M_{B,y}$ and $M_F$ (Figure 2.6). The importance of the quasi-static frequency region on the total response is assessed. The uncertainty and stochastic variation of the quasi-static frequency region is moreover evaluated. Based on the wind characteristics test, Article 3 determines the probable origin of the differences in loads when using the TIMESR, LES, Mann, and Kaimal wind fields. The response is evaluated in terms of DEM and spectral analysis.

The quasi-static contribution to the total DEM is found to be significant, especially for $M_{B,y}$ and $M_F$. There is a higher stochastic variation when only considering frequencies below 0.1 Hz in comparison to the whole frequency range, which is compensated by more simulations (6 seeds of 1 hour each). This number of simulations is necessary in order to have confidence in the comparisons of DEM of various input wind fields.

The wind characteristics test show that shear has negligible impact on the quasi-static response, while adding turbulence increases the energy level of the response spectra. Higher/lower co-coherence causes lower/higher spectral values of $M_z$ and $M_{T,y}$ and higher/lower spectral values of $M_{B,y}$ and $M_F$. As expected, large wind speed variations over the rotor plane cause reduced total loads on the rotor and therefore low spectral moments at the tower bottom and correspondingly at the blade root. Quad-coherence has negligible impact on the moments considered.

Large differences are found in the response caused by the four different turbulence models. These differences depend on the wind speed and stability situation considered. The response of using the Mann and Kaimal wind fields show certain differences. Those are, however, small compared to the differences against simulations where the LES and TIMESR wind fields are used. In general, the LES wind fields contain less turbulence (Article 2), which is reflected in the DEM and corresponding spectra. The Mann wind fields cause highest DEM of $M_z$ considering all atmospheric stability conditions. The higher $M_z$ is caused by the lower estimated co-coherence of horizontal distances. The co-coherence of vertical distances is rather quite similar across turbulence models, and correspondingly $M_{T,y}$ is similar. The shapes of the spectra of $M_{B,y}$ and $M_F$ are very similar to the shapes of the wind spectra of the input wind fields. In many of the considered situations, the TIMESR wind fields have a lot of energy in the wind spectrum compared to other wind fields, and thus also in the $M_{B,y}$ and $M_F$ spectra. To sum up, Article 3 clearly shows the large variation in response obtained when using various turbulence models and explains why these differences occur.

Research questions 2(b), (d), (e) and 4 are answered by Article 3. In this article, the differences in response obtained by using the Mann and Kaimal models are compared to

findings of previous works [20, 22, 18]. As expected, considering a different wind turbine structure, some deviations are found. In contrast to previous works, the results obtained are supported by the wind characteristics test. Moreover, it compares the standard turbulence models to models based on measurements and LES. Finally, Article 3 uniquely shows the importance of the quasi-static region.

## Article 4

In Article 4, the Mann model as recommended by the IEC standard is evaluated against turbulence models fitted to site. The purpose is to evaluate the performance of Mann against a model closely based on measurements (TIMESR), and assess whether fitting of the Mann parameters (FitMann) causes more realistic response of a bottom-fixed wind turbine.

One FINO1 situation is considered in Article 4, where the wind speed is about 12.5 m/s and neutral stratification exists. The input parameters of the FitMann model are adjusted by fitting the Mann spectrum to the measured spectrum of this situation. As expected, the wind spectrum of FitMann is closer to measurements and TIMESR than Mann, especially at lower frequencies. Although the fitting is not based on coherence estimates, the resulting co-coherence of FitMann varies slightly from Mann.

The impact of the turbulence models on the spectra and DEM of $M_z$, $M_{T,y}$, $M_{B,y}$ and $M_F$ of the bottom-fixed wind turbine is analysed. Both the low-frequency (f<0.1 Hz) and total moments are considered in the analysis. The low-frequency response is shown to have significant impact on the total response, especially at the tower bottom. The response caused by the FitMann model is closer to using TIMESR than Mann in $M_{B,y}$ and $M_F$. As found in Article 3, the wind spectrum has significant impact on the response spectrum at the tower bottom and blade root. TIMESR, reproducing the spectrum of the measured time series, is therefore assumed to produce realistic results. Correspondingly, the response caused by FitMann is assumed more realistic than Mann. It is more difficult to draw conclusions considering $M_z$ and $M_{T,y}$. The moments of Mann and FitMann are similar. Moreover, co-coherence has a large impact on these moments. Measurements of coherence are scarce, and thus it is not possible to determine which of the three models predicts the most realistic coherence and corresponding $M_z$ and $M_{T,y}$. In summary, FitMann is found to increase the accuracy of the estimated response considering the tower bottom and blade root bending moments, while improved coherence estimates are necessary to conclude the performance of FitMann on the tower top response.

Research questions 3 and 4 are answered by Article 4. The Mann parameters are fitted to site as in previous works [34, 35, 36, 37, 38, 39, 40, 41, 26, 27]. In contrast to these, Article 4 shows the resulting response of a large offshore wind turbine, and how it compares to using other turbulence models.

## Article 5

In Article 5, the TIMESR, Mann, Kaimal and LES wind fields are again compared, but in this article, their impact on the response of a floating wind turbine is in focus. The article highlights the differences in floater response when subject to different turbulence models.

Similar to Articles 2 and 3, wind fields are generated in various wind speed and atmospheric stability situations (Table 3.1). The wind spectra and co-coherence of these wind fields are presented. A wind characteristics test is again performed in order to understand the exclusive impact of shear, turbulence, and coherence on the floater response. The wind characteristics test is used to determine the probable origin of the differences in response when using the TIMESR, LES, Mann, and Kaimal wind fields. In Article 5, however, an even larger wind turbine is considered, a spar floater with a 15-MW generator. The standard deviations of the floater motions in surge, pitch, and yaw are assessed, in addition to the DEL of the tension in the upper part of the most heavily loaded mooring line (Figure 2.7). The spectra of the motions and tension are also used in the analysis.

From the wind characteristics test, it is found that shear of turbulent wind fields has negligible impact on the floater response. As for the bottom-fixed wind turbine, adding turbulence is found to increase the energy of the motion and tension spectra at all frequencies. A coherent wind field is found to cause higher spectral values in surge, pitch, and mooring line tension, with respect to a less coherent wind field. The natural frequencies of pitch and/or surge are found to be dominant for these motions and tension. Large spectral values at eigenfrequencies are sensitive to damping. On the other hand, less co-coherence, corresponding to large variations in wind speed over the rotor diameter, cause more significant yaw motions. Increased yaw motions with decreased co-coherence is according to expectations, considering the yaw moments observed for the bottom-fixed wind turbine (Article 3). In the wind characteristics test of Article 5, it is found that the pitch natural frequency is lower than expected when the wind turbine is operating. This phenomenon is studied further, demonstrating the dependence of wind speed on pitch natural period.

Large differences are found in the floater motions and tension with respect to turbulence model used. Comparing the Mann and Kaimal models, the Mann model is found to cause higher yaw standard deviation, while lower surge, pitch, and mooring line standard deviation and DEL due to the lower co-coherence estimates with respect to Kaimal. The TIMESR and LES models take atmospheric stability into account, causing higher standard deviations than the Kaimal and Mann models in surge and pitch in the unstable situation, and lower standard deviations and DEL of the motions and mooring line tension than the Kaimal and Mann models in the stable situation. In general, LES is found to cause low standard deviations and DEL due to the low turbulence levels obtained in these wind fields. On the contrary, the TIMESR wind fields tend to cause high standard deviations and DEL of the motions and tension due to the large-scale, low-frequency eddies they most often contain. Article 5 shows the differences in the response of a spar floater, and origin of these, one may expect when using various turbulence models. Floater specific response is in focus, but similarities to the bottom-fixed response of Article 3 are also drawn.

Research questions 2(c), (d) and (e) are answered by Article 5. The findings of using the standard turbulence models are compared to previous works [18, 19, 20, 21, 22]. Some deviations are found, as Article 5 considers a state-of-the-art wind turbine of 15 MW with spar foundation. As in Article 3, but in contrast to previous works considering floaters, the findings are supported by the wind characteristics test. Finally, Article 5 uniquely presents the differences in response by using the Kaimal, Mann, TIMESR and Mann wind fields in floating wind turbine simulations.

# 5 Conclusions and outlook

The purpose of this thesis is to highlight the differences and challenges related to the use of the IEC standard turbulence models in computing dynamic response of large offshore wind turbines, both bottom-fixed and floating. Existing literature is limited in terms of comparisons to more advanced turbulence models and quality assured measurements. Moreover, the rotor sizes previously considered when evaluating the wind turbine response are not state-of-the-art any longer. Finally, a thorough analysis of the origin of differences found has typically been left out.

This thesis presents a unique processing procedure for sonic anemometer measurements for offshore wind turbine applications. The processing procedure may be applied to other datasets, as already done by Hermile [109]. Following the proposed processing procedure, a comprehensive dataset has been compiled and may also be used in other works, as done by Myrtvedt et al. [110].

Wind fields generated by the Kaimal, Mann, TIMESR and LES models are furthermore compared, and their impact on the response of large offshore wind turbines is assessed with special focus on the low-frequency region (f<0.1 Hz). These comparisons are unique with respect to previous works. The response of both a bottom-fixed (monopile) and floating (spar) wind turbine is assessed.

Significant differences in response are observed when using the Kaimal and Mann input wind fields, although the wind shear, TI and wind spectra are alike. The Mann model estimates lower co-coherence than Kaimal, especially in the horizontal direction where the Mann model even estimates a negative co-coherence. The quasi-static $M_{B,y}$ (tower bottom bending moment fore-aft) and $M_F$ (blade root flapwise bending moment) DEM of the bottom-fixed wind turbine, and the surge, pitch, and mooring line standard deviations and DEL of the floater is larger when using the Kaimal model than the Mann model due to this difference in co-coherence. On the other hand, local variations over the rotor increase the $M_z$ (tower top yaw moment) DEM of the bottom-fixed and yaw motion standard deviation of the floater, and thus Mann causes higher values of these. As the natural frequencies of the floater appear at frequencies where the power spectral densities of the wind spectrum and the co-coherence are high, larger differences are in general seen in the floater than the bottom-fixed wind turbine. The low-frequency, quasi-static, response is although demonstrated to be a large contributor to the total response of the bottom-fixed wind turbine in consideration as well.

Using the Kaimal and Mann wind fields in offshore wind turbine simulations may not result in realistic response as these models are made for small onshore turbines and do not account for atmospheric stability. Compared to the LES and TIMESR wind fields, the wind characteristics of the Mann and Kaimal wind fields are quite similar. As expected, the wind fields of Kaimal and Mann are most similar to the LES and TIMESR wind fields of neutral stratification. The wind fields of TIMESR and LES show large differences for non-neutral conditions. These differences impact the dynamic response of the offshore wind turbines. It is time for the wind turbine standards and industry to consider more advanced turbulence models that account for stability.

TIMESR is considered realistic in its representation of the wind spectra, considering that it reproduces the measured wind spectra at several points in space. The shape of

the wind spectra is reflected in the low-frequency spectra of $M_{B,y}$ and $M_F$ of the bottom-fixed wind turbine and surge and pitch motions of the floater, demonstrating its large impact on these moments and motions. TIMESR is therefore considered to represent these moments and motions accurately, while Kaimal and Mann tend to underestimate them. They are both incapable to represent the large-scale fluctuations that are observed in measurements.

The TIMESR and LES models are in principle considered more realistic as they are based on measurements and physics to a larger degree than Kaimal and Mann. They do however have their own challenges. The TIMESR model requires realistic high-frequent measurements at site. The LES model requires high computational capacity. In this thesis, another great challenge of LES is highlighted: It is difficult to achieve desired output conditions. LES may result in a realistic atmospheric flow with desired stability, but it is challenging to obtain a desired combination of Obukhov length, shear, turbulence intensity and hub height wind speed. In this thesis, the authors experienced that it was difficult to achieve high enough turbulence intensity, particularly in the neutral situations. The inadequate turbulence intensity levels have consequences for the response. The LES model tends to cause a low overall response both for the bottom-fixed and floating wind turbine of this thesis.

In this thesis, a FitMann wind field is uniquely compared to other wind fields, and their impact on the response of a large offshore wind turbine is investigated. Being better at representing the actual wind spectrum than Mann, FitMann is also expected to cause more realistic $M_{B,y}$ and $M_F$ than Mann. The current thesis is not able to give a quantitative assessment of this improvement. The performance of FitMann vs. Mann in representing realistic $M_z$ and $M_{T,y}$ (tower top bending moment fore-aft) is rather uncertain. Due to the mentioned uncertainties of the improvements of the FitMann model over Mann, and the number of measurements required, FitMann may not always be a superior option to Mann.

A common conclusion of all five articles included in this thesis is that there is a great need for better coherence measurements offshore. With a better reference, one could easier determine which of the considered turbulence models that estimates coherence most realistically. Consequently, it would be easier to determine which turbulence model causes more realistic response, especially regarding the yaw moments and motions, which strongly depend on horizontal co-coherence. The need for better measurements is most apparent for horizontal separation distances.

## 5.1 Further work

This thesis opens up a number of research needs regarding offshore measurements, turbulence models and dynamic response of offshore wind turbines. Below, I discuss a few of these.

As stated above, this thesis shows that the response of offshore wind turbines clearly depends on the turbulence model chosen. It furthermore shows challenges of the IEC standard models, e.g. their ability to adapt to various atmospheric stability conditions. It also points at challenges of more advanced models, such as available measurements of high quality and computational costs. Further work should aim at finding an improved turbulence model that takes atmospheric stability into account. The improved model

should preferably not require extensive measurements or high computational efforts. The FINO1 quality assured dataset presented in this thesis can work as a reference in searching for an improved turbulence model. Improvements of turbulence models is an active field of research, and the University of Bergen together with other research partners have recently started a project on this topic [111]. I suggest starting off with including additional existing turbulence models in such a study. One could e.g. build on Article 4 and fit FitMann to various atmospheric stability conditions, or consider the models used in Rinker [88], Cheynet et al. [27], Putri et al. [22, 23, 89], Højstrup [90] or the TurbSim manual [51].

Another research possibility is to perform similar studies as Articles 3, 4 and 5, but consider two wind turbines in a row. Such a study would show the differences in response of a wind turbine subject to various turbulent wind fields combined with the wake from the wind turbine in front. Simulations with two wind turbines may be run in FastFARM [112]. Another option is to combine a turbulent wind field with a dynamic wake meandering model in SIMA and run the resulting wind field towards a wind turbine. The simple wake models that are commonly used today do not account for atmospheric stability, and may therefore be challenged by more complex models in such a study. In the suggested study, one could also discuss how close one can put bottom-fixed and floating wind turbines. Waves may play a bigger role in such simulations.

As mentioned above, it was found to be challenging to tune LES outputs to real conditions. This challenge could be studied further. One option is to run a sensitivity study of the impact of input parameters (e.g. surface heat flux, surface roughness and potential temperature profile) on desired output parameters (e.g. TI, Obukhov length and shear profile). Another option is to find innovative ways of controlling the desired parameters. In the SOWFA simulations of this thesis, the mean wind speed at hub height is controlled through the combination of a pressure gradient force and a simple controller.

The impact of controller on the dynamic response is not evaluated in this thesis. It is still clear that it has an impact, especially on the floater motions, as briefly mentioned in Article 5. Using another controller, one could e.g. expect larger or smaller motions. With larger or smaller total motions, the absolute differences caused by the various turbulence models may also vary. I therefore think that further studies on controller issues could be useful.

As highlighted above, there is a great need for understanding coherence of offshore wind, especially of points separated horizontally. Such knowledge could be achieved by setting up several meteorological masts with sonic anemometers. This setup is obviously expensive, and thus innovative setups such as presented in the COTUR project [81] may serve as a better solution.

# Bibliography


[1] P. R. Shukla, J. Skea, R. Slade, Khourdajie A. Al., R. van Diemen, D. McCollum, M. Pathak, S. Some, P. Vyas, R. Fradera, M. Belkacemi, A. Hasija, G Lisboa, S. Luz, and J. Malley. Climate change 2022: mitigation of climate change. Contribution of working group III to the sixth assessment report of the intergovernmental panel on climate change. Technical report, IPCC, Cambridge, UK and New York, USA, 2022. doi:10.1017/9781009157926.

[2] International Renewable Energy Agency. Future of wind: Deployment, investment, technology, grid integration and socio-economic aspects (a global energy transformation paper). Technical report, IRENA, Abu Dhabi, UAE, 2019. https://www.irena.org/-/media/Files/IRENA/Agency/Publication/2019/Oct/IRENA_Future_of_wind_2019.pdf. Accessed July 2, 2021.

[3] International Energy Agency. Offshore wind outlook 2019. Technical report, IEA, Paris, France, 2019. https://iea.blob.core.windows.net/assets/495ab264-4ddf-4b68-b9c0-514295ff40a7/Offshore_Wind_Outlook_2019.pdf. Accessed July 2, 2021.

[4] J. Lee and F. Zhao. Global offshore wind report 2021. Technical report, GWEC, Brussels, Belgium, 2021. https://gwec.net/wp-content/uploads/2021/09/GWEC-Global-Offshore-Wind-Report-2021.pdf. Accessed June 3, 2022.

[5] A. Buljan. Scotland's new floating wind projects – What we know so far, 2022. https://www.offshorewind.biz/2022/01/18/scotlands-new-floating-wind-projects-what-we-know-so-far/. Accessed May 23, 2022.

[6] A. Durakovic. Norway launches 30 GW by 2040 offshore wind investment plan, 2022. https://www.offshorewind.biz/2022/05/11/norway-launches-30-gw-by-2040-offshore-wind-investment-plan/. Accessed May 23, 2022.

[7] A. Buljan. Four EU countries set joint target of 150 GW of offshore wind by 2050, 2022. https://www.offshorewind.biz/2022/05/18/four-eu-countries-set-joint-target-of-150-gw-of-offshore-wind-by-2050/. Accessed May 23, 2022.

[8] European Commission. REPowerEU: affordable, secure and sustainable energy for Europe, 2022. https://ec.europa.eu/info/strategy/priorities-2019-2024/european-green-deal/repowereu-affordable-secure-and-sustainable-energy-europe_en. Accessed May 23, 2022.

[9] A. Durakovic. MingYang launches 16 MW offshore wind turbine, 2021. https://www.offshorewind.biz/2021/08/20/mingyang-launches-16-mw-offshore-wind-turbine/. Accessed June 6, 2022.

[10] P. Veers, K. Dykes, E. Lantz, S. Barth, C. L. Bottasso, O. Carlson, A. Clifton, J. Green, P. Green, H. Holttinen, et al. Grand challenges in the science of wind energy. *Science*, 366(6464):eaau2027, 2019. doi:10.1126/science.aau2027.

[11] A. Sathe, J. Mann, J. Gottschall, and M. S. Courtney. Can wind lidars measure turbulence? *Journal of Atmospheric and Oceanic Technology*, 28(7):853–868, 2011. doi:10.1175/JTECH-D-10-05004.1.

[12] V.-M. Kumer, J. Reuder, M. Dorninger, R. Zauner, and V. Grubišić. Turbulent kinetic energy estimates from profiling wind LiDAR measurements and their potential for wind energy applications. *Renewable Energy*, 99:898–910, 2016. doi:10.1016/j.renene.2016.07.014.

[13] B. Cañadillas, A. Bégué, and T. Neumann. Comparison of turbulence spectra derived from LiDAR and sonic measurements at the offshore platform FINO1. In *Proceedings of the 10th German Wind Energy Conference, DEWEK*, Bremen, Germany, 2010.

[14] F. Kelberlau and J. Mann. Cross-contamination effect on turbulence spectra from doppler beam swinging wind lidar. *Wind Energy Science*, 5(2):519–541, 2020. doi:10.5194/wes-5-519-2020.

[15] International Electrotechnical Commision. IEC 61400-1:2019 Wind energy generation systems - Part 1: Design requirements. Technical report, IEC, Geneva, Switzerland, 2019. https://webstore.iec.ch/publication/26423. Accessed July 2, 2021.

[16] J. Mann. The spatial structure of neutral atmospheric surface-layer turbulence. *Journal of Fluid Mechanics*, 273:141–168, 1994. doi:10.1017/S0022112094001886.

[17] J. C. Kaimal, J. C. Wyngaard, Y. Izumi, and O. R. Coté. Spectral characteristics of surface-layer turbulence. *Quarterly Journal of the Royal Meteorological Society*, 98(417):563–589, 1972. doi:10.1002/qj.49709841707.

[18] E. E. Bachynski and L. Eliassen. The effects of coherent structures on the global response of floating offshore wind turbines. *Wind Energy*, 22(2):219–238, 2019. doi:10.1002/we.2280.

[19] L. Eliassen and E. E. Bachynski. The effect of turbulence model on the response of a large floating wind turbine. In *ASME 2017 36th International Conference on Ocean, Offshore and Arctic Engineering*, Trondheim, Norway, 2017. doi:10.1115/OMAE2017-61179.

[20] P. Doubrawa, M. J. Churchfield, M. Godvik, and S. Sirnivas. Load response of a floating wind turbine to turbulent atmospheric flow. *Applied Energy*, 242:1588–1599, 2019. doi:10.1016/j.apenergy.2019.01.165.

[21] M. Godvik. Influence of wind coherence on the response of a floating wind turbine. In *Science meets Industry*, Stavanger, Norway, 2016.

[22] R. M. Putri, C. Obhrai, J. B. Jakobsen, and M. C. Ong. Numerical analysis of the effect of offshore turbulent wind inflow on the response of a spar wind turbine. *Energies*, 13(10):1–22, 2020. doi:10.3390/en13102506.

[23] R. M. Putri, C. Obhrai, and J. B. Jakobsen. Response sensitivity of a semisubmersible floating offshore wind turbine to different wind spectral models. In *Journal of Physics: Conference Series*, 2020. doi:10.1088/1742-6596/1618/2/022012.

[24] L. Eliassen and C. Obhrai. Coherence of turbulent wind under neutral wind conditions at FINO1. *Energy Procedia*, 94:388–398, 2016. doi:10.1016/j.egypro.2016.09.199.

[25] L. Eliassen and S. Andersen. Investigating coherent structures in the standard turbulence models using proper orthogonal decomposition. In *Journal of Physics: Conference Series*, Munich, Germany, 2016. doi:10.1088/1742-6596/753/3/032040.

[26] E. Cheynet. Influence of the measurement height on the vertical coherence of natural wind. In *Proceedings of the XV Conference of the Italian Association for Wind Engineering*, Napoli, Italy, 2019. doi:10.1007/978-3-030-12815-9_17.

[27] E. Cheynet, J. B. Jakobsen, and J. Reuder. Velocity spectra and coherence estimates in the marine atmospheric boundary layer. *Boundary-Layer Meteorology*, 169(3):429–460, 2018. doi:10.1007/s10546-018-0382-2.

[28] T. Foken and B. Wichura. Tools for quality assessment of surface-based flux measurements. *Agricultural and Forest Meteorology*, 78(1-2):83–105, 1996. doi:10.1016/0168-1923(95)02248-1.

[29] T. Foken, R. Leuning, S. R. Oncley, M. Mauder, and M. Aubinet. Corrections and data quality control. In *Eddy Covariance*, pages 85–131. Springer, Dordrecht, 2012. doi:10.1007/978-94-007-2351-1_4.

[30] D. Vickers and L. Mahrt. Quality control and flux sampling problems for tower and aircraft data. *Journal of Atmospheric and Oceanic Technology*, 14(3):512–526, 1997. doi:10.1175/1520-0426(1997)014<0512:QCAFSP>2.0.CO;2.

[31] T. Mücke, C. Harkness, and K. Argyriadis. Offshore wind turbulence model versus measurement. In *Proceedings of EWEA*, Copenhagen, Denmark, 2012. https://www.researchgate.net/profile/Tanja-Winter-2/publication/233918601_Offshore_Wind_Turbulence_-_Model_versus_Measurement/links/560d781108ae96742010cea6/Offshore-Wind-Turbulence-Model-versus-Measurement.pdf. Accessed June 27, 2022.

[32] M. Türk and S. Emeis. The dependence of offshore turbulence intensity on wind speed. *Journal of Wind Engineering and Industrial Aerodynamics*, 98(8-9):466–471, 2010. doi:10.1016/j.jweia.2010.02.005.

[33] B. Ernst and J. R. Seume. Investigation of site-specific wind field parameters and their effect on loads of offshore wind turbines. *Energies*, 5(10):3835–3855, 2012. doi:10.3390/en5103835.

[34] J. Mann. Wind field simulation. *Probabilistic Engineering Mechanics*, 13(4):269–282, 1998. doi:10.1016/S0266-8920(97)00036-2.

[35] A. Sathe, J. Mann, T. Barlas, W. A. A. M. Bierbooms, and G. J. W. van Bussel. Influence of atmospheric stability on wind turbine loads. *Wind Energy*, 16(7):1013–1032, 2013. doi:10.1002/we.1528.

[36] M. De Maré and J. Mann. Validation of the Mann spectral tensor for offshore wind conditions at different atmospheric stabilities. In *Journal of Physics: Conference Series*, Copenhagen, Denmark, 2014. doi:10.1088/1742-6596/524/1/012106.

[37] A. Peña, S.-E. Gryning, and J. Mann. On the length-scale of the wind profile. *Quarterly Journal of the Royal Meteorological Society*, 136(653):2119–2131, 2010. doi:10.1002/qj.714.

[38] A. Peña, S.-E. Gryning, J. Mann, and C. B. Hasager. Length scales of the neutral wind profile over homogeneous terrain. *Journal of Applied Meteorology and Climatology*, 49(4):792–806, 2010. doi:10.1175/2009JAMC2148.1.

[39] A. Chougule, J. Mann, A. Segalini, and E. Dellwik. Spectral tensor parameters for wind turbine load modeling from forested and agricultural landscapes. *Wind Energy*, 18(3):469–481, 2015. doi:10.1002/we.1709.

[40] A. Chougule, J. Mann, M. Kelly, and G. C. Larsen. Modeling atmospheric turbulence via rapid distortion theory: Spectral tensor of velocity and buoyancy. *Journal of the Atmospheric Sciences*, 74(4):949–974, 2017. doi:10.1175/JAS-D-16-0215.1.

[41] A. Chougule, J. Mann, M. Kelly, and G. C. Larsen. Simplification and validation of a spectral-tensor model for turbulence including atmospheric stability. *Boundary-Layer Meteorology*, 167(3):371–397, 2018. doi:10.1007/s10546-018-0332-z.

[42] M. Y. Mahfouz, M. Salari, S. Hernández, F. Vigara, C. Molins, P. Trubat, H. Bredmose, and A. Pegalajar-Jurado. Public design and FAST models of the two 15MW floater-turbine concepts. Technical report, University of Stuttgart, Stuttgart, Germany, 2020. http://corewind.eu/wp-content/uploads/files/publications/COREWIND-public-design-and-FAST-models-of-the-two-15mw-floater-turbine-concepts.pdf. Accessed July 2, 2021.

[43] M. Y. Mahfouz, C. Molins, P. Trubat, S. Hernández, F. Vigara, A. Pegalajar-Jurado, H. Bredmose, and M. Salari. Response of the International Energy Agency (IEA) wind 15 MW WindCrete and Activefloat floating wind turbines to wind and second-order waves. *Wind Energy Science*, 6(3):867–883, 2021. doi:10.5194/wes-6-867-2021.

[44] P. Trubat, C. Molins, D. Alarcon, V. Arramounet, and M. Y. Mahfouz. Mooring fatigue verification of the WindCrete for a 15 MW wind turbine. In *ASME 2021 3rd International Offshore Wind Technical Conference*, 2021. doi:10.1115/IOWTC2021-3553.

[45] M. Y. Mahfouz, T. Roser, and P. W. Cheng. Verification of SIMPACK-MoorDyn coupling using 15 MW IEA-wind reference models Activefloat and WindCrete. In *Journal of Physics: Conference Series*, 2021. doi:10.1088/1742-6596/2018/1/012024.

[46] P. Nicolò, A. Pegalajar-Jurado, S. Dou, H. Bredmose, and M. Stolpe. Gradient-based optimization of a 15 MW wind turbine spar floater. In *Journal of Physics: Conference Series*, 2021. doi:10.1088/1742-6596/2018/1/012032.

[47] A. Robertson, L. Sethuraman, J. Jonkman, and J. Quick. Assessment of wind parameter sensitivity on ultimate and fatigue wind turbine loads. Technical Report NREL/CP-5000-70445, NREL, Golden, Colorado, USA, 2018. https://www.nrel.gov/docs/fy18osti/70445.pdf. Accessed February 16, 2021.

[48] A. S. Monin and A. M. Obukhov. Basic laws of turbulent mixing in the surface layer of the atmosphere. *Contrib. Geophys. Inst. Acad. Sci. USSR*, 24(151):163–187, 1954. https://gibbs.science/efd/handouts/monin_obukhov_1954.pdf. Accessed June 27, 2022.

[49] T. Foken. 50 years of the Monin-Obukhov similarity theory. *Boundary-Layer Meteorology*, 119(3):431–447, 2006. doi:10.1007/s10546-006-9048-6.

[50] R. B. Stull. *An introduction to boundary layer meteorology*. Springer, 1988.

[51] B. J. Jonkman. TurbSim user's guide v2.00.00. Technical report, NREL, Golden, Colorado, USA, 2016. https://www.nrel.gov/wind/nwtc/assets/downloads/TurbSim/TurbSim_v2.00.pdf. Accessed June 24, 2022.

[52] A. J. Dyer. A review of flux-profile relationships. *Boundary-Layer Meteorology*, 7(3):363–372, 1974. doi:10.1007/BF00240838.

[53] J. A. Businger, J. C. Wyngaard, Y. Izumi, and E. F. Bradley. Flux-profile relationships in the atmospheric surface layer. *Journal of the Atmospheric Sciences*, 28(2):181–189, 1971. doi:10.1175/1520-0469(1971)028<0181:FPRITA>2.0.CO;2.

[54] S.-E. Gryning, E. Batchvarova, B. Brümmer, H. Jørgensen, and S. Larsen. On the extension of the wind profile over homogeneous terrain beyond the surface boundary layer. *Boundary-Layer Meteorology*, 124(2):251–268, 2007. doi:10.1007/s10546-007-9166-9.

[55] A. Peña, S.-E. Gryning, and C. B. Hasager. Measurements and modelling of the wind speed profile in the marine atmospheric boundary layer. *Boundary-Layer Meteorology*, 129(3):479–495, 2008. doi:10.1007/s10546-008-9323-9.

[56] A. Durakovic. World's largest, most powerful wind turbine stands complete, 2021. https://www.offshorewind.biz/2021/11/12/worlds-largest-most-powerful-wind-turbine-stands-complete/. Accessed May 5, 2022.

[57] P. S. Veers. Modeling stochastic wind loads on vertical axis wind turbines. In *25th Structures, Structural Dynamics and Materials Conference*, Palm Springs, California, USA, 1984. doi:10.2514/6.1984-910.

[58] P. S. Veers. Three-dimensional wind simulation. Technical report, Sandia National Laboratories, Albuquerque, New Mexico, USA, 1988.

[59] K. Saranyasoontorn, L. Manuel, and P. S. Veers. A comparison of standard coherence models for inflow turbulence with estimates from field measurements. *Journal of Solar Energy Engineering*, 126(4):1069–1082, 2004. doi:10.1115/1.1797978.

[60] B. H. Jørgensen, J. N. Sørensen, and M. Brøns. Low-dimensional modeling of a driven cavity flow with two free parameters. *Theoretical and Computational Fluid Dynamics*, 16(4):299–317, 2003. doi:10.1007/s00162-002-0082-9.

[61] A. M. Obukhov. Turbulence in an atmosphere with a non-uniform temperature. *Boundary-Layer Meteorology*, 2(1):7–29, 1971. doi:10.1007/BF00718085.

[62] A. J. M. Van Wijk, A. C. M. Beljaars, A. A. M. Holtslag, and W. C. Turkenburg. Evaluation of stability corrections in wind speed profiles over the North Sea. *Journal of Wind Engineering and Industrial Aerodynamics*, 33(3):551–566, 1990. doi:10.1016/0167-6105(90)90007-Y.

[63] S. Krohn. Danish wind turbines: an industrial success story, 2001. http://ele.aut.ac.ir/~wind/en/articles/success.htm. Accessed June 27, 2022.

[64] E. Möllerström, P. Gipe, J. Beurskens, and F. Ottermo. A historical review of vertical axis wind turbines rated 100 kW and above. *Renewable and Sustainable Energy Reviews*, 105:1–13, 2019. doi:10.1016/j.rser.2018.12.022.

[65] C. Lo. Vestas's multi-rotor wind turbine: are four rotors better than one?, 2020. https://www.power-technology.com/analysis/featurevestass-multi-rotor-wind-turbine-are-four-rotors-better-than-one-5001819/. Accessed May 9, 2022.

[66] W. Musial, P. Spitsen, P. Beiter, P. Duffy, M. Marquis, A. Cooperman, R. Hammond, and M. Shields. Offshore wind market report: 2021 edition. Technical report, U.S. Department of Energy, Washington D.C., USA, 2021. https://www.energy.gov/eere/wind/articles/offshore-wind-market-report-2021-edition-released. Accessed June 27, 2022.

[67] M. Froese. World's first floating wind farm delivers promising results, 2018. https://www.windpowerengineering.com/worlds-first-floating-wind-farm-delivers-promising-results/. Accessed May 9, 2022.

[68] A. Durakovic. Foundations for world's largest floating offshore wind farm under tow – Gallery, 2022. https://www.offshorewind.biz/2022/04/15/foundations-for-worlds-largest-floating-offshore-wind-farm-under-tow-gallery/. Accessed May 9, 2022.

[69] N. J. Abbas, D. S. Zalkind, L. Pao, and A. Wright. A reference open-source controller for fixed and floating offshore wind turbines. *Wind Energy Science*, 7(1):53–73, 2022. doi:10.5194/wes-7-53-2022.

[70] H. Glauert. Airplane propellers. In *Aerodynamic theory*, pages 169–360. Springer, Dordrecht, 1935.

[71] W. Froude. On the elementary relation between pitch, slip, and propulsive efficiency. *Transaction of the Institute of Naval Architects*, 19:22–33, 1878.

[72] S. Drzewiecki. *Méthode pour la détermination des éléments mécaniques des propulseurs hélicoïdaux*. imprimerie Gauthier-Villars et Fils, 1892.

[73] W. J. M. Rankine. On the mechanical principles of the action of propellers. *Transactions of the Institution of Naval Architects*, 6:13–39, 1865.

[74] R. E. Froude. On the part played in propulsion by differences of fluid pressure. *Transactions of the Institution of Naval Architects*, 30:390–405, 1889.

[75] National Renewable Energy Laboratory. OpenFAST, 2021. https://github.com/openfast. Accessed July 2, 2021.

[76] O. A. Hermundstad. Sima - SINTEF. https://www.sintef.no/programvare/sima/. Accessed February 16, 2021.

[77] V. D'andrea and J. Manuel. Study of the motions and nacelle accelerations of the Windcrete floating offshore wind turbine according to the IEC 64100-3 procedure. Master's thesis, Escola Tècnica Superior d'Enginyeria Industrial de Barcelona, 2020.

[78] International Electrotechnical Commision. IEC TS 61400-13:2015 Wind turbine generator systems - Part 13: Measurement of mechanical loads. Technical report, IEC, Geneva, Switzerland, 2015. https://webstore.iec.ch/publication/23971. Accessed February 16, 2021.

[79] A. Niesłony. Determination of fragments of multiaxial service loading strongly influencing the fatigue of machine components. *Mechanical Systems and Signal Processing*, 23(8):2712–2721, 2009. doi:10.1016/j.ymssp.2009.05.010.

[80] FuE-Zentrum FH Kiel GmbH. FINO - Forschungsplattformen in Nord- und Ostsee Nr. 1,2,3, 2019. https://www.fino-offshore.de/de/index.html. Accessed May 18, 2022.

[81] E. Cheynet, M. Flügge, J. Reuder, J. B. Jakobsen, Y. Heggelund, B. Svardal, P. Saavedra Garfias, C. Obhrai, J. Daniotti, N.and Berge, et al. The COTUR project: remote sensing of offshore turbulence for wind energy application. *Atmospheric Measurement Techniques*, 14(9):6137–6157, 2021. doi:10.5194/amt-14-6137-2021.

[82] C. Duscha, M. B. Paskyabi, and J. Reuder. Statistic and coherence response of ship-based lidar observations to motion compensation. In *Journal of Physics: Conference Series*, Trondheim, Norway, 2020. doi:10.1088/1742-6596/1669/1/012020.

[83] FuE-Zentrum FH Kiel GmbH. FINO1: Forschungsplattform in Nord- und Ostsee Nr. 1, 2022. http://www.fino1.de/de/. Accessed June 24, 2022.

[84] T. Neumann and K. Nolopp. Three years operation of far offshore measurements at FINO1. *DEWI-Magazin*, 30:42–46, 2007.

[85] M. Bakhoday-Paskyabi, I. Fer, and J. Reuder. Current and turbulence measurements at the FINO1 offshore wind energy site: analysis using 5-beam ADCPs. *Ocean Dynamics*, 68:109–130, 2018. doi:10.1007/s10236-017-1109-5.

[86] International Electrotechnical Commision. IEC 61400-3-1:2019 Wind energy generation systems - Part 3-1: Design requirements for fixed offshore wind turbines. Technical report, IEC, Geneva, Switzerland, 2019. https://webstore.iec.ch/publication/29360. Accessed July 2, 2021.

[87] International Electrotechnical Commision. IEC TS 61400-3-2:2019 Wind energy generation systems - Part 3-2: Design requirements for floating offshore wind turbines. Technical report, IEC, Geneva, Switzerland, 2019. https://webstore.iec.ch/publication/29244. Accessed July 2, 2021.

[88] J. M. Rinker. *An empirically based stochastic turbulence simulator with temporal coherence for wind energy applications*. PhD thesis, Duke University, 2016.

[89] R. M. Putri, C. Obhrai, and J. M. Knight. Offshore wind turbine loads and motions in unstable atmospheric conditions. In *Journal of Physics: Conference Series*, Trondheim, Norway, 2019. doi:10.1088/1742-6596/1356/1/012016.

[90] J. Højstrup. A simple model for the adjustment of velocity spectra in unstable conditions downstream of an abrupt change in roughness and heat flux. *Boundary-Layer Meteorology*, 21(3):341–356, 1981. doi:10.1007/BF00119278.

[91] A. G. Davenport. The spectrum of horizontal gustiness near the ground in high winds. *Quarterly Journal of the Royal Meteorological Society*, 87(372):194–211, 1961. doi:10.1002/qj.49708737208.

[92] M. B. Kristiansen. Mann 64bit turbulence generator, 2018. https://www.hawc2.dk/download/pre-processing-tools. Accessed February 16, 2021.

[93] M. Churchfield, S. Lee, and P. Moriarty. Overview of the Simulator fOr Wind Farm Application (SOWFA). Technical report, NREL, Boulder, Colorado, USA, 2012. https://www.nrel.gov/wind/nwtc/assets/pdfs/sowfa-tutorial.pdf. Accessed February 16, 2021.

[94] T. Von Kármán. Progress in the statistical theory of turbulence. *Proceedings of the National Academy of Sciences of the United States of America*, 34(11):530–539, 1948. doi:10.1073/pnas.34.11.530.

[95] L. Vollmer, G. Steinfeld, D. Heinemann, and M. Kühn. Estimating the wake deflection downstream of a wind turbine in different atmospheric stabilities: an LES study. *Wind Energy Science*, 1(2):129–141, 2016. doi:10.5194/wes-1-129-2016.

[96] N. Sedaghatizadeh, M. Arjomandi, R. Kelso, B. Cazzolato, and M. H. Ghayesh. Modelling of wind turbine wake using large eddy simulation. *Renewable Energy*, 115:1166–1176, 2018. doi:10.1016/j.renene.2017.09.017.

[97] J. D. Mirocha, D. A. Rajewski, N. Marjanovic, J. K. Lundquist, B. Kosović, C. Draxl, and M. J. Churchfield. Investigating wind turbine impacts on near-wake flow using profiling lidar data and large-eddy simulations with an actuator disk model. *Journal of Renewable and Sustainable Energy*, 7(4):043143, 2015. doi:10.1063/1.4928873.

[98] M. Abkar and F. Porté-Agel. Influence of atmospheric stability on wind-turbine wakes: A large-eddy simulation study. *Physics of Fluids*, 27(3):035104, 2015. doi:10.1063/1.4913695.

[99] M. L. Aitken, B. Kosović, J. D. Mirocha, and J. K. Lundquist. Large eddy simulation of wind turbine wake dynamics in the stable boundary layer using the Weather Research and Forecasting Model. *Journal of Renewable and Sustainable Energy*, 6(3):033137, 2014. doi:10.1063/1.4885111.

[100] X. Ning and D. Wan. LES study of wake meandering in different atmospheric stabilities and its effects on wind turbine aerodynamics. *Sustainability*, 11(24):6939, 2019. doi:10.3390/su11246939.

[101] S. Krüger, G. Steinfeld, M. Kraft, and L. J. Lukassen. Validation of a coupled atmospheric-aeroelastic model system for wind turbine power and load calculations. *Wind Energy Science*, 7(1):323–344, 2022. doi:10.5194/wes-7-323-2022.

[102] H. S Sørum, J.-T. H. Horn, and J. Amdahl. Comparison of numerical response predictions for a bottom-fixed offshore wind turbine. *Energy Procedia*, 137:89–99, 2017. doi:10.1016/j.egypro.2017.10.336.

[103] C. Bak, F. Zahle, R. Bitsche, T. Kim, A. Yde, L. C. Henriksen, M. H. Hansen, J. P. A. A. Blasques, M. Gaunaa, and A. Natarajan. The DTU 10-MW reference wind turbine. Technical report, DTU, Roskilde, Denmark, 2013. http://orbit.dtu.dk/ws/files/55645274/The_DTU_10MW_Reference_Turbine_Christian_Bak.pdf. Accessed February 16, 2021.

[104] E. E. Bachynski and H. Ormberg. Hydrodynamic modeling of large-diameter bottom-fixed offshore wind turbines. In *ASME 2015 34th International Conference on Ocean, Offshore and Arctic Engineering*, St. John's, Newfoundland, Canada, 2015. doi:10.1115/OMAE2015-42028.

[105] S. H. Sørum, J. R. Krokstad, and J. Amdahl. Wind-wave directional effects on fatigue of bottom-fixed offshore wind turbine. In *Journal of Physics: Conference Series*, Trondheim, Norway, 2019. doi:10.1088/1742-6596/1356/1/012011.

[106] E. Gaertner, J. Rinker, L. Sethuraman, F. Zahle, B. Anderson, G. E. Barter, N. J. Abbas, F. Meng, P. Bortolotti, W. Skrzypinski, G. N. Scott, R. Feil, H. Bredmose, K. Dykes, M. Shields, C. Allen, and A. Viselli. Definition of the IEA 15-Megawatt offshore reference wind turbine. Technical Report NREL/TP-5000-75698, NREL, Golden, Colorado, USA, 2020. doi:10.2172/1603478.

[107] C. Allen, A. Viselli, H. Dagher, A. Goupee, E. Gaertner, N. Abbas, M. Hall, and G. Barter. Definition of the UMaine VolturnUS-S reference platform developed for the IEA wind 15-megawatt offshore reference wind turbine. Technical Report NREL/TP-5000-76773, NREL, Golden, Colorado, USA, 2020. doi:10.2172/1660012.

[108] Y. Mahfouz, M. Salari, F. Vigara, S. Hernandez, C. Molins, P. Trubat, H. Bredmose, and A. Pegalajar-Jurado. D1.3. Public design and FAST models of the two 15MW floater-turbine concepts, 2020. doi:10.5281/zenodo.4385727.

[109] M. Hermile. Atmospheric stability effects on a spar-type floating wind turbine. Master's thesis, NTNU, 2021.

[110] M. H. Myrtvedt, A. Nybø, and F. G. Nielsen. The dynamic response of offshore wind turbines and their sensitivity to wind field models. In *Journal of Physics: Conference Series*, Trondheim, Norway, 2020. doi:10.1088/1742-6596/1669/1/012013.

[111] R. H Nyheim and J. Reuder. BOW project received funding, 2021. https://www.uib.no/en/bow/146173/bow-project-received-funding. Accessed June 29, 2022.

[112] J. Jonkman and K. Shaler. FAST.Farm user's guide and theory manual. Technical Report NREL/TP-5000-78485, NREL, Golden, Colorado, USA, 2021. https://www.nrel.gov/docs/fy21osti/78485.pdf. Accessed June 27, 2022.

# Paper 1

## Processing of sonic anemometer measurements for offshore wind turbine applications

Nybø A, Nielsen FG and Reuder J
*J. Phys. Conf. Ser.*, **1356/012006** (2019)

IOP Conf. Series: Journal of Physics: Conf. Series **1356** (2019) 012006 doi:10.1088/1742-6596/1356/1/012006

# Processing of sonic anemometer measurements for offshore wind turbine applications

**A Nybø, F G Nielsen and J Reuder**

Geophysical Institute, and Bergen Offshore Wind Centre (BOW), University of Bergen, Norway

E-mail: astrid.nybo@uib.no

**Abstract.** Quality assured measurements from offshore masts may provide valuable information of the characteristics of the offshore wind field, which is of high relevance for simulations of offshore wind turbines' dynamic response. In order to obtain these high quality data sets, a processing procedure tailored to offshore wind turbine applications must be followed. In this study, existing quality control routines applied in literature are evaluated, and a complete procedure is developed for sonic anemometer measurements. This processing procedure is applied to measurements at three heights from 16 months of measurements at FINO1. The processing procedure results in a data set of more than 6 000 30-minute periods of high quality time series showing a large variety in terms of wind speed and turbulence intensity. Together with an assessment of the stationarity, this processed data set is ready for use in offshore wind turbine research.

## 1. Introduction

Wind turbines in operation are exposed to and have to react on a complex flow environment, where vertical wind shear, turbulence intensity, coherence and atmospheric stability are closely interconnected [1–3]. The analysis of their dynamic response requires the understanding of the offshore wind characteristics and thus the availability of high quality wind measurements offshore.

Observations are rather sparse, as the infrastructural requirements connected to offshore measurements are considerable. In-situ measurements with cup or sonic anemometers require a mast or tower structure that is expensive, limited to one location and that causes additional disturbances in the flow measurements from certain directions. Lidar-based remote sensing can be performed from offshore platforms, buoys or ships and provides a more flexible measurement setup with respect to localization. The inherent volume averaging in the lidar measurements limits, however, the use of those data for the characterization of turbulence [4].

Sonic anemometers are robust instruments without moving parts that can provide high frequency measurements (typically 10 to 100 Hz) of the 3D wind field and the sonic temperature even in harsh offshore environments. The preparation of the raw data for further analysis requires a thorough and extensive quality control procedure, that removes unphysical values (e.g. spikes) or situations where the measurements are disturbed by flow-distortion or precipitation, assesses stationarity and organizes the data in appropriate time windows for the relevant applications. Quality control routines for sonic anemometer measurements have been described by e.g. Foken and Wichura [5], Vickers and Mahrt [6] and Foken et al. [7, 8]. They mainly focus on data

processing for the use in boundary layer meteorology, where a correct representation of the turbulent fluxes of heat, moisture and momentum is of highest importance. All the above publications mention spike detection procedures and stationarity tests, which are relevant for wind speed analysis as well. Time series designated for the use in load simulations for turbines might, however, require a more specific handling and quality control. The time resolution has to be high enough to allow for the simulations of high frequency phenomena, as, e.g., blade tip vibrations. The data set has, on the other hand, to be long enough to cover the relevant low frequency motions as well. Natural periods of a floating wind turbine are in the range of minutes. This requires time histories of wind in the order of at least 30 minutes. State of art turbines have rotor diameter of approximately 200 m, i.e. the height range from 20 m to 250 m above sea level is of interest in wind turbine applications.

The wind measurements from the FINO1-platform, assessed in this study, have earlier been analyzed from an offshore wind turbine perspective (e.g. [3, 9–13]). The quality control routines of the sonic data in the mentioned literature include the removal of periods where the wind origins from certain directions in order to exclude disturbances due to mast shadow, and the application of a stationarity test or removal of trends. The studies by Cheynet et al. [3, 9] also include the organization of the data in longer periods, the removal of situations where the turbulence intensity is not within reasonable limits and the correction of tilt angles of the sonic anemometers.

This study describes a thorough processing procedure of sonic wind measurements, starting from available raw data and ending in a complete set of processed time series. These measurements may further be used in analyzing characteristics of the offshore wind field relevant to the wind turbine, or even as input in wind turbine simulations in the design phase of offshore wind turbines. The main objective is to achieve a wide variety of undisturbed measurement situations for such further analysis.

## 2. Data

The measurements used in this study are performed at the German wind energy research platform FINO1 [14], located in the German Bight of the North Sea, approximately 45 km North of the German Island of Borkum, as shown in Figure 1a. FINO1 was deployed in July 2003 and consists of a jacket foundation carrying a 16x16 m working platform (20 m above mean sea level), an elevated helicopter deck (25 m) and an 81.5 m high meteorological mast with its highest measurement level at 101.5 m above mean sea level [15].

The mast is densely equipped with standard meteorological sensors for wind, temperature and humidity at levels between 30 and 100 m [18]. High frequency wind measurement by sonic anemometers (Figure 1b) are operationally performed at 40, 60 and 80 m. The 40 and 80 m data are sampled at 20 Hz, while the 60 m data are sampled at 10 Hz. The sonic raw data are stored in blocks of approximately ten minutes duration, as commonly used in wind research and engineering. The present study uses wind speed in three directions and temperature from the mentioned sonic anemometers from June 2015 to September 2016. This period coincides with an extensive offshore field campaign at FINO1 (OBLEX-F1, [19]) and was chosen due to the availability of a wide range of complementary met-ocean measurements that might be beneficial for future investigations. In this study, wind direction information from wind vanes is used to calibrate the sonic anemometers, and precipitation information, in the form of a flag indicating "rain" or "no rain", is used to remove disturbances.

For reference, data from cup anemometer measurements[1] are also presented. Measurements made at 100 m are used for the wind speed in order to avoid flow distortion due to the mast. These cup anemometer data are used together with wind vane measurements of wind direction at

[1] http://fino.bsh.de/


(a) (b)

**Figure 1.** Map of FINO1 and surrounding wind parks at the time of measurements (dark blue) in the North Sea (a) [16], and layout of the FINO1 mast (b) - the red dots indicate the locations of the sonic anemometers (modified from [17] © Forschungs- und Entwicklungszentrum Fachhochschule Kiel GmbH)

90 m. The availability of the 30-minutes blocks of cup anemometer and wind vane measurements for our investigation period is 95 and 96 % respectively.

As shown by Figure 1a, the wind speed measured at FINO1 may be influenced by nearby land to the East and South, in addition to surrounding wind farms. However, the wind coming from North-West, where the sonic anemometers are pointed towards, represents close to undisturbed offshore conditions.

## 3. Method

The measurements undergo a processing procedure that is followed by a stationarity assessment, illustrated in Figure 2.

### *3.1. Missing and formatted measurements*

Data are missing for some shorter periods, probably due to defects and maintenance on the measurement equipment. In cases where more than ten seconds are missing in a ten-minute period, the complete ten-minute period is disregarded.

Some additional ten-minute periods are disregarded due to issues with the data logger causing corrupted data files. These files are characterized by symbols at random positions in the data files, causing erroneous numbers.

The ten-minute blocks are not evenly distributed with time series of exactly ten minutes, but consists of e.g. a period of ten minutes and two seconds followed by a period of nine minutes and 58 seconds. In order to even these time series out, they are first organized in daily vectors and thereafter split into intervals of exactly ten minutes duration for further processing. Values are mirrored/deleted at the end of the day or before a missing ten-minute period when only a few seconds are missing/too many data points exist.

### *3.2. Spike detection and removal*

The next step of the processing procedure of the measured values is a spike detection and removal routine. Spikes are considered as unphysical outliers in the data, which may origin from single

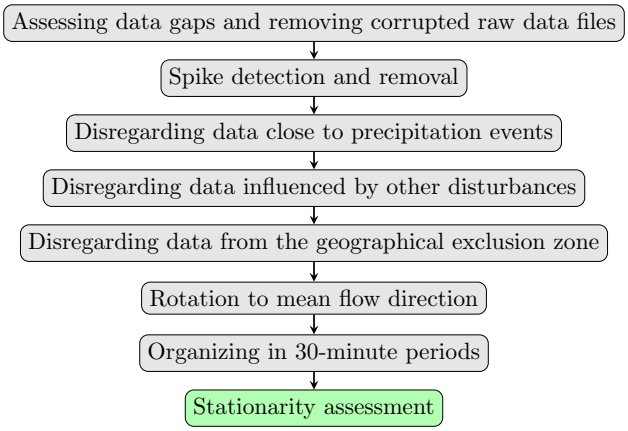


**Figure 2.** Scheme of the processing procedure followed by a stationarity assessment

water droplets or other sources of measurement errors. In the literature, the spike detection method by Højstrup is widely used [20]. Vickers and Mahrt [6] and Schmid et al. [21] describe methods based on his work, where spikes, $x'_{spike}$, are defined as extreme deviations from the mean, such that $|x'_{spike}| > a * \sigma$, where $a$ is a scaling factor (3-4 is normally used) and $\sigma$ is the standard deviation of the process. The methods are iterative, meaning that the mean and the standard deviation are computed again after the first spike removal, as the spikes would affect the statistics of the first iteration. The methods proposed by Vickers and Mahrt and Schmid et al. vary slightly, but they are both dependent on the iteration process, which is a disadvantage when handling very large data sets. Papale et al. [22] (based on Sachs [23]) proposes a similar method which is rather based on the median, avoiding the iteration process.

In this study, a method based on Rinker et al.'s [24] spike detection and removal procedure is applied. This method is chosen as it avoids iteration, it detects large gradients instead of data points, and it easily finds spikes extending over several data points. The method is based on calculation of differences between neighboring samples, $\Delta x$. If any of these differences are larger than a certain limit, they are defined as "extremes", $\Delta x_{ext}$. The limit is determined by a scaling factor, $a$, times the standard deviation of the differences between neighboring samples. When calculating this standard deviation, the spikes are excluded in the statistics by only using a given threshold, $b$, of the differences which have the lowest values, $\sigma_{\Delta x,b}$. By following this approach, the iteration procedure is avoided. In this study, an additional parameter, $c$, is introduced in the calculation of the limit in order to avoid detecting peaks that are large compared to surrounding values, but very low in absolute value. The spike detection and removal procedure is shown in Figure 3. A spike is detected when "extremes" are found at the beginning or end of each ten-minute interval, or two "extremes" with opposite directions are found within a maximum number of samples, also referred to as the spike width, $N_{spike}$. The spikes are replaced by the value before/after if found at the end/beginning of the ten-minute interval, and otherwise replaced with interpolation of the values before and after the spike.

The parameters required by the method of [24] are adjusted to detect the intended spikes of the sonic measurements of this study, corresponding to a spike width of six data points ($N_{spike} = 6$), a scaling factor of five ($a = 5$) and a threshold of 99 % ($b = 0.99$), in addition to the mentioned introduced parameter of 0.3 ($c = 0.3$). It is found that there is in general very

few spikes in the time series. However, some of the spikes may have very large values, thus a proper identification and removal routine is important to the quality of the time series. In the processed data set at all heights, there is in average 0.00002 % spikes, with the maximum in one processed 30-minute period being 0.2 %. All periods have far less spikes than the recommended maximum level by Vickers and Mahrt, 1 %, hence no ten-minute period is removed based on this criteria.

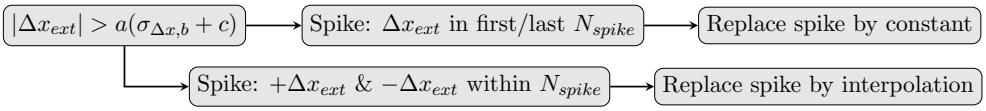


**Figure 3.** Scheme of the spike detection and removal procedure

*3.3. Precipitation*

It is common practice to exclude periods during and following precipitation when processing sonic anemometer measurements, as the precipitation may cause erroneous measurements [6, 8, 25, 26]. A consequence of this approach is, however, that the resulting time series are biased towards situations without precipitation. The precipitation information in the present study is limited to "rain" or "no rain" as mentioned in Section 2. As water droplets may stick to the transducers even after precipitation ends, disregarding the period of precipitation alone might not be sufficient. In this study, we chose to discard every ten-minute period when precipitation is registered, in addition to the preceding ten and succeeding 50 minutes.

*3.4. Other disturbances*

Particles located between the pair of transducers can potentially disturb the measurements. In addition to precipitation, the measurements may be affected by fog, frost, sea spray or larger aerosol particles. As we do not have any measurements to indicate these disturbances, and the study includes a few months where no precipitation information is available at all, we need to rely on characteristics observed during rainy periods in order to exclude these disturbances. In agreement with [25], we see a significant increase in standard deviation of the sonic temperature in rainy situations. We chose to exclude ten-minute periods where this standard deviation is higher than 0.3 K. A stricter threshold of 0.15 K is chosen for the months where no rain information is available. This approach may also remove some periods with significant trend in temperature, but these situations are probably not stationary and therefore anyway undesirable for further use.

*3.5. Geographical exclusion zone*

The sonic anemometers are pointed towards Northwest, being in the mast shadow when the wind blows from Southerly and Easterly directions, as shown by Figure 1b [27]. The orientation of the sonic anemometers and the potentially disturbed sector, also referred to as the "geographical exclusion zone", is shown in Figure 4. Wind blowing from North corresponds to 0 degrees, while wind from East corresponds to 90 degrees. We chose, in accordance with previous studies based on FINO1 sonic anemometer data [3, 9–11], to exclude the periods of potential disturbances. In this study, a very conservative approach is chosen, where all ten-minute periods with a mean wind direction between 45 and 225 degrees are excluded. The excluded wind directions, with winds coming from South and East, are also influenced by the proximity of land as they have already blown over the Netherlands and Germany (Figure 1a). The remaining data set is mostly undisturbed by such effects and thus represents realistic offshore wind conditions.

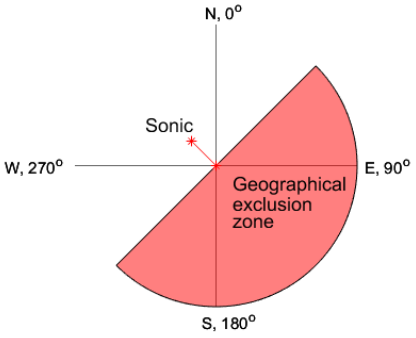


**Figure 4.** Illustration of the location of the sonic anemometers relative to the mast and the excluded wind directions (the geographical exclusion zone)

*3.6. Rotation*

For further analysis, e.g. related to the inflow of a wind turbine, we are interested in the mean wind speed in the mean flow direction, rather than the three components given by the sonic anemometers. There are mainly two ways of rotating the wind into the mean flow direction, the planar fit method and the double rotation method [28]. The two methods are quite similar, but treat the vertical velocity differently. The planar fit method only depends on a fixed tilt angle of the anemometer, allowing for a non-zero mean vertical velocity over the averaging periods. This is advantageous for a correct calculation of the fluxes, and the planar fit method is therefore widely used in boundary layer meteorology. The double rotation method depends on both a fixed tilt angle and the wind direction, leaving a zero mean vertical wind speed in all periods.

The double rotation method is chosen in this study mainly because wind turbine simulations are commonly performed with zero mean vertical velocity, which is also recommended or required by certain simulators. This may, however, cause some uncertainty in flux calculations, e.g. for determining stability. The double rotation method is used for all heights for 30-minute periods, but the 40 and 60 m data are rotated back to the mean flow direction at 80 m. In the processed data set at all heights, the average wind veer between 40 and 80 m corresponds to only one degree.

*3.7. Organizing in 30-minute periods*

The data are finally grouped in 30-minute continuous periods. During 30 minutes, we expect that all relevant frequency ranges for the wind turbine simulations are included, ranging from the very high frequencies relevant for blade tip vibrations to the slow floater motions requiring far longer periods. If ten minutes are missing in one 30-minute period, the whole 30-minute period is disregarded. The data may further be grouped into one hour periods, often used for wind turbine simulations, but the same 30-minute period may also be used twice with a smooth transition, as all relevant frequency ranges are assumed resolved within 30 minutes.

*3.8. Stationarity*

Natural wind is not a stationary process. However, most analysis of wind turbines assumes stationarity. In using measured wind data, a decision of what is "sufficient stationarity" must be made. As this criterion is strongly case dependent, we have chosen not to include stationarity tests as part of the processing procedure. A quantitative evaluation of the stationarity of a clearly non-stationary process, such as the wind speed, is also not straightforward. Including such tests could therefore remove close to stationary periods or even include too many non-stationary periods.

As for the previously introduced processing procedures, a qualitative stationarity analysis would have been an easier and more precise approach, but the amount of data excludes this

alternative. A common quantitative approach is developed by Foken and Wichura [5]. This method evaluates the variability of the mean of shorter intervals, e.g. five to ten minutes against the total mean of e.g. 30 to 60 minutes. Mahrt [29] has developed a similar test evaluating the standard deviation, which is combined with the Foken test by Cava et al [30]. These methods are widely used in meteorology, but their relevance to wind turbine applications may be questioned. The methods are developed for fluxes, not wind speeds. In addition, a time series with sudden small gusts will be considered stationary according to these methods. Several other methods exist in meteorology, but similar to the mentioned methods, most of these have not been developed with wind speed applications in mind. Ohbrai et al. [31] applied a stationarity test on FINO3 wind data, based on maximum variation between consecutive ten-minute mean values. This method could be used in our study with a maximum variation customized to the frequency of the measurements, but is disregarded as it would not capture non-stationarity due to a slow, but significant trend over the time series. Cheynet et al. [3, 9] has applied a two-step stationarity test in his studies. The first step is a linear trend test, which is adapted in this study and explained in the next paragraph. The second step is a reverse arrangement test described in Bendat et al. [32] and previously used for wind measurements by Chen et al. [33].

The processed time series of this study are already expected to be relatively stationary as rainy periods and periods with high standard deviation of temperature are removed. However, it is anyway recommended to test stationarity, e.g. by the two-step process explained in this paragraph. We may avoid de-trending the time series by rather applying the first step of the stationarity test of Cheynet [3, 9], in order to minimize the altering of the raw data. A maximum slope of 20 % is accepted over one hour ($\Delta t = 60min$), as shown by equation 1.

$$\frac{|\Delta U_{\Delta t}|}{\overline{U_{\Delta t}}} \leq \frac{0.2 * \Delta t(min)}{60min} \tag{1}$$

The second step requires that the maximum moving mean and moving standard deviation of each ten-minute block is less than 40 % off from the hourly mean and mean of the moving standard deviation.

$$max\left(\frac{|\overline{U_{60min}} - \overline{U_{10min}}|}{\overline{U_{60min}}}\right) \leq 0.4 \text{ and } max\left(\frac{|\overline{\sigma_{U_{10min}}} - \sigma_{U_{10min}}|}{\overline{\sigma_{U_{10min}}}}\right) \leq 0.4 \tag{2}$$

This simple two-step method gives a rough picture of the stationarity. For further precision, the frequency spectrum of the velocity variations in different parts of each time series should be evaluated, with special focus on the frequency range close to resonances of the wind turbine to be considered.

## 4. Results

After the processing, a complete data set ready for analysis is available. In the following paragraphs, we will visualize parts of the processing procedure for an example period, show the fractions of periods removed due to the different processes and at last present an overview of the complete processed data set.

The first four steps of the processing, assessing data gaps, spike detection and removal, removal of rainy periods and removal of periods of other disturbances, are visualized in Figure 5 for one day in September 2015. It is noticeable that the time series are discontinuous, especially towards midnight where we see many gaps. These gaps correspond to ten-minute intervals of missing data or corrupted raw data files. We can also observe the spike detection and removal process close to 18:00. The spike is probably detected in the temperature time series, but an interpolation is performed on all measured quantities. However, we observe another spike close to the mentioned one at 18:00 in both horizontal velocities, which is not detected by the spike

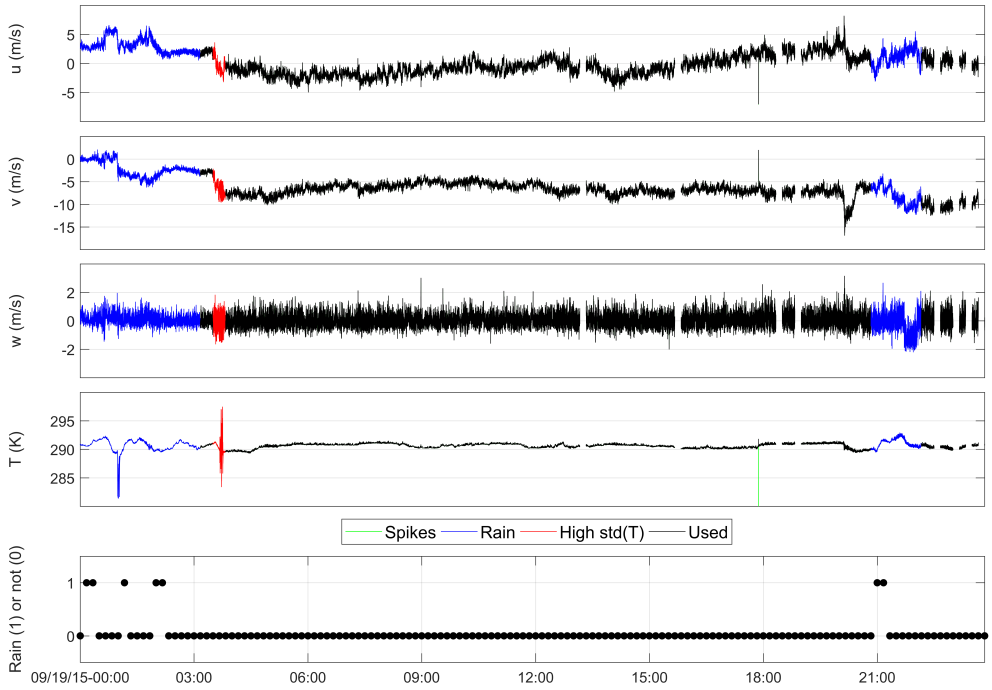


**Figure 5.** Visualization of the first four steps of the processing procedure with example time series of the three wind components and temperature, in addition to rain information for one day

routine. This is due to the length of the spike being longer than the chosen spike width of six data points used in the procedure. However, there is a sudden increase, and a sudden decrease with a plateau in between, typical for an unrealistic spike. This is therefore a good example that the processing procedure is not perfect, and that a manual inspection of certain time series may be necessary. The last subplot shows if there is rain or no rain in each ten-minute interval. There is a clear relation between precipitation and increased sonic temperature fluctuations. The figure shows that periods are removed both ten minutes before and 50 minutes after the precipitation is registered. In both rainy periods, it is obvious that this approach is necessary as the high fluctuations continues for a long time after the precipitation is registered. At about 04:00, it may even seem that a longer interval after precipitation should have been removed due to persistent large variations in both temperature and velocities. However, this ten-minute interval is removed in the next processing procedure that disregards periods of high temperature standard deviations. As shown in the figure, when unrealistic behavior is noticed at either one of the parameters, all measurements are removed. This is both due to the measurement principle being the same, so unnatural behavior is probably present in all parameters even though it is only obvious in one, and because all four parameters are necessary for further analysis. As mentioned earlier, it is also important to highlight that the processing procedure is not perfect, which is clearly shown by the non-detected spike close to 18:00 in this plot.

The data availability is distinctly reduced by the processing procedure, leaving only 27 %

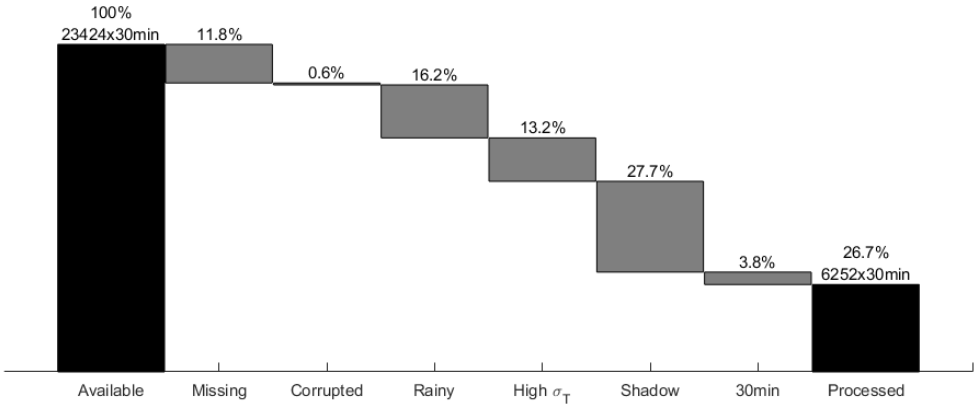


**Figure 6.** Total number of 30-minute periods from June 2015 to September 2016, fractions of removed data at all heights relevant to the total number of periods, and net remaining availability after processing of the sonic anemometer data at all heights

**Table 1.** Fractions (%) of removed data at all heights relevant to the total number of periods per season, and remaining availability (%) after processing of the sonic anemometer data at all heights in the last column

| Season | Missing | Corrupted | Rainy | High $\sigma_T$ | Shadow | 30min | Processed |
|---|---|---|---|---|---|---|---|
| Summer 15 | 53 | 1 | 0 | 20 | 11 | 4 | 12 |
| Autumn 15 | 5 | 2 | 25 | 7 | 34 | 4 | 24 |
| Winter 15/16 | 0 | 0 | 28 | 9 | 36 | 3 | 23 |
| Spring 16 | 3 | 0 | 14 | 22 | 28 | 5 | 28 |
| Summer+Sept. 16 | 1 | 0 | 15 | 9 | 30 | 4 | 42 |

of the entire period available for further analysis. However, this still corresponds to 6252 30-minute periods. The applicability of the processed data set depends on the aim of the further analysis of the data, but 6252 30-minute periods of high frequency data representing a large variety of offshore wind characteristics are more than enough to have significant relevance in offshore wind turbine research. Figure 6 shows the amount of data removed in each step of the processing procedure. The largest contributors are originally missing data, periods removed due to precipitation or high temperature standard deviation and periods where the wind origins from the geographical exclusion zone. Even though the latter excludes only 28 % of the complete period, it excludes close to 50 % of the available data after previous processing steps. The overview presented in Figure 6 is representative for measurements at all heights, meaning that if only the wind speed at 40 m is in the exclusion zone, periods of all heights are removed. The same procedure is followed for Table 1 and all following figures as well, but separate data sets are saved for each height in case only specific heights are interesting for further analysis. As mentioned earlier, we do not consider the stationarity assessment as part of the processing procedure, and the available time series presented in the figures of this section are therefore not

assessed in terms of stationarity yet.

Despite the reduced availability in the processed data set, it covers a wide range of relevant environmental conditions. Table 1 shows that all seasons are well represented, with the summer of 2016 compensating for the summer of 2015 having large amounts of missing data. Figures 7-9 present an overview of the processed data set in terms of wind speed, turbulence intensity and direction at 80 m height. The turbulence intensity, defined by the ratio of the standard deviation to the mean wind speed, is based on 20 Hz data over 30 minutes. It is clear from these figures that a wide range of offshore conditions is present in the processed data set, with wind speeds from zero to 24 m/s and turbulence intensities from a few percent to extreme values of more than 40 %. By comparing to the cup anemometer data with far better coverage (indicated by the red line in Figure 7 left and small wind rose in Figure 8 left), it is shown that the conditions covered by the sonic data set are representative for the selected period. There is a clear trend in the relation between the wind speed and the turbulence intensity, but a wide variety of turbulence intensity may still be found for most wind speeds. Figure 8 clearly shows that data with directions between 45 and 225 degrees are removed, but all other directions are represented in the processed time series.

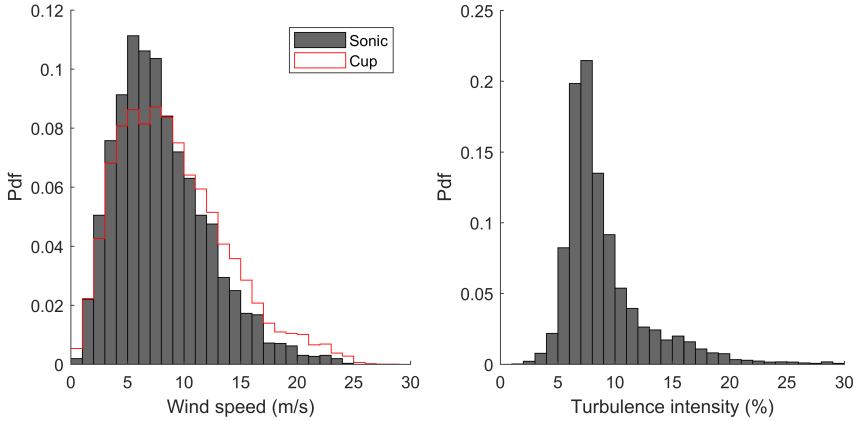


**Figure 7.** Probability density functions of 30-minutes mean wind speed (left) and turbulence intensity based on 20 Hz data over 30 minutes (right) at 80 m elevation after the processing procedure

Figure 9 shows the relation between wind speed and turbulence intensity and compares the 90th percentile of the FINO-1 data of this study, the IEC standards[2] [34, 35] and the findings of Ernst and Seume [13] and Türk and Emeis [12]. As expected, the measurements of this study fits better with the IEC offshore standard than the onshore, with an especially good fit above ten m/s. They are also well correlated with other FINO1 findings, but some deviations are present at intermediate wind speeds. The higher turbulence intensity of this study may be explained by the lower position of the sonic anemometer, the longer averaging interval, the higher frequency of measurements, and the difference in measurement device.

[2] Onshore: $\sigma = I_{ref}(0.75V_{hub} + 5.6m/s)$. Offshore: $\sigma = \frac{V_{hub}}{ln(z_{hub}/z_0)} + 1.28 * 1.44 * I_{ref}$ where the roughness length is given by $z_0 = \frac{A_c}{g}[\frac{\kappa * V_{hub}}{ln(z_{hub}}]^2$. $g$ is the gravitational acceleration, $\kappa$ is von Karman's constant (0.4) and $A_c$ is Charnock's constant (0.011). $I_{ref}$ is the typical turbulence intensity at 15 m/s, where 0.12, corresponding to turbulence class C, is used.

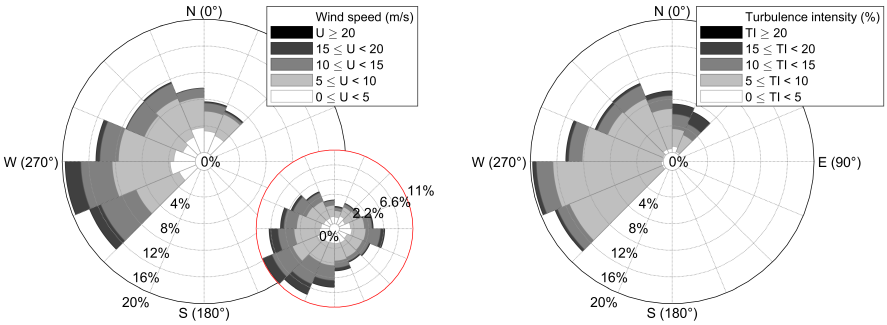


**Figure 8.** Wind direction dependent probability density functions of 30-minutes mean incoming wind speed (left (cup anemometer data in small circle)) and turbulence intensity based on 20 Hz data over 30 minutes (right) at 80 m elevation after the processing procedure

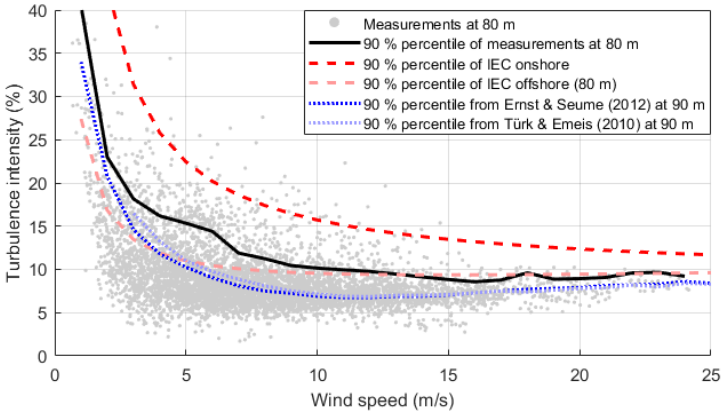


**Figure 9.** Turbulence intensity (based on 20 Hz data over 30 minutes) as function of wind speed of the processed FINO1-data set of this study, in addition to the 90th percentile of the the same data set, the IEC standards and literature findings of FINO1

## 5. Discussion

As mentioned in the results, a large data set of great variety in offshore wind conditions is ready for wind turbine research. However, there are also some limitations to the processed data set, which are already briefly mentioned. Even though the data set contains more than 6 000 30-minute periods of different situations, the data availability of the period is below 30 %. As shown by comparing to the cup anemometer data in Figure 7, the sonic anemometer data are more skewed towards lower wind speeds, leaving very few 30-minute periods of wind speeds higher than 20 m/s. This can be partly explained by the higher position of the cup anemometer, but it may also originate from the processing procedure resulting in the sonic data set with bias towards situations without precipitation. Last, the measurements are gathered over one year and three months, with the summer season represented twice. The statistics presented in Figures 7-9 may thus not be considered as statistics for one year at FINO1, but rather as an overview

of available situations for further use.

The processing procedure is thorough and quite conservative, with only 27 % availability after processing. Therefore, we expect that the risk of excluding data with valid measurements is larger than including data with errors in the processed data set. However, it was shown in Figure 5 that something very similar to an unrealistic spike was not detected. If only a small share of the data set, e.g. a few typical atmospheric conditions are analyzed further, and the quality requirements of these time series are very high, we therefore recommend a manual inspection prior to use, as illustrated in Figure 5.

Accepting the mentioned limitations, there are still a lot of applications for the processed data set. Figure 7-9 show the mean wind speed, the mean turbulence intensity and the mean direction, which are easily extracted. One may furthermore use the data set to calculate the roughness length of the ocean, the temperature fluxes and the Monin Obukhov length or Richardson number in order to classify the atmospheric stability. Taken into account the limited availability, it is probably more interesting to study some specific situations than trying to provide statistics of the characteristics at FINO1. These situations may be used to evaluate the co-variance between the mentioned parameters. In the frequency domain, further work could evaluate the energy spectra of the wind and temperature time series and study the coherence between the different heights in certain situations. The data set may also be used more directly towards the dynamic response of offshore wind turbines, e.g. by comparing to the standard turbulence models, wind profiles or turbulence intensities with height [34, 35].

## 6. Conclusions

In this study, existing quality control routines for sonic anemometer data are discussed and evaluated in terms of their relevance for offshore wind turbines. It is found that standard procedures, typically used in boundary layer meteorology, are not sufficient, and a tailored procedure for offshore wind turbine applications is necessary. This study presents a thorough processing procedure, applicable to sonic anemometer measurements for corresponding applications. The processing includes an assessment of data gaps due to instrument downtime, removal of corrupted raw data files, spikes, periods with precipitation or other disturbances and periods with wind speeds originating from the geographical exclusion zone, in addition to a coordinate transformation of the wind speeds to the mean flow direction and finally, organizing the data in 30-minute periods.

The processing procedure is applied to sonic anemometer measurements, routinely collected at the German offshore research platform FINO1, during the years 2015 and 2016. The applied conservative filtering reduces the raw data set of more than 20 000 30-minute periods to around 6 000. The remaining data set covers, however, a great variety of offshore conditions, despite the considerable reduction to 27 % of the original period.

The study is limited to the processing procedure and the presentation of the processed data set. For further use of the data, it is recommended to evaluate if additional stationarity tests, introduced in Section 3.8, should be applied. The proper choice of a corresponding method will always depend on the scientific question to address.

The data set will allow a wide range of applications related to offshore wind turbine design and analysis. Further studies will compare the characteristics of selected situations to standard turbulence models, and use these situations for studies of the dynamic response of offshore wind turbines.

## Acknowledgments

The authors would like to thank DEWI (Deutsches Windenergi Institut), and especially Richard Fruehmann, for providing the FINO1 high-resolution sonic anemometer data, and BSH (The Federal Maritime and Hydrographic Agency of Germany) for providing slow meteorological

reference data. We would also like to thank Martin Flügge and Etienne Cheynet for input and support.

## References

[1] Barthelmie R J, Crippa P, Wang H, Smith C M, Krishnamurthy R, Choukulkar A, Calhoun R, Valyou D, Marzocca P, Matthiesen D, Brown G and Pryor S C 2014 *Bull. Amer. Meteor. Soc.* **95** 743–756
[2] Emeis S 2014 *Meteorol. Appl.* **21** 803–819
[3] Cheynet E, Jakobsen J B and Reuder J 2018 *Bound.-Layer Meteorol.* **169** 429–60
[4] Sathe A, Mann J, Gottschall J and Courtney M S 2011 *J. Atmos. Ocean. Tech.* **28** 853–868
[5] Foken T and Wichura B 1996 *Agric. For. Meteorol.* **78** 83–105
[6] Vickers D and Mahrt L 1997 *J. Atmos. Ocean. Tech.* **14** 512–26
[7] Foken T, Leuning R, Oncley S R, Mauder M and Aubinet M 2012 Corrections and data quality control *Eddy Covariance* (Dordrecht: Springer) pp 85–131
[8] Foken T, Göckede M, Mauder M, Mahrt L, Amiro B and Munger W 2005 Post-field data quality control *Handboook of Micrometeorology* (Dordrecht: Springer) pp 181–208
[9] Cheynet E 2019 *Manuscript submitted to Lecture Notes in Civil Engineering*
[10] Mücke T, Harkness C and Argyriadis K 2012 *EWEA Copenhagen* **2102** 1–10
[11] Eliassen L and Obhrai C 2016 *Energy Procedia* **94** 388–98
[12] Türk M and Emeis S 2010 *J. Wind. Eng. Ind. Aerodyn.* **98** 466–71
[13] Ernst B and Seume J R 2012 *Energies* **5** 3835–55
[14] FuE-Zentrum FH Kiel GmbH 2019 FINO1: Forschungsplattformen in Nord- und Ostsee Nr. 1 URL `https://www.fino1.de/`
[15] Neumann T, Kolopp K, Strack M, Mellinghoff H, Söker H, Mittelstaedt E, Gerasch W J and Fischer G 2003 *DEWI Mag* 32–46
[16] 4C Offshore Ltd 2019 Global Offshore Renewable Map - 4C Offshore URL `https://www.4coffshore.com/offshorewind/`
[17] Forschungs- und Entwicklungszentrum Fachhochschule Kiel GmbH 2019 Fotos von FINO1 URL `https://www.fino1.de/de/medien/fotos.html`
[18] Neumann T and Nolopp K 2007 *DEWI Mag* **30** 42–46
[19] Bakhoday-Paskyabi M, Fer I and Reuder J 2018 *Ocean Dynam.* **68** 109–130
[20] Højstrup J 1993 *Meas. Sci. Technol.* **4** 153–57
[21] Schmid H P, Grimmond C S B, Cropley F, Offerle B and Su H B 2000 *Agric. For. Meteorol.* **103** 357–74
[22] Papale D, Reichstein M, Aubinet M, Canfora E, Bernhofer C, Kutsch W, Longdoz B, Rambal S, Valentini R, Vesala T and Yakir D 2006 *Biogeosciences* **3** 571–83
[23] Sachs L 1996 *Angewandte Statistik: Anwendung Statistischer Methoden* (Berlin: Springer)
[24] Rinker J M 2016 *An Empirically Based Stochastic Turbulence Simulator with Temporal Coherence for Wind Energy Applications* Ph.D. thesis Duke University
[25] Zhang R, Huang J, Wang X, Zhang J A and Huang F 2016 *J. Ocean Univ. China* **15** 389–98
[26] Emeis S 2010 *Measurement Methods in Atmospheric Sciences - In Situ and Remote* (Stuttgart: Borntraeger Science Publishers)
[27] Westerhellweg A, Neumann T and Riedel V 2012 *DEWI Mag* **40** 60–66
[28] Wilczak J M, Oncley S P and Stage S A 2001 *Bound.-Layer Meteorol.* **99** 127–50
[29] Mahrt L 1998 *J. Atmos. Ocean. Tech.* **15** 416–29
[30] Cava D, Donateo A and Contini D 2014 *Agric. For. Meteorol.* **194** 88–103
[31] Obhrai C, Kalvig S and Gudmestad O T 2012 *The 22nd Int. Offshore Polar Eng. Conf.* 440–50
[32] Bendat J S and Piersol A G 2011 *Random Data: Analysis and Measurement Procedures* Wiley Series in Probabillity and Statistics (Hoboken: John Wiley & Sons)
[33] Chen J, Hui M C and Xu Y L 2007 *Bound.-Layer Meteorol.* **122** 105–21
[34] International Electrotechnical Commision 2005 *IEC 61400-1 Wind Turbines - Part 1: Design requirements*
[35] International Electrotechnical Commision 2009 *IEC 61400-3 Wind turbines - Part 3: Design requirements for offshore wind turbines*

# Paper 2

## Evaluation of different wind fields for the investigation of the dynamic response of offshore wind turbines

Nybø A, Nielsen FG, Reuder J, Churchfield M, and Godvik M
*Wind Energy*, **23**/**9** (2020)

Received: 2 July 2019 | Revised: 27 February 2020 | Accepted: 9 April 2020
DOI: 10.1002/we.2518



WILEY

RESEARCH ARTICLE

# Evaluation of different wind fields for the investigation of the dynamic response of offshore wind turbines

Astrid Nybø[1] | Finn Gunnar Nielsen[1] | Joachim Reuder[1] | Matthew J. Churchfield[2] | Marte Godvik[1,3]

[1]Geophysical Institute and Bergen Offshore Wind Centre (BOW), University of Bergen, Bergen, Norway
[2]National Wind Technology Center, National Renewable Energy Laboratory, Boulder, Colorado, USA
[3]Equinor, Bergen, Norway

**Correspondence**
Astrid Nybø, Geophysical Institute and Bergen Offshore Wind Centre (BOW), University of Bergen, Allégaten 70, 5007 Bergen, Norway.
astrid.nybo@uib.no

## Abstract

As the size of offshore wind turbines increases, a realistic representation of the spatiotemporal distribution of the incident wind field becomes crucial for modeling the dynamic response of the turbine. The International Electrotechnical Commission (IEC) standard for wind turbine design recommends two turbulence models for simulations of the incident wind field, the Mann spectral tensor model, and the Kaimal spectral and exponential coherence model. In particular, for floating wind turbines, these standard models are challenged by more sophisticated ones. The characteristics of the wind field depend on the stability conditions of the atmosphere, which neither of the standard turbulence models account for. The spatial and temporal distribution of the turbulence, represented by coherence, is not modeled consistently by the two standard models. In this study, the Mann spectral tensor model and the Kaimal spectral and exponential coherence model are compared with wind fields constructed from offshore measurements and obtained from large-eddy simulations. Cross sections and durations relevant for offshore wind turbine design are considered. Coherent structures from the different simulators are studied across various stability conditions and wind speeds through coherence and proper orthogonal decomposition mode plots. As expected, the standard models represent neutral stratification better than they do stable and unstable. Depending upon the method used for generating the wind field, significant differences in the spatial and temporal distribution of coherence are found. Consequently, the computed structural design loads on a wind turbine are expected to vary significantly depending upon the employed turbulence model. The knowledge gained in this study will be used in future studies to quantify the effect of various turbulence models on the dynamic response of large offshore wind turbines.

**KEYWORDS**

coherence, offshore wind turbines, proper orthogonal decomposition mode, turbulence models, wind fields

## 1 | INTRODUCTION

The current standards of offshore wind turbine modeling recommend the use of a rather simple turbulence model to represent the wind characteristics.[1-3] These models are based upon knowledge of wind over land, small turbines, and fixed foundations. As the rotor size of offshore wind turbines becomes increasingly large,[4] the variation of the wind in time and space over the rotor diameter becomes increasingly important. For large, bottom-fixed, offshore wind turbines, the lowest relevant frequency for load analysis is the nominal rotor frequency of about 10 revolutions per minute. Moving towards floating wind turbines, one has to additionally account for the natural modes related to the rigid body motions. Depending upon the design, natural periods for the six rigid body modes of motion may range from a few seconds to at least 100 s.

The peer review history for this article is available at https://publons.com/publon/10.1002/we.2518.

These low-frequency natural periods represent new challenges to the description of the wind field. Both the turbulent energy at low frequencies and the spatial structure of the turbulence must be realistic to obtain realistic loads.

Either the Mann spectral tensor model,[5] hereafter denoted "Mann," or the Kaimal[6] spectral and exponential coherence model,[1] hereafter denoted "Kaimal," is recommended by the International Electrotechnical Commission (IEC) wind turbine design standard.[1] Several studies have shown that the response of a wind turbine is dependent on the turbulence model chosen.[7-10] The difference is predominant at low frequencies,[7,10] as mentioned, interesting for floating wind turbines. Based on this experience, it is highly relevant to evaluate the ability of the two turbulence models, Kaimal and Mann, to represent an offshore wind field.

Point statistics, such as wind speed and turbulence intensity (TI) at hub height, have great impact on the response of a wind turbine (e.g., Robertson et al.[11]). However, for larger rotors where the spatial and temporal distribution of the wind field is increasingly important, wind shear and coherent structures play an increasingly important role. The wind shear represents the variation of mean wind speed over the rotor height. The presence of coherent structures may be illustrated temporally by the coherence at a certain separation distance over various frequencies. Coherence is commonly referred to as correlation in frequency space.[12] Spatially, coherent structures may be identified by proper orthogonal decomposition over the rotor plane, hereafter denoted "POD."

The two simple turbulence models recommended by the standard generate wind fields with equal point statistics and shear. The coherence and POD modes are, however, dependent on the model chosen.[7,9,13,14] Previous studies by Eliassen and Ohbrai, Cheynet, and Cheynet et al. have compared turbulence models with offshore measurements, with a special focus on spectra and coherence.[13,15,16] They all use measurements from the offshore mast, FINO1, located in the North Sea.[17] Measurements from offshore masts provide crucial understanding of the offshore wind field. This is very valuable when evaluating wind field models. However, measurements should not necessarily be considered as the "truth." They are only made at a few spatial points and require proper processing and quality assurance. One may simulate offshore wind fields based on point measurements, using, for example, the TIMESR function in the turbulence simulator TurbSim,[18] but this requires several assumptions and simplifications.

Large-eddy simulations, hereafter denoted "LES," provide a more advanced method for generating the wind field based upon physical principles. It is based on solving momentum and pressure equations, requiring significant computational effort. Previous studies by, for example, Doubrawa et al.,[9] Simley and Pao,[19] Worsnop et al.,[20] and Berg et al.[21] compared the wind fields of Kaimal and/or Mann with LES. In contrast to comparisons with point measurements, this enables evaluations of, for example, lateral coherence and POD modes.

The turbulence models recommended by the IEC design standard are originally intended for neutral stratification.[1] The standard allows for an adaptation of turbulence intensity to non-neutral conditions. However, the other standard parameters are constant regardless of atmospheric stability conditions. It is shown by Sathe and Bierboms,[22] Eliassen et al.,[23] Holtslag et al.,[24,25] Doubrawa et al.,[9] and Sathe et al.[26] that the atmospheric stability influences the wind profile and turbulent structure of the wind field and therefore also the dynamic response of wind turbines. It is therefore relevant to evaluate the standard models also towards measurements or LES of other atmospheric stability conditions. This is especially interesting offshore, where the ambient turbulence is lower. This leads to a longer wake recovery, greatly dependent on stability conditions.

The current study evaluates the turbulence models recommended by the IEC design standard, Mann and Kaimal, from both a meteorological and wind turbine response point of view. The evaluation includes a comparison of the standard wind fields with offshore measurements and LES. Both processed raw data and wind fields created from these point measurements are used in the comparisons. The LES are run using the simulation tool SOWFA.[27] The study includes a description of the standard turbulence models and how they are used in industry. They are evaluated in different atmospheric stability conditions and at different wind speeds. The Kaimal and Mann spectral formulations both inherently assume neutral flow. In the present work, when it is referred to stable or unstable conditions for these spectral formulations, only the turbulence intensity and wind profile have been fitted to the flow conditions considered. In total, nine simulations are performed for each simulation method, covering below, close to, and above rated wind speed in unstable, neutral, and stable atmospheric conditions. We aim to highlight spatial and temporal differences in wind fields from various simulators across various atmospheric stability conditions. We will focus on differences that may play an important role for the dynamic response of large offshore wind turbines. These are illustrated through coherence and POD modes. Further work will use the various generated wind fields in dynamic response analysis, which will give further insight in the capabilities of the two standard turbulence models. Wind field simulations of slightly more than 1 h in duration are performed for this reason. Within 1 h, all relevant frequencies of large, bottom-fixed, and floating wind turbines are resolved and sufficiently represented. A total of 200 additional seconds are added in order to account for ramp up of the loads in modelling. The DTU 10-MW reference turbine will be used as reference where relevant.[28] This turbine has a diameter of 178.3 m, a hub height of 119 m, and a rated wind speed of 11.4 m/s.

The following section provides information on the methods used in the wind field analysis and explains the standard turbulence models, the measurements, and the LES, in addition to describing the details on the simulation of the different situations. Thereafter follows an overview of the generated wind fields and a comparison of the turbulent structures observed across simulation methods and atmospheric stability conditions. Last, conclusions are drawn on the basis of these results.

## 2 | DATA AND METHODS

### 2.1 | Wind field analysis

#### 2.1.1 | Point statistics

The mean wind speed and the turbulence intensity at hub height have large impact on the response of wind turbines. For comparisons of wind field characteristics from different wind field simulators, we strive to achieve similar values for these statistical parameters. Following this approach, we exclude the dominating effects of those bulk parameters on the dynamic response of wind turbines. This enables us to focus on differences related to the turbulent flow characteristics created by the different simulators, such as coherence and stability dependence of turbulent structures.

The turbulence intensity is defined as the standard deviation of the wind speed in the mean wind direction, $\sigma_u$, divided by the mean wind speed, $\bar{u}$. In wind energy-related meteorology, the turbulence intensity is commonly calculated from 1-Hz measurements, the typical temporal resolution of cup anemometers, averaged over 10 min. This frequency range is of high importance for wind turbine response. Sim et. al[29], among others, showed that the high-frequency region has less impact on the response. For floating wind turbines, the low-frequency region is of higher importance, but all relevant frequencies are resolved within a 10-min averaging interval.

#### 2.1.2 | Wind profile

In wind industry, either the power law or the logarithmic law are commonly used to formulate wind profiles.[1] Knowing the wind speed at one height and a few characterizing parameters of the atmosphere, the wind speed at a desired height is given by the mentioned relations.

The power law, the simplest of the two mentioned relations, is given by

$$\bar{u}(z) = \bar{u}_{ref}\left(\frac{z}{z_{ref}}\right)^{\alpha}, \tag{1}$$

where $\bar{u}$ is the mean wind speed at the actual height, $\bar{u}_{ref}$ is the wind speed at the reference height, $z$ is the actual height, $z_{ref}$ is the reference height, and $\alpha$ is the empirical power law exponent. The IEC design standard[1] defines the normal wind speed profile for the standard wind turbine classes to be given by the power law. The alpha exponent can be interpreted as a bulk parameter including the effects of surface roughness (expressed by the roughness length, $z_0$), and atmospheric stability.[30,31] The relative contribution of the two is, however, not easily distinguishable, particularly for offshore conditions where the surface roughness is variable, mainly depending on the wave height.

In contrast, the extended form of the logarithmic wind profile typically used in boundary layer meteorology allows for a separation between roughness and stability effects. The effect of atmospheric stability is here included by the introduction of a stability correction function, $\psi$.[32] However, in the wind industry,[1] this parameter is often excluded, thus assuming a neutral atmosphere. The logarithmic law is given by

$$\bar{u}(z) = \bar{u}_{ref}\left(\frac{ln\left(\frac{z}{z_0}\right) - \psi}{ln\left(\frac{z_{ref}}{z_0}\right) - \psi}\right). \tag{2}$$

The numerical coefficients in the stability function, $\psi$, vary slightly in the literature.[33] In TurbSim, the following formulation is used[18]:

$$\psi = \begin{cases} 0, & \textit{when neutral}, \\ -5\zeta, & \textit{when stable}, \\ 2\ln\frac{1+x}{2} + ln\frac{1+x^2}{2} - 2tan^{-1}(x) + \frac{\pi}{2}, & \textit{when unstable}, \end{cases} \tag{3}$$

where $x = (1 - 15\zeta)^{1/4}$. The stability parameter, $\zeta$, is defined in Section 2.1.3. The constants involved in this formulation (5 in stable conditions and 15 in the expression for x in unstable conditions) are in accordance with Dyer[34] and Businger et al.,[32] respectively.

The applicability of the logarithmic wind profile is limited to situations of at least moderate winds and a corresponding clearly nonzero friction velocity, but this is, in general, no issue for the wind speed range of wind turbine power production. Another more relevant limitation is arising from the fact that the logarithmic wind profile and the stability corrections are based on the theoretical framework of the Monin–Obukhov similarity theory (MOST).[35,36] MOST originated from and is validated by measurements over homogeneous land surfaces[37,38] and thus might not be fully representative of offshore conditions. In addition, it is limited to the so-called surface layer, where the turbulent fluxes are assumed to be constant with height. The surface layer roughly covers 10 % of the atmospheric boundary layer[39] and thus typically extends vertically over about 100 m for unstable and considerably less (in the order of a few tenths of meters) for stable conditions. Those limitations apply in general also to the power law formulation, and the appropriate characterization of wind profiles over the whole rotor disk of state-of-the-art wind turbines is therefore still a challenge,[40] particularly offshore. [41]

**TABLE 1** Stability classification after van Wijk et al.[43]

| Stability | Range |
|---|---|
| Very stable | 0<L<200 m |
| Stable | 200<L<1000 m |
| Near neutral | \|L\| >1000 m |
| Unstable | -1000<L<-200 m |
| Very unstable | -200<L<0 m |

### 2.1.3 | Stability classification

Considering the loading on a horizontal axis wind turbine, the blades will experience dynamic loads both due to wind shear and the turbulence characteristics of the inflow. The relative importance of these contributions will depend upon the stability condition. The Obukhov length, $L$, is a parameter commonly used for classifying atmospheric stability in the surface layer.[42] It expresses the ratio between shear effects and buoyancy effects in the production of turbulence. The Obukhov length is proportional to the vertical distance above the surface where the buoyancy effect dominate over the shear effects. Its formulation is given accordingly:

$$L = \frac{-\overline{\theta_v} u_*^3}{kg\left(\overline{w'\theta'}\right)_s}, \tag{4}$$

where $\overline{\theta_v}$ is the virtual potential temperature, $u_*$ is the friction velocity defined by Equation (5), $k$ is the von Karman constant, $g$ is the gravitational constant, $\left(\overline{w'\theta'}\right)_s$ is the surface vertical kinematic eddy heat flux, and $u'$, $v'$, and $w'$ are the longitudinal, lateral, and vertical velocity fluctuations, respectively.

$$u_*^2 = \sqrt{\overline{u'w'}^2 + \overline{v'w'}^2} \tag{5}$$

Table 1 shows the stability classification based on Obukhov length ranges from van Wijk et al.[43] This classification gives a wide range of stable and unstable Obukhov lengths. Gryning et al. propose alternative classification intervals, where $|L|>200$ is already considered near neutral.[40]

$\zeta$ is a nondimensional parameter, providing information on the stability of the atmosphere, given by the Obukhov length, and the height above the surface, $z$:

$$\zeta = \frac{z}{L}. \tag{6}$$

### 2.1.4 | Spectral analysis

The wind spectrum provides information of the power spectral density and is computed by a Fourier transform of the corresponding time series. In order to represent the time series, stationary conditions must be assumed. Most energy is located in the low-frequency region where turbulent energy is created, for example, by convection or vertical shear in the mean flow. This frequency range is also very relevant for offshore wind turbine response.[10] At midfrequencies is the inertial subrange characterized by the Kolmogorov slope of -5/3 ($S(f) \propto f^{(-5/3)}$), whereas turbulence dissipation happens at the highest frequencies. High-frequency sonic anemometer measurements typically resolve a considerable portion of the inertial subrange. The simple wind field simulators of this study are able to reproduce an energy spectrum similar to the measurements given a similar turbulence intensity level. The LES, on the other hand, is not able to reproduce the higher frequency region of the inertial subrange without substantial computational costs. The amount of high-frequency energy lost is dependent on both the temporal and spatial resolution[29]; fractal interpolation may enhance the energy level of the high-frequency region of the spectrum. The low-frequency region is, however, more important for the dynamic response of offshore wind turbines, so fractal interpolation or other techniques to enhance the energy in the higher frequency region are not considered in this study. The spectra of this study are estimated using Welch's algorithm[44] with a Hamming window, six segments, and 50 % overlapping. Detrended 60-min periods are used for the estimations.

Even though the simple turbulence models are able to achieve a similar energy spectrum at hub height, the spatial characteristics differ between the models. This may be represented by the coherence, which describes the correlation between two time series sampled at a given separation distance. The coherence is a function of the period of the fluctuations in the wind velocities and is thus conveniently described in the frequency domain. Coherence may be expressed as follows:

$$\gamma = \frac{|S_{xy}|}{\sqrt{S_{xx}S_{yy}}}, \tag{7}$$

where $S_{xx}$ and $S_{yy}$ are one-sided auto-spectra of the wind velocities at two different positions, $x$ and $y$, and $S_{xy}$ is the cross spectrum between these two. Equation (7) expresses the coherence in its absolute form, the root coherence. It may also be split in a real part, the co-coherence, and an imaginary part, the quad coherence. In engineering applications, the quad coherence is often ignored as it is assumed far less significant than the co-coherence. This has been the traditional approach in the wind energy industry. Veers[45] showed how the generation of a turbulent wind field for numerical analysis was simplified by ignoring the quad coherence, assuming that the wind velocity fluctuations are in phase. For Veers, in studying a 17-m diameter rotor, this was a reasonable assumption. However, the assumption can be questioned for state-of-the-art rotor diameters, now exceeding 200 m.

### 2.1.5 | Proper orthogonal decomposition

POD modes illustrate coherent structures or events in turbulent flows, as shown by Eliassen and Andersen [14] and Bachynski and Eliassen,[7] for example. In particular, the lowest modes, which explain the majority of the variation of the wind fields, are interesting for offshore wind turbines. These modes are the most anisotropic and are related to the large coherent structures found in the low-frequency part of the energy spectrum. In this study, only the POD modes of the longitudinal velocity component are considered. The POD modes, $\mathbf{\Phi}$, as formulated by Jørgensen et al.,[46] are defined by the matrices of eigenvectors, $\mathbf{G}$, eigenvalues, $\Lambda$, and the turbulent part of the wind field, $\mathbf{U}$:

$$\Phi = \mathbf{U}\mathbf{G}\mathbf{\Lambda}^{-1/2}, \tag{8}$$

where the matrix of orthonormal eigenvectors are defined as

$$\mathbf{G} = \begin{bmatrix} \mathbf{g_1} & \cdots & \mathbf{g_{n-1}} \end{bmatrix}, \tag{9}$$

the matrix of eigenvalues in decreasing order as

$$\Lambda = \begin{bmatrix} \lambda_1 & & \mathbf{0} \\ & \ddots & \\ \mathbf{0} & & \lambda_{n-1} \end{bmatrix}, \tag{10}$$

and the velocity matrix divided into time/space slices as

$$\mathbf{U} = \begin{bmatrix} \mathbf{u'_1} & \cdots & \mathbf{u'_n} \end{bmatrix}. \tag{11}$$

The eigenvalue problem is represented by the following equation:

$$\mathbf{R}\mathbf{G} = \mathbf{G}\Lambda, \tag{12}$$

where the auto-covariance matrix is defined as $\mathbf{R} = \mathbf{U}^\mathsf{T}\mathbf{U}$.

The wind field may be reconstructed by the POD modes from rearranging Equation (8):

$$\mathbf{U} = \Phi\mathbf{G}^\mathsf{T}\Lambda^{1/2}. \tag{13}$$

The least energetic POD modes may be excluded in the reconstruction, without significant loss of accuracy. The results of this study present the four most energetic POD modes and the amount of variation explained by these modes (eigenvalues) of various wind fields. For details of POD for turbulent flows, see Berkooz, Holmes, and Lumley.[47]

## 2.2 | Standard turbulence models

Both turbulence models recommended by the IEC wind turbine design standard,[1] the Mann uniform shear model (Mann) and the Kaimal spectrum and exponential coherence model (Kaimal), are stationary models, intended for neutral atmospheric conditions in the surface layer. The input parameters of the models are also suggested by the standards, being equal onshore and offshore.[1-3] The wind fields generated by the Mann and Kaimal models in the following use these standard inputs. The only exceptions are the turbulence intensities and wind profiles. These are fitted to the measurements for each stability condition and wind speed.

### 2.2.1 | The Mann uniform shear model

The Mann uniform shear model,[5,48] introduced in 1994, is a spectral tensor model based on von Karman's model[49] but assumes that the isotropic energy spectrum is rapidly distorted by a uniform mean velocity shear. It is emphasized by Mann[50] that the assumption of linear shear is not valid at low frequencies related to large eddies, and homogeneity is not valid for large vertical separations. The root coherence of Mann is given by the integral of the spectral tensor, $\phi$, and is commonly formulated as

$$\gamma = \frac{|\iint \phi_{ij}(\mathbf{k}) exp(-ik_y\delta_y) exp(-ik_z\delta_z) dk_y dk_z|}{\sqrt{\iint \phi_{ii}(\mathbf{k}) dk_y dk_z \phi_{jj}(\mathbf{k}) dk_y dk_z}}, \tag{14}$$

where $i$ and $j = 1, 2, 3$ for the longitudinal, lateral, and vertical turbulent wind components, $\mathbf{k}$ is the wave vector, $k_y$ the wave number in the lateral direction, $k_z$ the wave number in the vertical direction, $\delta_y$ the separation distance in the lateral direction, and $\delta_z$ the separation distance in the vertical direction. The root coherence is originally formulated by the wave spectrum, but may be transformed to frequency notation by the relation $f = \frac{k\bar{u}}{2\pi}$.

The Mann model is based on three parameters: $\alpha\epsilon^{2/3}$, the Kolmogorov constant multiplied with the rate of the viscous dissipation of specific turbulent kinetic energy to the two thirds, $l$, the length scale, and $\Gamma$, the nondimensional parameter related to the lifetime of the eddies. The

parameters suggested by the IEC standard are used,[1] with the exception of the turbulence intensity included in the determination of $\alpha\epsilon^{2/3}$, which is taken from measurements. The standard parameters are constant, even though several studies show that they are a function of atmospheric stability.[26,51,52]

The DTU Mann generator[53] is used to generate wind fields from the Mann model. A three-dimensional box of $32768 \times 64 \times 64$ nodes and grid size of 3.5 m in vertical and lateral directions are used for the simulations. In the main wind direction, the grid size varies with the mean wind velocity. In the present cases, the range is from 0.9 to 2.1 m. Assuming the validity of Taylor's hypothesis of "frozen" turbulence, this corresponds to 1 h and 200 s of simulation, through the relationship $\bar{u}T/N_x$, where $\bar{u}$ is the mean wind speed, $T$ is the total time, and $N_x$ is the number of grid points in the longitudinal direction. Additional 200 s are included to allow for transient effects to die out in future dynamic simulations of wind turbines and thus achieve 1 h of almost stationary response. The corresponding time step is 0.116 s.

#### 2.2.2 | The Kaimal spectrum and exponential coherence model

The other model recommended by the IEC is the Kaimal spectrum and exponential coherence model. [1,6] A two-parameter exponential coherence model for the wind velocity in the mean wind direction is used. Unlike the Mann model, no coherence is modeled for the lateral and vertical velocity components. The coherence for the velocity in the mean wind direction is given as

$$\gamma = \exp\left(-12\left((f\delta/\bar{u}_{hub})^2 + (0.12\delta/L_c)^2\right)^{0.5}\right), \tag{15}$$

where $f$ is the frequency, $\delta$ the magnitude of the separation distance on a plane normal to the mean wind direction, $\bar{u}_{hub}$ the wind speed at hub height, and $L_c$ the coherence scale parameter, defined as $8.1\Lambda_1$, where $\Lambda_1$ is the turbulence scale parameter in meters. According to this equation, the coherence is real and positive. This implies that all along-wind velocity variations over the cross section are in phase. Considering state-of-the-art rotor sizes, this is a doubtful assumption. Particularly in the vertical direction, significant phase shifts may be encountered. This issue will be addressed in the following.

A turbulence simulator from the National Renewable Energy Laboratory (NREL), TurbSim, [18] is used to compute the wind fields using the Kaimal model. In general, TurbSim creates turbulent wind fields from a chosen spectral model together with a chosen spatial coherence model. The shear profile is not accounted for in the turbulence generation but is added to the wind field afterwards. The software is commonly used to simulate wind fields with the Kaimal spectra and exponential coherence model defined by the IEC design standard.[1] The same grid resolution as for the Mann model is used in the lateral and vertical directions. Assuming Taylor's hypothesis of the Mann wind box, the temporal resolution is also approximately equal.

### 2.3 | Measurements

#### 2.3.1 | FINO-1

The offshore measurements used in this study are obtained from the German research platform FINO-1, located in the North Sea north of Borkum.[17] The platform is equipped with a meteorological mast with sonic anemometers located at 40, 60, and 80 m above sea level. Both wind speed and sonic temperature measurements are available at 10–20 Hz from these anemometers. Data from the period June 2015 to September 2016 are considered. These data have been thoroughly quality controlled as described by Nybø et al.[54] In the present work, samples of the data have been investigated further and used as input to TurbSim to create realistic 3D wind fields. These wind fields are subsequently compared with wind fields obtained by using standard turbulence models.

#### 2.3.2 | Processing measurement data

A processing procedure is applied to the measurements from the sonic anemometers in Nybø et al.,[54] resulting in a thoroughly quality assured data set of more than 6000 30-min periods. A conservative approach is followed, limiting the final availability to only 27 %. Data are unavailable or removed due to the following:

- instrument downtime,
- issues with the data logger,
- rain as the sonic anemometers give erroneous data during and following rain,
- other disturbances detected by high temperature standard deviation,
- mast shadow, nearby wind parks, and nearby land assuming only wind coming from north–west is undisturbed, and
- organizing data of 10 min into blocks of data of 30 min duration.

The impact of each of these steps on the overall availability is shown in Table 2. Additionally, a spike detection and removal procedure based on Rinker et. al[55] removes a few extreme samples. We assume that all relevant frequencies are resolved within 30 min. However, when 1-h periods with desired characteristics are available, these are used for wind turbine simulations.

| Total number of periods | Missing | Corrupted | Rainy | High $\sigma_T$ | Shadow | 30 min | Processed |
|---|---|---|---|---|---|---|---|
| 100 % | 11.8 % | 0.6 % | 16.2 % | 13.2 % | 27.7 % | 3.8 % | 26.7 % |
| 23 424 periods | | | | | | | 6 252 periods |

**TABLE 2** Total number of 30-min periods from June 2015 to September 2016, fractions of removed data at all heights relevant to the total number of periods, and net remaining availability after processing of the sonic anemometer data at all heights in the last column

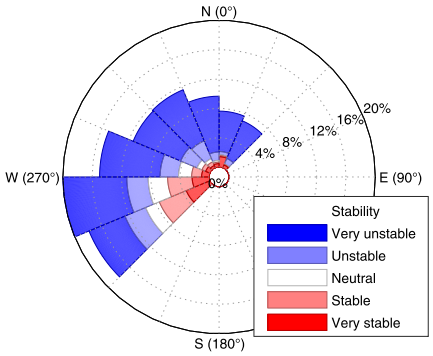


**FIGURE 1** Distribution of stability (at 40 m) as function of wind direction for 30-min periods of measurements at FINO1 [Colour figure can be viewed at wileyonlinelibrary.com]

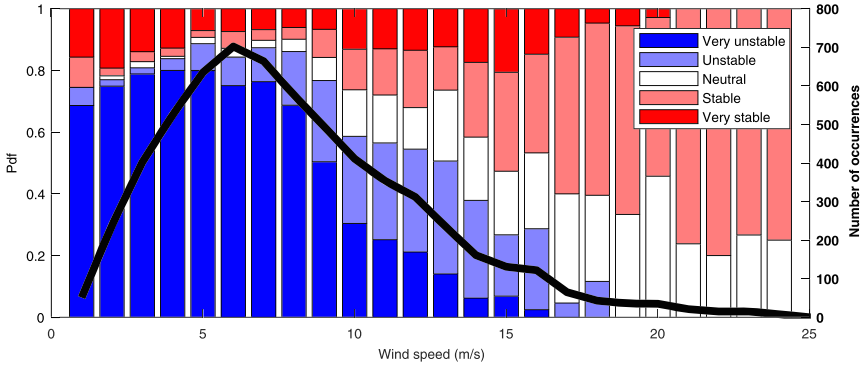


**FIGURE 2** Distribution of stability (at 40 m) as function of wind speed (at 80 m) for 30-min periods of measurements at FINO1. Solid line corresponding to the right axis represents the number of occurrences within each wind speed interval of 1 m/s [Colour figure can be viewed at wileyonlinelibrary.com]

### 2.3.3 | Characteristics at FINO-1 in given period

An overview of the wind speed, turbulence intensity, and direction of the processed data set is shown in Nybø et al.[54] The mean wind speed of the available periods is 8.1 m/s at 80 m above sea level. In the measured data, there is a wide range of turbulence intensities at low wind speeds. At higher wind speeds, the TI is typically in the range of 5 % to 10 %.

Figure 1 shows the distribution of stability classes as function of wind direction. After removing periods where the wind speed originates from the disturbed sector, we see that the most frequent wind direction is westerly. Higher wind speeds and neutral to stable conditions are more frequent in the western wind. As explained by Cheynet et al.,[16] the wind from southwest is typically stable due to the proximity of land and the corresponding transport of warm air over shorter fetches over sea, particularly during summer. Wind from northwest is more frequently associated with unstable conditions, caused by cold air advection over relatively warm sea, especially in the winter season.

With increasing wind speed, one expects more frequent neutral atmospheric stability. This relation is confirmed by the FINO1 measurements presented in Figure 2. Offshore, we still expect variations in atmospheric stability to exist even at high wind speeds. This is related to the low friction of the water surface, represented by the friction velocity in the Obukhov length calculation (Equation 4), causing stable conditions. Unstable conditions are generally less frequent offshore, but consistently with the findings of Cheynet et al.[16] and Krogsæter and Reuder,[56] Figure 2 shows that unstable situations are common at low wind speeds at FINO1.

### 2.3.4 | Generating realistic offshore wind fields from sonic measurements at different heights

An alpha version of the turbulence simulator TurbSim[18] is used to create wind fields based on specific measured situations. As mentioned earlier, this software is commonly used to simulate wind fields according to the IEC wind turbine design standard. Another option is to provide time series of measurements as inputs (TIMESR), used by, for example, Shaler et al.[57] With this option, TurbSim calculates the spectral amplitudes of

**TABLE 3** Decay coefficients from measurements used as inputs in TurbSim

| Wind speed (m/s) | Stability | $C_u$ | $C_v$ | $C_w$ |
|---|---|---|---|---|
| 7.5 | Unstable | 9.4 | 6.0 | 3.6 |
| 7.5 | Neutral | 13.8 | 6.6 | 3.8 |
| 7.5 | Stable | 28.5 | 24.0 | 21.6 |
| 12.5 | Unstable | 12.9 | 7.7 | 4.9 |
| 12.5 | Neutral | 12.5 | 8.1 | 4.7 |
| 12.5 | Stable | 52.5 | 42.2 | 31.0 |
| 18 | Unstable | 12.6 | 8.6 | 5.3 |
| 18 | Neutral | 11.9 | 7.7 | 6.3 |
| 18 | Stable | 68.9 | 29.6 | 29.7 |

the input time series. The spectral amplitudes of all simulated grid points in a yz plane are given by linear interpolation of the spectra of the input time series or "nearest neighbor" extrapolation. Input time series from the sonic anemometers at 40, 60, and 80 m above mean sea level are used with a sampling frequency of 10 Hz. Initially, TurbSim uses Veer's method[45] to generate random phases (dependent on seed) at each simulated point. Thereafter, the phases are modified using a coherence function and a recursive procedure, ensuring proper coherence between all points. In TIMESR, the phases are subsequently shifted so that the input time series of a reference point is reproduced in the output wind field.

The measured wind speed at 80 m above the surface is used as reference. This height is chosen due to its proximity to the hub height, assuming that the phase information at this height is more important for the rotor wind field. The Davenport coherence model is used to ensure coherence between the 80-m data and simulated points. The coherence of the three wind components, $K = u, v, w$, for two points in space, $i$ and $j$, is given by Equation (16) according to the Davenport model:

$$\gamma_{i,j_K} = \exp\left(-C * \frac{f\delta}{\bar{u}_m}\right), \tag{16}$$

where $C$ is the decay coefficient, $f$ is the frequency of measurements, $\delta$ is the separation distance, and $\bar{u}_m$ is the mean wind speed of the two points.[58] The fraction in the exponential is also referred to as the reduced frequency. In the TurbSim implementation, the decay coefficient is dependent on the velocity component, but independent of the separation direction. The decay coefficients obtained from measurements are used. All available vertical separation distances, 40–80, 40–60, and 60–80 m, are used to obtain these decay coefficients in order to reduce the statistical uncertainty. A further reduction in uncertainty would be expected if even more distances or longer periods were available. However, following the mentioned approach, we achieve decay coefficients specific for the selected situations, as given in Table 3. More advanced coherence models may be considered in further work. As highlighted by Cheynet et al.,[16] the Davenport model seems to fit quite well to the uu coherence and vv coherence at FINO1.

The mean wind speeds from the measurements at 80-m height, together with a wind profile, are added to the turbulence field in TurbSim. A logarithmic wind profile (Equation 2) is chosen, due to its dependence on stability (Equation 3). The roughness length is calculated from 40 and 80 m sonic anemometer measurements. We assume that the largest accessible separation distance is more representative for the shear profile over the rotor. Its robustness is, however, also checked towards the 60 m mean wind speed. The simulations are run with the same spatial and temporal resolution as the runs with the Kaimal spectrum and exponential coherence model.

## 2.4 | Large-eddy simulations

LES of the atmospheric boundary layer are performed to generate another source of inflow winds for this study. LES is attractive because it solves a filtered form of the governing equations of fluid flow and it directly resolves the larger, more important, energy-containing turbulent scale of the flow. Directly resolving all turbulent scales of the atmospheric boundary layer, down to the energy-dissipating scales, is not computationally possible now or in the foreseeable future, so LES is the best alternative. The effect of the unresolved scales on the resolved scales is modeled using a subgrid-scale turbulence model.

LES is performed using the NREL's Simulator fOr Wind-Farm Applications (SOWFA),[27] which is built upon the OpenFOAM CFD toolbox.[59] OpenFOAM provides all the base functionality of SOWFA through a wide variety of C++ classes for solving complex partial differential equation systems, and SOWFA provides specialized solvers, turbulence models, boundary conditions, forcings, and turbine models for performing atmospheric and wind plant LES. The incompressible governing equations are solved, but the momentum equation includes a Boussinesq buoyancy term, requiring the solution of a potential temperature equation. The system of governing fluid flow equations are discretized using the cell-centered, collocated variable finite volume method. Time advancement uses implicit backward-in-time discretization. A predictor–corrector approach involving sequential solutions for momentum, pressure, temperature, and turbulence quantities with a pressure projection step is used. Although we always use hexahedral meshes, the code's unstructured mesh handling allows us to add regions of arbitrary mesh refinement to resolve more turbulent content.

To generate the inflow winds, we perform periodic atmospheric LES in which the atmospheric boundary layer within a volume extending from the ground to 0.75—2 km vertically and 1.5–5 km horizontally is simulated. The domain size is dictated by the atmospheric stability, which dictates the largest turbulent structures present. The ground is modeled as a rough surface that applies stress to the flow above using Monin–Obukhov scaling laws. Heat flux at the surface can also be applied to achieve different atmospheric stability. A pressure gradient force combined with a

**TABLE 4** Large-eddy simulations computational domain and grid sizes

| Stability | Lx (m) | Ly $(m)_u$ | Lz (m) | T (s) | T (s) | dx (m) | dz (m) | dt (s) |
|---|---|---|---|---|---|---|---|---|
| **First step: Region covering the largest turbulent structures present** | | | | | | | | |
| Unstable | 5000 | 5000 | 2000 | 15000 | 10 | 10 | 10 | 0.25 (18 m/s), 0.333 (12.5 m/s), 0.5 (7.5 m/s) |
| Neutral | 5000 | 5000 | 1000 | 15000 | 10 | 10 | 10 | 0.25 (18 m/s), 0.333 (12.5 m/s), 0.5 (7.5 m/s) |
| Stable | 2500 | 1500 | 750 | 20000 | 5 | 5 | 5 | 0.125 (18 m/s), 0.25 (12.5 m/s), 0.5 (7.5 m/s) |
| **Second step: Region of localized grid resolution which captures smaller-scale flow features** | | | | | | | | |
| Unstable | 1250 | 300 | 300 | 5000 | 1.25 | 1.25 | 1.25 | 0.03125 (18 m/s), 0.04 (12.5 m/s), 0.0625 (7.5m/s) |
| Neutral | 1250 | 300 | 300 | 5000 | 1.25 | 1.25 | 1.25 | 0.03125 (18 m/s), 0.04 (12.5 m/s), 0.0625 (7.5m/s) |
| Stable | 1250 | 300 | 300 | 5000 | 1.25 | 1.25 | 1.25 | 0.03125 (18 m/s), 0.04 (12.5 m/s), 0.0625 (7.5m/s) |

simple controller is applied to drive the wind to a desired mean wind speed and direction at hub height. The initial potential temperature profile used is important, particularly because it dictates the location of the capping inversion and its strength, which then dictates atmospheric boundary layer height. The stability, mean profile shape, and turbulence characteristics cannot be precisely selected, but are the result of the chosen pressure gradient force, surface roughness, surface heat flux, and capping inversion height/strength. Depending on the stability, the simulations are run between 4 and 6 h to achieve a fully developed turbulent atmospheric boundary layer. By adjusting the simulation parameters described above over which we have control, the desired general flow characteristics (defined in Section 2.5) can be achieved. Details on how exactly we matched these conditions are discussed in Section 2.5.2.

It is the nature of LES that the solution changes as the computational mesh resolution is changed. The solution can also be affected by artificially constraining the largest turbulent scales. We chose overall domain sizes compatible with the largest scales that the different simulated conditions would produce. For example, unstable conditions produce large and tall convective structures requiring a larger and taller domain, whereas stable conditions have largest turbulent structures that are much smaller with a shallower boundary layer depth necessitating the use of a much smaller domain with higher resolution. The grid resolution necessary to well capture a turbulent atmospheric boundary layer, though, is not sufficient to capture the smaller turbulent scales that are important for predicting wind turbine loads. Because it would be computationally infeasible to use higher resolution throughout the entire computational domain, we locally refine down to higher resolution where the velocity is to be sampled, taking care that there is enough upstream fetch for the smaller scale turbulence to properly form. The simulations with the refinement box are run with somewhat finer time and space resolution as the Mann and TurbSim simulations. The computational domain and resolution details of LES are summarized in Table 4.

Within the refinement volume, yz planes are saved for further use. Taylor's hypothesis is assumed in order to achieve a wind speed volume by concatenating the extracted yz planes of velocity data in a format equivalent to the output of the DTU Mann Generator.

## 2.5 | Data selection and matching

### 2.5.1 | Measurements

We select nine time series for further use close to and above rated wind speeds for the DTU 10-MW reference turbine in stable, unstable, and neutral atmospheric conditions. In addition to wind speed and stability, the selection is based on turbulence intensity, stationarity, and quality of the data, as described in the following paragraphs. We choose situations with characteristics obtainable by LES, as we want to compare the effect on the dynamic response of a wind turbine of varying turbulent wind fields, disregarding the dominating effect of different wind profiles and turbulence intensities. Figure 3 shows the distribution of the available hourly data with respect to wind speed and turbulence intensity. In this figure, data blocks of 1-h duration are presented, with starting time every full and half hour. Thus, each 30-min period may be represented twice (10:30–11:00 both in the 1-h data blocks starting at 10:00 and 10:30). This is a meaningful presentation when used for selections, but one should be aware that the figure does not show the representative yearly statistics of FINO1. The turbulence intensity is calculated from 1 Hz 10-min periods averaged over each hour, where the standard deviation is calculated at 80 m and assumed constant with height. Hourly data are needed in the wind field simulations, as the outputs of the same length will further on be used for wind turbine analysis, where hourly simulations are favorable. Processed 30-min periods following each other, within the same 1 m/s wind speed bin, are grouped together in Figure 3. The selection of the mentioned 9 time series is based on characteristics at 119 m (hub height of DTU 10-MW reference turbine) of these complete hours.

The wind speed at 119 m is found by the log law (Equation 2), where the roughness length is calculated from the measured wind speeds at 40 and 80 m by solving Equation (2) for $z_0$. The mean thrust on the turbine increases with wind speed up to the rated wind speed, while the wind turbine controller reduces the thrust thereafter. Three mean wind speeds have been considered, below rated, approximately at rated, and above rated wind speed. The three cases are of interest for different reasons: below rated wind speed, the turbine is designed for maximum aerodynamic efficiency while the mean thrust has its maximum at rated wind speed. Above rated wind speed, a certain turbulence intensity corresponds to larger variations in the wind velocity than for the two previous cases. The below rated case is chosen at a typical wind speed at FINO1, close to 7.5 m/s. Instead of choosing exactly the rated wind speed, we choose to study the case just above, 12.5 m/s, in order to avoid being at the interface between two regions where the controller will jump between modes due to turbulence. Above rated, we choose the highest available wind speed from the processed FINO1 data set where all atmospheric stability conditions are present, 18 m/s.

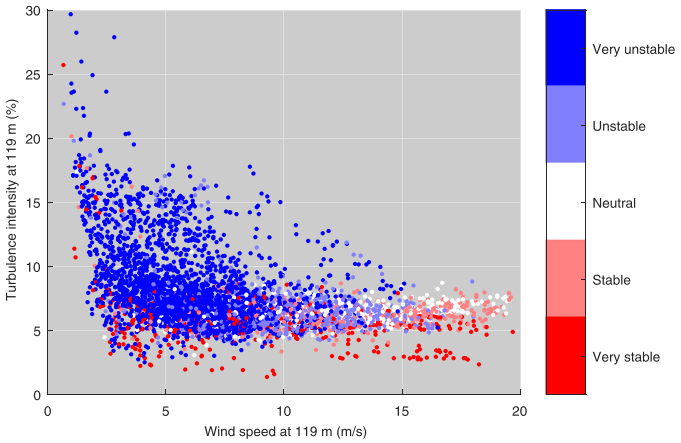


**FIGURE 3** Figure used in the selection process, showing turbulence intensity as a function of wind speed for hourly periods at 119 m (TI is based on the average of six 10-min intervals of 1 Hz) [Colour figure can be viewed at wileyonlinelibrary.com]

When selecting the nine situations, confidence in stability class is also considered. Every hourly period in the processed data set is classified in terms of atmospheric stability (found from 20 Hz data) according to Table 1. However, only three stability classes are used further, where very stable and stable both are categorized as stable. The Obukhov lengths are calculated from Equation (4) by using 40 m data. We assume that MOST is valid at 40 m and that the stability at 40 m is representative for the complete rotor area. We further assume that the error of using sonic temperature as the potential virtual temperature in Equation (4) is small close to sea level. These assumptions, in addition to the dependency of the rotation method chosen, are potential sources for uncertainty in the stability classifications. In order to avoid erroneous classification, measurements well within the corresponding stability ranges are chosen for further use. We also try to find the more stable/unstable case where possible, in order to better explore the effects of stability.

Periods with typical turbulence intensity for each stability class are chosen within wind speed bins of 1 m/s, also being within the obtainable range of LES. As discussed in Section 2.1.1, we strive to match turbulence intensities at hub height in order to avoid dominating effects by the point statistics. The turbulence intensity of unstable situations is typically higher than in stable situations, as shown in Figure 3. When choosing time intervals for analysis, less weight is put on roughness length and veer. The roughness length is low above sea level, and the veer is also found to be quite low, even though it is higher in stable situations than in neutral and unstable situations.

Furthermore, an evaluation of the stationarity is included in the selection of time series. The processed 1-h periods are already expected to be quite stationary, following the processing procedure. However, the stationarity is anyway tested following a two-step process, as described in Nybø et al.[54] This test evaluates both the linear trend and the moving statistics of the time series. Finally, a manual inspection of the time series is performed, in order to ensure high-quality data for the further investigations.

### 2.5.2 | Large-eddy simulation

For the LES, we strive to achieve the same hub height mean wind speed, turbulence intensity, stability, and shear profile as of the nine measurement cases. As mentioned in Section 2.4, the desired mean wind speed at turbine hub height is quite easily achieved using the pressure gradient force with a simple controller. Atmospheric stability, shear, and turbulence intensity cannot be precisely controlled and depend upon the combination of pressure gradient force, surface roughness, surface heat flux, and capping inversion height/strength chosen. Therefore, we ran many cases in which we manually adjusted these parameters before we achieved conditions that matched the measurement cases well enough. In searching for parameters that resulted in a reasonable match between simulation output and observations, we began by using the surface roughness calculated from the observations, a typical capping inversion height for each stability class (a higher inversion for unstable conditions and a lower inversion for stable conditions) but with a common inversion strength for all cases, and an informed initial guess at surface heat flux based on prior experience. Generally, these initial cases produced output somewhere within the neighborhood of the target values. To fine tune the results, we ran subsequent simulations in which we primarily adjusted the surface heat flux, and sometimes, we also adjusted the surface roughness and capping inversion height, until the results were within a desired margin of agreement with observations. Admittedly, it was difficult to produce LES wind fields with high enough turbulence intensity without compromising the values of shear and stability level.

Because the LES is somewhat idealized, without the constantly varying background forcing found in nature, the low-frequency part of the turbulent spectrum often has less magnitude than that of the observations. Additionally, this may be explained by the way the mean wind speed is quite strictly controlled at hub height. The planar-averaged wind speed at hub height is driven to match desired values every time step by modulating the global background pressure gradient force. Wind speeds at different points at hub height, though, are allowed to vary freely. The low-frequency part of the spectrum is dictated by the largest turbulent structures in the atmospheric boundary layer, which under unstable conditions can be a few kilometers in length. The idea of this mean wind speed controller assumes that the averaging plane is large enough, relative to the largest turbulent structures such that enough of them are sampled onto the plane to provide a statistically converged mean wind

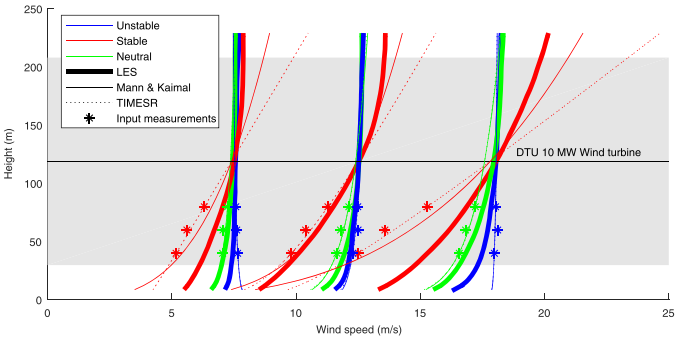


**FIGURE 4** Wind profiles of all generated wind fields in all selected situations: below, close to, and above rated in various stability conditions. The color code identifies the stability regime. Thin lines: Mann and Kaimal; dashed lines: TIMESR; bold lines: LES. The stars represent the sonic anemometer measurements chosen as input. The stable and unstable versions of Mann and Kaimal should be considered as neutral flows with turbulence intensities and wind profiles adapted to the given stability. LES, large-eddy simulations [Colour figure can be viewed at wileyonlinelibrary.com]

speed. Imagine an undersampled case in which only one of these largest structures is sampled on the averaging plane. In that case, the wind speed controller would attempt to force the flow such that this structure's velocity deviation from the desired mean in the plane is driven to zero. Because spectra are derived from point measurements, a point measurement in the plane would then effectively contain less wind speed fluctuation from this large turbulent structure. To remove this effect completely, extremely large domains are required. Moreover, there is less energy in the high frequency range of the velocity spectra of the LES than in measurements because LES, by definition, does not resolve the smaller turbulent scales, both in space and time. However, this part of the energy spectrum has minimal impact on the fatigue loads of wind turbines, as mentioned in Sections 2.1.1 and 2.1.4.

### 2.5.3 | Standard wind fields

Also in the standard simulations, using the DTU Mann Generator and TurbSim, we strive to achieve the same hub height wind speed, shear profile, and hub height turbulence intensity as for the corresponding measurements. This is both due to their impact on results, as mentioned for LES, and because these parameters are usually somehow related to site measurements in industrial design procedures.

We choose to scale the wind profiles of the simulated wind fields with the power law, according to the IEC design standard.[1] However, the shear exponent is fitted to the measurement situations. The wind speed at hub height from TIMESR is used in the scaling procedure in order to achieve the exact same wind speed at this height. The turbulence intensity is scaled with a height independent parameter to match the turbulence intensity of the measurements at hub height. We use the turbulence intensities from the average of six 10-min, 1-Hz blocks from measurements to scale the Mann and Kaimal wind fields of 1 h and 10 Hz. As Kaimal and Mann are stationary models, there is very little difference between the turbulence intensity from the mentioned frequency ranges of these fields. The scaling is done by TurbSim for the Kaimal wind fields, whereas the same procedure is followed manually for the Mann wind fields.

## 3 | RESULTS AND DISCUSSION

### 3.1 | Overview of situations

The following figures give an overview of the chosen situations. Figure 4 shows the mean wind profiles aimed to fit the chosen below rated, close to rated, and above rated wind speeds at the hypothetical hub height of the 10-MW DTU wind turbine of 119 m. As mentioned in Section 2, the power law is used for Kaimal and Mann scaling, with the empirical exponent fit to measurements. The logarithmic law is used for the TIMESR runs, explaining the minor difference to the standard models.

Figure 4 shows clearly the expected stability dependency of the wind profiles, with an increase in vertical wind shear from unstable over neutral to stable atmospheric conditions. All methods agree well for neutral and unstable atmosphere, whereas the discrepancies increase for stable conditions. In particular, the LES profiles for stable conditions deviate distinctly from the other methods and the basic measurements. This is a natural consequence of prioritizing point statistics, wind speed, and turbulence intensity at hub height, in the matching of LES and measurements.

Figure 5 shows the wind speed distribution at the hub location, in addition to key information of the different wind fields (average wind speed, turbulence intensity, and stability expressed by the Obukhov length) for all investigated situations. As expected, high standard deviations are observed for the unstable situations, whereas the stable situations have larger kurtosis. This is related to the larger eddies expected in unstable conditions relative to stable. The wind speed and standard deviation of the Kaimal and Mann fields are scaled in order to match the TIMESR simulations, but we still observe some minor deviations in the turbulence intensity. The standard wind fields assume a neutral atmosphere; thus, the Obukhov lengths are not given. We observe that the probability density functions are very similar for the two standard models. In comparison with TIMESR, there is higher kurtosis and minimal skewness.

For the LES, we observe that the turbulence intensity is far from TIMESR in several situations, even though we aimed at matching hub statistics. In particular, the neutral situations from the measurements are very turbulent, being close to the unstable situations at close to and

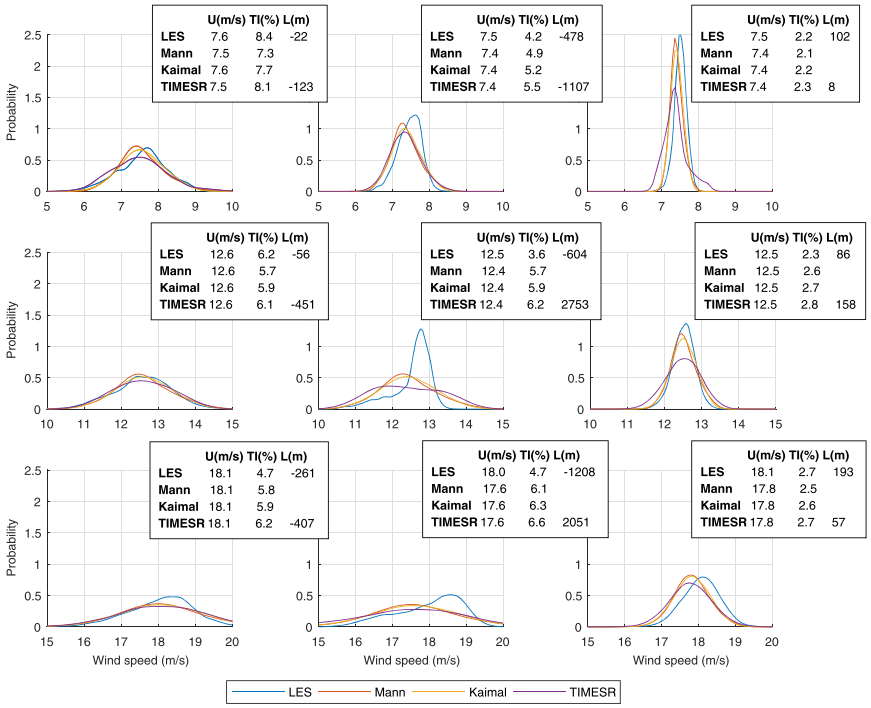


**FIGURE 5** Wind speed distribution of all generated wind fields at the hub location for unstable (left panels), neutral (center panels), and stable conditions (right panels). TI is calculated based on 10 Hz data over the average of six 10-min averaging intervals. The stable and unstable versions of Mann and Kaimal should be considered as neutral flows with turbulence intensities and wind profiles adapted to the given stability. LES, large-eddy simulations [Colour figure can be viewed at wileyonlinelibrary.com]

above rated wind speed. This is unfortunate because it hinders further comparisons between conditions of different atmospheric stability. The reason for the high measured TI in neutral conditions is not fully understood. These turbulent offshore conditions are difficult to achieve with LES. As mentioned in Section 2.5.2, the turbulence intensity is an output of LES and cannot be directly controlled by the inputs. The turbulence intensity is tuned towards the desired value by modifications in the surface roughness and the surface heat flux. However, compromises had to be made in order to achieve close to desired stability and shear profiles.

In contrast to the measurements, the Obukhov lengths of the LES are not strictly within the ranges of Table 1. In the neutral cases below and close to rated, the surface flux had to be increased significantly in order to achieve higher turbulence intensity. This leads to a decrease of the absolute Obukhov length to less than 1000, which is the neutral limit in Table 1. However, the absolute value of the Obukhov length from the LES in these cases is far higher than for the unstable cases. There are therefore distinct differences in the wind fields of the unstable, neutral, and stable cases. Moreover, they are within the neutral and near-neutral range of the classification ranges of Gryning et al.[40]

From the wind distributions in Figure 5, we also observe major differences between LES and TIMESR. In most situations, the LES distributions have distinct negative skewness and remarkably higher kurtosis. As for the comparison with the standard models, this reflects even lower standard deviations. Larger differences are found in the situations where the standard deviation deviates more, for example, at 12.5 m/s, in a neutral atmosphere. The LES are very stationary, most likely due to the method of controlling the wind speed in the precursor runs, mentioned in Section 2.4. A less strict control mechanism would probably lead to wider tales of the LES distributions.

## 3.2 | Comparison of wind fields

### 3.2.1 | Turbulent structures

Figure 6 shows xy planes close to hub height of the different wind fields for the close to rated wind speed of 12.5 m/s. The full lateral section of the wind fields is shown, whereas the longitudinal direction is represented by a snapshot of around 440-m length (corresponding to a time period of ~35 s), taken from the center of the wind field. The statistical characteristics of the wind fields are better explained by Figure 5, whereas Figure 6 gives a qualitative perspective of the structures of different simulators and atmospheric stability conditions.

We observe that the TurbSim wind fields (Kaimal and TIMESR) contain more fine turbulent structures than the Mann wind fields. The wind fields generated by LES show even coarser turbulent structures, which can, at least partly, be explained by the coarser spatial and temporal

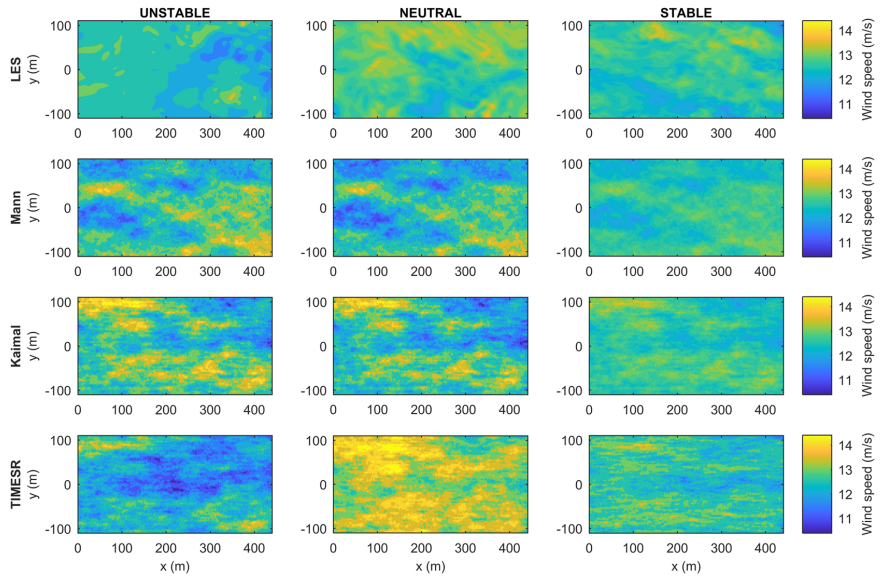


**FIGURE 6** xy planes close to hub height of the 12.5 m/s wind fields in various stability conditions at full lateral domain size (220.5 m) and for a snapshot in the longitudinal direction of 441-m length (corresponding to about 35 s). The x and y axes are scaled identically. The stable and unstable versions of Mann and Kaimal should be considered as neutral flows with turbulence intensities and wind profiles adapted to the given stability. LES, large-eddy simulations [Colour figure can be viewed at wileyonlinelibrary.com]

resolution of the domain. We see also a stretching of the eddies in the longitudinal direction in most of the wind fields, which is realistic considering the presence of a vertical shear profile.

When comparing across atmospheric stability conditions, we observe minor differences between the different runs of Kaimal and Mann. The seeds are equal in the different runs, and as stability is not accounted for by the simple models, only the turbulence intensity and mean wind speed can cause these minor differences. For instance, we see less variation of the wind speed in the stable situation with lower turbulence intensity (neutral and unstable turbulence intensities are almost equal in TurbSim and Mann runs at close to rated wind speed).

The same differences can be recognized in the TIMESR wind fields. The phase angles of the simulated points are determined by the seed, before they are correlated to the phase angles of the 80 m input time series by the Davenport coherence model. When the same seed is used, similar wind fields are therefore expected, with some deviations due to the variation of the phase angles and decay parameters of the inputs. Except for the difference in wind speed variation, explained by the difference in turbulence intensity, we may observe that the more stable the atmosphere, the finer and longer turbulent structures are observed in the TIMESR wind fields. This is according to expectations for the different atmospheric stability conditions.

In agreement with Doubrawa et al.,[9] we observe larger structures in the unstable LES case. As for the TIMESR cases, we also observe stretched structures in the longitudinal direction for the more stable the atmospheric conditions. Although excluded from this article, the same qualitative results are found in the structure plots of wind speeds below and above rated.

### 3.2.2 | Spectral analysis

In agreement with the turbulence intensities given by Figure 5 (middle), Figure 7 shows that the variance of the Kaimal, Mann, and TIMESR wind fields is similar. It is clearly visible that LES is not able to represent a realistic power level at frequencies above 0.1–1 Hz, consistent with Doubrawa et al.[9] and Sim et al.[29] This is due to the size of the refinement volume, as explained in Section 2.1.4. At periods larger than a few seconds, more important for floater behavior, the energy level is closer to the TIMESR wind fields in all situations. In the neutral 12.5 m/s case shown in Figure 7, the LES spectrum is slightly shifted towards lower energy levels in correspondence with the lower turbulence intensity achieved in the simulations. Spectral analysis of other wind speeds and atmospheric stability conditions (not shown) confirms that the energy level at low frequencies is highly dependent on the turbulence intensity. As expected, the energy level in stable situations is lower than in unstable situations.

Figure 8 (left) shows the co-coherence of an example TIMESR wind field compared with the input measurements at the largest available height as function of reduced frequency ($\frac{f\delta}{a_m}$). This figure illustrates the difference between the highly fluctuating co-coherence values from the input measurements and the smooth exponential decay from the derived TIMESR data set. This should be kept in mind when interpreting the corresponding curves that are compared with the coherence of the standard and LES data sets in Figures 9 and 10. As mentioned in Section 2.3.4, the fit to the Davenport model includes statistical errors that decrease with the length of the time series and number of time series. The

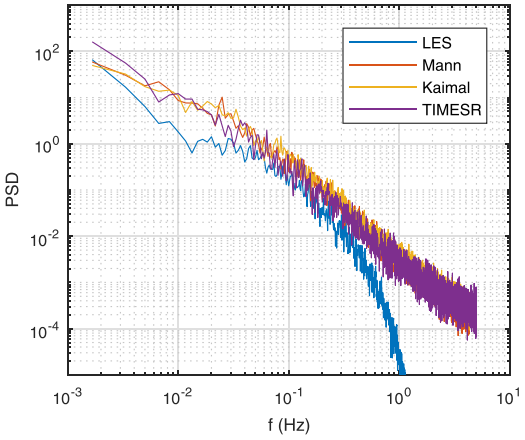


**FIGURE 7** Energy spectrum at hub location of the neutral 12.5 m/s case. LES, large-eddy simulations [Colour figure can be viewed at wileyonlinelibrary.com]

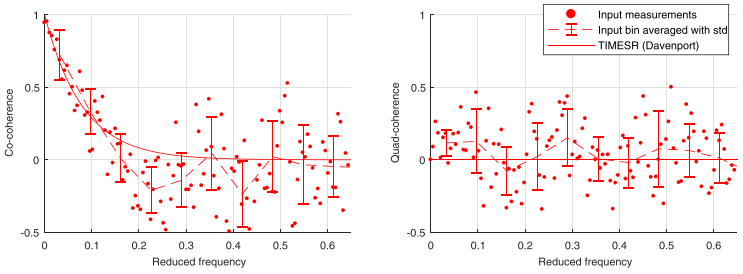


**FIGURE 8** Vertical coherence of measurements between 80 and 40 m for the neutral 12.5 m/s case [Colour figure can be viewed at wileyonlinelibrary.com]

Davenport coherence model forces the co-coherence to unity at zero reduced frequency, which fits well with the measurements in Figure 8 (left), but is often a poor assumption especially for large crosswind separations.[60] Figure 8 (right) shows the quad coherence of the same situation, often excluded due to its insignificance compared with the co-coherence. Both the Davenport model and the Kaimal model ignore the quad coherence, whereas the Mann model formulates the quad coherence, but only in the vertical direction. The vertical shear in the formulation of the Mann model causes a phase shift for time series separated vertically, but not laterally. According to the results of Figure 8 for 40-m separation distance, also observed for other wind speeds and atmospheric conditions, the quad coherence is significantly smaller than the co-coherence. However, the phase shift is not negligible. For larger separations, it may be even more significant. This may have importance to the loads on a wind turbine blade, as the turbulent velocity fluctuations at a certain frequency will not have the same phase along the length of the blade. Further, it is observed from Figure 8 (left) that the co-coherence may be negative in certain reduced frequency ranges. This implies an opposite phase of the turbulent velocity components. This effect will change the dynamic load pattern along a wind turbine blade significantly.

Assuming that the fitted Davenport coherence represents the coherence of the measurement situations fairly, we may evaluate and compare the standard and LES wind fields with the TIMESR fields on the basis of Figures 9, 10, and 11. It should first be mentioned that the coherence reduces drastically with reduced frequency in all models, being insignificant at reduced frequencies higher than 0.5 in all situations. As mentioned earlier, the lowest eigenfrequencies of bottom fixed turbines are about 10 revolutions per minute, corresponding to reduced frequencies above the limit of insignificance just mentioned. The impact of coherent structures is therefore expected to have larger effect on floaters, having far lower eigenfrequencies. The longest natural period relevant for floaters is related to the rigid body modes of motion and is typically about 100 s. This corresponds to reduced frequencies in the range 0.05 for 18 m/s at 0.5 D separation to 0.24 for 7.5 m/s at 1 D.

As shown by Figures 9 and 10, the co-coherence of the TIMESR wind fields is, as expected, higher for the unstable situations, whereas the co-coherence of the stable situations falls steeply with the reduced frequency. The eddies of an unstable atmosphere are by far larger than in a stable atmosphere, explaining this larger co-coherence over distances comparable with the rotor diameter. This trend is consistent with the findings of Cheynet et al.[16] As shown by Figure 5, the neutral and unstable TIMESR cases have similar characteristics at close to and above rated wind speeds, which is also the case for the co-coherence. The Davenport model is independent of the separation distance, except through the reduced frequency, illustrated by the equal curves in the horizontal pairs of subfigures in Figures 9 and 10. It is also independent of direction; thus, the TIMESR curves are equal in Figures 9 and 10.

Both the Mann model and the Kaimal model are independent of stability, shown by a single curve for each model in Figures 9 and 10. In contrast to the Davenport model, they are both dependent on the separation distance, resulting in less co-coherence with larger distance. Mann shows significant co-coherence at low reduced frequencies, but falls off steeply, whereas Kaimal starts off with lower co-coherence, but decays

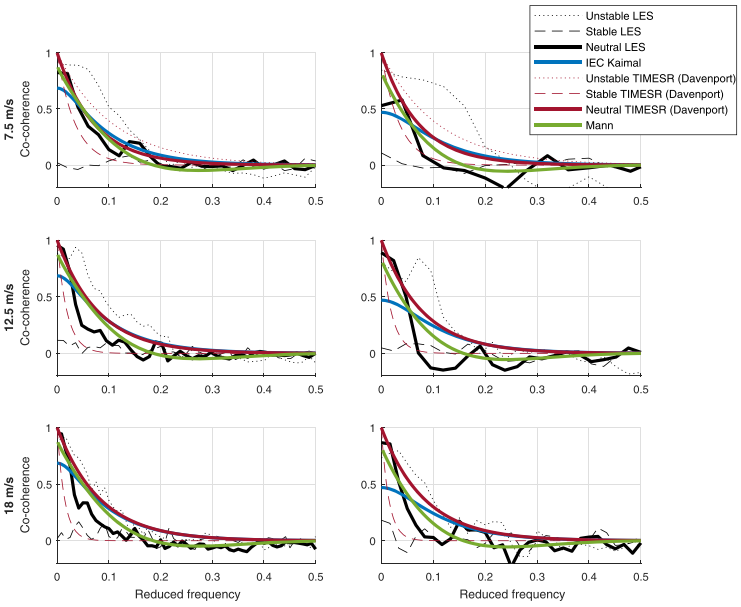


**FIGURE 9** Vertical co-coherence at 0.5 (left) and 1 diameter (right) separation distance for all generated wind fields. IEC, International Electrotechnical Commission; LES, large-eddy simulations [Colour figure can be viewed at wileyonlinelibrary.com]

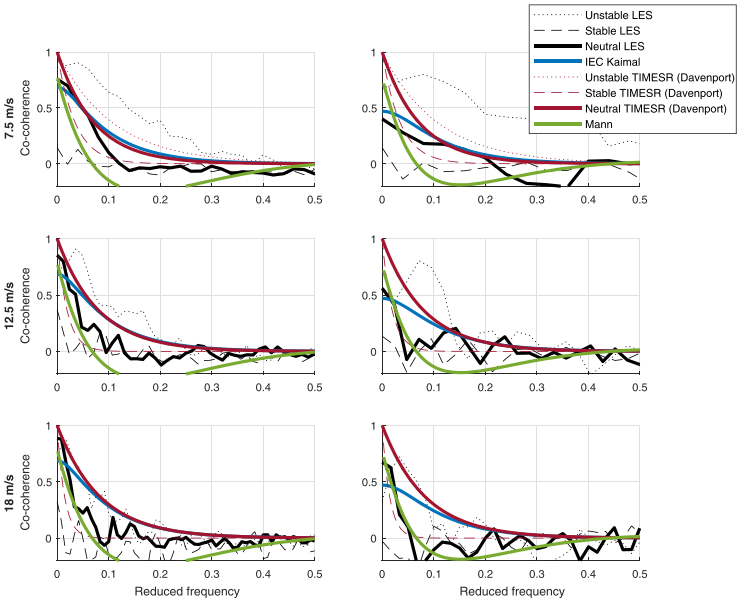


**FIGURE 10** Lateral co-coherence at 0.5 (left) and 1 diameter (right) separation distance for all generated wind fields. IEC, International Electrotechnical Commission; LES, large-eddy simulations [Colour figure can be viewed at wileyonlinelibrary.com]

slower. As the Davenport model always starts off at unity, the Mann model matches the TIMESR runs consistently better at the lowest reduced frequencies. However, this frequency range is not the most important for dynamic response, being lower than the natural frequencies of both bottom-fixed and floating wind turbines. Whether the Mann or Kaimal co-coherence fits better with TIMESR at higher frequencies depends on the stability of the TIMESR runs. The Kaimal co-coherence is closer to the neutral and unstable TIMESR runs from the intersection between Mann and Kaimal in both separation directions. This intersection appears at a reduced frequency close to 0.05 in the vertical co-coherence plots (Figure 9) and even closer to zero in the lateral plots (Figure 10). Mann matches the stable TIMESR curves overall better for the vertical co-coherence. Considering the co-coherence of lateral separations, Mann falls sharply, matching the stable case even better at low frequencies, but tends to fall below zero, which is not the case for Davenport. Kaimal as TIMESR, however, is independent of separation direction. From both figures, we observe a close to perfect match between Kaimal and neutral TIMESR at reduced frequencies higher than 0.05–0.15.

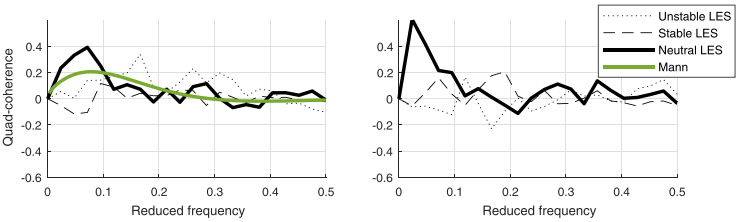


**FIGURE 11** Vertical (left) and lateral (right) quad-coherence at 1 diameter separation distance for 12.5 m/s. LES, large-eddy simulations [Colour figure can be viewed at wileyonlinelibrary.com]

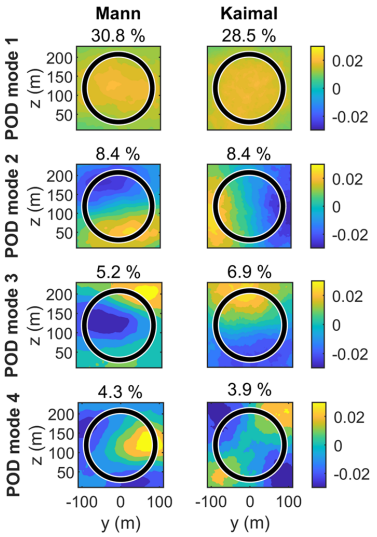


**FIGURE 12** POD modes 1–4 of Kaimal and Mann wind fields for the 12.5 neutral case. Explained variation per mode is given above each subplot. POD, proper orthogonal decomposition [Colour figure can be viewed at wileyonlinelibrary.com]

The evaluation of Kaimal and Mann so far is based on comparison with the measurements fit to a simple exponential model with all the expected statistical errors, but it may be as relevant to compare them with more advanced simulations such as LES. The coherence of the LES is averaged over all available vertical and lateral separations in order to reduce noise. The points furthest up and most right in the wind fields are used as reference in the cross-spectrum calculations. The co-coherence of the different LES fields follows the same pattern as TIMESR, with significantly stronger co-coherence for the unstable atmospheric conditions. This is consistent with the findings of Doubrawa et al.,[9] also comparing the coherence of LES wind fields of various stability conditions. In contrast to the TIMESR runs based on the Davenport model, the co-coherence is different to unity at zero reduced frequency. Consistently with the general trend, the co-coherence at very low frequencies is also lower the more stable the atmosphere. We even observe close to zero co-coherence in the most stable cases in both separation directions, for all reduced frequencies. In accordance with Figure 5, there is a larger difference between the unstable and neutral characteristics of the LES. For the largest separation distances (Figures 9 and 10 right), the co-coherence starts off at a lower co-coherence at zero reduced frequency, in consistency with Mann and Kaimal, but stays at a higher level for a larger range of frequencies. This is especially evident in the unstable case below rated. For neutral and unstable conditions, in the LES runs, it is found that the higher the wind speeds, the faster the decay of co-coherence, both vertically and laterally. This trend is similar for the stable case of TIMESR, but is less evident at other atmospheric conditions. As expected for the simple standard models, they fit better to the neutral LES cases. In most frequency ranges of the vertical co-coherence plots, Mann is a better fit to the neutral case of LES, in contrast to the comparisons with TIMESR where Kaimal was a better fit. For the lateral separations, such a general clear conclusion does not exist, as the neutral LES typically lays between the Kaimal and Mann co-coherence plots. Compared with the unstable and stable LES cases, Mann and Kaimal are both far off, with the closest match being the one resulting in higher or lower co-coherence, respectively.

The quad coherence is, as mentioned, only present in the Mann and LES wind fields. Figure 11 shows the vertical and lateral (only LES) quad coherence at 1 diameter separation distance for 12.5 m/s. Equivalent results are found for 7.5 and 18 m/s. As expected, the co-coherence (Figure 9 [right middle] and Figure 10 [right middle]) is significantly higher than the quad coherence in most wind fields. Still, the phase shift of Mann and some of the LES fields is not negligible for low frequencies where the coherence is most significant. We observe that the quad coherence of Mann is positive when the highest point is used as reference. This is consistent with the measured vertical coherence shown in Figure 8. It is more challenging to analyze the LES fields with all the present noise, but the quad coherence appears to be likewise positive. However, as for the co-coherence, the stable quad coherence is negligible, whereas the unstable and especially neutral quad coherence is more significant. To summarize, we observe a non-negligible quad coherence both from measurements and LES, which causes a phase shift that is

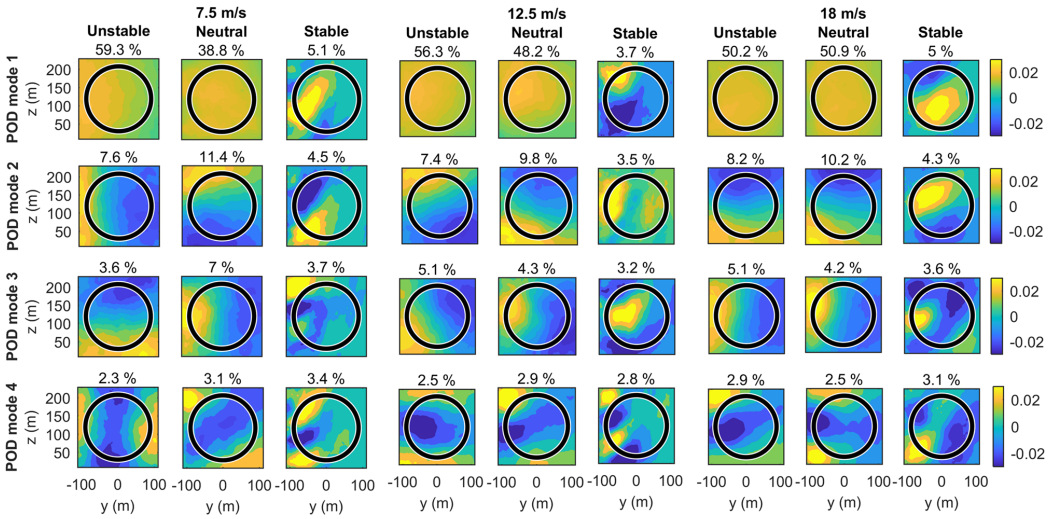


**FIGURE 13** POD modes 1–4 of large-eddy simulation wind fields for the 12.5 m/s case in all atmospheric conditions. Explained variation per mode is given above each subplot. POD, proper orthogonal decomposition [Colour figure can be viewed at wileyonlinelibrary.com]

expected to have an impact on the dynamic response of offshore wind turbines. The Kaimal and TIMESR wind fields used in this study are not able to reflect this. Response analysis must be performed in order to assess the impact of the phase shifts and to compare the impact of the different quad coherence formulations.

### 3.2.3 | Proper orthogonal decomposition

As mentioned in Section 2.1.5, POD modes may illustrate coherent structures in turbulent flows. In Figures 12, 13, and 14, the first four POD modes and the amount of variation explained by each of these modes are shown for the various wind fields. Being independent of stability, and using the same seed for all wind speeds, the POD modes and the amount of variation explained by each mode of Kaimal and Mann are approximately equal for all wind fields. The neutral 12.5 m/s case is illustrated in Figure 12. Almost one third of the variation of the wind fields of both models is explained by the first mode. The Mann modes seem to be stretched in the lateral direction, whereas Kaimal is more centered around the hub. Furthermore, Kaimal has the extremes outside the rotor diameter (illustrated by the black circles), whereas the extremes of the Mann modes tend to appear inside the rotor area. We expect that this may cause higher loads on the wind turbine. Our findings are consistent with those of Bachynski and Eliassen[7] and Eliassen and Andersen.[14]

Studying the POD modes of all simulators, we observe several similarities, especially when disregarding the stable case of LES. The number of coherent structures increases with the number of modes, while the size of these structures decreases. The first modes explain a major part of the variation in the wind fields. Among the general differences, we observe that the TurbSim wind fields are more fine structured than Mann, which again is more fine structured than LES, coinciding with the observations in Figure 6. Moreover, we observe that TIMESR and LES, similar to Kaimal, but in contrast to Mann, typically have extremes outside the rotor diameter. This is dependent on the domain size chosen relative to the rotor diameter. In the first mode, we observe no clear stretching of the pole in neither LES or TIMESR. For the second and higher modes, there are typically dipole structures that appear in opposite direction relative to each other in the second and third modes. These are both observations coinciding with Kaimal, but different to Mann. The shape of the POD modes and the magnitude of explained variation, based on Kaimal, are generally in better agreement with LES and TIMESR than for Mann. We may therefore conclude that Kaimal represents the modes most realistically, but still with large differences depending on stability, especially regarding the part explained by each mode.

When comparing the atmospheric stability conditions, we observe that the mode shapes in the neutral and unstable cases are similar both in LES and TIMESR. Larger parts of the variation are explained by the first modes in most of these situations, meaning that these modes contain more turbulent kinetic energy relative to the stable situations. This is expected based on the similarities seen in previous figures as well. However, we see distinct differences to the stable cases, especially for the LES. The dominance of a few energetic modes are far less pronounced in these cases. This is consistent with the results shown in Figures 9 and 10, where the co-coherence is negligible for the stable LES cases.

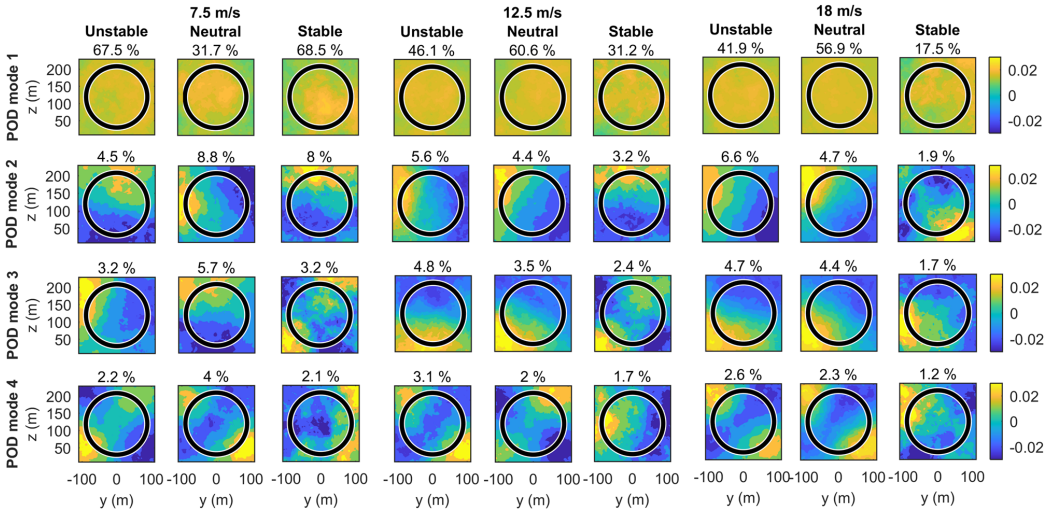


**FIGURE 14** POD modes 1–4 of TIMESR wind fields for the 12.5 m/s case in all atmospheric conditions. Explained variation per mode is given above each subplot. POD, proper orthogonal decomposition [Colour figure can be viewed at wileyonlinelibrary.com]

## 4 | CONCLUSIONS

The development towards larger, more flexible, and floating wind turbines offshore triggers the need for an efficient and appropriate way to model the inflow conditions with realistic turbulent structures over the full stability range in an offshore environment. In this study, we have evaluated different wind field simulation techniques commonly used by the industry from both a meteorological and an offshore wind turbine response perspective. The wind fields recommended by the IEC wind turbine design standard, the Mann spectral tensor model and the Kaimal spectral and exponential coherence model, are compared with measurements and LES. Point measurements from the offshore mast FINO1 are used as input to the wind field generator TurbSim by using the TIMESR method. The four generation methods (Mann, Kaimal, TIMESR and LES) are used to create wind fields of three mean wind speeds in order to evaluate the differences in the main load regimes for a large offshore wind turbine: below, close to, and above rated wind speed. The standard wind fields, assuming neutral stratification, are compared with TIMESR and LES wind fields at various atmospheric stability conditions.

Our findings show expected differences between the various stability conditions in the LES and TIMESR wind fields. The unstable wind fields have less wind shear, higher turbulence intensity, and larger structures than the neutral and stable ones. More significant coherent structures are also found in the unstable situations. This is obvious from the temporal and spatial distributions of coherence, illustrated by high values of the frequency-dependent co-coherence and significant dominance of the first POD modes.

Significant coherent structures in the along-wind direction are obtained by all models. As expected, the standard wind fields represent the neutral situations better than the unstable and stable ones. Considering the co-coherence as function of reduced frequency, we cannot conclude whether the Kaimal or Mann model is most realistic. This is due to conflicting results when comparing the standard models with TIMESR and LES, respectively. Moreover, the LES co-coherence is noisy and the measurements may not be well represented by the fitted Davenport model. It is furthermore worth noticing that a nonzero quad coherence is only obtained by LES and Mann (vertically) models. The phase shift of the coherence may have significant impact on the loads of a wind turbine, which TIMESR and Kaimal are not able to represent. Considering the POD modes, we also see great similarities between Mann and Kaimal. However, by studying the structures of the first POD modes, Kaimal appears to be a better match to TIMESR and LES than Mann.

Neither the TIMESR nor LES wind fields can be considered as completely realistic representations of offshore wind fields. There is a need for measurements that better characterize coherence, both vertically and horizontally and over a distance on the order of modern large offshore turbines, in order to better compare models with measurements. A corresponding field campaign, with central participation of several authors of this manuscript, is at the moment ongoing. Three scanning lidar systems are deployed in a triangular setup at the Norwegian west coast, operating in a synchronized mode to measure lateral and vertical coherence in the wind field up to 3 km offshore. LES is emerging as a valuable tool as graphics processing unit (GPU) computers are becoming more readily available, but improvements are necessary in order to be able to easily tune inputs to produce desired outputs of shear and TI observed offshore. Anyway, a comparison of the standard turbulence models to TIMESR and LES, which are still considered more realistic, shows that it is time for more advanced turbulence models with inputs adapted to various stability conditions.

The wind field comparisons give valuable insight in the various generation methods and resulting coherent structures. It is clear that the spatial and temporal distributions of coherence differ significantly across generation methods and atmospheric stability conditions. This will have an impact on the dynamic response of large offshore wind turbines. From the results of this work, the effect of the various wind field characteristics on the response is still unclear. Further work will investigate these effects on a large bottom fixed and floating offshore wind turbine.

## ACKNOWLEDGEMENTS

The authors would like to thank DEWI (Deutsches Windenergi Institut), and especially Richard Fruehmann, for providing the FINO1 high-resolution sonic anemometer data, and BSH (The Federal Maritime and Hydrographic Agency of Germany) for providing slow meteorological reference data. We would also like to thank Etienne Cheynet for input and support. A portion of this research was performed using computational resources sponsored by the U.S. Department of Energy's Office of Energy Efficiency and Renewable Energy and located at the National Renewable Energy Laboratory.

This work was authored in part by the National Renewable Energy Laboratory, operated by Alliance for Sustainable Energy, LLC, for the U.S. Department of Energy (DOE) under Contract No.DE-AC36-08GO28308. Funding provided by the U.S. Department of Energy Office of Energy Efficiency and Renewable Energy Wind Energy Technologies Office. The views expressed in the article do not necessarily represent the views of the DOE or the U.S. Government. The U.S. Government retains and the publisher, by accepting the article for publication, acknowledges that the U.S. Government retains a nonexclusive, paid-up, irrevocable, worldwide license to publish or reproduce the published form of this work, or allow others to do so, for U.S.Government purposes.

## ORCID

*Astrid Nybø* https://orcid.org/0000-0002-7438-7936
*Finn Gunnar Nielsen* https://orcid.org/0000-0002-1576-2409
*Joachim Reuder* https://orcid.org/0000-0002-0802-4838
*Matthew J. Churchfield* https://orcid.org/0000-0001-9906-7288

## REFERENCES

1. International Electrotechnical Commision. IEC 61400-1 Wind energy generation systems - Part 1: Design requirements. https://webstore.iec.ch/publication/26423. Accessed May 28, 2019; 2019.
2. International Electrotechnical Commision. IEC 61400-3-2 Wind energy generation systems - Part 3-1: Design requirements for fixed offshore wind turbines. https://webstore.iec.ch/publication/29360. Accessed May 28, 2019; 2019.
3. International Electrotechnical Commision. IEC 61400-3-2 Wind energy generation systems - Part 3-2: Design requirements for floating offshore wind turbines. https://webstore.iec.ch/publication/29244. Accessed May 28, 2019; 2019.
4. Fraunhofer. Turbine size. http://windmonitor.iee.fraunhofer.de/windmonitor_en/4_Offshore/2_technik/3_Anlagengroesse/, Accessed May 27, 2019; 2019.
5. Mann J. The spatial structure of neutral atmospheric surface-layer turbulence. *J Fluid Mech*. 1994;273:141-168. https://doi.org/10.1017/S0022112094001886
6. Kaimal J, Wyngaard J, Izumi Y, Coté O. Spectral characteristics of surface-layer turbulence. *Quart J Royal Meteorol Soc*. 1972;98(417):563-589. https://doi.org/10.1002/qj.49709841707
7. Bachynski E, Eliassen L. The effects of coherent structures on the global response of floating offshore wind turbines. *Wind Energy*. 2019;22(2):219-238. https://doi.org/10.1002/we.2280
8. Eliassen L, Bachynski EE. The effect of turbulence model on the response of a large floating wind turbine. In: ASME 2017 36th International Conference on Ocean, Offshore and Arctic Engineering; 2017; Trondheim, Norway:1–10.
9. Doubrawa P, Churchfield MJ, Godvik M, Sirnivas S. Load response of a floating wind turbine to turbulent atmospheric flow. *Appl Energy*. 2019;242:1588-1599. https://doi.org/10.1016/j.apenergy.2019.01.165
10. Godvik M. Influence of wind coherence on the response of a floating wind turbine. In: Science Meets Industry; 2016; Stavanger, Norway:1–12. http://www.norcowe.no/doc//konferanser/2016/SMI Stavanger presentasjoner/Godvik Statoil Influence of the wind coherence on the response of a floating wind turbine.pdf
11. Robertson A, Sethuraman L, Jonkman J, Quick J. Assessment of wind parameter sensitivity on extreme and fatigue wind turbine loads. In: 2018 Wind Energy Symposium; 2018; Kissimmee, Florida:1728.
12. Ropelewski CF, Tennekes H, Panofsky HA. Horizontal coherence of wind fluctuations. *Bound Layer Meteorol*. 1973;5(3):353-363. https://doi.org/10.1007/BF00155243
13. Eliassen L, Obhrai C. Coherence of turbulent wind under neutral wind conditions at FINO1. *Energy Proced*. 2016;94:388-398. https://doi.org/10.1016/j.egypro.2016.09.199
14. Eliassen L, Andersen S. Investigating coherent structures in the standard turbulence models using proper orthogonal decomposition. *J Phys Conf Ser*. 2016;753(3):32040. https://doi.org/10.1088/1742-6596/753/3/032040
15. Cheynet E. Influence of the measurement height on the vertical coherence of natural wind. In: Proceedings of the XV Conference of the Italian Association for Wind Engineering Ricciardelli F, Avossa AM, eds. Springer International Publishing; 2019; Cham:207-221.

16. Cheynet E, Jakobsen JB, Reuder J. Velocity spectra and coherence estimates in the marine atmospheric boundary layer. *Bound Layer Meteorol*. 2018;169(3):429-460. https://doi.org/10.1007/s10546-018-0382-2
17. FuE-Zentrum FH Kiel GmbH. FINO1: Forschungsplattformen in Nord- und Ostsee Nr. 1. https://www.fino1.de/. Accessed January 09, 2019; 2019.
18. Kelley N, Jonkman B. TurbSim - NWTC Information Portal. https://nwtc.nrel.gov/TurbSim. Accessed May 27, 2019; 2016.
19. Simley E, Pao LY. A longitudinal spatial coherence model for wind evolution based on large-eddy simulation. In: Proceedings of the American Control Conference; 2015; Chicago, IL, USA:3708-3714.
20. Worsnop RP, Bryan GH, Lundquist JK, Zhang JA. Using large-eddy simulations to define spectral and coherence characteristics of the hurricane boundary layer for wind-energy applications. *Bound Layer Meteorol*. 2017;165(1):55-86. https://doi.org/10.1007/s10546-017-0266-x
21. Berg J, Natarajan A, Mann J, Patton EG. Gaussian vs non-Gaussian turbulence: impact on wind turbine loads. *Wind Energy*. 2016;19(11):1975-1989. https://doi.org/10.1002/we.1963
22. Sathe A, Bierbooms W. Influence of different wind profiles due to varying atmospheric stability on the fatigue life of wind turbines. *J Phys Conf Ser*. 2007;75(1):012056. https://doi.org/10.1088/1742-6596/75/1/012056
23. Eliassen L, Jakobsen JB, Obhrai C. The effect of atmospheric stability on the fatigue life of offshore wind turbines. In: Proceedings of the Twenty-second (2012) International Offshore and Polar Engineering Conference; 2012; Rhodes, Greece:330-336.
24. Holtslag MC, Bierbooms WAAM, Van Bussel GJW. Wind turbine fatigue loads as a function of atmospheric conditions offshore. *Wind Energy*. 2016;19(10):1917-1932. https://doi.org/10.1002/we.1959
25. Holtslag MC, Bierbooms WAAM, Van Bussel GJW. Estimating atmospheric stability from observations and correcting wind shear models accordingly. *J Phys Conf Ser*. 2014;555:012052. https://doi.org/10.1088/1742-6596/555/1/012052
26. Sathe A, Mann J, Barlas T, Bierbooms WAAM, Van Bussel GJW. Influence of atmospheric stability on wind turbine loads. *Wind Energy*. 2013;16(7):1013-1032. https://doi.org/10.1002/we.1528
27. Churchfield M, Lee S. SOWFA | NWTC Information Portal. https://nwtc.nrel.gov/SOWFA. Accessed February 04, 2019; 2015.
28. Bak C, Zahle F, Bitsche R, et al. The dtu 10-mw reference wind turbine. http://orbit.dtu.dk/ws/files/55645274/The_DTU_10MW_Reference_Turbine_Christian_Bak.pdf. Accessed May 27, 2019; 2013.
29. Sim C, Manuel L, Basu S. A comparison of wind turbine load statistics for inflow turbulence fields based on conventional spectral methods and large eddy simulation. In: 48th AIAA Aerospace Sciences Meeting Including the New Horizons Forum and Aerospace Exposition; 2013; Orlando, Florida:829.
30. Irwin JS. A theoretical variation of the wind profile power-law exponent as a function of surface roughness and stability. *Atmospher Environ (1967)*. 1979;13(1):191-194. https://doi.org/10.1016/0004-6981(79)90260-9
31. Emeis S. Current issues in wind energy meteorology. *Meteorol Appl*. 2014;21(4):803-819. https://doi.org/10.1002/met.1472
32. Businger JA, Wyngaard JC, Izumi Y, Bradley EF. Flux-profile relationships in the atmospheric surface layer. *J Atmos Sci*. 1971;28(2):181-189. https://doi.org/10.1175/1520-0469(1971)028<0181:FPRITA>2.0.CO;2
33. Högström U. Non-dimensional wind and temperature profiles in the atmospheric surface layer: a re-evaluation. *Bound Layer Meteorol*. 1988;42(1):55-78. https://doi.org/10.1007/BF00119875
34. Dyer AJ. A review of flux-profile relationships. *Bound Layer Meteorol*. 1974;7(3):363-372. https://doi.org/10.1007/BF00240838
35. Monin AS, Obukhov AM. Basic laws of turbulent mixing in the surface layer of the atmosphere. *Contrib Geophys Inst Acad Sci USSR*. 1954;24(151):163-187.
36. Foken T. 50 years of the Monin–Obukhov similarity theory. *Boundary-Layer Meteorology*. 2006;119(3):431-447. https://doi.org/10.1007/s10546-006-9048-6
37. Haugen DA, Kaimal JC, Bradley EF. An experimental study of Reynolds stress and heat flux in the atmospheric surface layer. *Quart J Royal Meteorol Soc*. 1971;97(412):168-180. https://doi.org/10.1002/qj.49709741204
38. Hess GD, Hicks BB, Yamada T. The Impact of the Wangara experiment. *Bound Layer Meteorol*. 1981;20(2):135-174. https://doi.org/10.1007/BF00119899
39. Stull RB. *An Introduction to Boundary Layer Meteorology*. Dordrecht: Springer Netherlands; 1988.
40. Gryning SE, Batchvarova E, Brümmer B, Jørgensen H, Larsen S. On the extension of the wind profile over homogeneous terrain beyond the surface boundary layer. *Bound Layer Meteorol*. 2007;124(2):251-268. https://doi.org/10.1007/s10546-007-9166-9
41. Peña A., Gryning S-E, Hasager C. B.. Measurements and modelling of the wind speed profile in the marine atmospheric boundary layer. *Boundary-Layer Meteorology*. 2008;129(3):479-495. https://doi.org/10.1007/s10546-008-9323-9
42. Obukhov AM. Turbulence in an atmosphere with a non-uniform temperature. *Bound Layer Meteorol*. 1971;2(1):7-29. https://doi.org/10.1007/BF00718085
43. Van Wijk AJM, Beljaars ACM, Holtslag AAM, Turkenburg WC. Evaluation of stability corrections in wind speed profiles over the North Sea. *J Wind Eng Ind Aerodyn*. 1990;33(3):551-566. https://doi.org/10.1016/0167-6105(90)90007-Y
44. Welch P. The use of fast fourier transform for the estimation of power spectra: a method based on time averaging over short, modified periodograms. *IEEE Trans Audio Electroacoustics*. 1967;15(2):70-73. https://doi.org/10.1109/TAU.1967.1161901
45. Veers P. Modeling stochastic wind loads on vertical axis wind turbines. In: 25th Structures, Structural Dynamics and Materials Conference; 1984; Palm Springs,CA,U.S.A.:910.
46. Jørgensen BH, Sørensen JN, Brøns M. Low-dimensional modeling of a driven cavity flow with two free parameters. *Theoret Comput Fluid Dyn*. 2003;16(4):299-317. https://doi.org/10.1007/s00162-002-0082-9
47. Berkooz G, Holmes P, Lumley JL. The proper orthogonal decomposition in the analysis of turbulent flows. *Annual Rev Fluid Mech*. 1993;25(1):539-575. https://doi.org/10.1146/annurev.fl.25.010193.002543
48. Mann J. Wind field simulation. *Probabil Eng Mech*. 1998;13(4):269-282. https://doi.org/10.1016/S0266-8920(97)00036-2
49. Von Kármán Theodore. Progress in the statistical theory of turbulence. *Proc National Acad Sci USA*. 1948;34(11):530-539. https://doi.org/10.1073/pnas.34.11.530
50. Mann J. Atmospheric turbulence. In: Peña A, Hasager CB, Lange J, Anger J, Badger M, Bingöl F, Bischoff O, Cariou J-P, Dunne F, Emeis S, Harris M, Hofsäss M, Karagali I, Laks J, Larsen SE, Mann J, Mikkelsen T, Pao LY, Pitter M, Rettenmeier A, Sathe A, Scanzani F, Schlipf D, Simley E, Slinger C,

Wagner R, Würth I, eds. *Remote Sensing for Wind Energy Wind Energy*. Denmark: DTU Wind Energy; 2013:52–71. http://orbit.dtu.dk/files/55501125/Remote_Sensing_for_Wind_Energy.pdf

51. Chougule A, Mann J, Segalini A, Dellwik E. Spectral tensor parameters for wind turbine load modeling from forested and agricultural landscapes. *Wind Energy*. 2015;18(3):469-481. https://doi.org/10.1002/we.1709
52. De Maré M, Mann J. Validation of the Mann spectral tensor for offshore wind conditions at different atmospheric stabilities. *J Phys Conf Ser*. 2014;524(1):012106. https://doi.org/10.1088/1742-6596/524/1/012106
53. DTU Wind Energy. Pre-processing tools. http://www.hawc2.dk/download/pre-processing-tools. Accessed May 27, 2019; 2018.
54. Nybø A, Nielsen FG, Reuder J. Processing of sonic anemometer measurements for offshore wind turbine applications. *J Phys Conf Ser*. 2019;1356(1):012006. https://doi.org/10.1088/1742-6596/1356/1/012006
55. Rinker JM.. An empirically based stochastic turbulence simulator with temporal coherence for wind energy applications. *Ph.D. Thesis*; 2016.
56. Krogsæter O, Reuder J. Validation of boundary layer parameterization schemes in the weather research and forecasting (wrf) model under the aspect of offshore wind energy applications—part ii: boundary layer height and atmospheric stability. *Wind Energy*. 2015;18(7):1291-1302. https://doi.org/10.1002/we.1765
57. Shaler K, Jonkman J, Doubrawa P, Hamilton N. FAST.Farm response to varying wind inflow techniques. In: AIAA Scitech 2019 Forum; 2019; Golden, CO (United States).
58. Davenport AG. The spectrum of horizontal gustiness near the ground in high winds. *Quart J Royal Meteorol Soc*. 1961;87(372):194-211. https://doi.org/10.1002/qj.49708737208
59. OpenFOAM: The Open Source CFD Toolbox. https://openfoam.org/. Accessed May 28, 2019; 2019.
60. Kristensen L, Jensen NO. Lateral coherence in isotropic turbulence and in the natural wind. *Bound Layer Meteorol.* 1979;17(3):353-373. https://doi.org/10.1007/BF00117924

**How to cite this article:** Nybø A, Nielsen FG, Reuder J, Churchfield MJ, Godvik M. Evaluation of different wind fields for the investigation of the dynamic response of offshore wind turbines. *Wind Energy*. 2020;1-21. https://doi.org/10.1002/we.2518

# Paper 3

## Quasi-static response of a bottom-fixed wind turbine subject to various incident wind fields

Nybø A, Nielsen FG and Godvik M
*Wind Energy*, **24**/**12** (2021)

Received: 15 December 2020 | Revised: 1 March 2021 | Accepted: 3 April 2021

DOI: 10.1002/we.2642

RESEARCH ARTICLE

WILEY

# Quasi-static response of a bottom-fixed wind turbine subject to various incident wind fields

Astrid Nybø[1] | Finn Gunnar Nielsen[1] | Marte Godvik[1,2]

[1]Geophysical Institute and Bergen Offshore Wind Centre (BOW), University of Bergen, Bergen, Norway

[2]R&T, Equinor ASA, Bergen, Norway

**Correspondence**
Astrid Nybø, Geophysical Institute and Bergen Offshore Wind Centre (BOW), University of Bergen, Allégaten 70, 5007 Bergen, Norway.
Email: astrid.nybo@uib.no

## Abstract

In the design of offshore wind farms the simulated dynamic response of the wind turbine structure includes loading from turbulent wind. The International Electrotechnical Commission (IEC) standard for wind turbine design recommends both the Mann spectral tensor model and the Kaimal spectral model combined with an exponential coherence formulation. These models give deviating wind loads. This study compares these two models to a large eddy simulations model and a model based on offshore wind measurements. The comparisons are performed for three situations, covering unstable, neutral and stable atmospheric conditions. The impact of the differences in the wind fields on the quasi-static response of a large bottom-fixed wind turbine is investigated. The findings are supported by an assessment of the impact of individual wind characteristics on the turbine responses. The wind model based on measurements causes high tower bottom and blade root flapwise bending moments due to a high wind load at very low frequencies. Low and negative horizontal coherence is obtained using the Mann spectral tensor model. This causes relatively large yaw moments as compared to the results using the other wind models. The largest differences in response are seen in the stable situation. We furthermore show that the quasi-static wind load has great impact on the total damage equivalent moments of the structure. From the results, we conclude that in the design of large offshore wind turbines one should carefully consider the structure of the turbulent wind. Further, longer simulations than recommended by the standards should be used to reduce uncertainty in estimated response.

**KEYWORDS**
coherence, damage equivalent moments, offshore wind turbines, quasi-static response, spectral response, turbulence models

## 1 | INTRODUCTION

For the last decades, there has been significant yearly additions to the total installed wind energy capacity world wide.[1] In the recent years, the offshore installations are approaching a significant level, being 10% of total wind energy installations in 2019. The trend of moving offshore is driven by the available areas and superior wind conditions, but hindered by the additional complexity and costs.

In the design of offshore wind turbines, a realistic modelling of the incident wind field is important to determine the corresponding response. The recently published design standards for offshore wind turbines from the International Electrotechnical Commission (IEC)[2–4] still recommend two turbulence models initially developed for onshore small rotors in neutral atmospheric stability conditions. These are the Mann spectral tensor model, hereafter denoted 'Mann',[5] and the Kaimal spectral model combined with an exponential coherence formulation, hereafter denoted 'Kaimal'.[6] For design purposes it is common to assume that if the wind field has a given shear profile and turbulence intensity, the response of the wind turbine is not very dependent upon the spectral and coherence model used. On the contrary, previous studies[7–12] have shown that the structural loads in the response of the wind turbine are sensitive to the model chosen.

Both the research community (e.g., previous works[7,11–15]) and the industry (e.g., previous works[16]) look for improved turbulence models. They should be valid for large rotors (200 m in diameter) and account for variations in atmospheric stability conditions. The importance of a proper coherence model increases with the rotor diameter. The complexity of models are therefore increased and more site parameters are included. Several studies[7,11,12,14,17] group wind fields by stability and evaluate its impact on response. The improved certainties in the response of the offshore wind turbines may still not be worth the additional computational time and/or measurements required. In order to make the right compromise, one needs to evaluate the differences in the response using various input wind fields, and furthermore the origin of these differences.

In Nybø et al,[18] the Kaimal and Mann wind fields are compared to large eddy simulations, hereafter denoted 'LES', and wind fields based on offshore measurements, hereafter denoted 'TIMESR'. The comparisons were made for several wind speeds and atmospheric stability conditions. The current study aims to evaluate the response of a bottom-fixed wind turbine subject to the four wind spectral formulations; Kaimal, Mann, LES and TIMESR. The models are fitted to measurement situations covering stable, unstable and neutral atmospheric conditions. None of the studies mentioned above compare the responses of a wind turbine in the different wind fields presented.

In order to determine the origin of the differences in response in TIMESR, LES, Mann and Kaimal, the wind characteristics are first isolated and their effect on response evaluated. The response is evaluated in terms of damage equivalent moments, hereafter denoted as 'DEM', but more importantly the response spectra. By comparing spectral characteristics of the wind and response, it is easier to determine the origin of the response differences.

The wind induced quasi-static response ($f < 0.1$ Hz) is in focus, in order to exclusively study the wind impact on response. It is seen from Holtslag et al.[14] and Haaskjold et al,[7] for example, that the low-frequency region has a large impact on the overall response of bottom-fixed wind turbines. This work will furthermore show that the spectral formulations of Mann, Kaimal, LES and TIMESR vary significantly in the low-frequency region below 0.1 Hz. The uncertainty and stochastic variation in this region is furthermore assessed. To the author's knowledge, spectral analysis of the origin of differences in quasi-static response from various input wind fields has never been done before.

## 2 | DATA AND METHODS

### 2.1 | Wind fields

In this study, a number of incident wind fields are used in the analysis of a bottom-fixed wind turbine. These wind fields are introduced in Section 1 as Kaimal, Mann, TIMESR and LES. Measurements from sonic anemometers at an offshore mast outside Germany (FINO1)[19,20] are used as inputs to the various models according to Figure 1. In a previous study,[18] these wind fields are properly described and compared to each other.

In order to evaluate the wind fields, some definitions of wind characteristics are needed. The turbulence intensity, TI, is defined by the standard deviation of the wind speed in the mean wind direction, $\sigma_u$, and the mean wind speed, $\bar{u}$, according to Equation (1). In the following, TI is referred to hub height.

$$TI = \frac{\sigma_u}{\bar{u}} \tag{1}$$

According to the IEC wind turbine design standard,[2] the variation of mean wind speed with height, the wind shear, is described by the power law:

$$\bar{u}(z) = \bar{u}_{ref}\left(\frac{z}{z_{ref}}\right)^{\alpha}. \tag{2}$$

$\bar{u}$ is the mean wind speed at height $z$, and $\bar{u}_{ref}$ is the wind speed at a reference height, $z_{ref}$. $\alpha$ is the empirical power law exponent. As seen in Figure 1, the logarithmic law is used for the TIMESR profile. This law takes atmospheric stability into account when describing the variation of wind speed with height.

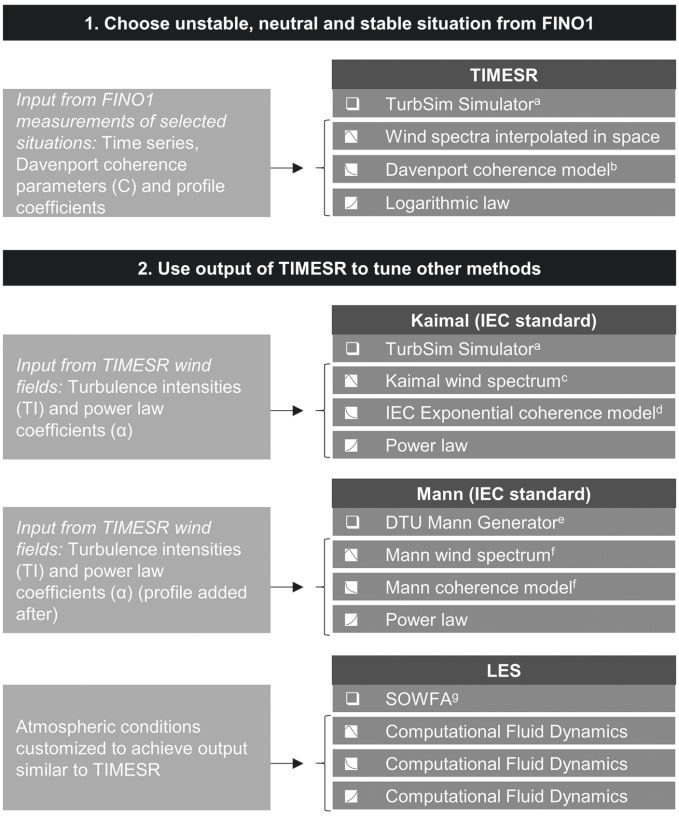


**FIGURE 1** Scheme of wind field models, describing inputs, simulation software, spectra and coherence models and profile laws. a =[21], b=[22], c=[6], d=[2], e=[23], f=[5] and g=[24]

The coherence is used to quantify the correlation between the wind speed at two different locations in frequency space. Frequently, the root-coherence, or the coherence in its absolute form, is used for this purpose. The root-coherence is given by

$$|\gamma| = \frac{|S_{xy}|}{\sqrt{S_{xx}S_{yy}}}, \tag{3}$$

where $S_{xx}$ and $S_{yy}$ are one-sided auto-spectra of the wind velocities at two different positions, $x$ and $y$, and $S_{xy}$ is the cross spectrum between these two. The coherence, $\gamma$, may be split in a real part, the co-coherence (Re[$\gamma$]), and an imaginary part, the quad-coherence (Im[$\gamma$]). The coherence between two positions separated by a horizontal distance, $\delta_y$, is referred to by $\gamma_y$, and a vertical distance, $\delta_z$, by $\gamma_z$. The Davenport coherence model[22] is defined by a decay parameter, $C$, according to the following equation:

$$\gamma = \exp\left(-C*\frac{f\delta}{\bar{u}_m}\right), \tag{4}$$

where the frequency is represented by $f$ and the mean wind speed between the two locations by $\bar{u}_m$. Only the coherence of the along wind component, the uu-coherence, is analysed in this work, thus in the following coherence refers to the uu-coherence if not stated otherwise. It is shown by e.g. Robertson et al.[25] that the uu-coherence is more important for the response of a 5-MW wind turbine than the vv- and ww-coherence. We assume that the u-component is still the most important when considering a larger wind turbine. It should however be noted, that the vv- and ww-coherence may have larger significance when considering several wind turbines where wake meandering matters.[26]

In Nybø et al,[18] a number of wind fields were simulated in various wind speed and stability conditions. In the present study, focus is on a wind speed just above rated in unstable, neutral and stable stratification. Further characteristics of these situations are listed in Table 1. It should be noted that the Kaimal and Mann wind fields are intended for neutral situations, so only the TI and shear is adapted when they are referred to as stable or unstable. A brief analysis of the wind speed impact on the wind turbine response is also performed, where wind fields are fitted to measurements of 7.5 and 18 m/s in neutral stratification. One hour of continuous simulation has been performed in order to properly resolve the low-frequency region.

It was a goal to achieve similar main characteristics (mean wind speed and TI at hub and shear) across models in order to easier compare differences in response due to varying formulation of wind spectra, turbulent structures and coherence. This was not fully achieved for the 12.5 m/s neutral situation, which may be observed in the range of TI in Table 1. It was challenging to achieve high enough TI in neutral conditions in LES, resulting in only 3.6%, while other models are closer to 6%. The resolution and size of the LES domain are finer and larger than given in Table 1, but interpolations are performed in order to compare at the same grounds. Figure 1 shows that TIMESR is based on measurements to a large degree. However, measurements are only conducted at a few vertical locations on the mast. The decay parameters are estimated from time series separated vertically. The decay of coherence is assumed to follow the Davenport model with equal decay parameters for horizontal and vertical separation distances. Based on the above, this model may be considered the most realistic one, but it has clear limitations and should not be considered 'true'.

Figures 2–4 show the wind spectra, co- and quad-coherence of the different simulated wind fields. For details on the spectral procedures, see Nybø et al.[18] All three figures are limited to the very low-frequency region below 0.1 Hz, where the major part of the energy and large co- and quad-coherence are observed. For the low-frequency fluctuations, only a few oscillations are achieved in the 1-hr simulations. Therefore, there is significant uncertainty associated to the spectra, co- and quad-coherence. In the calculation of these spectral properties, stationarity is assumed. TIMESR is based on 1 hr of measurements. Natural wind is not truly a stationary process, but the chosen situations are considered stationary using the criteria given in Nybø et al.[20] These criteria define stationarity based on the linear trends and moving statistics of the time series. Mann and Kaimal are stationary models, and the generated LES wind fields of this study are also found to be stationary based upon the criteria described above.[18]

In Figure 2 one observes that the energy level of the spectra decrease from unstable to stable situations (be aware of the different scales). Across stability conditions, one observes extreme values at 0.0017 Hz (lowest frequency in spectrum) for most models. Note that these values are very dependent on the block length used in the Fourier transform. With a longer block length, the extremes are moved to even lower

**TABLE 1** Summary of wind field characteristics of the close to rated wind speed situation

| Parameters | Unstable | Neutral | Stable |
|---|---|---|---|
| Mean wind speed at 119 m | 12.6 m/s | 12.4 m/s | 12.5 m/s |
| Turbulence intensity | 5.6–6.4 % | 3.6–6.2 % | 2.3–3.1 % |
| Power law exponent | 0.02–0.03 | 0.05–0.06 | 0.2 |
| | **All** | | |
| Grid size horizontally and vertically | 3.5 m | | |
| Domain size horizontally and vertically | 220.5 m | | |
| Simulation time | 1 hr | | |
| Time step | 0.1 s | | |

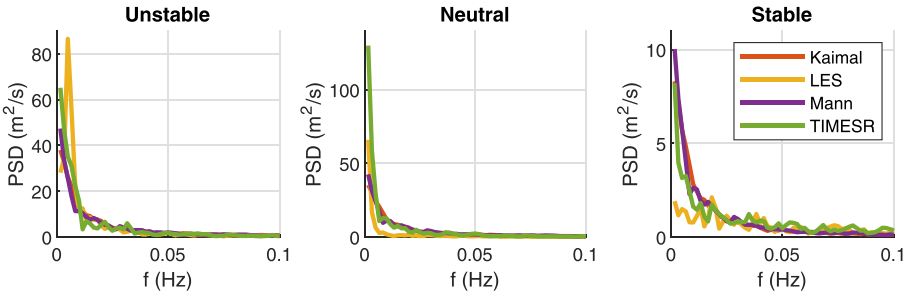


**FIGURE 2** Wind spectra at 119 m for 12.5 m/s (note the different scales). The mean spectra of six 1-hr realisations are shown. PSD = Power spectral densities. Frequency step, $\Delta f = 0.0017$ Hz [Colour figure can be viewed at wileyonlinelibrary.com]

frequencies, but the same trends are observed. The difference in TI between LES and other models in the neutral situation is observed in Figure 2 (middle). The power spectral densities of LES are lower than of other models, especially in the region 0.0033–0.04 Hz. The wind spectra of Mann and Kaimal are very similar, as the Mann inputs are customized to fit the Kaimal spectrum according to the IEC wind turbine design standard.[2]

Figures 3 and 4 show the co- and quad-coherence at 0.7D separation distance normal to the wind direction of wind turbines with about 180- and 80-m diameter, respectively. Distances in the order of the diameter of the wind turbine are assumed to be most relevant for tower response. Figure 3 is therefore most relevant for the analysis of the DTU 10 -MW wind turbine, while Figure 4 is rather relevant for wind turbines common

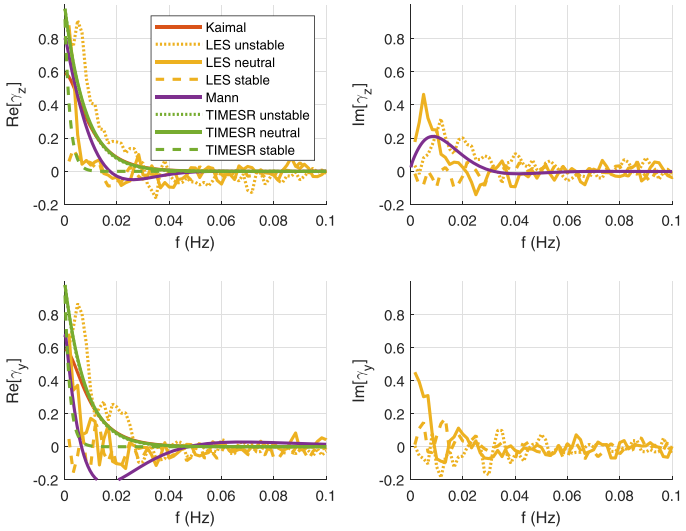


**FIGURE 3** Co- (left) and quad-coherence (right) with 0.7D vertical (top) and horizontal (bottom) separation distances for wind fields of 12.5 m/s and neutral atmospheric conditions. D=178.3 m (DTU 10-MW reference turbine) [Colour figure can be viewed at wileyonlinelibrary.com]

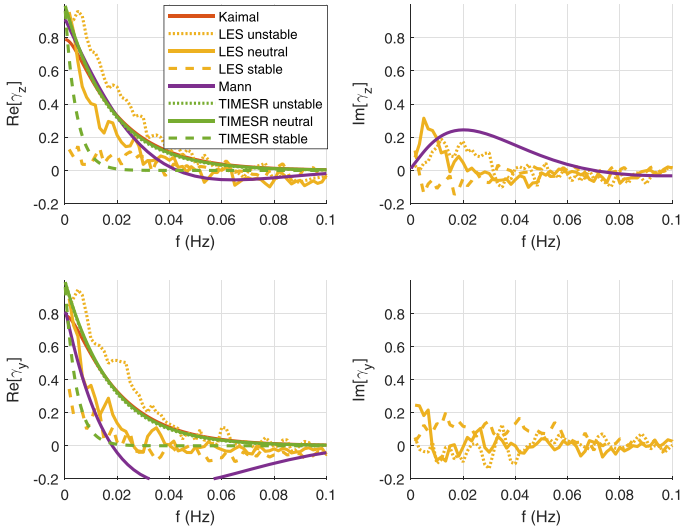


**FIGURE 4** Co- (left) and quad-coherence (right) with 0.7D vertical (top) and horizontal (bottom) separation distances for wind fields of 12.5 m/s and neutral atmospheric conditions. D=80 m (1–2 MW) [Colour figure can be viewed at wileyonlinelibrary.com]

20 years ago. The two figures show that a wind field hitting a large wind turbine is less coherent than the wind field hitting a smaller turbine. One observes that the co- and quad-coherence are close to zero over about 0.05 Hz in Figure 3. The comparison of Figures 3 and 4 shows that the importance of a proper coherence model increases with the rotor diameter, and design standards must be updated accordingly.

The co-coherence is higher in unstable situations than stable, clearly shown by LES in Figures 3 and 4. The stable TIMESR co-coherence is also decaying fast with frequency, but the neutral and unstable values of co-coherence are rather similar. The chosen unstable and neutral situations are in general very similar, also shown by Table 1, Figure 2 and Nybø et al.[18] Nybø et al.[18] found increasing co-coherence with increasing wind speed. In the literature, it is common to focus on the positive co-coherence for wind turbine purposes.[2,27–29] However, significant negative co-coherence and non-zero quad-coherence are observed in LES and Mann in Figures 3 and 4. The corresponding phase shifts between two time series separated in space are expected to influence the quasi-static response of a wind turbine. The quad-coherence is typically significant at frequencies where the co-coherence lies between zero and unity.

## 2.2 | Response

A slightly modified version of the DTU 10-MW reference turbine is used in the present study.[30] The modifications on the turbine itself are performed by Bachynski and Ormberg,[31] while Sørum et al.[32] designed the monopile foundation. The wind turbine, foundation and soil characteristics used in the current study are equal to the base model of Sørum et al,[32] with the exception of a slightly larger monopile diameter. The water depth is 30 m and the monopile extends 43 m below the mud line. The lowest point of the monopile is fixed in all degrees of freedom. The wind turbine has a hub height of 119 m and a diameter of 178.5 m. The lowest natural frequencies are the 1st tower side-side and fore-aft modes at about 0.23 Hz. At 12.5 m/s, the first excitation frequency, 1P, is 0.16 Hz. All natural frequencies and excitation frequencies are thus higher than the low-frequency region ($f < 0.1$ Hz) in focus in the present study. This region shows exclusively the quasi-static response as all natural frequencies are well above the frequency range considered.

During operation, large dynamic loads are expected close to the rated wind speed, 11.4 m/s. To stay above, but close to the rated wind speed, 12.5 m/s is chosen as the mean wind speed. From the simulation results it is observed, with a few exceptions, that the power output is constant at 10 MW throughout the duration of the simulations. For the TIMESR simulations in neutral atmospheric conditions the power drops below 10 MW in 3%–5% of the simulation time. This can be attributed to the high power density of the wind spectra at very low frequencies. The filter frequency for the generator speed controller is set to 0.2 Hz; thus, the control system is active in the low-frequency region.

The aero-hydro-servo-elastic tool SIMA[33] is used for the wind turbine simulations. The aerodynamic loads are calculated with the blade element momentum theory. The simulations are performed with a time step of about 0.01 s and a total length of 3800 s. The last hour of the simulations is used for analysis, reserving the initial 200 seconds for transient effects to die out.

For details on the number of SIMA runs conducted for this study, see Table 2. Simulations with specific wind characteristics, referred to in Table 2 under 'Wind characteristics tests', are run in order to evaluate the effect of shear, turbulence and coherence independently. The simulations referred to under 'Wind characteristics tests' are all discussed in Section 3.3. Some of them are run with only one realisation as their characteristics differ distinctly, while others require higher certainty. The wind fields of Kaimal, Mann and TIMESR are run with six different realisations, further discussed in the statistical analysis of Section 3.2. The mean characteristics of the six TIMESR realisations are used as inputs to the six Kaimal and Mann realisations. LES is only run with one realisation per stability and wind speed due to the computational efforts required.

The tower top yaw moment, hereafter denoted $M_z$, the tower top bending moment fore-aft, $M_{T,y}$, the tower bottom bending moment fore-aft, $M_{B,y}$, and the blade root flapwise bending moment, $M_F$, are considered in the response analysis. Only the dynamic response is considered, thus any reference to response corresponds to the dynamic response. Mean values have not been assessed. The mentioned responses are impacted by different characteristics in the wind. $M_{B,y}$ and $M_F$ are, for example, expected to be large if the wind turbine is subject to a fully coherent wind field over the rotor, while $M_z$ and $M_{T,y}$ will be larger if there are large variations in the wind field. Horizontal variations in the wind field is expected to influence the yaw moment while vertical variations may influence the fore-aft moments. The flapwise bending moment is, on the other hand, expected to be less dependent on direction. The fore-aft moments are expected to be far larger than the side-side moments, thus the side-side moments are not considered any further in this study.

The response is evaluated in terms of spectra and DEM. The response spectra are estimated using Welch's algorithm[34] with a Hamming window, six segments, and 50% overlapping. The standard deviation of the response time series, for example, used by Haaskjold et al.[7] also indicates the damage experienced by the wind turbine. However, it only takes into account the amplitudes of the response, without accounting for the number of oscillations. The DEM, $R_{eq}$, takes into account the amplitudes of the time series, $R_i$, the number of cycles, $n_i$, and the Wöhler curve exponent of the material, $m$, according to Equation (5).[35]

$$R_{eq} = \left( \frac{\Sigma_i (R_i^m n_i)}{n_{eq}} \right)^{1/m} \tag{5}$$

**TABLE 2** Summary of simulated wind fields, number of realisations and SIMA runs

| Method | Number of wind realisations and SIMA runs | |
|---|---|---|
| *Wind characteristics tests* | | |
| Uniform wind | | 1 |
| Sheared wind | | 1 |
| Turbulent sheared wind with $\gamma = 1$ | | 1 |
| Turbulent sheared wind with $\gamma_y = 1$ | | 1 |
| Turbulent sheared wind with $\gamma_z = 1$ | | 1 |
| Turbulent sheared wind with $\mathrm{Im}[\gamma_z] \neq 0$ | | 6 |
| Turbulent sheared wind with $\mathrm{Im}[\gamma_z] = 0$ | | 6 |
| Turbulent sheared wind allowing for $\mathrm{Re}[\gamma_y] < 0$ | | 6 |
| Turbulent sheared wind replacing $\mathrm{Re}[\gamma_y] < 0$ by 0 | | 6 |
| Turbulent sheared wind replacing $\mathrm{Re}[\gamma_y] < 0$ by $\lvert\mathrm{Re}[\gamma_y]\rvert$ | | 6 |
| *Response analysis* | | |
| Kaimal | 12.5 m/s: | 6 per stability |
| | 7.5 and 18 m/s: | 1 |
| LES | | 1 per stability and wind speed |
| Mann | 12.5 m/s: | 6 per stability |
| | 7.5 and 18 m/s: | 1 |
| TIMESR | 12.5 m/s: | 6 per stability |
| | 7.5 and 18 m/s: | 1 |

The rainflow algorithm developed by Nieslony[36] is used to compute the DEM, where half-cycles are weighted as $n_i = 0.5$. This practice is recommended by the IEC standard.[35] It is shown by Stewart et al.[37] that there may be large differences in fatigue damage with simulation length, depending on the way half-cycles are treated. In the same article, it is shown that weighting half-cycles as 0.5 results in less sensitivity to simulation length than ignoring them or counting them as full cycles. $n_{eq}$ is the equivalent number of response cycles, in this case for an equivalent frequency of 1 Hz. For the Wöhler curve exponent, 10 (composite material) is used for calculating the blade equivalent moment, and 3 (steel) for calculating the tower equivalent moments.

In order to evaluate the response from the low-frequency region exclusively, the time series are low-pass filtered at 0.1 Hz. The high-frequency components of the fast Fourier transform of the original time series are cut. The low-pass filtered time series are thereafter produced by inverse Fourier transformation. To avoid distortions of the ends of the filtered time series, a leader/trailer corresponding to 10% of the initial time history is introduced before applying the FFT. The leader/trailer is a mirror of the beginning/end of the time series linearly ramped off to zero. The low-pass filter is applied in a region of low gradients.

The focus of this study is on the aerodynamic loads, thus no waves or current are present in the simulations. By including aligned waves typical for the North Sea ($H_s$=3.2 m and $T_p$=8.8 s), it was observed that the waves had negligible impact on the DEM of $M_z$, $M_{T,y}$ and $M_F$. The contribution to the DEM of the wind alone was about 70% of the total DEM for $M_{B,y}$. Waves are not considered further as the aim of this work is to investigate the importance of the low-frequency wind loads.

## 3 | RESULTS AND DISCUSSION

### 3.1 | Importance of the low-frequency region

This study focuses on the quasi-static response at frequencies below 0.1 Hz. In the following, we illustrate the importance of this low-frequency region on the total response.

From the response spectra, one may observe the frequency dependent amplitudes, but it is not straight-forward to interpret the dependence of the number of oscillations. In Figure 5 (left), one observes the spectrum of the $M_z$ with a Kaimal wind field input. There are high peaks at low frequencies, but given the few oscillations of these cycles, their impact on DEM is not as high.

In order to evaluate the importance of the low-frequency region on the total damage, a low-pass filter at a number of frequencies on the original time series is used. This gives the cumulative contribution to DEM, as shown in Figure 5 (middle). This plot converges to the DEM of the

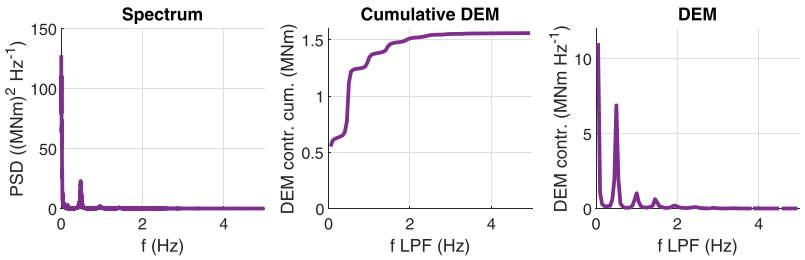


**FIGURE 5** Overview of procedure for determining frequency-dependent damage equivalent moment (DEM). f LPF is the cutoff frequency in the low-pass filter. Contr. = contribution, cum. = cumulative. A Kaimal wind field of about 12.5-m/s mean wind speed is used [Colour figure can be viewed at wileyonlinelibrary.com]

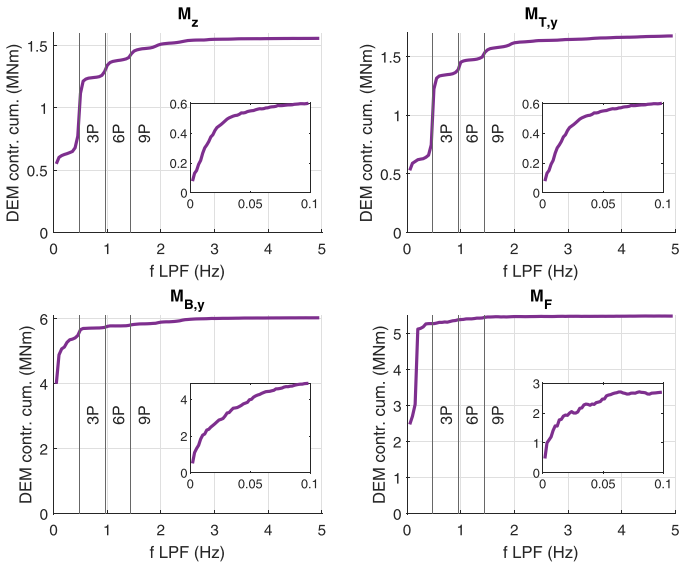


**FIGURE 6** Cumulative contribution to DEM of a Kaimal wind field with a mean wind speed of about 12.5 m/s. f LPF is the cutoff frequency in the low-pass filter (0.05 Hz for the large plots and 0.0017 Hz for the smaller boxes), contr. = contribution, cum. = cumulative [Colour figure can be viewed at wileyonlinelibrary.com]

original time series. The gradient of the cumulative contribution provides the frequency dependent contribution to DEM shown in Figure 5 (right). This method is further explained by Bergami and Gaunaa.[38] The low-pass filter described above is used with intervals of 0.05 Hz. As it is applied even in regions of high gradients, distortions may appear. Still, expected results are observed, similar to the spectra, but with higher impact from higher frequencies. The obtained frequency dependent DEM is dependent on the low-pass filter chosen; thus, the results should be considered qualitatively, not quantitatively.

Figure 6 shows the cumulative contribution to DEM for all considered responses using the same Kaimal input wind field. It shows that low frequencies are very important for $M_{B,y}$ and $M_F$. Large eddies covering most of the rotor area cause large tower bottom and blade root moments, for example for $M_F$ almost all damage is caused by responses below 0.25 Hz. In contrast to the tower response, the blade response is strongly influenced by the 1P frequency at about 0.16 Hz. Smaller eddies at higher frequencies covering only a small fraction of the rotor area have more significant impact on the tower top moments. For $M_z$ and $M_{T,y}$ the responses at the blade passing frequency, 3P as well as the multiples, 6P and 9P, contribute significantly to the damage. However, the quasi-static response at the lowest considered frequency is the largest single contributor to the DEM of all the four responses considered when considering frequency intervals of 0.05 Hz shown by the large plots of Figure 6.

It should be highlighted again, that there are large uncertainties associated with the low-frequency region of the wind spectra, the coherence and the response spectra. These uncertainties are reduced by using not too short block lengths in the FFT, long time series, and several realisations of these as discussed in Section 3.2.

## 3.2 | Statistical reliability of the quasi-static response

The IEC wind turbine standard[2] states that the total period of wind data should be long enough to ensure statistical reliability. More specifically, at least 1 hr of simulation should be run. To investigate whether the IEC recommendation is robust enough for comparison of turbulence models, specifically in the low-frequency region, the following analysis is performed.

First, it should be mentioned that the wind fields generated in this study are assumed to be stationary, as discussed in Section 2.1. However, Figure 2 shows that the time duration considered is not much longer than the duration of the large energy containing eddies. Therefore, the wind fields considered cannot be considered truly stationary. The small boxes of Figure 6 show that frequencies below 0.1 Hz matter significantly to the total DEM, but also that the very lowest frequencies considered (e.g., below 0.01 Hz) are not at all dominant for the total DEM. Due to limited contribution from the very low frequencies, the non-stationarity of the wind fields is assumed to have minor effect on the results.

The stochastic variation of the response time series may be evaluated in terms of the relative variance. Bendat and Piersol[39] show that the relative variance is inversely proportional to the bandwidth of the process, $B$, and the duration of the time series, $T$. For a boxcar power spectral density function, the relative variance is given by:

$$\frac{var[\hat{\psi}^2]}{\psi^4} \approx \frac{1}{BT}, \tag{6}$$

where $\hat{\psi}^2$ is the estimated variance of each simulated time series, while $\psi^2$ is the variance achieved by an infinite number of simulations. $\psi^4$ is estimated by using the square of the mean variance of the simulated time series. As the spectra are not boxcar shaped in the present case and the convergence of Equation (6) is slow with respect to the number of realisations needed, the result is used in a qualitatively sense.

A comparison between the relative variance (Equation (6)) of the total response time series and the low-frequency one is performed for 1 hr simulation split in six 10-min time series. The comparison confirms that the stochastic variation is stronger when considering only the low frequencies (not shown). In this section, the standard recommendation is thus compared towards a six times longer time series, hereby referred to as follows:

- '60MIN': Six simulations of duration 60 min. Each with different seed number and thus considered statistically independent.
- '10MIN': One of the above 60-min series are split into six 10-min series (IEC standard). These 10-min series are also assumed statistically independent.

Assuming a bandwidth limited Gaussian process, one should expect the relative variance to be inversely proportional to the simulation time, Equation (6), i.e the relative variance for the 10MIN should be about six times larger than that of the 60MIN. In Table 3, the relative variance of 10MIN is divided by the relative variance of 60MIN. For all responses and wind fields considered, the uncertainty is significantly reduced by increasing the total time by a factor 6. For most wind fields, the reduction is higher for $M_{B,y}$ and $M_F$ than $M_z$ and $M_{T,y}$. The values shown represent the mean of using six different 60-min realisations in the 10MIN relative variance. As mentioned, there is large uncertainty in the relative variance. This is observed by large variations among the different realisations (not shown). The reduction in uncertainty with duration shown by the relative variance in Table 3 is reflected in the DEM, as explained below.

**TABLE 3** $\frac{\frac{var[\hat{\psi}^2]}{\psi^4}_{10MIN}}{\frac{var[\hat{\psi}^2]}{\psi^4}_{60MIN}}$ for the response time series

| | $M_z$ | $M_{T,y}$ | $M_{B,y}$ | $M_F$ |
|---|---|---|---|---|
| TIMESR | 3.9 | 2.0 | 45.3 | 24.4 |
| $\text{TIMESR}_{\text{LPF}}$ | 3.9 | 1.6 | 45.8 | 32.8 |
| Kaimal | 35.1 | 5.9 | 14.9 | 33.2 |
| $\text{Kaimal}_{\text{LPF}}$ | 27.2 | 7.8 | 14.4 | 17.3 |
| Mann | 10.0 | 2.9 | 14.9 | 4.2 |
| $\text{Mann}_{\text{LPF}}$ | 6.9 | 4.3 | 14.3 | 20.3 |

*Note*: LPF = low-pass filtered at 0.1 Hz.

Figure 7 shows the various response spectra, using wind fields according to Kaimal, Mann, TIMESR and LES in neutral stability conditions. The spectra of $M_{B,y}$ and $M_F$ are narrower than $M_{T,y}$ and $M_z$. The lower bandwidths cause higher uncertainty in the relative variances. The response dependent uncertainty may also be observed in Figure 8. This figure shows the low-frequency DEM of the various input wind fields. The ranges in strong colors represent the stochastic variation (60MIN) from the minimum value to the maximum value of the six realizations. In agreement with the bandwidths, there are larger ranges at the tower bottom and blade root than at the tower top. Figure 8 also shows the stochastic variation of 10MIN in black lines. The reduced range going from 10MIN to 60MIN illustrates the reduced stochastic variability when increasing the total duration of simulation.

From Figure 8 it is observed that the stochastic variations between results from individual realizations (range in dark colors) may be larger than the differences between turbulence models. This is, for example, the case for Mann and Kaimal at $M_F$ in the 12.5-m/s situation. From the mean values, shown by white lines, one observes that Kaimal leads to significant higher damage than Mann. However, if running only 1 realization of 3600 s, we could have achieved opposite results. This confirms that we need several 1-hr simulations in order to achieve reliable results for comparisons of the low-frequency responses.

To sum up, there is a stronger stochastic variation when focusing exclusively on the low-frequency region, which is compensated by more simulations. This is necessary in order to achieve higher certainty when comparing the DEM of the various input wind fields. It is furthermore seen that the stochastic variation is higher at the tower bottom and blade root than at the tower top.

## 3.3 | Expected impact of shear, turbulence and coherence

The individual impact of shear, turbulence level and coherence on the different responses are considered in the following. The impact of coherence of vertical and horizontal separation distances is considered separately, with a special focus on quad-coherence and negative co-coherence. The different wind fields considered are described in Table 4. All the wind fields have close to rated wind speed at hub height.

No impact from shear on the response for frequencies below 0.1 Hz is expected. Figure 9 shows the spectra of the responses corresponding to the wind fields W1–W6. Comparing W1 (uniform flow) and W2 (shear flow), it is observed that the sheared wind field enhances responses at 3P for the tower moments and 1P for the blade moment. For other frequencies, no significant differences are observed. When no turbulence is present, only the rotor frequencies (1P, 3P) and multiplies of these (6P, 9P,…) contribute to the damage of the wind turbine.

Adding turbulence to the wind field, the distinct narrow peaks at e.g. 3P of the W1 and W2 spectra are becoming less distinct. Except for this, the responses generally increase in the whole frequency range, and in particular in the low-frequency region, below 0.1 Hz.

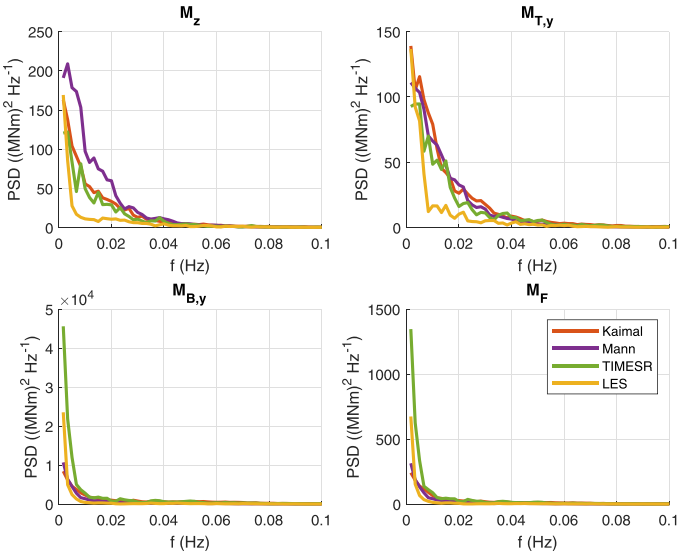


**FIGURE 7** Response spectra of the wind turbine subject to wind fields of 12.5 m/s and neutral atmospheric conditions. The mean spectra of six 1-hr realisations are shown. PSD = Power spectral densities. Frequency step, Δf = 0.0017 Hz [Colour figure can be viewed at wileyonlinelibrary.com]

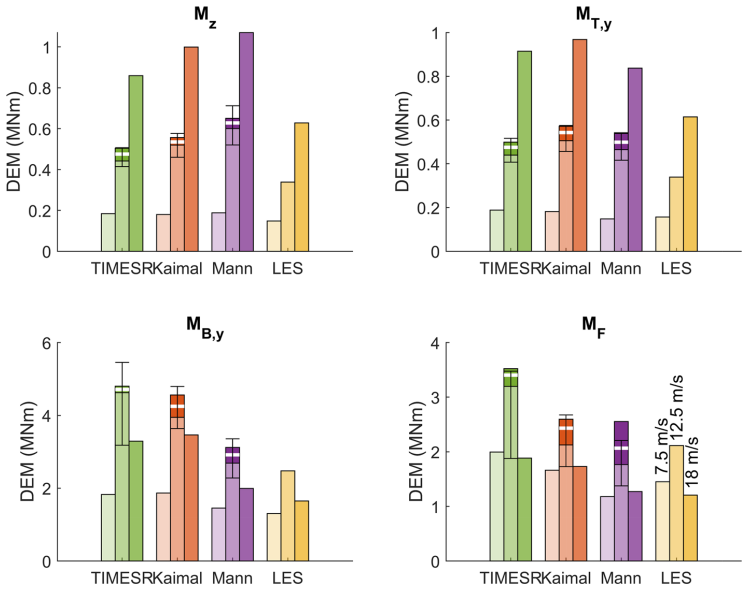


**FIGURE 8** Damage equivalent moments of the low-pass filtered response time series for three input wind speeds. For 12.5 m/s, the mean (white lines) and the range (dark colors) of six 1-hr realisations (60MIN) are shown, in addition to the range (black lines) of six 10-min realisations (10MIN) [Colour figure can be viewed at wileyonlinelibrary.com]

**TABLE 4** Wind fields used in studying the various contributions to turbine loads. Mid rules separate different generation techniques where the first block is generated in SIMA, the second is based on a TurbSim Kaimal wind field and the third is generated from a slightly modified version of Cheynet's generator

| Code | Wind field | $\alpha$ | TI | Same TS in hor. cells | Same TS in ver. cells + shear | Description |
|---|---|---|---|---|---|---|
| W1 | Uniform wind | 0 | 0% | yes | yes | |
| W2 | Sheared wind | 0.06 | 0% | yes | yes | |
| W3 | Turbulent sheared wind with $\gamma = 1$ | 0.06 | 6% | yes | yes | TS from hub height Kaimal wind field (W6). |
| W4 | Turbulent sheared wind with $\gamma_y = 1$ | 0.06 | 6% | yes | no | TS from mid Kaimal wind field (W6). |
| W5 | Turbulent sheared wind with $\gamma_z = 1$ | 0.06 | 6% | no | yes | TS from mid Kaimal wind field (W6). |
| W6 | Kaimal | 0.06 | 6% | no | no | According to the IEC standard. |
| W7 | Turbulent sheared wind with $\mathrm{Im}[\gamma_z] \neq 0$ | 0.06 | 6% | yes | no | Kaimal spectrum with Davenport $\mathrm{Re}[\gamma_z]$ (arbitrary C's) and $\mathrm{Im}[\gamma_z]$ from Equation (7), with $C_1 = 5$ and $C_2 = 10$. |
| W8 | Turbulent sheared wind with $\mathrm{Im}[\gamma_z] = 0$ | 0.06 | 6% | yes | no | Same as W7, but $C_1$=0 and $C_2$=0. |
| W9 | Turbulent sheared wind allowing for $\mathrm{Re}[\gamma_y] < 0$ | 0.06 | 6% | no | yes | Kaimal spectrum with $\mathrm{Re}[\gamma_y]$ from Equation (8), with $C_3 = 4\pi$, $C_4 = 5$ and $C_5 = 0.035$. |
| W10 | Turbulent sheared wind replacing $\mathrm{Re}[\gamma_y] < 0$ by 0 | 0.06 | 6% | no | yes | Same as W9, but $\mathrm{Re}[\gamma_y] < 0$ replaced by 0. |
| W11 | Turbulent sheared wind replacing $\mathrm{Re}[\gamma_y] < 0$ by $\lvert\mathrm{Re}[\gamma_y]\rvert$ | 0.06 | 6% | no | yes | Same as W9, but $\mathrm{Re}[\gamma_y] < 0$ replaced by positive equivalent. |

*Note* : Hor. = horizontal and ver. = vertical

A wind field with high co-coherence over the rotor as compared to a wind field with low co-coherence, causes lower moments at the tower top and higher moments at the tower bottom and blade root. Low coherence is associated with large variations in the wind velocity over the blades, causing significant local moments. Figure 9 shows that low horizontal co-coherence (W5) causes significant $M_z$, while low vertical co-coherence (W4) causes high $M_{T,y}$. These observations are in agreement with the findings of Putri et al. and Doubrawa et al.[11,12] A simplified illustration showing the impact of the co-coherence on response is given in Figure 10. 'A' is a simplified version of W5, 'B' of W4 and 'C' of W3, while 'D' shows the situation at higher frequencies. Wind fields with low correlation of the wind speed (W4, W5 and W6) over the rotor area, either vertically or horizontally, cause reduced total loads on the rotor, which again reduce $M_{B,y}$. On the contrary, a co-coherence approaching one implies that the forces on the rotor blades act in phase and thus create a large $M_{B,y}$. Similarly, the $M_F$ will be large. Although not shown in Figure 9, a wind field with very low coherence for all separation distances are expected to cause low local and global moments, as illustrated by 'D' in Figure 10.

The impact of quad-coherence is found to be almost negligible from comparisons of W7 and W8. The largest difference is found at the tower bottom, where $M_{B,y}$ is increased by 3% when accounting for quad-coherence. To include quad-coherence, the Davenport model (Equation (4)) is supplied by an imaginary part as proposed by Cheynet.[40] The quad-coherence for a vertical separation distance, $\delta_z$, is generated according to

$$\mathrm{Im}[\gamma_z] = C_1 * \frac{f * \delta_z}{\bar{u}} * \exp\left(-C_2 \frac{f * \delta_z}{\bar{u}}\right). \tag{7}$$

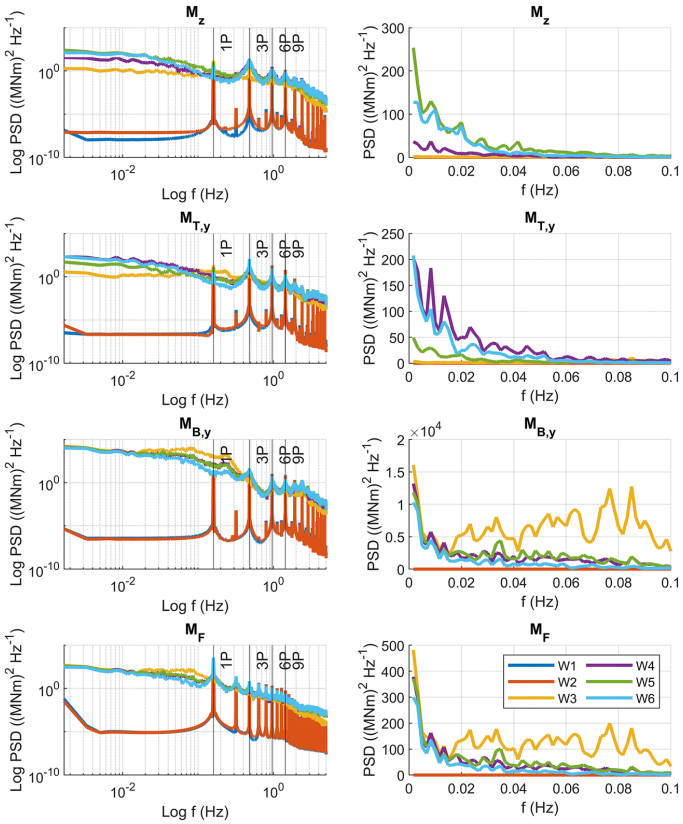


**FIGURE 9** Response spectra of wind turbine response using wind fields W1-W6 of Table 4. Responses plotted using double logarithmic scale to the left; to the right the low-frequency response ($f < 0.1$ Hz) is plotted using linear scales. PSD = Power spectral densities. Frequency step, $\Delta f = 0.0017$ Hz [Colour figure can be viewed at wileyonlinelibrary.com]

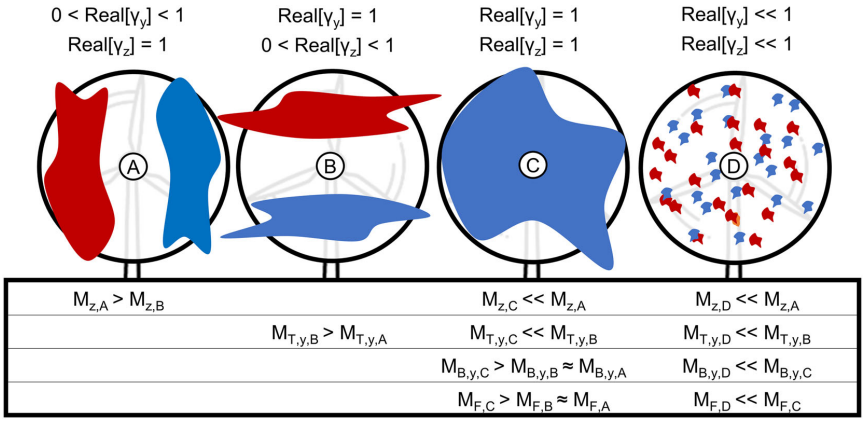


**FIGURE 10** Illustration of the impact of co-coherence and eddy size on response. Different colors represent uncorrelated eddies. M refers to the dynamic moments [Colour figure can be viewed at wileyonlinelibrary.com]

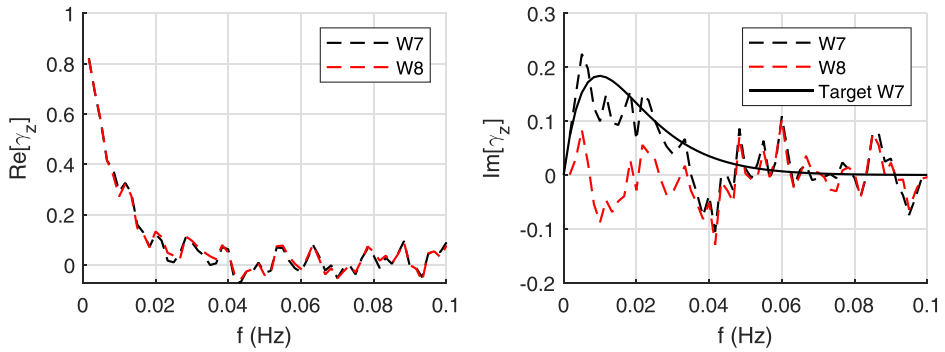


**FIGURE 11** Co- (left) and quad-coherence (right) with 0.7D of DTU 10-MW vertical separation distance of the wind fields W7 & W8 of Table 4. The mean coherence of six 1-hr simulations are shown [Colour figure can be viewed at wileyonlinelibrary.com]

With the decay parameters, $C_1$ and $C_2$, given in W7 of Table 4, the quad-coherence obtained is similar to Mann and lower than LES, as shown in Figure 11. The quad-coherence of the Mann and LES wind fields considered in this study is thus expected to have minor importance for the $M_z$, $M_{T,y}$, $M_{B,y}$ and $M_F$.

Keeping the negative co-coherence causes lower moments at the tower bottom and somewhat increased yaw moments in the low-frequency range as compared to the moments obtained when replacing the negative co-coherence with the absolute value or zero. The negative co-coherence for a horizontal separation distance, $\delta_y$, is generated according to the principles outlined by Cheynet:[41]

$$\mathrm{Re}[\gamma_y] = \cos\left(C_3 * \frac{f * \delta_y}{\bar{u}}\right) * \exp\left(-\frac{\delta_y * \sqrt{(C_4 * f)^2 + C_5^2}}{\bar{u}}\right). \tag{8}$$

With the decay coefficients, $C_{3-5}$, given in W9 of Table 4, the negative co-coherence is similar to Mann. The co-coherence of wind fields W9-W11 is shown in Figure 12, and its corresponding impact on the response spectra in Figure 13. Keeping the negative co-coherence (W9) rather than using the absolute value (W11), increases the $M_z$ and $M_{T,y}$ in the same frequency range where the co-coherence of W9 and W11 differ (considering a separation distance of 0.7D). As may be expected, $M_z$ is stronger influenced by the negative horizontal co-coherence than the fore-aft moment. Keeping the negative co-coherence (W9) causes increased local moments in the top of the turbine, but reduces the total horizontal force at the tower top, causing lower moments at the bottom of the tower. Across responses, the differences in co-coherence

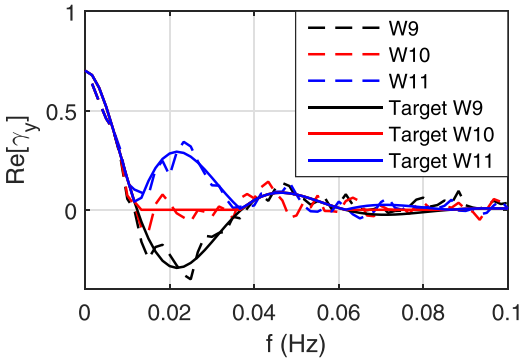


**FIGURE 12** Co-coherence with 0.7D of DTU 10-MW horizontal separation distance of the wind fields W9-W11 of Table 4. The mean co-coherence of six 1-hr simulations are shown [Colour figure can be viewed at wileyonlinelibrary.com]

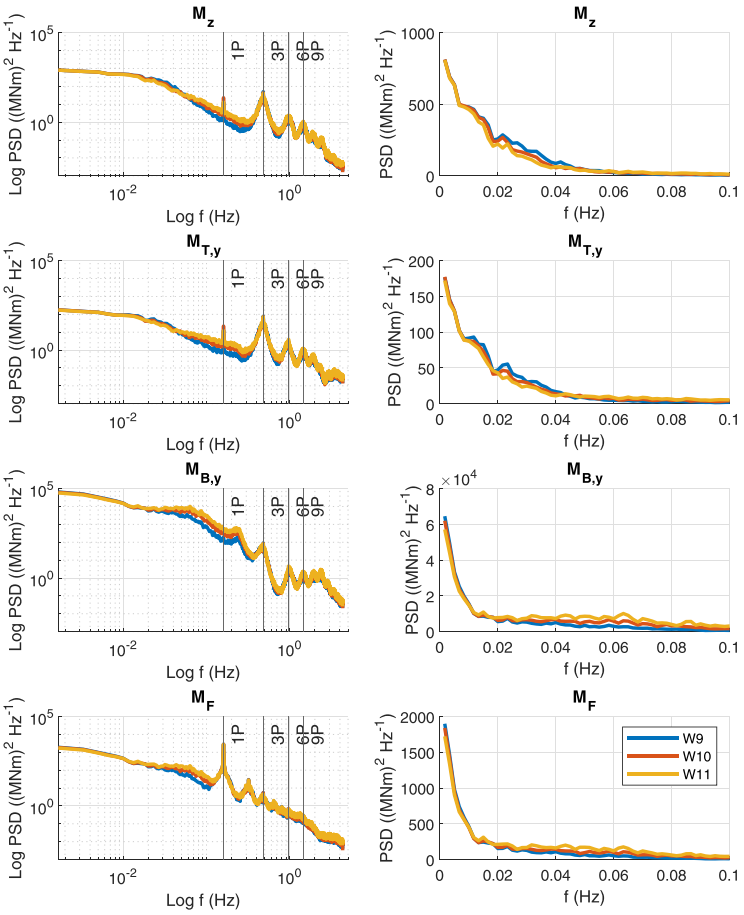


**FIGURE 13** Response spectra of wind turbine response using wind fields W9–W11 of Table 4. Responses plotted using double logarithmic scale to the left; to the right the low-frequency response ($f < 0.1$ Hz) is plotted using linear scales. The mean spectra of six 1-hr realizations are shown. PSD = power spectral densities. Frequency step, $\Delta f = 0.0017$ Hz [Colour figure can be viewed at wileyonlinelibrary.com]

influence the spectral densities at frequencies even higher than 0.1 Hz. This indicates that the co-coherence on length scales much smaller than the rotor diameter influences the responses. By comparing Figures 3 and 4, one observes that as the separation distance is reduced, the coherence persists at higher frequencies. Considering the DEM of the complete response time series, using the absolute value of the co-coherence (W11), rather than ignoring the negative values of co-coherence (W10) or keeping the negative values (W9), leads to higher DEM values for all considered responses. The differences are in the order of 10% for $M_z$, $M_{T,y}$ and $M_F$, while the $M_{B,y}$ is increased by 50% when the negative co-coherence is replaced by the absolute value. It may be assumed that the negative co-coherence present in Mann, being similar to W9, alters the wind turbine response as compared to coherence formulations that contain positive co-coherence only.

The coherence of the across wind and vertical wind components may also influence the loads. The effects of these components of the wind field are not analysed in the present study.

### 3.4 | Modelling of the low-frequency region

Above, it is shown that the low-frequency region is important for the structural damage. The IEC recommendation on the number of realizations of the simulations is furthermore considered to be too uncertain for comparing the DEM of using various input wind fields in this region. Further, the possible influence of shear, turbulence and coherence on the response is analysed. In the following, focus will be upon the response in the low-frequency region, that is, response at frequencies less than the first natural frequency of the tower and less than 1P. The response using wind fields generated by TIMESR, LES, Mann and Kaimal are considered.

The computed responses of SIMA simulations with the various wind fields are low-pass filtered and the DEM calculated. The results are presented in Figure 8 and Figure 14. The variation of the six realizations of 1 hr at 12.5 m/s are shown for all wind fields except for LES.

Figure 8 shows that, as the dynamic thrust force is highest at the rated wind speed, so are the DEM at the blade root and tower bottom. The local moments at the tower top, on the other hand, keep increasing with increasing wind speed. Only one realization is run for the above and below rated wind speed, so the results of these situations should thus not be used for comparisons across models where the results are very similar.

The response spectra, see Figures 7,15 and 16, show the frequency dependent response using the three stability situations at 12.5 m/s. It is obvious both from the DEM and the spectral response that the stable situation cause less dynamic loads. The responses of the unstable and neutral situations are rather similar, reflecting the similarities of the two chosen situations. None of the wind field models cause consistently the highest or lowest DEM throughout the responses and stability conditions considered.

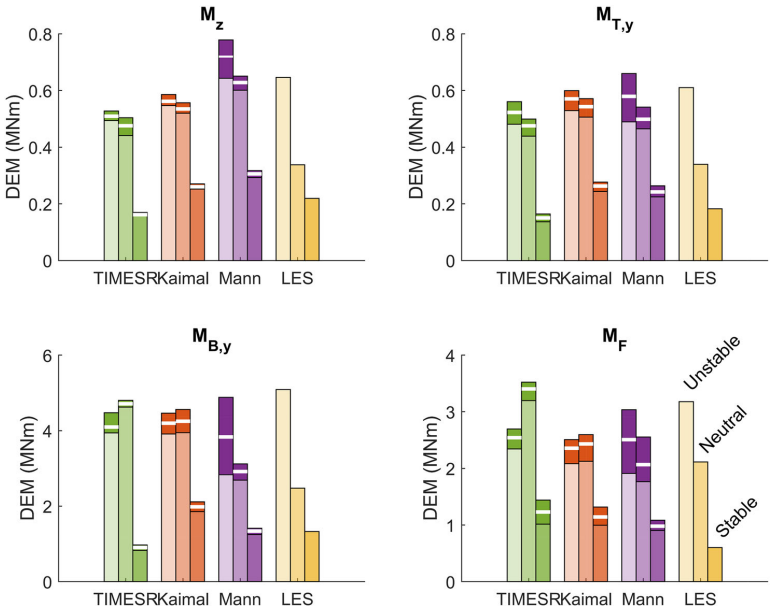


**FIGURE 14** Damage equivalent moments of the low-pass filtered response time series for three input stability conditions at 12.5 m/s. The range (dark) and mean (white lines) of six 1-hr realizations are shown [Colour figure can be viewed at wileyonlinelibrary.com]

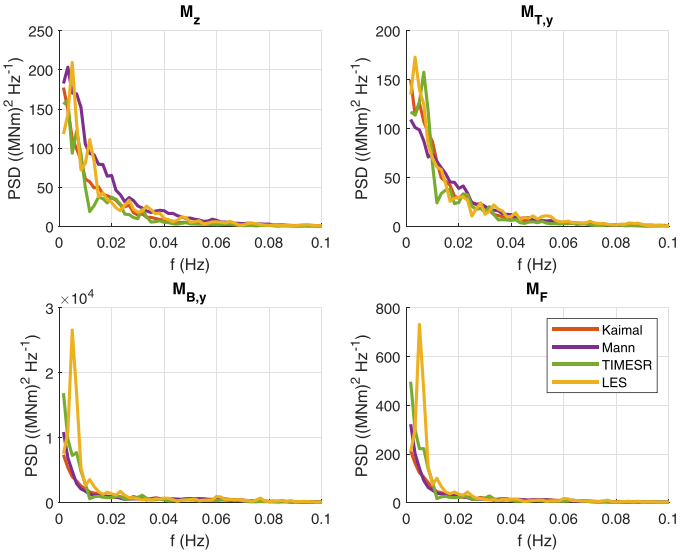


**FIGURE 15** Response spectra of the wind turbine subject to wind fields of 12.5 m/s and unstable atmospheric conditions. The mean spectra of six 1-hr realizations are shown. PSD = power spectral densities. Frequency step, $\Delta f = 0.0017$ Hz [Colour figure can be viewed at wileyonlinelibrary.com]

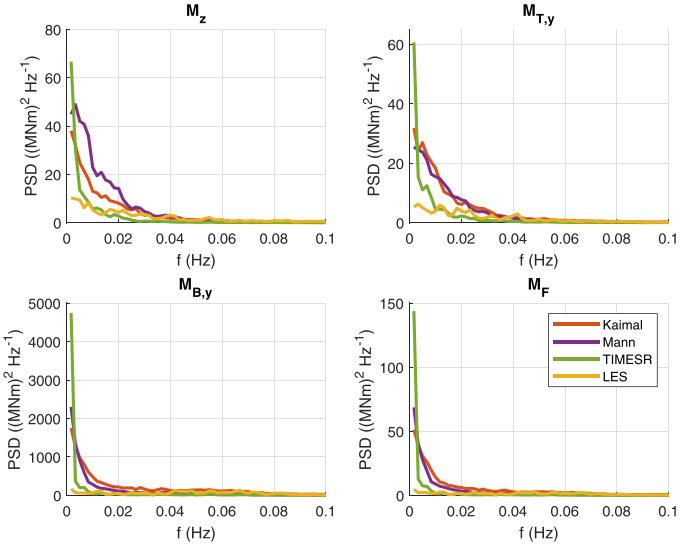


**FIGURE 16** Response spectra of the wind turbine subject to wind fields of 12.5 m/s and stable atmospheric conditions. The mean spectra of six 1-hr realizations are shown. PSD = power spectral densities. Frequency step, $\Delta f = 0.0017$ [Colour figure can be viewed at wileyonlinelibrary.com]

In agreement with Section 3.3, one sees that the TI has a strong impact on response. The LES wind field has a very low TI in the neutral situation, which is reflected in all the DEM and spectral responses, especially in the frequency range 0.005–0.03 Hz.

It is also clear that the shape of the wind spectra have great impact on the response. In the unstable situation, a distinct behaviour of LES across the spectral responses is again obvious. In contrast to the responses of other input wind fields, LES predicts a peak in response at a frequency higher than 0.0017 Hz (lowest frequency in spectrum). The same shift of energy towards higher frequencies is seen in the wind spectra

(Figure 2, left). For the stable situation (Figure 16), one observes that the responses in the LES wind field are lower than in the other wind fields. This is a consequence of the lower spectral densities of the wind spectra, see Figure 2. However, the co-coherence of LES in the stable situation is also very low, being close to zero for most frequencies (Figure 3). As illustrated in Figure 10, low coherence at small separation distances are associated with small uncorrelated eddies, which will contribute to overall low dynamic moments. The low coherence of TIMESR at frequencies above 0.0017 Hz in the stable situation (Figure 3), cause corresponding low responses of the TIMESR input wind field. TIMESR and LES take the atmospheric stability conditions in the wind modelling into account to a larger extent than Kaimal and Mann. In contrast to Kaimal and Mann, where only the TI and shear are adapted when they are referred to as stable or unstable, TIMESR and LES adapt also the turbulence and coherence to the given stability. This seems to greatly impact the quasi-static response in the stable situation.

Considering all models and stability conditions, the Mann wind fields result in highest DEM of $M_z$. The spectral amplitudes of $M_z$ in Mann are significantly higher at frequencies below 0.045 Hz compared to the spectral amplitudes in other wind fields (Figure 7,15 and 16 (all left top)). This is expected considering its low horizontal co-coherence, see Section 3.3, Putri et al.[12] and Doubrawa et al.[11] The wind fields W4 and W6 demonstrate that wind fields with low horizontal co-coherence cause high yaw moments, see Figure 9 (top), which is also illustrated in Figure 10. There is, however, a very low co-coherence of TIMESR in the stable situation as well, but this does not result in a consistently high $M_z$. This may indicate that the negative horizontal co-coherence, present in Mann but not TIMESR, has a strong impact on $M_z$.

$M_{T,y}$ is expected to be influenced by the vertical co-coherence, which is similar across wind field models (Figure 3). Figures 7,15 and 16 (all right top) show that the corresponding response spectra follow each other closely with the exceptions in LES and TIMESR already mentioned.

The $M_{B,y}$ spectra (Figures 7,15 and 16 (all left bottom)) are heavily influenced by the shape of the wind spectra in unstable and neutral conditions. There are strong similarities, especially at the lowest frequencies. Figure 14 shows that higher frequencies matter for the DEM despite the high spectral densities at the very low frequencies. One, for example, observes higher spectral densities of Kaimal than Mann at higher frequencies in all stability conditions, which leads to higher total damage. From Figure 3, one observes that Mann has highest co-coherence at very low frequencies, but Kaimal at higher frequencies. Figure 9 showed that more co-coherence cause more response at the tower bottom, explaining the differences of Mann and Kaimal. This is in contradiction to the findings of Putri et al.[12] and Bachynski and Eliassen,[10] who did not see any significant effect of co-coherence on the response in Mann versus Kaimal in $M_{B,y}$. These studies are not directly comparable to the present study, as they focus on floating wind turbines subject to waves with corresponding platform movements.

The wind spectra in neutral and unstable situations seem to influence $M_F$ even stronger (Figures 7,15 and 16 (all right bottom)). One sees clear similarities between the response spectra of $M_{B,y}$ and $M_F$, but the very low frequencies seems to be dominating for the DEM of $M_F$. When comparing the responses at low frequencies, one should keep in mind the relatively large statistical uncertainty.

## 4 | CONCLUSIONS

In this study, focus is on the low-frequency response of a bottom-fixed offshore wind turbine. The effect of various turbulence models are studied. First, the wind spectra and coherence of the input wind fields, Kaimal, Mann, TIMESR and LES are compared. The turbulence models are fitted to an unstable, a neutral and a stable common situation offshore. The wind characteristics of the neutral and unstable situations are found to be very similar, while the stable situation has larger shear, lower TI and less coherence.

Next, the importance of the low-frequency, quasi-static response for some key response quantities is evaluated. The responses considered cover the tower top yaw moment, the tower top fore-aft bending moment, the tower bottom fore-aft bending moment and the blade root flapwise bending moment. The quasi-static response is shown to have a significant contribution to the DEM of these responses. The importance of the low-frequency region is higher at the tower bottom and blade root than at the tower top.

The stochastic variation of the response is furthermore evaluated with a focus on the quasi-static frequency region. The number of realizations of simulations recommended by the IEC is considered to be too uncertain for the present analysis. A total of 6 hr wind field simulations are therefore performed for Kaimal, Mann and TIMESR in order to simulate the response.

In order to identify the reasons for the differences in responses using Kaimal, Mann, TIMESR and LES, the impacts of shear, turbulence and coherence on response are analysed separately. Shear is found to have negligible impact in the low-frequency region, while increased turbulence level generally increases the response in the whole frequency range. With increasing co-coherence, the tower top yaw and bending moments are reduced, while the tower bottom and blade root bending moments are increased. The quad-coherence has negligible impact on the response parameters considered.

In this study, the wind shear, TI and wind spectra of Kaimal and Mann are alike, yet there are significant differences in response. These are explained by the differences in turbulence and coherence formulations. The co-coherence of Mann is low compared to Kaimal, even negative at some frequencies. This explains the lower response in Mann wind compared to Kaimal at the tower bottom and blade root. It is likely that the high yaw response in Mann is also related to its low and negative co-coherence, specifically between horizontal separation distances.

In agreement with the literature, this study shows that the response of the structure in Kaimal and Mann differ. Compared to the other considered models, LES and TIMESR, however, Kaimal and Mann give quite similar results. TIMESR, for example, stands out giving high DEM in the

tower bottom and blade root in the neutral and unstable situations. The shape of the response spectra of the tower bottom and blade root bending moments are similar to the wind spectra in these situations. Compared to other wind fields, TIMESR has very large spectral amplitudes in the lowest considered frequencies, which is reflected in the response spectra. In other words, the large variation in wind speed of large eddies observed in TIMESR cause high DEM at the tower bottom and blade root.

Compared to Mann, Kaimal and TIMESR, the wind characteristics of LES and the corresponding response differ distinctively with stability. LES has different input parameters, more complex formulations and severely increased computational costs compared to the other models. As the TI, wind shear and coherence are resulting parameters rather than inputs, it is more difficult to customize the simulations to certain situations. As an example, obtaining high enough TI in the neutral situation was difficult, which dominated the corresponding response.

The largest differences between models are found in the stable situation. In contrast to Mann and Kaimal, there are clear dependencies of stability on the response spectra of TIMESR and LES. The low response of LES and TIMESR in stable conditions is expected to be related to few energetic large eddies and corresponding insignificant forces.

The four wind field models result in large differences in the estimated DEM of the quasi-static response even when all models are fit to the same offshore situation. Thus, the choice of turbulence model is important to the fatigue life estimates in design of bottom-fixed wind turbines. A correct modelling of turbulence and coherence becomes more important with increasing rotor diameters. It is not possible to conclude which turbulence model is superior, as no full field measurements are included in the study. This study shows that the horizontal coherence impacts the response, but measurements of the actual horizontal coherence are rare.

Further work will include fitting the input parameters of the Mann model to measured data. The characteristics of the Mann wind field, such as the eddy size and lifetime may thus be fitted to given situations. Furthermore, studies will be performed on a floating wind turbine subject to the wind fields used in this study. With its low natural frequencies of the rigid body motions, even higher significance of the low-frequency region of the response spectrum is expected. The differences between the response of various wind fields are thus expected to be even clearer.

## ACKNOWLEDGEMENTS

The authors would like to thank Maylinn Haaskjold Myrtvedt for cooperation on the bottom-fixed wind turbine. Her recent paper was a great inspiration source for this work. We would also like to thank Stian Høegh Sørum for sharing his bottom-fixed DTU wind turbine model and experience with the model with us. For providing LES wind fields and associated support, we would like to thank Matthew J. Churchfield at the National Renewable Energy Laboratory. A portion of the research was performed using computational resources sponsored by the Department of Energy's Office of Energy Efficiency and Renewable Energy and located at the National Renewable Energy Laboratory. We would like to thank Etienne Cheynet, our colleague at the Geophysical Institute, for his support on coherence modelling. Last, we would like to thank Joachim Reuder, also our colleague at the Geophysical Institute, for his support on a prior wind field study which paved the way for this work.

## PEER REVIEW

The peer review history for this article is available at https://publons.com/publon/10.1002/we.2642.

## DATA AVAILABILITY STATEMENT

The data that support the findings of this study are available from the corresponding author upon reasonable request.

## ORCID

*Astrid Nybø* https://orcid.org/0000-0002-7438-7936

## REFERENCES

1. Lee J, Zhao F, Dutton A, et al. Global offshore wind report 2020. tech. rep., Brussels: GWEC; 2020. https://gwec.net/global-offshore-wind-report-2020/. Accessed February 16, 2021.
2. International Electrotechnical Commision. IEC 61400-1 Wind energy generation systems—Part 1: Design requirements. tech. rep., Geneva: IEC; 2019. https://webstore.iec.ch/publication/26423. Accessed February 16, 2021.
3. International Electrotechnical Commision. IEC 61400-3-1:2019 Wind energy generation systems—Part 3-1: Design requirements for fixed offshore wind turbines. tech. rep., Geneva: IEC; 2019. https://webstore.iec.ch/publication/29360. Accessed February 16, 2021.
4. International Electrotechnical Commision. IEC TS 61400-3-2:2019 Wind energy generation systems - Part 3-2: Design requirements for floating offshore wind turbines. tech. rep., Geneva: IEC; 2019. https://webstore.iec.ch/publication/29244. Accessed February 16, 2021.
5. Mann J. The spatial structure of neutral atmospheric surface-layer turbulence. *J Fluid Mech*. 1994;273:141-168.
6. Kaimal JC, Wyngaard JC, Izumi Y, Coté OR. Spectral characteristics of surface-layer turbulence. *Q J Roy Meteor Soc*. 1972;98(417):563-589.
7. Myrtvedt MH, Nybø A, Nielsen FG. The dynamic response of offshore wind turbines and their sensitivity to wind field models. *J Phys Conf Ser*. 2020;1669:12013.
8. Eliassen L, Bachynski EE. The effect of turbulence model on the response of a large floating wind turbine. In: *ASME 2017 36th Int Conf Ocean, Offshore and Arctic Engineering*. Trondheim, Norway; 2017:1-10. https://doi.org/10.1115/OMAE2017-61179

9. Godvik M. Influence of wind coherence on the response of a floating wind turbine. In: *Science meets Industry*. Stavanger, Norway; 2016:1-12. http://www.norcowe.no/doc//konferanser/2016/SMIStavangerpresentasjoner/GodvikStatoilInfluenceofthewindcoherenceontheresponseofafloatingwindturbine.pdf
10. Bachynski EE, Eliassen L. The effects of coherent structures on the global response of floating offshore wind turbines. *Wind Energy*. 2019;22(2):219-238.
11. Doubrawa P, Churchfield MJ, Godvik M, Sirnivas S. Load response of a floating wind turbine to turbulent atmospheric flow. *Appl Energ*. 2019;242:1588-1599. https://doi.org/10.1016/j.apenergy.2019.01.165
12. Putri RM, Obhrai C, Jakobsen JB, Ong MC. Numerical analysis of the effect of offshore turbulent wind inflow on the response of a spar wind turbine. *Energies*. 2020;13(10):1-22. https://doi.org/10.3390/en13102506
13. Putri RM, Obhrai C, Knight JM. Offshore wind turbine loads and motions in unstable atmospheric conditions. *J Phys Conf Ser*. 2019;1356:12016.
14. Holtslag MC, Bierbooms WM, van Bussel GJW. Wind turbine fatigue loads as a function of atmospheric conditions offshore. *Wind Energy*. 2016;19(10):1917-1932.
15. Hanssen-Bauer W, de Vaal JB, Tutkun M, Asmuth H, Ivanell S, Stenbro R. Dependence of wind turbine loads on inlet flow field. *J Phys Conf Ser*. 2020;1618:62065.
16. Argyriadis K. Validation of turbulence models - DNV GL. https://www.dnvgl.com/cases/validation-of-turbulence-models-86603. Accessed February 16, 2021; 2016.
17. Eliassen L, Jakobsen JB, Obhrai C. The effect of atmospheric stability on the fatigue life of offshore wind turbines. In: *Proc 22nd Int Offshore and Polar Engineering Conf*. Rhodes, Greece; 2012:330-336. https://www.onepetro.org/conference-paper/ISOPE-I-12-206
18. Nybø A, Nielsen FG, Reuder J, Churchfield M, Godvik M. Evaluation of different wind fields for the investigation of the dynamic response of offshore wind turbines. *Wind Energy*. 2020;23(9):1810-1830.
19. FuE-Zentrum FH Kiel GmbH. FINO1: Forschungsplattformen in Nord- und Ostsee Nr. 1. http://www.fino1.de/en/. Accessed February 16, 2021; 2019.
20. Nybø A, Nielsen FG, Reuder J. Processing of sonic anemometer measurements for offshore wind turbine applications. *J Phys Conf Ser*. 2019;1356:12006.
21. Jonkman BJ. TurbSim User's Guide v2.00.00. tech. rep., Golden: NREL; 2016.
22. Davenport AG. The spectrum of horizontal gustiness near the ground in high winds. *Q J Roy Meteor Soc*. 1961;87(372):194-211.
23. Kristiansen MB. Mann 64bit turbulence generator. https://www.hawc2.dk/download/pre-processing-tools. Accessed February 16, 2021; 2018.
24. Churchfield M, Lee S, Moriarty P. Overview of the Simulator fOr Wind Farm Application (SOWFA). tech. rep., NREL; 2012. https://www.nrel.gov/wind/nwtc/assets/pdfs/sowfa-tutorial.pdf. Accessed February 16, 2021.
25. Robertson A, Sethuraman L, Jonkman J, Quick J. Assessment of wind parameter sensitivity on ultimate and fatigue wind turbine loads. NREL/CP-5000-70445, NREL; 2018. https://www.nrel.gov/docs/fy18osti/70445.pdf. Accessed February 16, 2021.
26. Shaler K, Jonkman J, Doubrawa P, Hamilton N. FAST.farm response to varying wind inflow techniques. NREL/CP-5000-72893, NREL; 2019. https://www.nrel.gov/docs/fy19osti/72893.pdf. Accessed February 16, 2021.
27. Veers PS. Three-dimensional wind simulation, Sandia National Laboratories; 1988. https://prod-ng.sandia.gov/techlib-noauth/access-control.cgi/1988/880152.pdf. Accessed February 16, 2021.
28. Eliassen L, Obhrai C. Coherence of turbulent wind under neutral wind conditions at FINO1. *Enrgy Proced*. 2016;94:388-398.
29. Saranyasoontorn K, Manuel L, Veers PS. A comparison of standard coherence models for inflow turbulence with estimates from field measurements. *J Sol Energ-T ASME*. 2004;126(4):1069-1082.
30. Bak C, Zahle F, Bitsche R, et al. The DTU 10-MW reference wind turbine. tech. rep., DTU; 2013. http://orbit.dtu.dk/ws/files/55645274/The_DTU_10MW_Reference_Turbine_Christian_Bak.pdf. Accessed February 16, 2021.
31. Bachynski EE, Ormberg H. Hydrodynamic modeling of large-diameter bottom-fixed offshore wind turbines. In: *Proc Int Conf OMAE*. St. John's, Newfoundland, Canada; 2015:1-9. https://doi.org/10.1115/OMAE2015-42028
32. Sørum SH, Krokstad JR, Amdahl J. Wind-wave directional effects on fatigue of bottom-fixed offshore wind turbine. *J Phys Conf Ser*. 2019;1356:12011.
33. Hermundstad OA. Sima—SINTEF. https://www.sintef.no/programvare/sima/. Accessed February 16, 2021.
34. Welch PD. The use of fast Fourier transform for the estimation of power spectra: A method based on time averaging over short, modified periodograms. *IEEE Trans Audio Electroacoust*. 1967;15(2):70-73.
35. International Electrotechnical Commision. IEC TS 61400-13: wind turbine generator systems—Part 13: Measurement of mechanical loads. tech. rep., IEC; 2015. https://webstore.iec.ch/publication/23971. Accessed February 16, 2021.
36. Niesłony A. Determination of fragments of multiaxial service loading strongly influencing the fatigue of machine components. *Mech Syst Signal Pr*. 2009;23(8):2712-2721.
37. Stewart G, Lackner M, Haid L, Matha D, Jonkman J, Robertson A. Assessing fatigue and ultimate load uncertainty in floating offshore wind turbines due to varying simulation length. In: *Proc 11th Int Conf Structural Safety and Reliability, ICOSSAR 2013*. New York, United States; 2013:1-8. https://doi.org/10.1201/b16387-33
38. Bergami L, Gaunaa M. Analysis of aeroelastic loads and their contributions to fatigue damage. *J Phys Conf Ser*. 2014;555:12007.
39. Bendat JS, Piersol AG. *Random Data: Analysis and Measurement Procedures*. California, United States: John Wiley & Sons; 1971.
40. Cheynet E. Wind field simulation (the fast version). https://doi.org/10.5281/ZENODO.3774136. Accessed Feburary 16, 2021; 2020.
41. Cheynet E, Jakobsen JB, Snæbjörnsson J, et al. Application of short-range dual-Doppler lidars to evaluate the coherence of turbulence. *Exp Fluids*. 2016;57:1-17.


**How to cite this article:** Nybø A, Nielsen FG, Godvik M. Quasi-static response of a bottom-fixed wind turbine subject to various incident wind fields. *Wind Energ*. 2021;1–19. https://doi.org/10.1002/we.2642

# Paper 4

## Analysis of turbulence models fitted to site, and their impact on the response of a bottom-fixed wind turbine

Nybø A, Nielsen FG and Godvik M
*J. Phys. Conf. Ser.*, **2018/012028** (2021)

# Analysis of turbulence models fitted to site, and their impact on the response of a bottom-fixed wind turbine

**A Nybø[1], FG Nielsen[1] and M Godvik[1,2]**

[1] Geophysical Institute, and Bergen Offshore Wind Centre, University of Bergen, Norway
[2] Equinor, Bergen, Norway

E-mail: astrid.nybo@uib.no

**Abstract.** This study compares a wind field recommended by the wind turbine design standards to more realistic wind fields based on measurements. The widely used Mann spectral tensor model with inputs recommended by the standard, is compared to FitMann, the Mann model with inputs fitted to measurements and TIMESR; using measured time series combined with the Davenport coherence model. The Mann model produces too low energy levels at the lowest frequencies of the wind spectra, while the wind spectra generated by FitMann approaches the measured values. TIMESR reproduces the measured spectral values at all frequencies. The different models give similar vertical coherence, while the Mann and FitMann models give lower horizontal coherence than TIMESR. Investigating the wind loads on a bottom-fixed 10-MW wind turbine, the spectra for the tower bottom fore-aft and blade root flapwise bending moment follow the shape of the wind spectra closely at low frequencies. The low-frequency range is important for the blade root and in particular the tower bottom bending moment. Thus, the TIMESR model, followed by FitMann, is assumed to give the most accurate fatigue estimates. For the specific situation analysed in this study, the FitMann model gives only 18 and 5 % lower estimates than TIMESR of the tower bottom and blade root damage equivalent bending moments, while the Mann model gives 27 % and 12 % lower estimates. The tower top yaw and fore-aft bending moments depend on the wind coherence. For the specific situation analysed in this study, the FitMann model gives 9 and 5 % higher estimates of the tower top yaw and tower top damage equivalent (bending) moments compared to TIMESR, while the Mann model gives 23 % and 18 % higher estimates. Since only measurements of the vertical coherence are available, it is not clear which model is superior for the tower top moments. However, the importance of a proper coherence model is documented.

## 1. Introduction

In the design of wind turbines, turbulence models are used to simulate wind fields for load estimation. The International Electrotechnical Commission (IEC) wind turbine design standards [1–3] recommend e.g. the Mann spectral tensor model [4] for this purpose. The IEC standards further recommend a set of input parameters to this model, where only the turbulence intensity and wind profile are fit to actual site conditions.

The trends in the wind industry point towards larger rotor sizes and an increasing interest for offshore locations. These trends are partly connected, as the largest wind turbines are placed offshore due to easier blade transportation. Offshore, weather conditions are harsher and the total structural loads higher. With larger rotors, a larger variation in wind characteristics over

**Table 1.** Summary of wind field characteristics of the chosen situation.

| | |
|---|---|
| Hub mean wind speed | 12.4 m/s |
| Hub turbulence intensity | 6 % |
| Power law exponent | 0.06 |
| Stability | Neutral |

the swept area is expected. Therefore, a correct representation of turbulent wind becomes more important. In this context, the standard Mann model is challenged.

Fitting the input parameters of the Mann model to actual site conditions may serve as an alternative to easily adapt an existing well known model to various conditions, without adding time, cost and complexity excessively. This has been performed in academia to a large extent (e.g. by Mann [5], Sathe et al. [6], de Maré and Mann [7], Cheynet et al. [8, 9], Peña et al. [10, 11] and Chougule et al. [12–14]). Chougule et al. [13, 14] developed the Mann model further to account for buoyancy effects, requiring additional input parameter(s). The wind industry also challenges the widely used turbulence models recommended by the standard, as they are made for small turbines and for flow over flat terrain in neutral atmospheric conditions [15]. Fitting of the Mann parameters gives opportunities for evaluating the design of wind turbines in e.g. various atmospheric stability conditions. Even within neutral stability conditions, fitting of Mann to measurements may alter the corresponding response as compared to using the input parameters recommended by the IEC standard.

In this study, a fitting of the input parameters of the Mann model to neutral offshore conditions is performed, and the corresponding response of an offshore wind turbine is evaluated. This model, hereafter denoted FitMann, is compared to the Mann model with standard inputs, hereafter denoted Mann, and another easily available and fast turbulence model closely based on measurements, hereafter denoted TIMESR [16]. The latter model is originally based on Veer's model from 1988 [17], and uses time series and coherence parameters obtained from measurements as inputs. The turbulent structures of the wind fields generated by Mann, FitMann and TIMESR are evaluated in terms of the wind spectrum and coherence. The wind fields are used as inputs in a simulation tool for wind turbine design purposes, and the corresponding response is evaluated. The simulations are performed on a 10-MW bottom-fixed wind turbine. It is previously found [18] that the quasi-static response is important for the overall response, especially for the tower bottom and blade root flapwise bending moment. The response, in terms of response spectra and damage equivalent moments, is therefore evaluated with a special focus on frequencies below 0.1 Hz, hereafter denoted the low-frequency region. The mentioned literature covers fitting of the Mann model to various stability conditions over a range of different surfaces, but none of them compare the corresponding wind turbine response to the response obtained by using wind fields from other turbulence models.

## 2. Data and methods

### *2.1. Wind fields*

Measurements from the offshore meteorological mast FINO1, located in the North Sea, are used as basis in this study. Sonic anemometers provide high-frequent measurements of the wind speed at several heights, which are processed according to Nybø et al. [19]. The TIMESR, Mann and FitMann models are used to create wind fields based on point measurements from three anemometers separated vertically in the range 40-80 meters above sea-level.

In the present study, only one specific wind condition is considered, see Table 1. The result from this specific case is thus not valid as life-time evaluation of the wind turbine, including

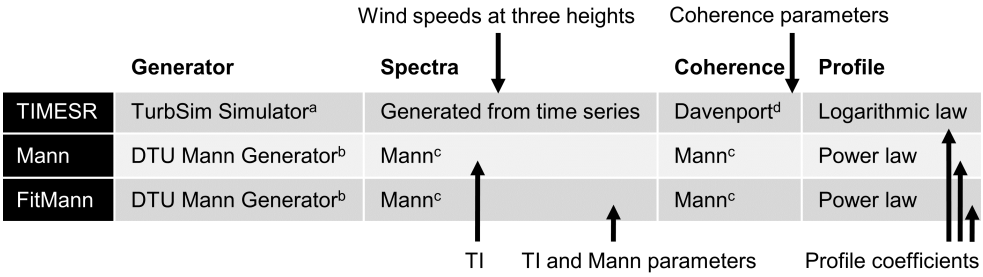


**Figure 1.** Scheme of wind field models, simulation software, spectra and coherence models and profile laws. Inputs from the FINO1 measurements are illustrated by the arrows. a from Jonkman [16], b from DTU Wind Energy [21], c from Mann [4] and d from Davenport [22].

**Table 2.** Input parameters to the DTU Mann Generator.

| Model | $\alpha\epsilon^{2/3}(m^{3/4}s^{-2})$ | $L(m)$ | $\Gamma$ |
|---|---|---|---|
| Mann | 0.0229 | 33.6 | 3.9 |
| FitMann | 0.0168 | 73.6 | 3.8 |

all relevant wind speeds, atmospheric stability conditions etc. The chosen situation is almost stationary for one hour and has close to neutral stratification. The specific condition is thus well suited to be modelled by the numerical wind field models included in this study. The buoyancy term is not included in the Mann model as it is defined in the IEC standards and used by the offshore wind industry. It can therefore not simulate stable or unstable atmospheric conditions by definition. A mean wind speed just above rated wind speed is selected as this is considered crucial to the fatigue damage to the structure. The chosen situation has a typical turbulence intensity for the given wind speed at FINO1. The wind shear is rather low, even for offshore conditions. Türk et al. [20] found a power law coefficient of approximately 0.1 for the relevant wind speed at FINO1, and considerably lower for unstable atmospheric conditions. This indicates that the near-neutral atmospheric conditions of the chosen situation may be closer to unstable than stable.

The three wind fields are generated according to Figure 1. TIMESR uses time series from 40, 60 and 80 m above sea-level as input, creating spectra equal to the measured spectra at the input heights. The Davenport coherence model is applied in TIMESR, with parameters obtained from the coherence in the measurements. The profile coefficients (power law exponent of the power law and surface roughness of the logarithmic law) are found from the measured mean wind speeds at 40 and 80 m. The vertical mean velocity profiles obtained by the three models are very similar, even if different formulations of the vertical profile are used.

The turbulence characteristics of the wind fields generated by Mann are dependent on only three input parameters, namely the Kolmogorov constant multiplied with the rate of the viscous dissipation of specific turbulent kinetic energy to the two thirds, $\alpha\epsilon^{2/3}$, the length scale, $L$, and the non-dimensional parameter related to the lifetime of the eddies, $\Gamma$. IEC recommends $L$ and $\Gamma$ values according to the first row of Table 2 for wind turbines with hub heights higher than 60 m. $\Gamma = 0$ corresponds to isotropic turbulence and the von Kármán turbulence spectrum. Increasing $\alpha\epsilon^{2/3}$, moves the entire wind spectrum to higher energy levels, while increasing $L$ and

$\Gamma$ rather increases the energy level at low frequencies.

In Mann, as used in this study, the $L$ and $\Gamma$ given by the IEC wind turbine design standard are used. The standard recommends that $\alpha\epsilon^{2/3}$ is calculated according to Equation 1 [1, 4].

$$\alpha\epsilon^{2/3} = \frac{55}{18} * 0.4754 * \sigma_{iso}^2 l^{-2/3}. \tag{1}$$

The length scale parameter, $l$, is given by 0.8 times the turbulence scale parameter, $\Lambda_1$, which is 42 m for large wind turbines (hub height $\geq$ 60 m). The unsheared, isotropic variance, $\sigma_{iso}$, is according to the IEC standard given as 0.55 times the variance of the wind speed in the mean wind direction, $\sigma_1$. In the wind field generated by Mann in this study, $\sigma_1$ is calculated from the turbulence intensity, $TI$, and the wind speed, $\overline{u}_m$, of the measured time series, according to Equation 2.

$$\sigma_1 = TI * \overline{u}_m. \tag{2}$$

In FitMann, $\alpha\epsilon^{2/3}$, $L$ and $\Gamma$ are determined in order to fit the spectra generated by Mann to the spectra of the measured data at 80 m [23]. All Mann parameters are fitted simultaneously to the spectra of u, v, w and the real part of the cross spectrum of uw. A non-linear least-square fit is used. The spectrum and coherence still follow Mann formulations, thus the wind spectra of measurements are not reproduced as in TIMESR. The spectra of the time series at 80 m are estimated using Welch's algorithm [24] with a Hamming window, six segments, and 50 % overlapping. The spectra are bin averaged [25] before the fitting is performed. There is large uncertainty related to the very first frequency of the wind spectra, 0.0017 Hz, as it is only realized once within each block of the FFT. This frequency is still included in the fitting procedure, as it is important for response, and this study aims to achieve wind fields with similar characteristics and corresponding response as the measured time series.

The input parameters of Mann and FitMann are given in Table 2. The very large length scale obtained by FitMann moves the wind spectra to higher energy levels at low frequencies. This also indicates that the wind field is closer to a slightly unstable than a slightly stable situation. In order to conserve the total energy, the energy levels at higher frequencies are consequently reduced in the spectrum generated by FitMann, reflected in the lower $\alpha\epsilon^{2/3}$ as compared to the spectrum generated by Mann. The $\alpha\epsilon^{2/3}$ of Mann is found according to Equation 1.

All wind fields are generated with similar domain sizes, covering the entire rotor. The grid size in the rotor plane is 3.5 m, and the time step is about 0.1 s. Six realizations of one hour each are run for TIMESR, Mann and FitMann in order to reduce statistical uncertainty. A previous study [18] found that the IEC recommendation [1] of a total of one hour simulation is insufficient when comparing the responses, in particular in the low-frequency region. The results presented in this study correspond to the mean of the six 1-hour realizations.

We analyse the variations in turbulent structures in the wind fields generated by TIMESR, Mann and FitMann by their spectra and coherence. The turbulence intensities and wind profiles obtained by the different methods are similar to the values given in Table 1. The wind spectra are estimated as outlined above.

The root-coherence is calculated from the cross-spectrum, $S_{xy}$, and the auto-spectra, $S_{xx}$ and $S_{yy}$, of two time series separated in space, according to Equation 3.

$$|\gamma| = \frac{|S_{xy}|}{\sqrt{S_{xx}S_{yy}}}. \tag{3}$$

Only the real part of the coherence ($\mathrm{Re}(\gamma)$) of the wind speed in the along wind direction is considered in this study. In other words, the uu-co-coherence is referred to as simply coherence. The imaginary part of the coherence, the quad-coherence ($\mathrm{Im}(\gamma)$), is disregarded. In TIMESR,

the Davenport coherence model is used, according to Equation 4.

$$\gamma = \exp\left( - C * \frac{f\delta}{\overline{u}_m} \right). \tag{4}$$

The Davenport coherence model is dependent on frequency, $f$, separation distance between the two considered time series, $\delta$, mean wind speed, $\overline{u}_m$, and a decay coefficient, $C$. In TIMESR, the decay coefficients of the u, v and w components are calculated from the time series of FINO1 separated vertically.

The wind characteristics described by the wind spectra and the coherence influence the response of the wind turbine. The response in the low-frequency region is mainly quasi-static. The shape of the wind spectrum is expected to have strong impact on the response spectra of the blade root and tower bottom bending moments, as discussed in more detail in Nybø et al. [18].

Considering coherence of separation distances of about 0.5-1 rotor diameter, we can expect the following. In a fully coherent wind field, a homogeneous load hits the rotor, causing large bending at the tower bottom. The same is seen for a homogeneous load hitting the blade causing large moments at the blade root. With lower coherence, loads will partly cancel out and therefore cause low bending at the tower bottom, while high local moments at the tower top. Low horizontal coherence is expected to cause high yaw moments, while low vertical coherence is expected to cause high fore-aft moments at the top.

### *2.2. Response*

The aero-hydro-servo-elastic tool, SIMA [26], is used for the wind turbine simulations. The interactions between the wind and the turbine are in this simulation tool computed using the blade element momentum theory. The different wind fields are used as inputs to SIMA, and the various responses are given as outputs.

The analyses are performed on the DTU reference turbine with a bottom-fixed foundation [18]. This wind turbine has a rated power of 10 MW, a rated wind speed of 11.4 m/s, a hub height 119 m and a diameter of 178.3 m [27].

The tower top yaw moment, $M_z$, the tower top bending moment fore-aft, $M_{T,y}$, the tower bottom bending moment fore-aft, $M_{B,y}$, and the blade root flapwise bending moment, $M_F$, are considered in this study. Side-side moments are excluded as these are much smaller than the fore-aft moments when subject to only wind loads. No sea waves are present in the simulations. In this study, only the dynamic response of the wind turbine is analysed. Mean values are not assessed.

The response spectra and damage equivalent moments are presented in the following. The response spectra are obtained using the same procedure as for the wind spectra. The damage equivalent moments, referred to as DEM, indicate the wind loads' impact on the structural fatigue. The DEM is calculated according to Equation 5, where $R_i$ is the amplitudes of the response time series, $n_i$ is the corresponding numbers of cycles, and $m$ the Wöhler curve exponent of the material [28]. Rainflow counting is used to isolate and define cycles into individual events. The obtained equivalent moment, $R_{eq}$, is related to the equivalent number of load cycles in the length of the time series, $n_{eq}$, assuming a frequency of 1 Hz for the equivalent load process.

$$R_{eq} = \left( \frac{\Sigma_i (R_i^m n_i)}{n_{eq}} \right)^{1/m}. \tag{5}$$

In this study, the value of m is 10 (composite material) for the calculation of the blade equivalent moment and 3 (steel) for the calculation of the tower equivalent moments. It should be kept in mind that the differences across methods obtained in this study would be even larger if one rather compared the fatigue lifetime of the structure.

It is found in a previous study [18] that the low-frequency region (f < 0.1 Hz) has major impact on the total DEM of the wind turbine for the current configuration. The low frequencies were found to be of particular importance for the tower bottom and blade root flapwise bending moment. In the following we thus focus on the low-frequency response. These values are found by low-pass filtering the response time series at 0.1 Hz prior to calculating the DEM.

## 3. Results and discussion

### *3.1. Wind fields*

The wind fields generated by TIMESR, Mann and FitMann are compared to each other, and to measurements where possible. All wind fields have equivalent turbulence intensity and mean wind speed profile, thus only the turbulent structures are compared.

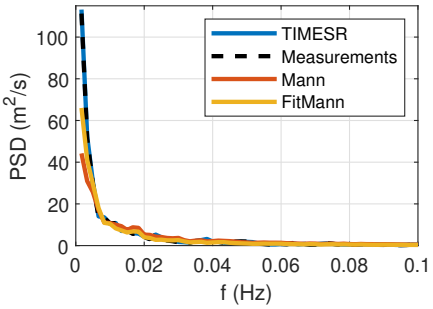


**Figure 2.** Wind spectra at 80 m for f < 0.1 Hz in *linear* scales. PSD = Power spectral densities. Frequency step, Δf = 0.0017 Hz.

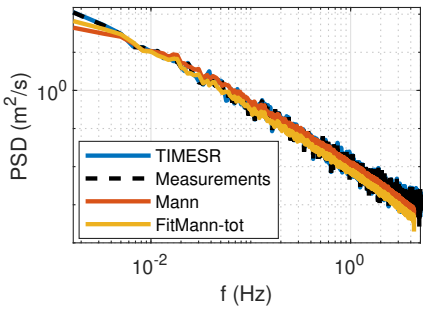


**Figure 3.** Wind spectra at 80 m in *logarithmic* scales. PSD = Power spectral densities. Frequency step, Δf = 0.0017 Hz.

The wind spectra at 80 m are shown in Figures 2–3. As the spectral values increase as the frequency tends to zero, the results are sensitive to the duration of the time series considered. TIMESR is able to reproduce the spectrum of measurements at 80 m with high accuracy in the complete frequency region. The spectrum generated by the Mann model has lower energy than the measurements in the lowest range of frequencies. The Mann model is made for neutral atmospheric conditions. The chosen situation seems to be closer to slightly unstable atmospheric conditions than slightly stable, with lots of energy in the very low-frequency region, a relatively high TI and a relatively low power law exponent. Compared to the wind spectrum generated by Mann, the wind spectrum generated by FitMann approaches measurements at low frequencies, which are important for response, but falls below at higher frequencies. This is according to expectations considering the input values given in Table 2. The spectra at hub height (not shown), are very similar to those shown in Figures 2–3.

The coherence of vertical separation distances is shown in Figures 4–5. As expected, the coherence of all models is high at low frequencies, corresponding to large eddies, and decays towards zero for higher frequencies and smaller eddies. The decay of coherence is similar across models for small (40 m) and large (125 m) separation distances. TIMESR, Mann and FitMann all model coherence similarly to the measurements (Figure 4), at least for frequencies below 0.05 Hz. The decay parameters of TIMESR are calculated from measurements, but the coherence is assumed to follow a simple model, Davenport. A previous study has shown that the fit to Davenport is good for neutral situations at FINO1 [29]. However, Figure 4 shows that the

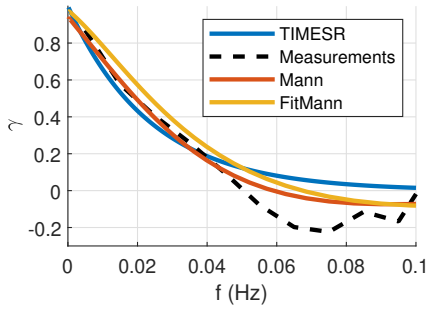


**Figure 4.** Coherence between two time series separated *vertically* by 40 m (0.22 D). The coherence of measurements is bin-averaged and the coherence of models are based on their respective formulas; thus the smooth curves.

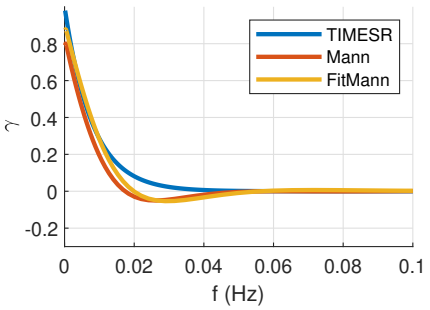


**Figure 5.** Coherence between two time series separated *vertically* by 125 m (0.7 D). The coherence of models are based on their respective formulas; thus the smooth curves.

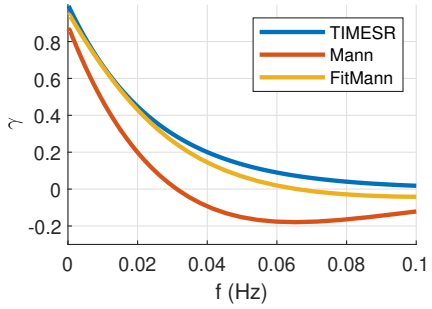


**Figure 6.** Coherence between two time series separated *horizontally* by 40 m (0.22 D). The coherence of models are based on their respective formulas; thus the smooth curves.

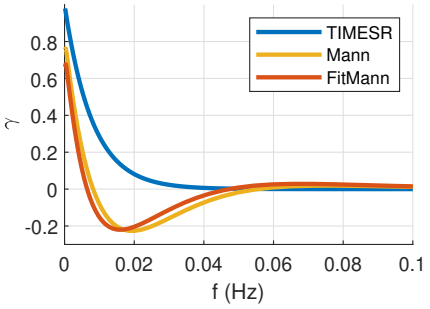


**Figure 7.** Coherence between two time series separated *horizontally* by 125 m (0.7 D). The coherence of models are based on their respective formulas; thus the smooth curves.

coherence of measurements is negative at some frequencies, which the Davenport model is not able to reproduce.

The Mann model predicts a significant quad-coherence ($\mathrm{Im}(\gamma)$) between two time series separated vertically (not shown), but it is common to disregard this imaginary part of the coherence in the literature [17, 30, 31]. A previous study [18] has shown that the assumption of minor impact of quad-coherence on the response of the current configuration (DTU 10-MW bottom-fixed, for $M_z$, $M_{T,y}$, $M_{B,y}$ and $M_F$) is fair.

Figures 6–7 show the coherence between two time series separated horizontally. No measurements are available for this case. TIMESR predicts a slowly decaying coherence, while the coherence generated by Mann decays fast to a bottom at negative values before reaching zero. At large distances (0.7 D = 125 m), the coherence generated by FitMann follows the coherence generated by Mann (Figure 7). The coherence generated by FitMann approaches the coherence

generated by TIMESR for smaller separation distances, ending up in similar coherence curves at 0.22 D = 40 m (Figure 6). Again, it should be kept in mind that TIMESR corresponds to the Davenport coherence model with decay parameters obtained from measurements separated vertically. As no measurements of horizontal coherence are considered in this study, it is not possible to determine which model predicts horizontal coherence most realistically. The value of the horizontal coherence is important for e.g. yaw loads. Thus, altering the input parameters for the Mann model may alter yaw loads, even though no direct fitting of the coherence is performed.

*3.2. Response*

The wind fields generated by TIMESR, Mann and FitMann are used as input in SIMA, and the corresponding response of the bottom-fixed wind turbine is given as output. In the following, the computed responses as obtained by using the various wind fields are compared. The low-frequency part (f < 0.1 Hz) of the response spectra is used in the comparison. The corresponding DEM allows for comparisons of the fatigue damage of the wind turbine when subject to the different wind fields. The DEM of the low-frequency and complete frequency range are assessed.

The low-frequency response spectra of the tower bottom bending moment fore-aft, $M_{B,y}$, are shown in Figure 8. TIMESR, Mann and FitMann all cause high energy levels at the very first frequencies, followed by a sharp decay. TIMESR causes higher response in $M_{B,y}$ than FitMann, which again causes higher response than Mann. There are great similarities between the wind spectra, Figure 2, and the response spectra, Figure 8, as should be expected due to the combined effect of quasi-static response and a high coherence. As shown in Figures 4–7, TIMESR generates a higher coherence than Mann and FitMann at most frequencies, also pointing towards higher tower bottom response. High coherence causes a large homogeneous force at tower top, and corresponding large moments at the tower bottom. Figures 12–15 show the DEM of the low-pass filtered response time series (f < 0.1 Hz) by squares, and the DEM of the total response time series by circles. The squares of Figure 12 confirm the trends from the response spectra; TIMESR causes the highest damage, followed by FitMann (21 % lower than TIMESR) and Mann (38 % lower than TIMESR). Low frequencies dominate for the total DEM of $M_{B,y}$, clearly shown by the small difference between the low-frequency DEM and the DEM of the total time series. This is in contrast to the other responses considered, Figures 13–15, where there are larger gaps between DEM of low and all frequencies. The differences between models are approximately the same for the low-frequency DEM and the total DEM of $M_{B,y}$ (FitMann 18 % lower than TIMESR and Mann 27 % lower than TIMESR in total DEM). A correct representation of the wind spectrum and the coherence at low frequencies are of utmost importance for a good estimation of the total DEM of $M_{B,y}$.

There are great similarities in the response of the blade root (Figures 9 and 13) and the tower bottom bending moments (Figures 8 and 12). The blade root damage equivalent bending moments of FitMann and Mann are 18 % and 39 % lower than TIMESR when considering only the low frequencies, and 5 % and 12 % when considering the whole frequency range. The shape of the wind spectra has great impact on the response of the blade root flapwise bending moment, $M_F$. Compared to the tower top, there is much more energy at the very lowest frequencies in the response spectra of $M_{B,y}$ and $M_F$. As seen from Figure 2, the wind spectrum generated by FitMann is much closer to TIMESR than Mann at the very first frequencies, but it still has significantly lower energy levels. As previously mentioned, the large energy levels at low frequencies (and the low power law exponent) of the chosen situation indicate that the near-neutral atmospheric conditions are closer to unstable than stable. If a situation with atmospheric conditions closer to neutral were chosen, the gap between TIMESR and Mann/FitMann in the energy spectrum could possibly be reduced. Consequently, a smaller gap between TIMESR and Mann/FitMann in the response of $M_{B,y}$ and $M_F$ would be expected. In order to improve

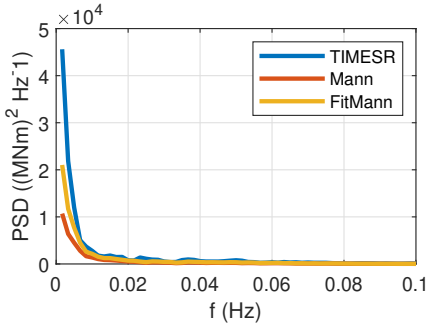


**Figure 8.** $M_{B,y}$ response spectra of the wind turbine subject to various input wind fields. PSD = Power spectral densities. Frequency step, $\Delta$f = 0.0017 Hz.

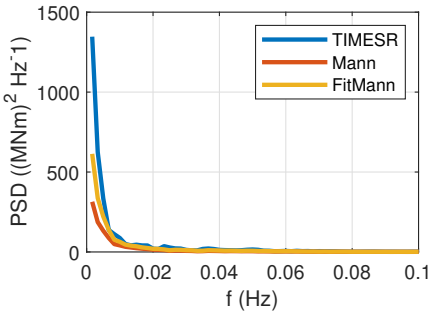


**Figure 9.** $M_F$ response spectra of the wind turbine subject to various input wind fields. PSD = Power spectral densities. Frequency step, $\Delta$ = 0.0017 Hz.

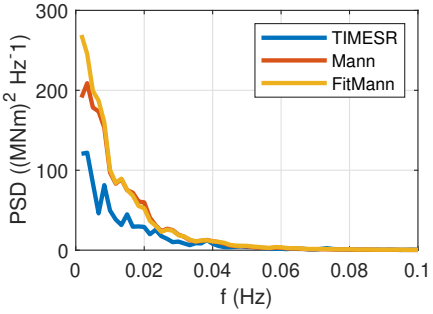


**Figure 10.** $M_z$ response spectra of the wind turbine subject to various input wind fields. PSD = Power spectral densities. Frequency step, $\Delta$f = 0.0017 Hz.

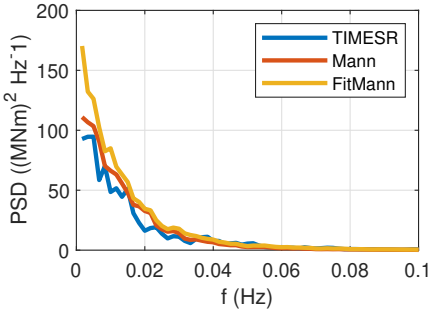


**Figure 11.** $M_{T,Y}$ response spectra of the wind turbine subject to various input wind fields. PSD = Power spectral densities. Frequency step, $\Delta$f = 0.0017 Hz.

the fit of the wind spectrum at very low frequencies, we found alternative FitMann-parameters by fitting the Mann spectrum to only the low-frequency region (f < 0.1 Hz) of measurements. The wind spectrum of the alternative fit is slightly higher at the very lowest frequencies, at the expense of a poorer fit and lower energy levels already at 0.0067 Hz and upwards. The response of $M_{B,y}$ and $M_F$ when using the wind field generated by TIMESR as input is assumed to be quite realistic as the wind spectrum of measurements is reproduced in the model, and the shape of the wind spectrum has great impact on these responses. The DEM of the total response time series of the alternative Mann fitting is further away from TIMESR than the original FitMann at both $M_{B,y}$ and $M_F$, thus the alternative Mann fitting is disregarded from further analysis.

Focusing on the tower top yaw moment, $M_z$, one observes a slower decay of the response spectra towards higher frequencies compared to the tower bottom and blade root (Figure 10). There are large differences between the response of using wind fields generated by TIMESR and the two Mann models, but minor differences between using wind fields generated by Mann and FitMann as input in the wind turbine response analysis. The response of using wind

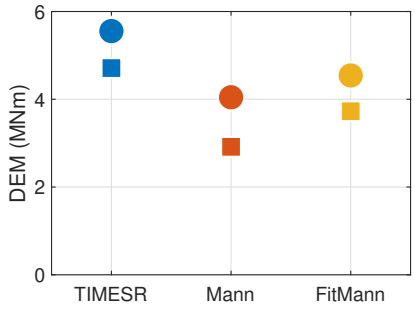


**Figure 12.** $M_{B,y}$ damage equivalent moments of the wind turbine subject to various input wind fields. □ = DEM of low frequencies (f < 0.1 Hz), ○ = DEM of all frequencies.

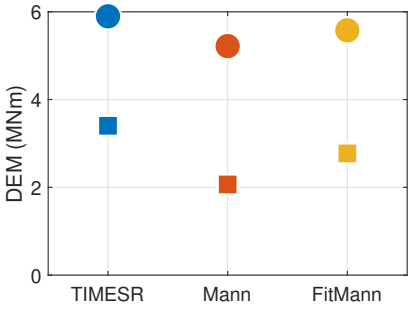


**Figure 13.** $M_F$ damage equivalent moments of the wind turbine subject to various input wind fields. □ = DEM of low frequencies (f < 0.1 Hz), ○ = DEM of all frequencies.

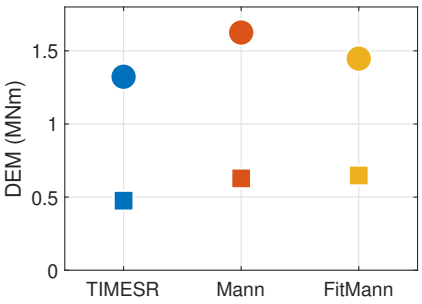


**Figure 14.** $M_z$ damage equivalent moments of the wind turbine subject to various input wind fields. □ = DEM of low frequencies (f < 0.1 Hz), ○ = DEM of all frequencies.

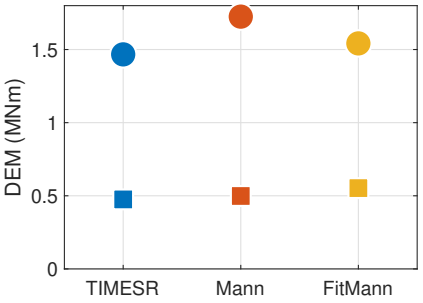


**Figure 15.** $M_{T,Y}$ damage equivalent moments of the wind turbine subject to various input wind fields. □ = DEM of low frequencies (f < 0.1 Hz), ○ = DEM of all frequencies.

fields generated by Mann or FitMann is higher compared to using the wind field generated by TIMESR for $M_z$. The yaw response is strongly impacted by the wind spectra and the horizontal coherence. Uncorrelated eddies in the horizontal direction (low coherence) cause local loads and corresponding yaw moments. Figure 7 shows that the coherence generated by Mann and FitMann is much lower than that of TIMESR at 0.7 D, and even negative at some frequencies. The coherence generated by Mann stays significantly lower than that of TIMESR for all relevant separation distances, while the coherence generated by FitMann approaches that of TIMESR towards 0.2 D. The high response of using wind fields generated by Mann and FitMann is reflected in the DEM of the low-frequency range, see Figure 14. The DEM of the low-frequency range of Mann and FitMann are 32 % and 36 % higher than TIMESR respectively. Low frequencies have less impact on the total DEM at tower top than tower bottom. This is observed by the relatively large distance between the DEM of the low frequencies and the

DEM of the complete frequency range. Considering the DEM of the complete frequency range, using the wind field generated by FitMann causes a response similar to using the wind field generated by TIMESR (FitMann 9 % higher than TIMESR), as compared to using the wind field generated by Mann (Mann 23 % higher than TIMESR). It is still not reasonable to conclude that FitMann causes a more realistic response than Mann. The yaw response is as mentioned strongly influenced by the horizontal coherence. As this study includes no measurements of the horizontal coherence, it is impossible to determine which model estimates the horizontal coherence most realistically. The resulting DEM of all frequencies of using the wind field generated by FitMann is closer to the resulting DEM of using the wind field generated by TIMESR as compared to using the wind field generated by Mann, probably because of the lower energy levels at frequencies higher than 0.1 Hz in the wind spectrum. The rotation frequencies (3P, 6P, 9P etc.) have larger impact on the response at tower top than at tower bottom. The higher coherence generated by FitMann at smaller separation distances may also have an impact on the response at higher frequencies.

There are great similarities in the response of the tower top bending moment fore-aft (Figures 11 and 15) and the tower top yaw moment (Figures 10 and 14). Low coherence is expected to cause high response of both. The tower top bending moment fore-aft, $M_{T,y}$, is stronger influenced by the vertical coherence, which is quite similar across methods. This is reflected in the response, where there are slightly less differences in the fore-aft response than yaw. The $M_{T,y}$ DEM of FitMann and Mann are 16 % and 5 % higher than TIMESR when considering only the low frequencies, and 5 % and 18 % when considering the whole frequency range. Following the same logic as for the tower top yaw, uncorrelated eddies in the vertical direction (less vertical coherence) cause local loads and corresponding fore-aft moments at the tower top.

## 4. Conclusions and further work

In this study, we have modelled offshore wind fields using various techniques and by fitting parameters using measured wind data. The wind field generated by TIMESR is closely based on measurements, the wind field generated by Mann is made with only TI fitted to site, while the wind field generated by FitMann is based on the same model as Mann, but with input parameters fitted to the wind spectra of measurements. The three models are compared in terms of spatial and temporal distribution of turbulent structures, before they are used as input in wind turbine simulations. As expected, the wind spectrum generated by TIMESR reflects the measurements better than the wind spectrum generated by Mann with standard parameters. The Mann model does not reach the high energy levels of measurements at low frequencies. The wind spectrum generated by FitMann approaches the wind spectrum generated by TIMESR at low frequencies, important for response, while it falls below at very high frequencies. The findings are based on wind fields fitted to one hour of measurements. The trends of the results are still expected to be valid for most situations. FitMann will represent the wind spectrum of measurements better than Mann, due to the fitting of the input parameters. However, the quantitative differences across models will vary depending on the chosen situation. Considering coherent structures, the three models predict similar coherence between two time series separated vertically, while FitMann and especially Mann predict much lower coherence than TIMESR for time series separated horizontally.

It is clear that the low-frequency region of the wind spectra has major impact on the response of the tower bottom and blade root bending moments. TIMESR, using input time series to model wind spectra, is therefore assumed to cause the most realistic response at tower bottom and blade root. The smaller gap between the wind spectra generated by FitMann and TIMESR than Mann and TIMESR at low frequencies is reflected in the response spectra. Therefore, we conclude that using a wind field generated by FitMann as input in wind turbine design analysis

when evaluating the response of the tower bottom bending moment fore-aft and blade root flapwise bending moment of a bottom-fixed wind turbine most likely gives more realistic results than using the Mann formulation with standard parameters. Again, the quantitative differences across models will vary depending on the chosen period of measurements.

The results show that the response at low frequencies ($f < 0.1$ Hz) has major impact on the total damage equivalent moments of the tower bottom bending fore-aft. It is therefore important to model the wind spectra and coherence of these frequencies correctly in order to achieve a correct representation of the fatigue damage at tower bottom.

The measurements from the offshore mast provide no information on the coherence of time series separated horizontally, and only limited information on the coherence of time series separated vertically. Therefore, we are not able to conclude which model predicts coherence most realistically. The coherence has large impact on the response at tower top. We are not able to conclude whether using the wind field generated by FitMann as input in wind turbine design analysis when evaluating the response of the tower top yaw moment and the tower top bending moment fore-aft cause more realistic results than using the wind fields generated by TIMESR or Mann.

This study has shown that there are significant differences in response across models even when a neutral atmospheric stability situation is considered. It is expected that Mann with standard inputs is more capable of representing neutral than non-neutral situations. If fit to other stability conditions, we expect to see larger differences between models, so FitMann may improve the results even further. Further work should include a fit to unstable and stable situations in the analysis.

**Acknowledgments**
The authors would like to thank Etienne Cheynet, a colleague at Bergen Offshore Wind centre and Geophysical Institute, for his support on fitting of Mann parameters and corresponding analysis.

**References**

[1] International Electrotechnical Commission 2019 *IEC 61400-1 Wind energy generation systems - Part 1: Design requirements* (Geneva)
[2] International Electrotechnical Commission 2019 *IEC 61400-3-1 Wind energy generation systems - Part 3-1: Design requirements for fixed offshore wind turbines* (Geneva)
[3] International Electrotechnical Commission 2019 *IEC TS 61400-3-2 Wind energy generation systems - Part 3-2: Design requirements for floating offshore wind turbines* (Geneva)
[4] Mann J 1994 *J. Fluid. Mech.* **273** 141–68
[5] Mann J 1998 *Probabilist. Eng. Mech.* **13** 269–82
[6] Sathe A, Mann J, Barlas T, Bierbooms W A A M and van Bussel G J W 2013 *Wind Energy* **16** 1013–32
[7] De Maré M and Mann J 2014 *J. Phys.: Conf. Ser.* **524** 012106
[8] Cheynet E 2019 Influence of the measurement height on the vertical coherence of natural wind *Proc. of the XV Conf. of the Italian Association for Wind Engineering (Napoli)* vol 27 ed Ricciardelli F and Avossa A M (Cham: Springer) pp 207–21
[9] Cheynet E, Jakobsen J B and Obhrai C 2017 *Enrgy. Proced.* **137** 414–27
[10] Peña A, Gryning S E, Mann J and Hasager C B 2010 *J. Appl. Meteorol. Clim.* **49** 792–806
[11] Peña A, Gryning S E and Mann J 2010 *Q. J. Roy. Meteor. Soc.* **136** 2119–31
[12] Chougule A, Mann J, Segalini A and Dellwik E 2015 *Wind Energy* **18** 469–81
[13] Chougule A, Mann J, Kelly M and Larsen G C 2017 *J. Atmos. Sci.* **74** 949–74
[14] Chougule A, Mann J, Kelly M and Larsen G C 2018 *Bound.-Lay. Meteorol.* **167** 371–97
[15] Ghobadi M 2016 DNV GL brings wind industry leaders together in "Validation of Turbulence Models" - DNV GL URL `https://www.dnvgl.com/news/dnv-gl-brings-wind-industry-leaders-together-in-validation-of-turbulence-models--77607`
[16] Jonkman B J 2016 *TurbSim User's Guide v2.00.00* (Golden)
[17] Veers P S 1988 *Three-Dimensional Wind Simulation* (Albuquerque: Sandia National Labs)
[18] Nybø A, Nielsen F G and Godvik M 2021 *Wind Energ.* 1–19
[19] Nybø A, Nielsen F G and Reuder J 2019 *J. Phys. Conf. Ser* **1356** 012006

[20] Türk M, Grigutsch K and Emeis S 2008 *DEWI-Magazin*
[21] DTU Wind Energy 2018 Pre-processing tools URL `http://www.hawc2.dk/download/pre-processing-tools`
[22] Davenport A G 1961 *Q. J. Roy. Meteor. Soc.* **87** 194–211
[23] Cheynet E 2020 ECheynet/fitMann1994 1.3 URL `https://zenodo.org/record/3774088`
[24] Welch P D 1967 *IEEE Trans. Audio Electroacoust.* **15** 70–3
[25] Cheynet E 2020 ECheynet/binAveraging: Averaging noisy data into bins URL `https://zenodo.org/record/3818011`
[26] Hermundstad O A Sima - SINTEF URL `https://www.sintef.no/programvare/sima/`
[27] Bak C, Zahle F, Bitsche R, Yde A, Henriksen L C, Nata A and Hansen M H 2013 *Description of the DTU 10 MW Reference Wind Turbine*
[28] International Electrotechnical Commision 2015 *IEC TS 61400-13: Wind turbine generator systems - Part 13: Measurement of mechanical loads* (Geneva)
[29] Cheynet E, Jakobsen J B and Reuder J 2018 *Bound.-Lay. Meteorol.* **169** 429–60
[30] Eliassen L and Obhrai C 2016 *Enrgy. Proced.* **94** 388–98
[31] Saranyasoontorn K, Manuel L and Veers P S 2004 *J. Sol. Energ-T. Asme* **126** 1069–82

# Paper 5

## Sensitivity of the dynamic response of a multimegawatt floating wind turbine to the choice of turbulence model

Nybø A, Nielsen FG and Godvik M
*Wind Energy*, (2022)

Received: 9 July 2021 | Revised: 11 November 2021 | Accepted: 10 January 2022

DOI: 10.1002/we.2712

RESEARCH ARTICLE

WILEY

# Sensitivity of the dynamic response of a multimegawatt floating wind turbine to the choice of turbulence model

Astrid Nybø[1] | Finn Gunnar Nielsen[1] | Marte Godvik[1,2]

[1]Geophysical Institute and Bergen Offshore Wind Centre (BOW), University of Bergen, Bergen, Norway

[2]Equinor, Stavanger, Norway

**Correspondence**
Astrid Nybø, Geophysical Institute and Bergen Offshore Wind Centre (BOW), University of Bergen, Allégaten 70, Bergen 5007, Norway.
Email: astrid.nybo@uib.no

## Abstract

In the design of offshore wind turbines, it is important to make a realistic estimate of the wind load. This is particularly important for floating wind turbines, having natural frequencies in a frequency range where the wind loads are high and large turbulent structures exist. This study shows that turbulence modelling greatly impacts the response of a 15-MW floating wind turbine. The turbulence models recommended by the International Electrotechnical Commission (IEC) are challenged by considering two additional models: Large Eddy Simulations (LES) and an approach using input from offshore wind measurements (TIMESR). The two standard models, the Kaimal spectrum with IEC coherence model (Kaimal) and the Mann spectral tensor model (Mann), differ in their coherence formulation. This results in higher standard deviations for the surge and pitch motions, and lower for the yaw motion, when applying Kaimal in comparison to Mann. For the specific floater of this study, more damage is obtained in the mooring lines when applying Kaimal. Applying the more realistic models, LES and TIMESR, increases the range of response further, concluding that the two standard turbulence models may lead to incorrect estimations of the response of a floating wind turbine. LES and TIMESR take atmospheric stability into account, which is proven to alter the response significantly.

**KEYWORDS**
coherence, floating wind turbines, spectral response, turbulence models

## 1 | INTRODUCTION

Several recent reports[1–3] point towards energy from offshore wind as a key resource in the future renewable energy market. The cost of energy from offshore wind has been reduced significantly over the last years, and this trend is expected to continue. A key to this cost reduction is the development of larger wind turbines with corresponding large rotors. Rotor diameters in excess of 200 m are now state of art. The availability of shallow water areas with good wind conditions is limited; however, worldwide huge deep-water areas suited for floating wind turbines are available. Thus, the understanding of the dynamic behaviour of wind turbines on floating support structures is important.

For large rotors, a good understanding of the wind induced loads is important to obtain proper estimates of the dynamics of the support structure and the corresponding fatigue damage. The wind industry relies upon standards from, for example, the International Electrotechnical Commission[4–6] (IEC) for wind turbine design. These standards recommend two simplistic turbulence models for estimating wind loads over periods between minutes and hours. These models are the Kaimal wind spectrum[7] combined with an exponential coherence model, in the

following referred to as 'Kaimal', and the Mann spectral tensor model,[8] in the following referred to as 'Mann'. More complex models like Large Eddy Simulations (LES) are able to create wind fields in a more realistic manner. Their large disadvantage, however, is the additional computational effort required. An additional option is to use wind time series and coherence as obtained from measurements. Here, the challenge is to construct a complete wind field from a few point measurements. A procedure for this is implemented in the method referred to as 'TIMESR' by TurbSim.[9]

A previous study by Nybø et al.[10] shows that the turbulent characteristics of the Kaimal, Mann, LES and TIMESR wind fields vary significantly. The coherent structures over the rotor plane are modelled differently. In contrast to Kaimal and Mann, TIMESR and LES can take atmospheric stability into account when modelling the eddies of the wind fields. In TIMESR, coherence estimates obtained from measured time series in various atmospheric stability conditions may be fitted to a coherence model and used in the generation of eddies. A stable atmosphere is typically characterised by low turbulence levels, high variation of wind speed with height and small eddies. An unstable atmosphere, on the other hand, has higher turbulence levels, lower variation of wind speed with height and large long-lasting coherent structures. In the North Sea, stable conditions are typically obtained in summer, when warm air is transported over cold sea. Similarly, unstable conditions are typically obtained during winter when cold wind blows over warm sea.

The differences in wind characteristics across turbulence models impact the dynamic response of offshore wind turbines. The variation of wind speed over the rotor is greater for larger wind turbines, typically placed offshore, than for small onshore wind turbines developed decades ago. With larger offshore wind turbines, it becomes more important to model these wind variations correctly. Nybø et al.,[11] evaluated the differences in response of a large bottom-fixed wind turbine using Kaimal, Mann, LES and TIMESR wind fields. Significant differences were found in the response, even in wind fields with similar wind speeds and turbulence levels at hub height. It was found that differences in coherent structures have large impact on differences in response for all atmospheric stability conditions. Coherent wind fields cause, for example, larger tower bottom fore-aft bending moments, while less coherent wind fields cause larger tower yaw bending moments.

Nybø et al.[11] found that the differences in response of using the different turbulence models are mainly seen at frequencies below 0.1 Hz. Most of the energy in the wind spectra and most of the large coherent structures are present in this frequency region. In contrast to bottom-fixed wind turbines, studied by Nybø et al.,[11] floating wind turbines have natural frequencies at low frequencies. The natural frequencies of the floater motions surge, pitch and heave have major impact on the response of a floater. As these natural frequencies are found in the low-frequency region where the wind load is high and the modelling of coherent structures varies significantly across turbulence models, even larger differences in response are expected when using different wind fields for floating wind turbines. The impact of turbulence models on the dynamic response of floating wind turbines is documented by previous studies.[12–18]

In the present study, the differences in response of using Kaimal, Mann, TIMESR and LES are evaluated in terms of standard deviation (STD) of the motions of the support structure. Further, the damage equivalent load (DEL) in the upper part of the most heavily loaded mooring line is computed. The differences in STD of motions and DEL obtained using the various wind fields are evaluated in various wind speeds and atmospheric stability conditions. In order to properly understand the origin of the differences, the impact of wind shear, turbulence level and especially coherence on response is tested for the specific structure.

In comparison to the previous studies mentioned above, a larger wind turbine is analysed in the present study. The IEA 15-MW[19] has a rotor size which is expected to be relevant for commercial scale in a few years. This turbine together with the Windcrete[20] spar foundation is analysed in the present study. Using both turbulence models recommended by the standard, an LES model and a model based on measurements for floater response comparisons, also makes this study unique in comparison to the previous studies mentioned above. Last, the present study uniquely supports its conclusions by a thorough analysis of the impact of specific wind characteristics on floating wind turbine response.

## 2 | DATA AND METHODS

In the following, the wind fields used in this study, TIMESR, Kaimal, Mann and LES, are introduced. Basic equations and principles are given in order to compare these wind fields in various stability and wind speed situations. The differences in wind fields are analysed by the turbulence intensity and wind spectrum at hub and coherence over a distance in the order of the rotor diameter.

Furthermore, the offshore wind turbine in consideration is introduced together with the simulation software and corresponding simulation choices. The response parameters and statistical parameters of the response analysis are defined.

### 2.1 | Wind fields

The TIMESR, Kaimal, Mann and LES wind fields are all simulated for situations covering three wind speeds and three stability conditions. The main wind characteristics of these situations and other main specifics of the domain are covered in Table 1. The three wind speed situations are run in neutral conditions, which Kaimal and Mann are originally intended for. The three situations of different atmospheric stability are run at just above rated wind speed where the wind turbine experiences high loads.

**TABLE 1** Summary of wind field characteristics

| | 7 m/s | 13 m/s | | | 18 m/s |
|---|---|---|---|---|---|
| | Neutral | Stable | Neutral | Unstable | Neutral |
| Mean wind speed at 135 m | 7.4–7.5 m/s | 12.9–13.0 m/s | 12.5 m/s | 12.6 m/s | 17.7–18.1 m/s |
| Turbulence intensity at 135 m | 3.6–5.7% | 2.0–2.8% | 3.0–5.9% | 5.5–6.1% | 4.6–6.6 % |
| Power law exponent | 0.04 | 0.2 | 0.05–0.06 | 0.02–0.03 | 0.06 |
| Obukhov length (TIMESR & LES) | −1107 & −798 | 158 & 86 | 2753 & −1049 | −451 & −56 | 2051 & −1208 |
| | | | All | | |
| Grid size horizontally and vertically | | | 4.2 m | | |
| Domain size horizontally and vertically | | | 264.6 m | | |
| Simulation time | | | 1 h | | |
| Time step | | | 0.1 s | | |

*Note*: The ranges given for mean wind speed and TI are the ranges obtained in analysing the generated wind fields. The stable and unstable Mann and Kaimal wind fields should be considered as neutral flows with TI and wind profiles adapted to the given stability, and thus, the Obukhov lengths are not given for these wind fields. The resolution and domain of LES are originally larger than indicated in this table, but interpolations are performed in order to compare at the same grounds.

The mean wind speed in the mean wind direction, $\overline{u}$, together with the STD, $\sigma_u$, defines the turbulence intensity, *TI*, by

$$TI = \frac{\sigma_u}{\overline{u}}. \tag{1}$$

$\overline{u}$ and TI are referred to hub height in the following. TI is calculated from 1-Hz data averaged over 10 min. The wind profile is defined by the power law exponent, $\alpha$, in Table 1, which is given by Equation (2).

$$\overline{u}(z) = \overline{u}_{ref}\left(\frac{z}{z_{ref}}\right)^{\alpha}. \tag{2}$$

$\overline{u}$ is the mean wind speed at height $z$, and $\overline{u}_{ref}$ is the wind speed at a reference height, $z_{ref}$. The power law exponents are calculated from mean wind speeds at 40 and 80 m. The atmospheric stability condition is given by the Obukhov length,[21] *L*, in Table 1. It relates buoyancy and shear effects in the generation of turbulence, and is given by Equation (3).

$$L = \frac{-\overline{\theta_v}u_*^3}{kg\left(\overline{w'\theta'}\right)_s}. \tag{3}$$

$\overline{\theta_v}$ is the virtual potential temperature, $u_*$ is the friction velocity defined by Equation (4), $k$ is the von Karman constant, $g$ is the gravitational constant, $\left(\overline{w'\theta'}\right)_s$ is the surface vertical kinematic eddy heat flux and $u', v'$ and $w'$ are the longitudinal, lateral and vertical velocity fluctuations, respectively.

$$u_*^2 = \sqrt{\overline{u'w'}^2 + \overline{v'w'}^2}. \tag{4}$$

The Obukhov length is calculated with a reference height 40 m above sea level. In accordance with van Wijk et al.,[22] the atmosphere is considered near-neutral when the absolute value of the Obukhov length is above 1000, that is, low effect of buoyancy. A negative value closer to zero corresponds to an unstable atmosphere, while a positive value closer to zero corresponds to a stable atmosphere. The LES wind field at 7 m/s is not neutral according to these limits. The Obukhov length is rather low as a positive surface heat flux had to be added in order to achieve an acceptable turbulence intensity. This case is still considered neutral in the current study, as the absolute value of the Obukhov length is far from zero.

The TIMESR and Kaimal wind fields are generated by Turbsim,[9] Mann by the DTU Mann generator[23] and LES by SOWFA.[24] A short description of the generation of the different wind fields is summarized under 'Response analysis' in Table 2. The coherence, which is referred to

**TABLE 2** Summary of simulated wind fields

| Method | Description | Seeds |
|---|---|---|
| *Response analysis* | | |
| TIMESR | Wind spectra interpolated in space and Davenport coherence model | 6/case |
| Kaimal | Kaimal wind spectrum and IEC exponential coherence model | 6/case |
| Mann | Mann wind spectrum and coherence model | 6/case |
| LES | Computational fluid dynamics | 1/case |
| *Wind characteristics test (just above rated wind speed)* | | |
| Uniform | No wind shear or turbulence | 1 |
| Wind shear | No turbulence, but wind shear similar to Kaimal[a] neutral wind field | 1 |
| Fully coherent | TS from hub height of Kaimal[a] neutral wind field | 1 |
| Horizontally coherent | TS from horizontal centre of Kaimal[a] neutral wind field repeated horizontally | 1 |
| Vertically coherent | TS from vertical centre of Kaimal[a] neutral wind field repeated vertically (+shear) | 1 |
| Negative coherence | Kaimal spectrum with $\mathrm{Re}[\gamma_y]$ from Equation (7), with $C_1 = 4\pi$, $C_2 = 5$ and $C_3 = 0.035$ | 6 |
| Neg. coh. = 0 | Same as 'Negative coherence' but $\mathrm{Re}[\gamma_y] < 0$ replaced by 0 | 6 |
| Neg. coh = pos. coh. | Same as 'Negative coherence' but $\mathrm{Re}[\gamma_y] < 0$ replaced by positive equivalent | 6 |

[a]Refers to the Kaimal wind spectrum and IEC exponential coherence model.
*Note*: TS = time series, case = wind speed and stability situation, neg. = negative, pos. = positive, coh. = coherence.

**TABLE 3** Inputs to TIMESR, Kaimal, Mann and LES turbulence models

| Method | Inputs |
|---|---|
| TIMESR | Wind speed time series, profile coefficients and Davenport coherence parameters from measurements |
| Kaimal | Mean wind speed, TI and power law coefficient from TIMESR |
| Mann | Mean wind speed, TI and power law coefficient from TIMESR |
| LES | Atmospheric input conditions giving similar stability, wind speed profile and TI to TIMESR |

in this table, describes the frequency dependent correlation between two time series separated in space. Spatial coherence in all directions is present in all the wind fields considered. In the results of this study, only the real part of the coherence of the along wind component, the uu-co-coherence, is presented; thus, any reference to coherence corresponds to this parameter. It is given by Equation (5), where $S_{ii}$ and $S_{jj}$ are one-sided auto-spectra of the wind velocities at two different positions, $i$ and $j$, and $S_{ij}$ is the cross spectrum between these two.

$$\mathrm{Re}(\gamma) = \mathrm{Re}\left(\frac{S_{ij}}{\sqrt{S_{ii}S_{jj}}}\right). \tag{5}$$

Sonic anemometer measurements from the offshore mast FINO1,[25,26] located in the North Sea close to Germany, are used to generate the various wind fields according to Table 3. In TIMESR, the time series from three point measurements separated vertically are used directly. The Davenport coherence model (Equation 6) is used, where $C$ is the decay coefficient obtained from measurements, $f$ is the frequency, $\delta$ is the separation distance between the two points considered and $\overline{u}_m$ is the mean wind speed between them.

$$\gamma = \exp\left(-C\frac{f\delta}{\overline{u}_m}\right). \tag{6}$$

The Davenport model is a very simple model for estimating coherence. It is still found to fit well to measurements of the uu-coherence at FINO1 as shown by Cheynet et al.[27] and exemplified by Nybø et al.[10] The TIMESR model is the only model of this study taking measurements into account in the estimation of coherence. The mean wind speeds, TI and power law coefficients, used as inputs in Kaimal and Mann, vary with the different wind speed and stability situations. The Kaimal and Mann wind fields are in this study generated according to the IEC standard[4]; thus, the coherent structures do not depend on atmospheric stability. It is possible to fit input parameters of these models to different

atmospheric stability conditions, but this is not an inherent part of the models. Detailed information about the wind fields may be found in Nybø et al.[10] The wind fields of the present study are generated in a similar manner but for a larger domain customized to a larger wind turbine.

In order to see the isolated effects of wind shear, turbulence and coherence on the response of the 15-MW floating wind turbine, the wind fields under 'Wind characteristics test' of Table 2 are simulated. The impact of coherence is tested in detail, covering the impact of low/high positive coherence, horizontal/vertical separation distance and negative/zero/positive coherence. The wind fields of the two first rows of 'Wind characteristics test' of Table 2 are generated in OpenFAST[28] (see Section 2.2), the wind fields of rows 3–5 from a Kaimal wind field (Kaimal wind spectrum and IEC exponential coherence model) and the wind fields of rows 6–8 from the principles outlined by Cheynet et al.[29]

Cheynet et al. propose the relation given by Equation (7) for the co-coherence, where $\delta_y$ is a horizontal separation direction and the Cs are decay coefficients. As observed from the expression, the co-coherence becomes negative at certain frequencies. Using the Cs of Table 2, the negative coherence corresponds well with the results of Mann's formulation. The coherence formulation given by Equation (7) is only used to evaluate the impact of negative coherence in the present study.

$$\mathrm{Re}[\gamma_y] = \cos\left(C_1 \frac{f\delta_y}{\overline{u}}\right) \exp\left(-\frac{\delta_y \sqrt{(C_2 f)^2 + C_3^2}}{\overline{u}}\right). \tag{7}$$

In Nybø et al.,[11] the impact of the imaginary part of the coherence, the quad-coherence, on response was thoroughly investigated. A similar test is performed for the floater of the present study. As in Nybø et al.,[11] negligible effects of quad-coherence are observed; thus, the details of these results are omitted from the following discussion.

It was found in Nybø et al.[11] that six 1-h realizations of the wind fields are needed. The different realizations are obtained by picking random seed numbers in generating random phases for the velocity time series. Still, LES is only run with one seed due to the computational effort required. Some of the wind characteristics test methods are also run with only one seed. This is because their characteristics differ distinctively; thus, statistical certainty is achieved in the corresponding response comparisons even when only one realization is used.

The wind spectra of varying wind speeds and stability conditions are shown in Figure 1. The wind spectra are estimated using Welch's algorithm[30] with a Hamming window, six segments, and 50% overlapping. For all cases, the Kaimal and Mann wind spectra are almost identical to each other. This is according to expectations as the Mann inputs are found by a fit to the Kaimal spectrum according to the IEC-61400.[4] The figure furthermore shows that TIMESR has high energy levels at the very lowest frequencies in most cases. One-hour measured wind time series are used as input to TIMESR. The wind spectra of the measured wind speeds at 40-, 60- and 80-m elevation are reproduced by TIMESR. At the reference height, 80 m, also the time series is reproduced. The measurements may have large scale fluctuations even though the chosen time series are considered stationary based on the criteria given in Nybø et al.[26] These criteria define stationarity based on the linear trends and moving statistics of the time series. The lower limit of frequency considered in the spectral figures is 0.0017 Hz. This corresponds to a block length in the Fast Fourier Transform (FFT) of approximately 10 min. Using a longer block length in the FFT, the extreme values observed at 0.0017 Hz are moved to even lower frequencies, but the same trends are observed. The upper limit is chosen at 0.05 Hz as the highest energy levels are present below this limit. The energy levels increase from low to high wind speeds and stable to unstable situations for all wind fields (note the different scales).

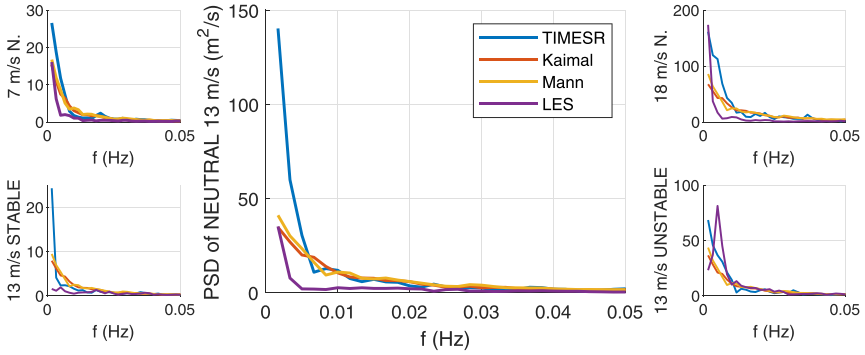


**FIGURE 1** Wind spectra at hub height. Top plots, from left to right: 7, 13 and 18 m/s, all neutral stability conditions. Bottom plots, from left to right: stable, neutral and unstable stability conditions, all 13 m/s. PSD = power spectral densities, N. = neutral

Table 1 shows a range of TI for each wind speed and stability situation. All situations have TI that are typical for the given wind speed and stability at FINO1.[10] The chosen unstable situation has a rather low TI in comparison to other unstable situations with a wind speed of about 13 m/s but still typical. Situations with very high TI tend to be non-stationary and are therefore disregarded. The LES wind fields have TI far below the TIMESR, Kaimal and Mann wind fields. It was a challenge to achieve desired TI especially in the neutral situations of LES. The TI is an output rather than input of LES. The obtained TI is sensitive to the surface roughness and surface heat flux. These parameters were tuned to obtain the desired TI and still satisfying the criteria of a neutral stability and desired wind shear. In reality, neutral atmospheric stability conditions rarely exist. It is often a brief period of time as the atmospheric boundary layer (ABL) transitions from one stability to another. The assumptions of a 'canonical' LES applied in this study do not hold in such a transitional state. These assumptions are flow in quasi-equilibrium state, driving pressure gradient constant with height, horizontally homogeneous flow and flow over waves represented by flow over a flat very low roughness wall. As limited information is available from FINO1, the reasons for high TI in neutral conditions are uncertain, and the corresponding atmospheric input conditions to LES are limited. This explains the large differences in TI between LES and the other wind fields in the neutral situations, which are also reflected in the wind spectra.

The coherence of a vertical and horizontal separation distance of 168 m (0.7 rotor diameters) is shown in Figures 2 and 3, respectively. The coherence typically starts off at a high value for low frequencies, decaying towards 0 with increasing frequencies. At frequencies higher than the maximum value in the figures (0.05 Hz), the decay continues. The coherence of distances between the radius and the diameter of the rotor is expected to be highly relevant for response. With smaller separation distances, the curves of Figures 2 and 3 are stretched towards higher frequencies. The same stretching is seen for increasing wind speed, shown by higher coherence at higher frequencies for 18 than 7 m/s. The

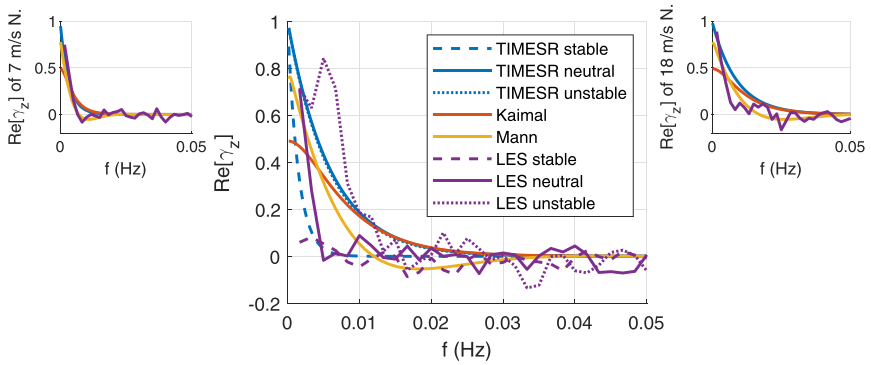


**FIGURE 2** Vertical coherence of 0.7 D (168 m). The coherence of the wind fields of various atmospheric stability conditions are all shown in the mid figure. The coherence of Kaimal and Mann is independent of stability. The solid blue line lies on top of the dotted blue line. N. = neutral

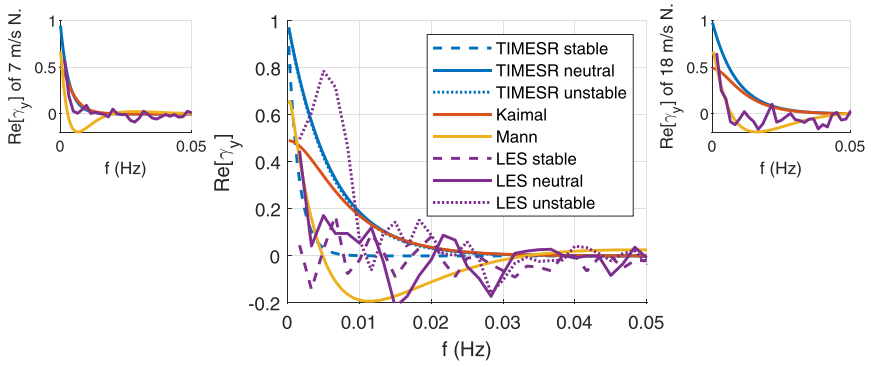


**FIGURE 3** Horizontal coherence of 0.7 D (168 m). The coherence of the wind fields of various atmospheric stability conditions are all shown in the mid figure. The coherence of Kaimal and Mann is independent of stability. The solid blue line lies on top of the dotted blue line.
N. = neutral

coherence increases from stable to unstable atmospheric conditions. This is especially clear for LES, where the stable situation has close to zero coherence in the whole frequency range. The coherence of the neutral 13 m/s TIMESR wind field is close to the unstable. The stable TIMESR situation has significantly lower coherence than the neutral and unstable situations, but it starts off at unity. This is an assumption and a limitation of the Davenport coherence model used in TIMESR. Kaimal and Mann are independent of atmospheric stability. In contrast to the observations of the wind spectra (Figure 1), significant differences between these two models are observed in the vertical and horizontal coherence (Figures 2 and 3). Mann has a much lower coherence than Kaimal, even negative at some frequencies. This difference is larger with horizontal separation distance. In fact, the coherence of Kaimal and TIMESR are independent on the direction of the separation distance, while significant differences are observed both for Mann and LES. To sum up, the coherence of TIMESR and LES in the stable situation is low. In fact, LES and especially Mann have low coherence in all situations except LES in the unstable situation. The coherence of TIMESR neutral, TIMESR unstable and Kaimal are intermediate and rather similar.

## 2.2 | Structure and response characteristics considered

The wind turbine structure used in this study corresponds to the IEA 15-MW reference turbine[19] supported by the WindCrete floater,[20] as shown in Figure 4. The rotor diameter is 240 m and the rated wind speed is 10.59 m/s. More information on the rotor specifics is found in Gaertner et al.[19] The WindCrete floater is a 155-m-deep spar structure made from concrete. It has three main mooring lines with delta connections towards the floater. The design is carried out for a Gran Canaria site with a water depth of 200 m. The natural periods with a passive rotor are found to be about 78 s for surge and sway, 42 s for pitch and roll, 34 s for heave and 11 s for yaw. The IEA 15-MW reference tower has been replaced by a concrete tower with a hub height of 135 m in the WindCrete design.

NREL's Reference OpenSource Controller (ROSCO[32]) with variable speed torque control below rated wind speed and collective blade pitch control (constant torque) above rated wind speed is used. The proportional and integral gains of the pitch controller are tuned by the Ziegler–Nichols method[33] for the specific structure in order to avoid instabilities in the platform pitch motion. This is a simplistic approach for handling possible dynamic instabilities of the floater motions. More advanced controller options are discussed in, for example, Skaare et al.[34,35] The signals are filtered prior to input to the controller. The period of the second-order low-pass filter used is 14 s. The controller is thus active at all natural periods important for response but does not react on wave induced motions. Due to the simplistic control system, some unexpected fluctuations in power appear when the wind turbine is subject to turbulent wind. These fluctuations are, however, not considered to influence the computed motion responses to any significant degree. The 13 m/s wind speed case is close to rated wind speed. However, throughout the simulations, a constant torque is observed, proving that the controller is staying in the 'above rated state'. More information on the controller used, hydrodynamics, mooring system and tower are found in Mahfouz et al.[20]

The aero-hydro-servo-elastic tool OpenFAST[28] is used for analysing the response of the wind turbine. The various wind fields are used as inputs to this software. In the LES, the three velocity components are stored at an yz-plane (x = constant) each time step. The stored velocity time series are subsequently transformed to a 'wind-box' on 'Mann-format' to be read by OpenFAST. The aerodynamic loads on the structure are calculated by the blade element momentum theory. The simulations are run for 3800 s. The first 200 s are discarded to remove transient effects. A time step of 0.01 s is used.

In this work, the focus is on floater specific response, more specifically on mooring line tensions and rigid body motions of the floater. Only the dynamic response is analysed in the results section; thus, any reference to response corresponds to dynamic response. Mean motions and mean tensions are only included in response probability distributions. The same trends are seen in the tensions of the six bridle lines and the three

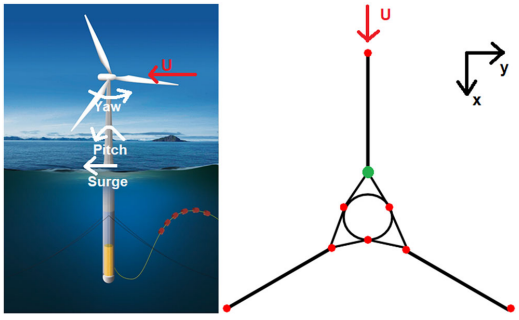


**FIGURE 4** Scheme of the Windcrete model, including rigid body motions and mooring layout31

mooring lines. The tension is largest at the connection point between the bridles and the mooring line in front of the wind turbine in the mean wind direction (green dot of Figure 4); thus, this tension is presented in the following. Godvik[16] found strong similarities in bridle tension and yaw motion. In our results, the yaw motion is dominated by quasi-static loads (i.e., loads at frequencies well below the natural frequencies), while the bridle tensions are dominated by the surge and in some cases the pitch natural frequencies. The bridle tensions are not studied any further. The focus of this study is furthermore on the largest platform motions: surge and pitch. The yaw motion is also studied as this motion is expected to be strongly impacted by differences in wind characteristics across turbulence models. The considered motions are illustrated in Figure 4.

The floating wind turbine response subject to the various wind fields is evaluated in terms of DEL of the mooring line and STD of the platform motions. The DEL, $R_{eq}$, is given by

$$R_{eq} = \left( \frac{\Sigma_i (R_i^m n_i)}{n_{eq}} \right)^{1/m} \tag{8}$$

where $R_i$ is the amplitude of the time series, $n_i$ the number of cycles and $n_{eq}$ the equivalent number of response cycles for an equivalent frequency of 1 Hz in this case. The Wöhler exponent, $m$, for the mooring line made of chain is assumed to be 3, corresponding to steel. For more information on the procedure for determining DEL, see Nybø et al.[11]

Figure 5 shows the probability distributions of the platform motions and the mooring line tension for the neutral 13 m/s situation. The distributions are all close to Gaussian. A mean surge motion of about 7 m and a mean pitch motion of about 2.7° are observed. The standard deviations of surge and pitch are 0.3–0.9 m and 0.15–0.35° in this case. The mean yaw motion is close to zero with a standard deviation of 0.15–0.3°.

As the focus of this study is to analyse the impact of various wind fields on response, the wind turbine simulations are run without waves and current. In agreement with Mahfouz et al.,[20] the impact of the hydrodynamic forces on the wind turbine structure was found to be small in comparison to the aerodynamic forces. Mahfouz et al. explain this by low hydrodynamic forces on their chosen location, a large wind turbine and large inertia of the physical system. Waves may still cause local forces and fatigue of some components in extreme conditions. Non-linear wave excitation loads and coupled wind-wave effects may excite loads at lower frequencies than the primary wave frequencies. These non-linear load effects are assumed small compared to the direct wind loads on the turbine and are not considered in this work.

In order to analyse the origin of the differences in computed STD and DEL obtained by the different wind formulations, the response spectra are studied. In the response spectra shown, the frequency range is limited to 0–0.05 Hz. As mentioned in Section 1, the natural frequencies of surge, pitch and heave have major impact on the response of a floating wind turbine. These frequencies are all well within the 0- to 0.05-Hz range. The quasi-static response is also expected to be highest in this range, considering the large amplitudes of the wind loading at low frequencies

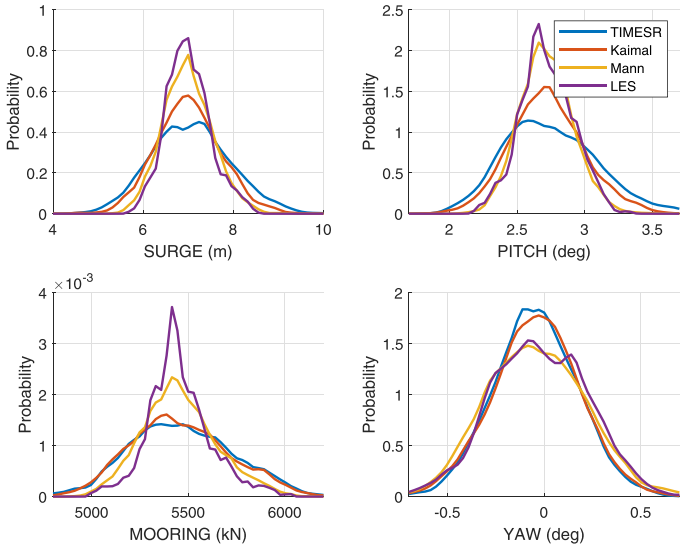


**FIGURE 5** Response distribution of platform motions and mooring line tension in the neutral 13 m/s situation

(Figure 1). Higher frequencies than 0.05 Hz are therefore considered to have minor impact on the damage and motions of the specific floating wind turbine of this study.

## 3 | RESULTS AND DISCUSSION

In the following, the differences in the floating wind turbine response from using TIMESR, Kaimal, Mann or LES input wind fields are analysed in detail. First, the effect of wind shear, turbulence and especially variations of coherence on the response is studied. Findings of this wind characteristics test are taken into consideration when comparing the response of using TIMESR, Kaimal, Mann or LES.

### 3.1 | Wind characteristics test

Figures 6 and 7 show the impact of various wind characteristics on response, using the wind fields under 'Wind characteristics test' in Table 2. They also clearly show which frequencies are important for the various motions and the mooring line tension considered in this study. As expected, the natural frequencies of surge and pitch are dominant for the platform surge and pitch motions, respectively. Additionally, the quasi-static load has some impact on the platform surge and pitch motions. Typically for a spar platform, the natural frequency of pitch is also important for the surge motion. The surge-pitch coupling is explained by the vertical position of the point of reference for surge being at the mean sea level, not at the centre of rotation of the platform. The centre of rotation, defined as the vertical position with minimum horizontal displacement, is typically far below the sea level for a spar platform. The location depends upon the external loading and is in most cases close to the centre of gravity. For the structure analysed in the present study, the centre of rotation is approximately 82 m below sea level. The computed mooring line tension shows no peak at the pitch natural frequency but is totally dominated by the surge natural frequency. This is explained by the fact that the mooring lines are attached to the hull at 90 m below sea level, that is, close to the centre of rotation. In contrast to the three responses mentioned, the natural frequencies matter less for platform yaw response, which is dominated by quasi-static response.

In the spectra of the platform surge and pitch motions (top plots of Figures 6 and 7), peaks are observed at a lower frequency than expected from the pitch decay test. The pitch decay test is performed by giving the structure an initial pitch displacement of 10° and releasing it without any external forces acting. Similar decay tests were performed while the wind turbine was operating. Uniform wind fields of a few constant wind speeds were used. The results are illustrated in Figure 8. An increased period of oscillation is observed when the turbine is acting, in particular

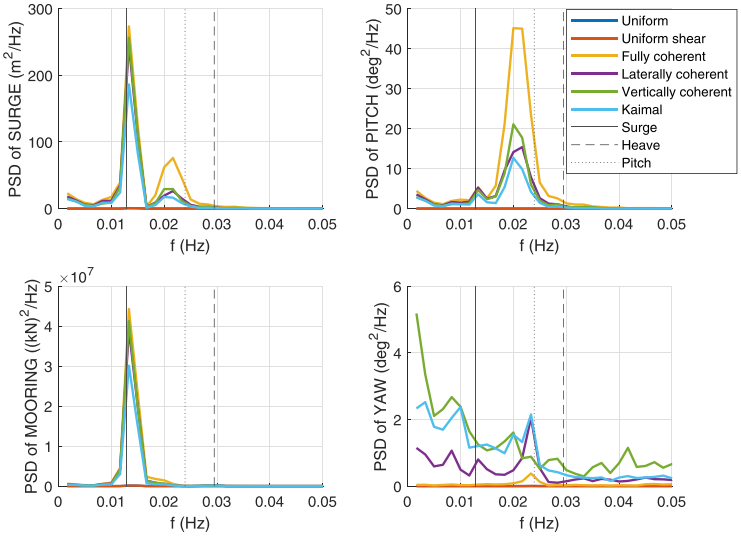


**FIGURE 6** Response spectra showing the impact of wind shear, turbulence and positive coherence on platform motions and mooring line tension. The red lines (Uniform shear) lie on top of the dark blue (Uniform). The vertical lines denoted surge, heave and pitch show the corresponding natural frequencies for these modes from OpenFAST decay tests. PSD = power spectral densities

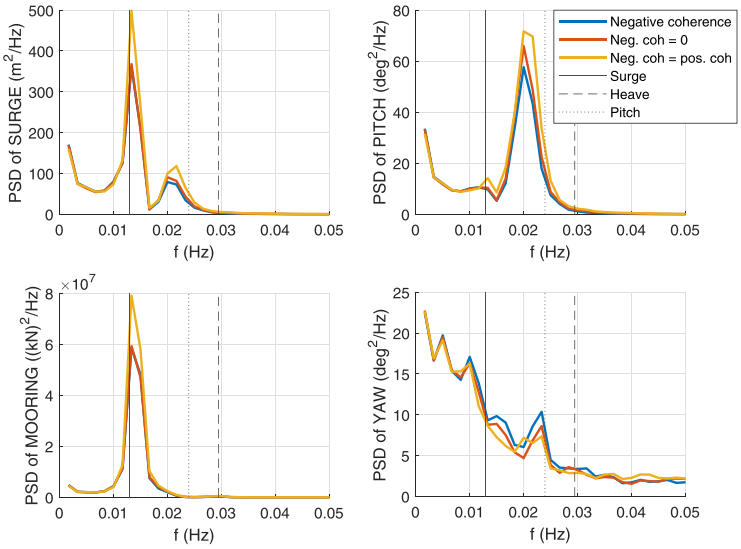


**FIGURE 7** Response spectra showing the impact of negative coherence on platform motions and mooring line tension. The red lines lie on top of the blue for surge and mooring. The vertical lines denoted surge, heave and pitch show the corresponding natural frequencies for these modes from OpenFAST decay tests. PSD = power spectral densities

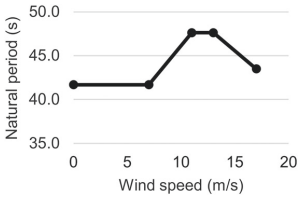


**FIGURE 8** Pitch decay periods with various incident wind speeds

close to the rated wind speed. To investigate this phenomenon further, OpenFAST simulations with uniform wind fields of harmonic oscillatory wind speeds were performed. Mean wind speeds of 7 and 13 m/s were used. The wind speed was varied harmonically with an amplitude of 1 m/s. The period of oscillation was varied between 40 and 50 s in steps of 0.5 s. For 7 m/s mean wind speed, maximum pitch response was obtained for a period of oscillation of 40.5 s, while for 13 m/s, the period of maximum pitch response was 48 s, confirming the trends of Figure 8. Our results are in accordance with Souza and Bachynski,[36] who explain the increased pitch natural period by an apparent inertia and damping effects induced by the thrust force on the wind turbine. The sensitivity of pitch natural period to wind speed proves the importance of performing coupled analysis in the design of wind turbines. In the spectra of the platform yaw motion (bottom right plots of Figures 6 and 7), a peak is observed at the roll natural frequency. The roll natural frequency is almost identical to the pitch natural frequency obtained at zero wind speed. The observed yaw motion at this frequency is thus due to a roll–yaw coupling.

Comparing steady, uniform wind fields with and without shear, it is found that the wind shear has negligible impact on the surge and pitch motions and the mooring line tension. However, adding the wind shear approximately doubles the STD of the yaw motion. This is due to increased roll motion at the natural frequency. As the responses are small, this effect is not visible in Figure 6. The combination of blade rotation and wind shear force in the rotor plane causes higher STD of roll. Consequently, the centre of the rotor plane deviates from the tower axis, causing higher STD of yaw. The extreme increase of yaw STD described above is observed only with no turbulence present. The effect of wind shear in a turbulent wind field was investigated further by comparing the response of using a Mann input wind field with a power law coefficient of 0.06 and 0. The differences in roll and yaw STD were less than 1%. Consequently, no impact of the minor differences in wind shear in the turbulent wind fields Kaimal, Mann, TIMESR and LES is expected on response.

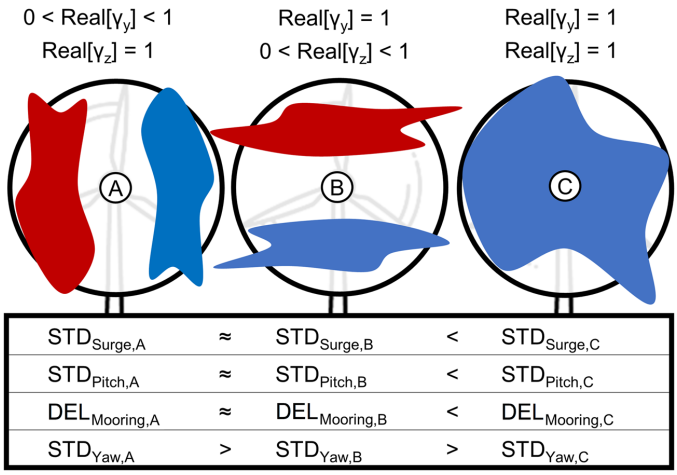


**FIGURE 9** Illustration of the impact of coherence on platform motions STD and mooring line DEL. Different colours represent uncorrelated eddies. Case A illustrates a case where there is large coherence in the vertical direction over a length scale similar to the rotor diameter; that is, the dynamic wind speed is similar over this length scale. In the horizontal direction, the coherence is assumed to be lower, causing uncorrelated variations in the wind speed between the two sides of the rotor disc. In case B, large coherence in the horizontal direction is assumed, while there are uncorrelated variations in the wind speed in the vertical direction. In case C, the flow is assumed coherent over most of the rotor disc. As indicated in the table, the three cases excite the different modes of motion differently

Figure 6 shows that higher turbulence levels cause higher energy levels in the complete frequency range, as was found for a bottom-fixed wind turbine in Nybø et al.[11] Without any turbulence (Uniform and Uniform shear), any significant response is only seen at the natural frequencies of the system. Based on this, the variations in turbulence levels between TIMESR, Kaimal, Mann and LES (see, e.g., TI intervals in Table 1) are expected to influence response.

A completely coherent wind field (Fully coherent) causes higher surge and pitch motions and corresponding mooring line tension compared to a more realistic wind field like Kaimal (keep in mind that Kaimal refers to the Kaimal wind spectrum and IEC exponential coherence model). This is especially clear for the motions at the pitch natural frequency, dominant for the pitch motion. A fully coherent wind field causes increased total loads on the rotor and correspondingly large pitch motions. The platform pitch STD is 84% higher when using the fully coherent wind field in comparison to Kaimal, while the surge STD is 38% higher and the mooring DEL 27% higher. The same trends were seen for the tower base of the bottom-fixed wind turbine in Nybø et al.[11] The surge and pitch motions and the mooring line tension are independent of the direction of coherence. The global pitch motion is dominated by the thrust force times the distance between the rotor centre and the water line rather than the local force distribution over the rotor disc. Considering local response, such as the tower top damage equivalent bending moment, the vertical distribution of forces over the rotor disc is the key driver. Thus, the vertical coherence is an important parameter. This expectation is confirmed for a bottom-fixed wind turbine in Nybø et al.[11] The dynamic yaw motion increases significantly with less coherence, especially less horizontal coherence. As seen in Nybø et al.,[11] a wind field with low coherence and corresponding large local forces over the rotor causes high local moments. Specifically, we see the same behaviour in the yaw motions of the floater and the tower yaw moment of the bottom-fixed wind turbine. The impact of coherence on response described above is illustrated in a simplified manner in Figure 9.

When using a wind field containing negative coherence in some frequency range, the surge and pitch motions and the mooring line tension are lower in comparison to using a wind field where this negative coherence is replaced by 0 or its positive equivalent; see Figure 7. For frequencies higher than about 0.03 Hz, the same trend is seen for the platform yaw motion, but at lower frequencies, negative coherence causes higher energy levels. Again, the same trends are seen for the tower yaw moment of Nybø et al.,[11] and the yaw motions of the floater considered in the present study.

## 3.2 | Impact of turbulence model on floater response

In the following, the differences in floater response by using TIMESR, Kaimal, Mann and LES are evaluated. Figure 10 summarizes these differences in terms of STD of the surge, pitch and yaw motions and DEL of the mooring line tension. As expected, the surge and pitch STD and

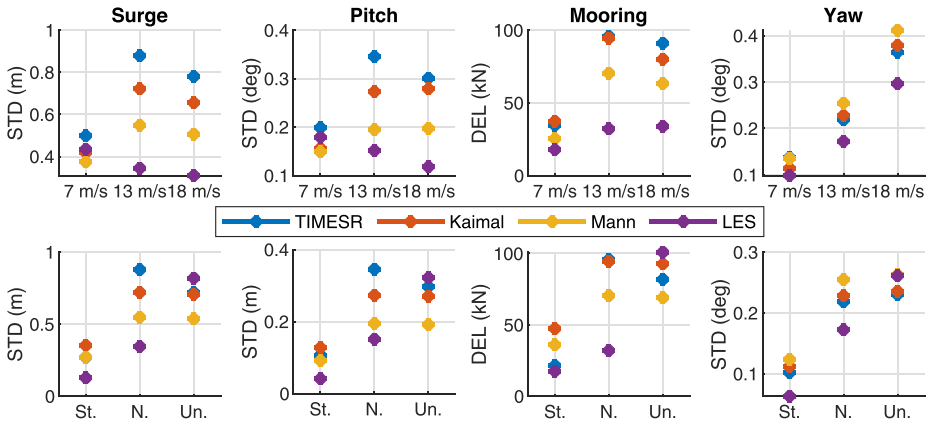


**FIGURE 10** Standard deviations (STD) and damage equivalent loads (DEL) of response time series for three wind speeds (top plots) and three atmospheric stability conditions (bottom plots). N. = neutral, Un. = unstable, St. = stable. Mann unstable yaw is at the same value as LES

| *Response* | | 7 m/s | 13 m/s | | | 18 m/s | *Cause* | |
|---|---|---|---|---|---|---|---|---|
| **Method** | **STD/DEL** | **Neutral** | **Stable** | **Neutral** | **Unstable** | **Neutral** | **γ** | **$PSD_{Wind}$** |
| *Surge (STD), pitch (STD) & mooring line tension (DEL)* | | | | | | | | |
| TIMESR | High | ■ | | ■ | | ■ | High | High |
| Kaimal | High | ■ | ■ | ■ | ■ | ■ | High | |
| Mann | Low | ■ | ■ | ■ | ■ | ■ | Low (-) | |
| LES | High | | | | ■ | | High | High |
| LES | Low | | ■ | ■ | | ■ | Low | Low |
| *Yaw (STD)* | | | | | | | | |
| Mann | High | ■ | ■ | ■ | ■ | ■ | Low (-) | |
| LES | High | | | | ■ | | | High |
| LES | Low | ■ | ■ | ■ | | ■ | | Low |

**FIGURE 11** Summary of response (left) and wind characteristics causing this response (right) of using TIMESR, Kaimal, Mann and LES wind fields. Relevant wind speed and atmospheric stability situations are marked in the middle. For example, the surge STD, pitch STD and mooring line DEL of TIMESR are high for all wind speeds in neutral stability conditions due to high coherence and high energy levels of the wind spectra. $\gamma$ = coherence, (−) = negative, PSD = power spectral densities

mooring line DEL are largest close to the rated wind speed for most wind fields. The STD of the yaw motion, on the other hand, increases with wind speed. Also as expected, stable atmospheric conditions, with corresponding low TI, lead to lower STD and DEL. The trends across turbulence models are similar for the surge and pitch motions and the mooring line tension. When using, for example, the Mann wind field, these are relatively low, while the STD of the yaw motion is rather high. Based on the findings of the wind characteristics test, this indicates that coherence plays an important role. Figure 10 furthermore shows that the response of using the LES wind fields is low in most situations. This may rather be a consequence of a lower turbulence level. The origin of the differences in floater response by using TIMESR, Kaimal, Mann and LES is discussed further in the following. These results are summarized in Figure 11.

Taking a closer look at the surge motions, TIMESR leads to the highest STD for all wind speeds in neutral atmospheric conditions. A similar trend is seen in the stable situation, while the LES wind field leads to highest STD in the unstable situation. These trends are reflected in the response spectra of Figure 12. At the natural frequency of surge, having major impact on the motions, Kaimal and TIMESR cause relatively high energy levels for all situations. The high PSD of using these two in comparison to Mann and LES is expected to be related to the differences in coherence between the wind fields. As observed in Section 3.1, high coherence is expected to cause high surge response at the surge natural

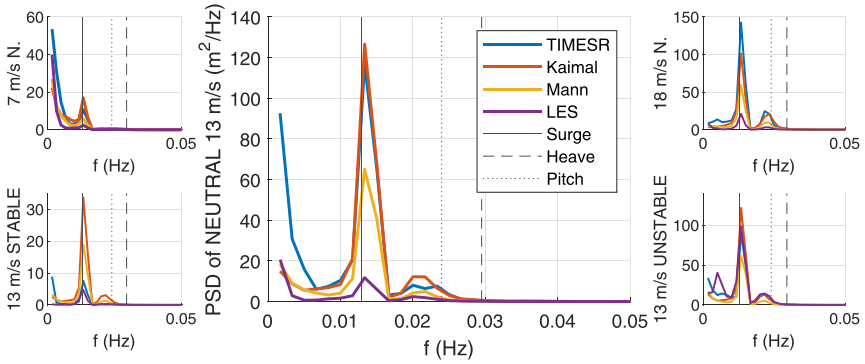


**FIGURE 12** Platform surge motions of the floating wind turbine. Top plots, from left to right: 7, 13 and 18 m/s, all neutral stability conditions. Bottom plots, from left to right: stable, neutral and unstable stability conditions, all 13 m/s. The vertical lines denoted surge, heave and pitch show the corresponding natural frequencies for these modes from OpenFAST decay tests. PSD = power spectral densities, N. = neutral

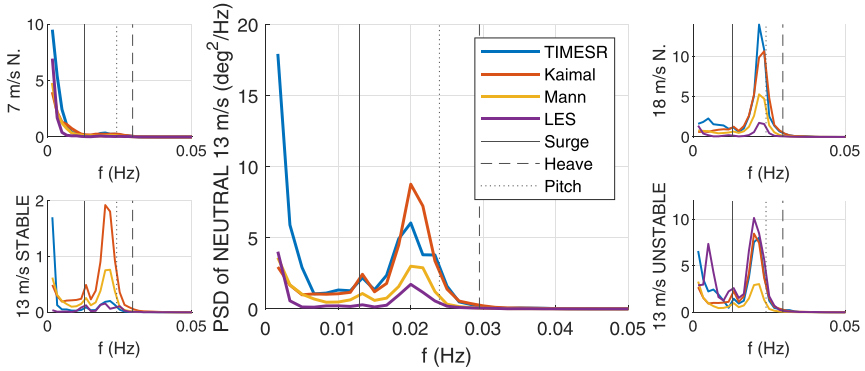


**FIGURE 13** Platform pitch motions of the floating wind turbine. Top plots, from left to right: 7, 13 and 18 m/s, all neutral stability conditions. Bottom plots, from left to right: stable, neutral and unstable stability conditions, all 13 m/s. The vertical lines denoted surge, heave and pitch show the corresponding natural frequencies for these modes from OpenFAST decay tests. PSD = power spectral densities, N. = neutral

frequency. Figures 2 and 3 show that the coherence of TIMESR and Kaimal are high in most situations, while the coherence of Mann is low. The differences between Kaimal and Mann in the present study are consistent with the findings of Eliassen and Bachynski.[14,15] They also explain the high surge response of using Kaimal by the more uniform forcing over the rotor. The low coherence of TIMESR in the stable situation is also reflected by a lower response at the surge natural frequency.

The quasi-static response impacts the surge STD as well, especially for the low wind speed (top left plot of Figure 12). At these low frequencies, there are clear similarities between the response spectra and the wind spectra, where the TIMESR wind fields generally have high energy levels. These high energy levels correspond to large variations in the mean wind speed or non-stationary conditions. The stationary turbulence models defined by the IEC standard, Mann and Kaimal, are not able to reproduce these large scale fluctuations. They are originally intended for small onshore wind turbines with high natural frequencies in comparison to floating wind turbines. In the design of onshore wind turbines, shorter time series are thus required in order to evaluate the dynamic response. Typically, 10-min time series are used for onshore wind turbine design, while 1-h or even longer time series are required for floating wind turbine design. The longer the time series, the more large scale fluctuations are seen in observations. The high energy levels at very low frequencies in the TIMESR wind fields, and corresponding high energy levels in the surge motion at similar frequencies, show that large scale fluctuations should be modelled in input wind fields. This is as mentioned not possible by the turbulence models defined by the IEC standard. Available options for representing large scale fluctuations are, for example, the TIMESR model used in the present study, adding large scale fluctuations to the standard Kaimal and Mann models, or LES with configurations allowing for large

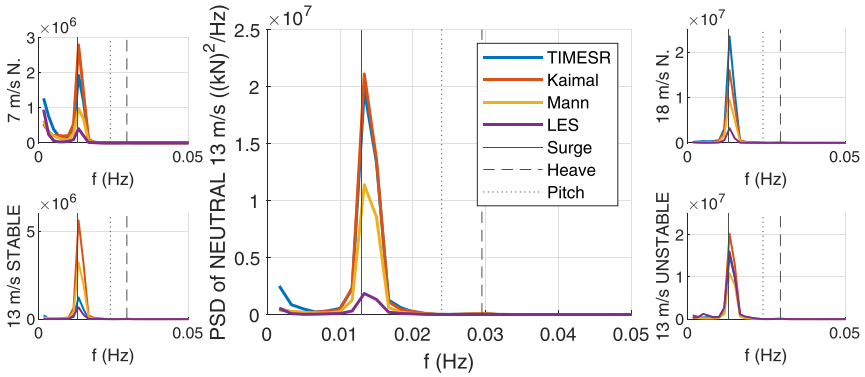


**FIGURE 14** Mooring line tension of the floating wind turbine. Top plots, from left to right: 7, 13 and 18 m/s, all neutral stability conditions. Bottom plots, from left to right: stable, neutral and unstable stability conditions, all 13 m/s. The vertical lines denoted surge, heave and pitch show the corresponding natural frequencies for these modes from OpenFAST decay tests. PSD = power spectral densities, N. = neutral

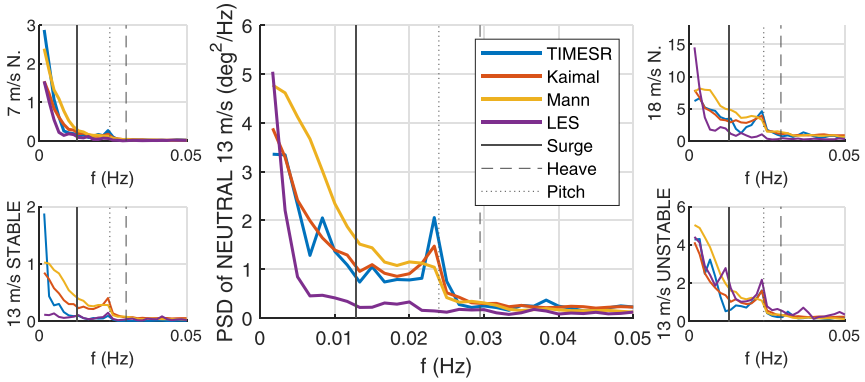


**FIGURE 15** Platform yaw motions of the floating wind turbine. Top plots, from left to right: 7, 13 and 18 m/s, all neutral stability conditions. Bottom plots, from left to right: stable, neutral and unstable stability conditions, all 13 m/s. The vertical lines denoted surge, heave and pitch show the corresponding natural frequencies for these modes from OpenFAST decay tests. PSD = power spectral densities, N. = neutral

scale fluctuations. As shown by Nybø et al.,[37] the input parameters of the Mann model may also be fitted to observations in order to approach the high energy levels of the TIMESR wind spectra and corresponding response.

The LES wind fields have high coherence and high energy levels in the unstable situation, which is also reflected by a higher surge STD in Figure 10. In most other situations, the coherence and particularly TI of the LES wind fields are very low, which cause low energy levels for all frequencies.

Figure 10 shows that the same trends are seen for the pitch and surge motions. The STD of TIMESR and Kaimal is in most cases high, while the STD of Mann and LES is lower. Kaimal is found to cause higher pitch STD than Mann for the different platforms analysed by Eliassen and Bachynski[14,15] as well. Together with the quasi-static frequency region, the natural frequency of pitch is dominant for the pitch motion (Figure 13). The trends of pitch PSD at pitch natural frequency are similar to the surge PSD at the surge natural frequency. At 7 m/s, there is relatively low energy levels at the pitch natural frequency due to a large positive thrust gradient which damps the system. The response spectra at this wind speed are therefore a reflection of the wind spectra, with, for example, a similar trend of Mann and Kaimal.

The differences in coherence between TIMESR, Kaimal, Mann and LES cause the differences in the mooring line DEL. Kaimal and TIMESR, which have the highest coherence in most situations, cause the highest DEL. In Doubrawa et al.[17] they rather found that the mooring line DEL was larger when using Mann instead of Kaimal. In Eliassen and Bachynski,[14,15] the order of Mann and Kaimal was found to be dependent on wind

speed. The mooring line tensions and the corresponding order of Mann and Kaimal depend on the floater and mooring design. Figure 14 shows that, for the design used in the present study, the surge motions are dominant for all wind speeds. The high DEL of using Kaimal, as seen in the surge STD, is therefore according to expectations. Relative to the pitch and surge motions, the differences in turbulence level of the wind fields have less impact on the differences in mooring line tensions. Figure 10 shows that the TIMESR DEL is correspondingly lower.

In contrast to the surge and pitch motions and the mooring line tension, the Mann wind fields cause large yaw STD. This is reflected in the response spectra of Figure 15, especially at frequencies lower than the pitch natural frequency. Based on the findings of Section 3.1 and Figure 3, it is clear that the low and negative horizontal coherence of Mann cause these high energy levels. Godvik,[16] Putri et al,[12] and Eliassen and Bachynski[14,15] also observed a large STD of Mann compared to Kaimal in the yaw motion. Some of the LES wind fields have low horizontal coherence as well. However, their low turbulence levels dominate the PSD of yaw motions.

The trends across turbulence models are similar in the yaw STD of the floater and the damage equivalent moment of the tower top yaw in Nybø et al.[11] The Mann wind fields cause high yaw response in all situations considered. The same similarities are found between the other considered responses of the floater (platform surge STD, platform pitch STD and mooring line DEL) and the tower bottom fore-aft bending moment of the bottom-fixed wind turbine. In most of the situations, TIMESR and Kaimal cause the highest motions and damage relative to Mann. The LES wind fields cause low overall STD and DEL due to the low turbulence levels.

## 4 | CONCLUSIONS

This study challenges the applicability of the standard turbulence models, Kaimal and Mann, by studying the wind induced response of a large floating wind turbine subject to Kaimal, Mann, LES and TIMESR wind fields. More specifically, the surge, pitch and yaw motions of the floater and corresponding fatigue damage of a mooring line are analysed. For the 15-MW floating wind turbine with spar foundation analysed in this study, the surge motions are dominant for the mooring line tension.

First, the impact of various wind characteristics on the dynamic response of the floating wind turbine is evaluated. Wind shear is found to have negligible impact on the platform motions and the mooring line tension considered. As expected, turbulence greatly impacts all considered platform motions and the mooring line tension over the entire frequency range. A coherent wind field causes higher surge and pitch STD and mooring line DEL in comparison to a wind field with less coherence over separation distances in the order of the rotor diameter. The yaw STD is increased when the horizontal coherence becomes low or even negative over such distances.

The differences in floater response of using Mann versus Kaimal wind fields are significant. The turbulence intensities, mean wind speeds, wind shear and wind spectra are equivalent in the two models. It is rather the differences in coherence between the two that cause the differences in response. Kaimal, with higher coherence, causes larger surge and pitch STD, and corresponding larger mooring line DEL. Mann, with lower and even negative horizontal coherence, causes higher STD of the yaw motion. The differences in platform surge, pitch and yaw STD of using the Kaimal or Mann wind fields are consistent with previous findings.

In contrast to Mann and Kaimal, TIMESR and LES take atmospheric stability into account in the generation of turbulent structures. In the unstable situation, large and energetic coherent structures are present in these wind fields, causing corresponding high STD of the surge and pitch motions in comparison to the standard models. In the stable situation, on the other hand, smaller and less energetic eddies present in TIMESR and LES cause low motion and mooring line response.

Great similarities are found in the response analysis of the floater structure of the present study and the bottom-fixed wind turbine of Nybø et al.[11] The same trends across turbulence models are seen in the surge and pitch motions and the mooring line tension as in the tower bottom fore-aft bending moment. Similarly, the yaw motion and tower yaw bending moment react equivalently to differences in coherence. However, the differences across turbulence models are larger for the floater, having natural frequencies in the frequency range where large variations in the wind fields exist.

Using LES wind fields, generally low motion and mooring line responses are observed relative to the standard models. This is attributed to the low TI achieved and, in particular, the low energy levels in the low frequency range of the LES wind spectra. It is challenging to tune LES outputs to observations with limited information on the atmospheric conditions, especially in the neutral situations. LES may create far more realistic wind fields than simple models such as Kaimal and Mann but may still cause less realistic response if failing to reproduce important wind characteristics such as TI. The great impact of TI on response shows the importance of measuring turbulence at site and accurately represent TI in the design process of offshore wind turbines.

TIMESR, using measured wind velocities as input, causes larger motion and mooring line responses than the standard turbulence models in most of the situations considered. This is partly due to the presence of large scale, low-frequency fluctuations captured by TIMESR. Such low-frequency phenomena are not modelled in the stationary (standard) turbulence models: Kaimal and Mann. This study clearly demonstrates that both standard turbulence models are consequently likely to underestimate the surge and pitch response of the floating wind turbine. The higher coherence estimates obtained by the TIMESR model also lead to higher surge and pitch STD and corresponding higher mooring line DEL. The TIMESR yaw STD is low compared to the yaw predicted using the standard turbulence models. This is a combined effect of the frequency

distribution of turbulence and the horizontal coherence. Due to lack of measurements, little is known about the horizontal coherence. This study demonstrates the need for improved knowledge about the coherence of the wind field. This need increases with the diameter of the rotor.

## ACKNOWLEDGEMENTS

The authors would like to thank Vegard Milde, an MSc student at the University of Bergen, for cooperation on the OpenFAST model of the spar floater. For providing LES wind fields and associated support, we would like to thank Matthew J. Churchfield at the National Renewable Energy Laboratory. A portion of the research was performed using computational resources sponsored by the Department of Energy's Office of Energy Efficiency and Renewable Energy and located at the National Renewable Energy Laboratory.

## PEER REVIEW

The peer review history for this article is available at https://publons.com/publon/10.1002/we.2712.

## DATA AVAILABILITY STATEMENT

The data that support the findings of this study are available from the corresponding author upon reasonable request.

## ORCID

*Astrid Nybø* https://orcid.org/0000-0002-7438-7936

## REFERENCES

1. International Renewable Energy Agency. Future of wind: deployment, investment, technology, grid integration and socio-economic aspects (A Global Energy Transformation paper). tech. rep., Abu Dhabi, IRENA; 2019. https://www.irena.org/-/media/Files/IRENA/Agency/Publication/2019/Oct/IRENA_Future_of_wind_2019.pdf. Accessed July 2, 2021.
2. International Energy Agency. Offshore wind outlook 2019, Paris, IEA; 2019. https://iea.blob.core.windows.net/assets/495ab264-4ddf-4b68-b9c0-514295ff40a7/Offshore_Wind_Outlook_2019.pdf. Accessed July 2, 2021.
3. Wind Europe. Our energy, our future. tech. rep., Brussels, Wind Europe; 2019. https://windeurope.org/wp-content/uploads/files/about-wind/reports/WindEurope-Our-Energy-Our-Future.pdf. Accessed July 2, 2021.
4. International Electrotechnical Commision. IEC 61400-1 Wind energy generation systems - Part 1: design requirements. tech. rep., Geneva, IEC; 2019. https://webstore.iec.ch/publication/26423. Accessed July 2, 2021.
5. International Electrotechnical Commision. IEC 61400-3-1:2019 Wind energy generation systems - Part 3-1: design requirements for fixed offshore wind turbines. tech. rep., Geneva, IEC; 2019. https://webstore.iec.ch/publication/29360. Accessed July 2, 2021.
6. International Electrotechnical Commision. IEC TS 61400-3-2:2019 Wind energy generation systems - Part 3-2: design requirements for floating offshore wind turbines. tech. rep., Geneva, IEC; 2019. https://webstore.iec.ch/publication/29244. Accessed July 2, 2021.
7. Kaimal JC, Wyngaard JC, Izumi Y, Coté OR. Spectral characteristics of surface-layer turbulence. *Q J Roy Meteor Soc*. 1972;98(417):563-589.
8. Mann J. The spatial structure of neutral atmospheric surface-layer turbulence. *J Fluid Mech*. 1994;273:141-168.
9. Jonkman BJ. TurbSim User's Guide v2.00.00. tech. rep., Golden, NREL; 2016.
10. Nybø A, Nielsen FG, Reuder J, Churchfield M, Godvik M. Evaluation of different wind fields for the investigation of the dynamic response of offshore wind turbines. *Wind Energy*. 2020;23(9):1810-1830.
11. Nybø A, Nielsen FG, Godvik M. Quasi-static response of a bottom-fixed wind turbine subject to various incident wind fields. *Wind Energ*. 2021:1-19.
12. Putri RM, Obhrai C, Jakobsen JB, Ong MC. Numerical analysis of the effect of offshore turbulent wind inflow on the response of a spar wind turbine. *Energies*. 2020;13(10):1-22. https://doi.org/10.3390/en13102506
13. Putri RM, Obhrai C, Jakobsen JB. Response sensitivity of a semisubmersible floating offshore wind turbine to different wind spectral models. *J Phys Conf Ser*. 2020;1618:22012.
14. Eliassen L, Bachynski EE. The effect of turbulence model on the response of a large floating wind turbine. In: ASME 2017 36th Int Conf Ocean, Offshore and Arctic Engineering. Trondheim, Norway; 2017. https://doi.org/10.1115/OMAE2017-61179
15. Bachynski EE, Eliassen L. The effects of coherent structures on the global response of floating offshore wind turbines. *Wind Energy*. 2019;22(2):219-238.
16. Godvik M. Influence of wind coherence on the response of a floating wind turbine. *Science meets Industry*. Stavanger, Norway; 2016. http://www.norcowe.no/doc//konferanser/2016/SMIStavangerpresentasjoner/GodvikStatoilInfluenceofthewindcoherenceontheresponseofafloatingwindturbine.pdf
17. Doubrawa P, Churchfield MJ, Godvik M, Sirnivas S. Load response of a floating wind turbine to turbulent atmospheric flow. *Appl Energ*. 2019;242:1588-1599. https://doi.org/10.1016/j.apenergy.2019.01.165
18. Myrtvedt MH, Nybø A, Nielsen FG. The dynamic response of offshore wind turbines and their sensitivity to wind field models. *J Phys Conf Ser*. 2020;1669:12013.
19. Gaertner E, Rinker J, Sethuraman L, et al. Definition of the IEA 15-Megawatt offshore reference wind turbine. Tech. Rep. NREL/TP-5000-75698, Golden, NREL; 2020. https://www.nrel.gov/docs/fy20osti/75698.pdf. Accessed July 2, 2021.
20. Mahfouz MY, Salari M, Hernández S, et al. Public design and FAST models of the two 15MW floater-turbine concepts. tech. rep., Stuttgart, University of Stuttgart; 2020. http://corewind.eu/wp-content/uploads/files/publications/COREWIND-public-design-and-FAST-models-of-the-two-15mw-floater-turbine-concepts.pdf. Accessed July 2, 2021.
21. Obukhov AM. Turbulence in an atmosphere with a non-uniform temperature. *Bound.-Layer Meteorol*. 1971;2(1):7-29.

22. Van Wijk AJM, Beljaars ACM, Holtslag AAM, Turkenburg WC. Evaluation of stability corrections in wind speed profiles over the North Sea. *J Wind Eng Indust Aerodyn*. 1990;33(3):551-566.
23. Danmarks Tekniske Universitet. Mann 64bit turbulence generator. https://www.hawc2.dk/download/pre-processing-tools. Accessed July 2, 2021; 2018.
24. Churchfield M, Lee S, Moriarty P. Overview of the Simulator fOr Wind Farm Application (SOWFA). tech. rep., Golden, NREL; 2012. https://www.nrel.gov/wind/nwtc/assets/pdfs/sowfa-tutorial.pdf. Accessed July 2, 2021.
25. FuE-Zentrum FH Kiel GmbH. FINO1: Forschungsplattformen in Nord- und Ostsee Nr. 1. http://www.fino1.de/en/. Accessed July 2, 2021; 2019.
26. Nybø A, Nielsen FG, Reuder J. Processing of sonic anemometer measurements for offshore wind turbine applications. *J Phys Conf Ser*. 2019;1356:12006.
27. Cheynet E, Jakobsen JB, Reuder J. Velocity spectra and coherence estimates in the marine atmospheric boundary layer. *Bound Layer Meteorol*. 2018;169(3):429-460.
28. National Renewable Energy Laboratory. GitHub - OpenFAST. https://github.com/openfast. Accessed July 2, 2021; 2021.
29. Cheynet E, Jakobsen JB, Snæbjörnsson J, et al. Application of short-range dual-Doppler lidars to evaluate the coherence of turbulence. *Exp Fluids*. 2016;57:1-17.
30. Welch PD. The use of fast Fourier transform for the estimation of power spectra: a method based on time averaging over short, modified periodograms. *IEEE Trans Audio Electroacoust*. 1967;15(2):70-73.
31. Vázquez D'andrea JM. Study of the motions and nacelle accelerations of the Windcrete floating offshore wind turbine according to the IEC 64100-3 procedure. *Master's Thesis*: Escola Tècnica Superior d'Enginyeria Industrial de Barcelona. Barcelona; 2020.
32. National Renewable Energy Laboratory. GitHub - NREL/ROSCO. https://github.com/NREL/ROSCO. Accessed July 2, 2021; 2021.
33. Ziegler JG, Nichols NB. Optimum settings for automatic controllers. *Trans ASME*. 1942;64(11):759-765.
34. Skaare B, Hanson TD, Nielsen FG. Importance of control strategies on fatigue life of floating wind turbines. In: Proc Int Conf OMAE. San Diego, California, USA; 2007:493-500. https://doi.org/10.1115/OMAE2007-29277
35. Skaare B. Development of the hywind concept. In: Proc Int Conf OMAE. Trondheim, Norway; 2017. https://doi.org/10.1115/OMAE2017-62710
36. Souza CES, Bachynski EE. Changes in surge and pitch decay periods of floating wind turbines for varying wind speed. *Ocean Eng*. 2019;180:223-237.
37. Nybø A, Nielsen FG, Godvik M. Analysis of turbulence models fitted to site, and their impact on the response of a bottom-fixed wind turbine. *J Phys Conf Ser*. 2021;2018:12028.


**How to cite this article:** Nybø A, Gunnar Nielsen F, Godvik M. Sensitivity of the dynamic response of a multimegawatt floating wind turbine to the choice of turbulence model. *Wind Energy*. 2022;1-17. doi:10.1002/we.2712

Graphic design: Communication Division, UiB / Print: Skipnes Kommunikasjon AS


uib.no

ISBN: 9788230850770 (print)
9788230848395 (PDF)